INFORMATION TO USERS

This manuscript has been reproduced from the microfilm master. UMI films the text directly from the original or copy submitted. Thus, some thesis and dissertation copies are in typewriter face, while others may be from any type of computer printer.

The quality of this reproduction is dependent upon the quality of the copy submitted. Broken or indistinct print, colored or poor quality illustrations and photographs, print bleedthrough, substandard margins, and improper alignment can adversely affect reproduction.

In the unlikely event that the author did not send UMI a complete manuscript and there are missing pages, these will be noted. Also, if unauthorized copyright material had to be removed, a note will indicate the deletion.

Oversize materials (e.g., maps, drawings, charts) are reproduced by sectioning the original, beginning at the upper left-hand corner and continuing from left to right in equal sections with small overlaps.

Photographs included in the original manuscript have been reproduced xerographically in this copy. Higher quality 6" x 9" black and white photographic prints are available for any photographs or illustrations appearing in this copy for an additional charge. Contact UMI directly to order.

Bell & Howell Information and Learning
300 North Zeeb Road, Ann Arbor, MI 48106-1346 USA
800-521-0600

UMI®

Université d'Ottawa · University of Ottawa

Indoor Infrared Wireless Communication Channels

by

Mohammad Reza Pakravan, B.Sc., M.Sc.

A thesis submitted to
the School of Graduate Studies and Research
University of Ottawa
in partial fulfillment of the requirements
for the degree of

Doctor of Philosophy in Electrical Engineering

Ottawa-Carleton Institute for Electrical and Computer Engineering
School of Information Technology and Engineering
Faculty of Engineering
University of Ottawa
Ottawa, Ontario, Canada

Ottawa, Ontario, Canada
March 2000

ABSTRACT

The emergence of portable computing devices is expected to accelerate the introduction of wireless Local Area Networks (LANs). Portable devices require connectivity with low power consumption, small size and weight. The demand for inexpensive, high-speed communication links satisfying these requirements has encouraged the research on infrared wireless communications.

In this thesis, the fundamentals of infrared communications and different suitable configurations are reviewed. The basic nature of the infrared channel, the differences between the infrared channel and radio frequency channel and the important communication problems faced by infrared systems are explained. An infrared channel simulation algorithm that is used to estimate its impulse response is described. An extensive set of measurements has been performed to investigate the effects of receiver rotation, receiver shadowing, receiver displacement, transmission configuration and communications environments on the characteristics of the infrared channel. The characteristics of the wide-band measurement system that was used to collect the infrared channel transfer functions are presented. The objectives, procedures, results and conclusions of these measurements are discussed and reported.

Diffusers are an important element of infrared transmission systems. They are used to control the radiation pattern of the transmitter for efficiency and eye-safety. Holographic diffusers have been designed and manufactured to provide better infrared radiation patterns. These diffusers were used in the measurement setup to assess the performance enhancements that can be achieved by using holographic diffusers. The results show uniform and efficient use of optical power and better tolerance to shadowing by using these devices.

ACKNOWLEDGMENTS

All praise is due to Allah, the Lord of the Worlds, the Beneficent, the Merciful. Who is the creator, who taught with the pen and who taught man what he knew not. My thanks to his representative in this world, the Imam of the time, Mahdi (AJ) who is the source of all favors and knowledge.

I wish to express my sincere gratitude to my thesis supervisor, Dr. Mohsen Kavehrad, for his constant support and encouragement during the course of my Ph.D. program. In addition, many thanks to my Co-supervisor, Dr. Abbas Yongacoglu who provided me with the required support and encouragement.

I would like to thank Dr. H. Hashemi, Dr. Q. Jiang Dr. E. Simova and Dr. D. Falconer and for all the useful information they provided me and inspiring discussions that we had during my research.

My beloved wife showed constant understanding and was supportive. A mere acknowledgment by no means compensates the hardship she had to go through on the account of my research work.

Last, but not least, special thanks to my parents who always supported me in the wonderful world of science and encouraged me in getting over all the difficulties.

TABLE OF CONTENTS

LIST OF FIGURES

LIST OF TABLES

ACRONYMS

APD	Avalanche Photodiode
AWGN	Additive White Gaussian Noise
CDF	Cumulative Density Function
dBo	Optical dB (10 $\log_{10}(x)$)
dBe	Electrical dB (20 $\log_{10}(x)$)
DD	Direct Detection
EMI	Electromagnetic Interference
FOV	Field-Of-View
FSK	Frequency Shift Keying
FWHM	Full Width at Half Maximum
IEEE	Institute of Electrical and Electronic Engineering
IrDA	Infrared Data Association
IrLAP	IrDA Link Access Protocol specification
IrLMP	IrDA Link Management Protocol specification
IM	Intensity Modulation
IR	Infrared
ISI	Intersymbol Interference
LAN	Local Area Network
LD	Laser Diode
LED	Light Emitting Diode
LOS	Line of Sight
L-PPM	L position Pulse Position Modulation
LTI	Linear Time Invariant

MSC	Multi Sub-carrier Modulation
OOK	On-Off Keying
PAM	Pulse Amplitude Modulation
PDA	Personal Data Assistants
PDF	Probability Density Function
PL	Path Loss
PPM	Pulse Position Modulation
PSD	Power Spectral Density
RF	Radio Frequency
SIR	IrDA Serial Infrared link specification
SNR	Signal to Noise Ratio
UHF	Ultra High Frequency

CHAPTER ONE

1 INTRODUCTION

1.1 MOTIVATION

Wireless communications has transformed the life of people during the recent years. Rapid developments in wireless personal communications devices such as pagers and cellular phones have created a different society with its own characteristics. One of the promising new techniques that could be used to enhance the capabilities of the new generations of communications devices is the use of infrared wireless access.

Infrared light provides an alternative method for communications that has some advantages over radio frequency signaling. These advantages may fit some particular applications and provide a much more economical communication scheme. For example, infrared light is being widely used for short distance point to point connection of portable computers and handheld devices.

The potential offered by infrared communications can be achieved only when details of infrared light generation, modulation, propagation and detection could be well understood. The research in this thesis has been focused on investigating the characteristics of the infrared channel and its dependencies upon parameters such as receiver location, receiver orientation and transmission configuration. This provides better understanding of the expected behavior of this channel and the results can be used for designing better communication devices that use infrared light as their carrier.

1.2 OUTLINE OF THE THESIS

This thesis is organized into nine chapters. The first chapter covers motivations and gives a brief outline of the thesis and its contributions. In the second chapter, fundamentals of the infrared communications systems are reviewed and different optical configurations used for these systems are illustrated. The basic nature of the infrared channel is explained and modeled and the differences between an infrared channel and a radio frequency channel are discussed. Important parameters of an infrared system are defined and described and the characteristic of background noise sources that is of particular importance for infrared systems is briefly reviewed.

Simulation and measurement of infrared channel are two important tools that are needed to investigate the effects of channel parameters on the channel behavior. Chapter 3 covers the details of simulation of an infrared channel and describes the simulation mechanisms and its parameters. A wideband measurement system that has been used for characterization of infrared channel is described. A brief overview of the measurement setup and its parameters is presented. The measurement procedure, system calibration and data processing algorithms are explained in this chapter.

Chapter 4 investigates the effects of transmission configuration on the characteristics of the infrared channel. Different configurations are presented and compared in terms of their ability to reduce the channel path loss or provide more uniform distribution of the received optical power in a given area. Advantages and disadvantages of the proposed schemes based on their multipath dispersion as well as implementation suitability are also investigated in this chapter. It is shown that an appropriate configuration can have an important impact on the coverage area of an infrared system.

Chapter 5 presents the results of the measurements performed to investigate the effects of rotation on the infrared channel characteristics. These measurements were conducted in different rooms in the School of Information Technology and Engineering at the University of Ottawa. They contain more than 6000 sets of measured channel transfer functions. They form a unique and comprehensive database that can be used to extract general site-independent behavioral characterizations of infrared channel. The measurement procedure and the obtained results are presented. Using these results, an algorithm is presented that can

accurately predict the variation of channel path loss for a rotating receiver without performing measurements.

Chapter 6 investigates the effects of receiver displacement on the characteristics of the infrared channel. Simple mathematical models are developed to provide an analytical view on the channel variation with respect to displacement. Sets of measurements have been performed to investigate this effect in real-life environment. The measurement procedure and its results are also presented in this chapter. The results of these measurements are used to design an algorithm that can be used to accurately predict the variation of channel path loss and channel delay spread as a result of receiver displacement.

Chapter 7 addresses the issue of shadowing and its impact on the characteristics of indoor infrared channel. Measurement setup is used to collect 320 channel transfer functions that correspond to different shadowing scenarios. Important parameters that specify the shadowing are identified and their effects on the channel characteristics are presented.

One of the important parts of an infrared communication system is the diffuser that is employed at the transmitter to change its radiation pattern. Using the ideas developed and presented in Chapter 4, two holographic diffusers have been designed and manufactured. These diffusers were used in the measurement set up to assess the performance enhancements that could be achieved by using holographic diffusers. The results of this exercise are presented in Chapter 8.

Chapter 9 contains the conclusions of this research and suggestions for possible future research activities in this field.

1.3 THESIS CONTRIBUTIONS

The results reported in this thesis build upon teamwork led by Dr. Kavehrad. The research was supported by grants from the Canadian Institute for Telecommunication Research (CITR). The measurement setup that has been extensively used to perform the channel measurements was designed and built primarily by Dr. Q. Jiang who worked as a research associate in broadband communications research laboratory (BCRL) at the University Of Ottawa. Measurements of the rotation effect and shadowing effects were performed by Dr. H. Hashemi and Ming Tai. Parts of the measurements of the displacement effects were also performed by them and the rest were performed by the author. Dr. Eli Simova implemented

the holographic diffusers based on author's specifications and helped the author with the measurements that investigated their importance for infrared systems.

Contributions of the author during this research are summarized below.

- Enhancement to the simulation algorithm presented in Chapter 3 to increase its speed and allow it to be used for simulation of multiple sources with controlled field-of-view configurations.
- Investigation of different transmission configurations on the channel characteristics using the simulation algorithm. Propose several power efficient configurations and compare their merits for different applications.
- Contribution to the specifications and design parameters of the measurement setup.
- Contributions to the implementation of the measurement setup by providing help in the development of the interface between computer and the measurement system.
- Proposing the measurements to include the diffuse configuration and building the glass diffuser head of the setup for this purpose.
- Contribution to the measurement planning and execution for rotation and shadowing measurements.
- Processing all the recorded data from the measurements. That includes the measurements addressing the effects of rotation, displacement, shadowing and transmission configurations. Programs have been developed to convert files, normalize and preprocess results, calculate channel parameters in time and frequency domain, present results in appropriate formats and save them for further modeling analysis.
- Providing data processing algorithms to differentiate between the effects of noise+interference and the infrared channel in the recorded results.
- Processing the recorded data for the rotation measurements using a piecewise linear algorithm. Results are used to illustrate and explain the general behavior of the channel transfer function in different frequencies for a rotating receiver.
- Provide an algorithm that can be used to accurately predict the angle of maximum received optical power in a rotating receiver.
- Using the rotation results to show that the variation of the channel path loss with respect to rotation angle can be accurately modeled using a 4^{th} order polynomial curve fitting algorithm and by knowing only 5 equally spaced points in the span of 0° to 180°.

- The one-bounce simulation results have a considerable error at the ends of the curve that relates the variation of channel path loss to the elevation angle of the receiver. It is shown that this error can be predicted from the knowledge of the system configuration. Provide an algorithm to estimate this error and thereby enhance the results of the simulation algorithm
- Propose an algorithm to extend the above observation to include enhancement of the accuracy of the entire path loss curve for a rotating receiver. Use the measurement results to show the improvements in the path loss estimate using the proposed algorithm.
- It is shown that when the receiver is rotated, the channel path loss and the channel delay spread are correlated. The measurement results are used to derive the equation that relates these two parameters.
- Perform parts of the measurements addressing the effects of receiver displacement on the channel characteristics.
- Analyze the results of these measurements and present the effects of the receiver displacement on channel characteristics.
- The one-bounce simulation algorithm provides channel parameters that are not accurate. Using the results of the displacement measurements, an algorithm has been developed and proposed that can enhance the accuracy of the estimated channel path loss and channel delay spread using the knowledge of the transmission and reception configuration when the receiver is displaced.
- It is shown that when the receiver is displaced, the channel path loss and the channel delay spread are highly correlated. Using the measurement results, the equation relating these two parameters is found and reported.
- The results of the shadowing measurements are processed, analyzed and presented. Three important parameters that determine the amount of shadowing are described and their respective effects are presented.
- Specifying the transmission pattern for the desired holographic diffusers.
- Performing the measurements that investigate the effects of holographic diffusers on channel characteristics.

- Analyzing the measurement results to compare the holographic diffusers against the glass diffusers. Demonstrate advantages offered by holographic diffusers in terms of uniform power distribution and providing a link with more resistance to shadowing.

CHAPTER TWO

2 INFRARED LIGHT FOR INDOOR WIRELESS COMMUNICATIONS

2.1 INTRODUCTION

The emergence of portable terminals is expected to accelerate the introduction of wireless Local Area Networks (LANs). Portable devices require low power consumption, small size and weight. The demand for inexpensive, high-speed links satisfying these requirements has encouraged the research on infrared wireless communications. Using infrared (IR) light for indoor wireless communications is a promising technique with its own advantages compared to radio frequency waves (RF) [82][83][84][103]. At infrared, there is an abundance of bandwidth, which is free from regulation at the moment. Infrared light does not pass through walls and therefore is confined to the same room in which it originates. Hence, each room is a separate cell without mutual interference with its neighbors. This is a major advantage for infrared compared to RF because it allows many neighboring cells in a large building to operate independent infrared links without any interference problem. Infrared devices are immune to electromagnetic interference (EMI) and this makes them an interesting choice for environments with high levels of EMI such as factories [66][29]. It should be noted that light itself is an electromagnetic wave and from a physical point of view, EMI includes infrared light frequencies. However, light detectors used in infrared receivers operate in a frequency range that is far above the frequency of devices that use radio waves. Therefore, these systems are

immune from interference caused by radio wave communication devices or electrical devices that generate radio waves in their operations.

Infrared devices are compact, consume little power and due to high volume production of commercial devices operating in this wavelength region such as compact disks and remote controllers, can be very inexpensive.

Using infrared for indoor communications has its own disadvantages, too. Due to the limited range of optical signals and their blockage by solid objects, the transmitter and the receiver must be located in the same room. If ad-hoc networking for peer-to-peer computer networking is desired, this does not impose a limitation. However, if connection to a backbone wired network is desired, a base station or access point is required for each room. This could potentially increase the installation cost of a wireless infrared-based network compared to its RF counterpart. Optical transmission is also very sensitive to shadowing by solid objects. Although there are techniques to reduce this sensitivity, there is no way an optical device can compete with a low frequency range RF device in its tolerance to shadowing and blockage.

Recently, there has been a growing interest in using infrared technology for wireless communications. Computer networking seems to be an interesting application for infrared technology [67]. A major interest is in using infrared as a means of wireless transmission of signals for the existing LANs using IEEE 802.11 standards. Allowing wireless connection to a backbone cabled LAN without the need for changing the LAN protocols is a major interest for commercial applications [15][67][106][34][117]. Currently, there are some available commercial products that operate on Ethernet™ or Token ring™ networks [50][41]. These products allow a user to install an infrared device in their computer and connect to the backbone LAN through a base station as if they are connected using physical wires. IEEE 802.11 group has been formed to standardize wireless access to existing cabled LANs through infrared and RF carriers.

There has also been some works in using infrared for transferring signals with IEEE 488 and RS-232/RS-423/RS-422 format [16][17]. Infrared can also be used for low cost, consumer appliances. A remote TV controller is a typical example. Other recent works have used infrared for transmission of high quality, audio signals to small portable receivers [4][18] or to theater stereo speakers [27][48]. In some museums, an infrared transmitter is mounted on the ceiling nearby a picture or sculpture. A viewer who is standing in front of the picture can listen to the audio description of the artwork that is delivered through infrared to a receiver mounted

on top of his headphone as he is viewing it. This is a good example of an application where the limited range of infrared allows co-existence of many independent, non-interfering transmission cells within a limited area.

One of the most successful initiatives for implementation of infrared technology for data communication is the Infrared Data Associations (IrDA). In late 1993, an industrial group spearheaded by HP, IBM, and Sharp was founded to set and support hardware and software standards, which create infrared communications links. The Association's charter is to create an interoperable, low-cost, low-power, half-duplex, serial data interconnection standard that supports a walk-up, point-to-point user model that is adaptable to a wide range of applications and devices. IrDA standards support a broad range of computing, communications, and consumer devices. IrDA connectivity is being incorporated into most PC notebooks to bring the most cost-effective and easy to use support available for wireless technologies. The important features of IrDA standard are:

- Simple and low cost implementation
- Low power requirement
- Directed, point-to-point connectivity
- Efficient and reliable data transfer.

There are few US, European or other international regulatory constraints for infrared. Manufacturers can ship IrDA-enabled products globally without any constraints, and IrDA functional devices can be used by international travelers wherever they are, and interference problems are minimal.

IrDA has developed some standards for infrared communications. In September 1993, IrDA determined the basis for the IrDA SIR Data Link Standards. In June 1994, IrDA published the IrDA standards, which includes Serial Infrared (SIR) Link specification, Link Access Protocol (IrLAP) specification, and Link Management Protocol (IrLMP) specification. IrDA released extensions to SIR standard including 4Mb/S in October 1995. The IrDA standard specification has been expanded to include high-speed extensions from 1.152 Mbps and 4.0 Mbps. This extension will require an add-in card to retrofit existing PC's with high-speed infrared, and synchronous communications controller or equivalent.

In 1995, several market leaders announced or released products with IR features based on IrDA standards. These products include components, adapters, printers, PC's, personal data assistants (PDA), notebook computers, LAN access, and software applications. In November

1995, Microsoft Corporation announced that it has added support for IrDA connectivity to the Microsoft Windows 95 operating system, enabling low-cost wireless connectivity between Windows 95 based PC's and peripheral devices. This support will be maintained in the future releases of the Windows operating system.

IrDA featured devices are predicted to be widespread for the business and mobile environments in future homes and offices. It is estimated that 80-90% of notebooks shipped in 1998 have the IrDA port installed. Future PC bus architectures will allow many connected devices to be accessed via a single IrDA access point. Widespread adoption of infrared is driven by the low cost of implementing the cordless convenience feature in new products.

Some of the infrared consumer applications available today and in the future include printing a document directly from a notebook, synchronizing electronic telephone books and schedulers, exchanging business cards between handheld PC's, sending and receiving faxes or email directly from a notebook PC through a cellular or traditional public telephone, or storing bank records from ATM machines by making a simple, walk up and point infrared connection.

Industrial and service data collection applications will expand dramatically utilizing mobile IrDA enabled devices to improve control, documentation and docking procedures in the workplace. Future devices will be able to access home entertainment, security, and automated environment control systems.

There is also a rapidly growing interest in using infrared for broadband indoor wireless communications [51][11]. Future portable computers need wide band connections to the cabled backbone LANs to transfer high data rates in multimedia communications. Data rates of more than 10 Mbps are needed for true multimedia communications in the future portables. Speaking of this range of data rates, there are major technological limitations ahead of both RF and infrared technology. Noting that a portable terminal has a limited battery power and has to be inexpensive, lightweight and small, the challenge of providing such a service is an important research area for scientific community.

Theoretical studies on modulation and coding aspects of a broadband indoor infrared system have been done by many researchers [23][5][6][20][8][62][61][63][9]. Among different modulation techniques, On-Off Keying (OOK) and L-Pulse Position Modulation (L-PPM) seem to be more attractive for infrared communications. OOK is simple and easier to equalize. L-PPM is more power efficient but is generally more complex to equalize. A brief overview of

the common modulation schemes for infrared communication systems is presented in the last section of this chapter.

2.2 OPTICAL CONFIGURATIONS

Indoor-unguided optical communications can be implemented in several different ways. Figure 1 [12] shows different possible configurations for an optical link. A directed LOS configuration, illustrated in this figure, uses a collimated beam from the transmitter to the receiver and a narrow Field-Of-View (FOV) receiver. Alignment between the receiver and transmitter is essential in this configuration. Such a configuration is suitable for one-to-one communications and for each additional receiver, there is a need for an additional transmitter looking into that direction. In this configuration, light signal is confined to a narrow beam and the receiver with a limited FOV detects only the light signals from the transmitter direction. There are almost no reflections of light by other objects detected by the receiver and therefore there is no multipath problem in this configuration. Confinement of light to a limited direction also allows a more efficient use of optical energy in carrying information. Power levels can be increased up to the safety limits, increasing the resulting SNR for this configuration. Hence, it is possible to achieve very high data rates using this configuration.

Yen and Crawford [124] presented a wireless link using narrow beam infrared transmitters with a beamwidth of 3° in the base station and 2° in the portables. They reported a bit rate of 1 Mbps over a 50 m range using 165 mW from the base station to the portable and 5 mW from the portable to the base station. Chu and Gans [24] proposed a system using several 1° pencil beams each carrying 1 mW optical power. They achieved a data rate of 50 Mbps over a range of 30m. There are also commercial products on the market using this configuration. BICC Communication is marketing a product that can achieve a range of 24 m at a rate of 4 Mbps. A.T.S. Communications Co. [50] is selling Ethernet compatible devices using narrow 6° beam transceivers to transfer LAN traffic at a rate of 10 Mbps in a ring configuration.

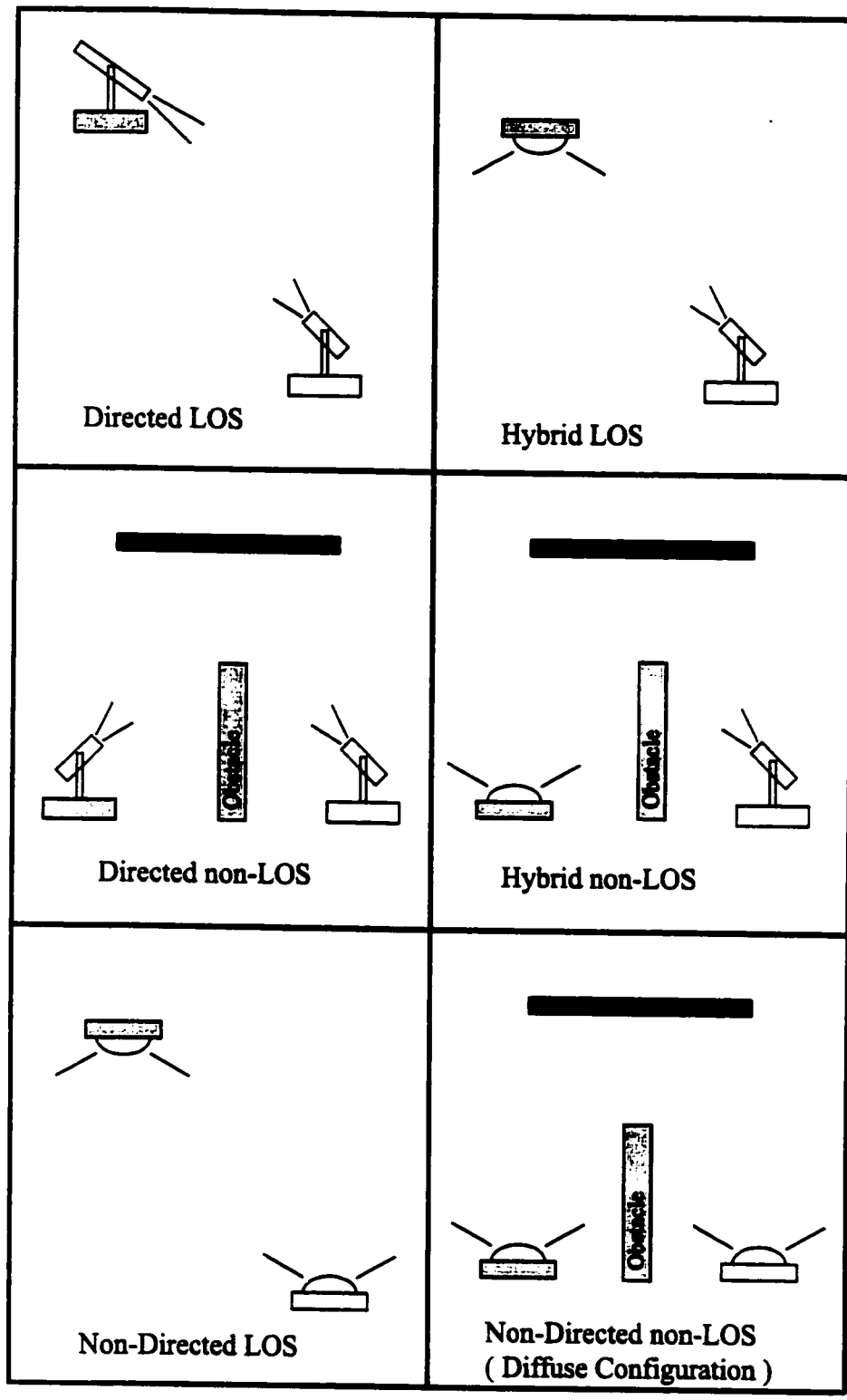

Figure 1. Configurations for optical wireless links (from [12])

There are reports of very high-speed commercial devices as well. For example, a bit rate of 125 Mbps was achieved by using a transmitter beamwidth of 1° and a receiver FOV of 6° over a 30 m range by JDL 889-LS transceivers built by JOLT, Ltd. [53]. McCullagh, *et al.* [73] proposed a directed LOS link capable of achieving speeds of up to about 1 Gbps. Their proposed system also includes a tracking mechanism in the base station that follows the position of the portable and sends optical signals in a narrow beam to the proper direction.

The IrDA Physical Layer Specification can also be categorized in this type of configurations. It sets a standard for the infrared transceiver, the modulation or encoding/decoding method, as well as other physical parameters. IrDA uses infrared with peak wavelength of 0.85 to 0.90 micrometer. The transmitter's minimum and maximum intensity is 40 and 500 mW/Sr within a 30° cone. The receiver's minimum and maximum sensitivity is 0.0040 and 500 mW/cm^2 within a similar 30° cone. The link length is zero to 1 m directed LOS with a bit error rate of less than 10^{-8}.

Directed LOS configuration is not capable of handling many-to-one and one-to-many communications links. A directed non-LOS configuration shown in Figure 1 may solve this problem (second row, left). A common point is used for all the transmitters and all the receivers to look at for proper reception of optical energy. Narrow beam transmitters and narrow FOV receivers are used in this configuration. The common point on the ceiling reflects the incoming beam according to a Lambertian pattern, making it possible for all terminals across the room looking toward the common point to receive a portion of the optical energy from that point. The radiation pattern of a Lambertian source and its associated parameters are described in Chapter 3. Such a configuration was proposed by Minami, *et al.* [76] for peer-to-peer communications of their wireless modem operating at 19.2 kbps. A product by Photonics group developed in 1985 used this configuration to achieve a bit-rate of 230 kbps over a 22 meters range. Similar ideas was also proposed in [123] and [85] using directed beams toward some diffusing spots on the ceiling to provide diversity against shadowing.

A hybrid LOS configuration is made by putting a repeater or a base station on the ceiling and transmitting up-link signals using a wide beamwidth. A narrow FOV receiver then picks up the optical energy by looking in the transmitter direction. Minami used this configuration for base to portable communications of their optical modem operating at 19.2 kbps. A similar work reported by Nakata, *et al.* [80] used this configuration to achieve a bit rate of 1 Mbps over a

range of 5 m by transmitting 300 mW in a wide beam of 120° in the downlink and a 10° beam in the uplink.

Hybrid non-LOS system is made by allowing an infrared source to transmit optical energy in a wide beam, illuminating the entire ceiling of a room. A narrow FOV receiver is then used to collect the light from the ceiling or a proper direction. This configuration is also shown in Figure 1 in the second row, right graph.

None of the mentioned configurations is suitable for portable many-to-many wireless communications. A portable communication system needs to operate without any alignment requirement. Therefore, the only possible choices are non-directed configurations, either LOS or non-LOS known as a diffuse configuration throughout this thesis.

A non-directed non-LOS configuration was first proposed by Gfeller, *et al.* [39]. In this configuration, the transmitter illuminates the ceiling with a wide beam and a wide FOV receiver detects the signal energy from the reflected rays. Such an arrangement does not require alignment between the transmitter and the receiver. Gfeller showed that the ratio of the light reflected from the surface of typical office materials is in the range of 40% to 90% in the infrared wavelength region. He also showed that in most cases, the pattern of reflected light could be described by a Lambertian pattern. This shows that reflections do not weaken the signals too much and a receiver would be capable of receiving energy from the reflected rays. In a diffuse configuration, the ceiling acts as a distributed source of optical energy. Therefore, this configuration is much more tolerant to shadowing than its counterparts, because it is difficult to block the wide FOV receiver from seeing the ceiling. It is obvious that in a diffuse configuration, the receiver should detect a signal from a sum of delayed and attenuated pulses that arrive at the receiver after multiple reflections. A result of this process, multipath distortion, is the major drawback of this configuration that limits transmission at high data rates.

A non-directed LOS configuration is also illustrated in Figure 1. The receiver in this configuration has a wide field of view. Therefore, there is no need for alignment. However, the path between transmitter and receiver should be kept unobstructed. This configuration uses optical energy more efficiently and results in much less distortion due to multipath. The direct path between transmitter and receiver carries most of the received energy, forcing the multipath effect to be negligible compared to that in the diffuse configuration. Importance of LOS path makes this system more sensitive to shadowing compared to diffuse configuration.

It is possible to use several passive reflectors to provide multi-LOS coverage for an indoor environment [85]. Although such a system still relies on an unobstructed path LOS, due to the existence of multiple sources, the system is more tolerant to shadowing.

There are other important aspects in the design of an optical wireless communication system. Background radiation of other optical sources such as sunlight, fluorescent and incandescent lamps produce a strong noise component in the signal detected by a photodetector [64]. Therefore, narrow-band optical bandpass filters should be used to reduce the amount of detected background radiation. In a non-directed configuration, this filter should have a wide FOV to be able to detect the incoming beams from all directions. This makes the design of such a filter a challenging problem [19][12][69-28].

Another important aspect of optical design of a system is the radiation pattern of a transmitter and the transmission area. Eye safety limits restrict the power emitted from infrared point sources [47][1]. To increase the coverage of a transmitter, the transmitted infrared power has to be increased. To increase the transmitter power without exceeding the eye-safety limits, the radiation area or the radiation pattern of the transmitter should be increased. That implies the use of diffusers for the transmitter. Diffusers are particularly important if a laser diode is the source of infrared transmission. Laser diodes usually have a more focused beam and are capable of transmitting higher levels of optical power with a shorter optical line-width. Therefore, diffusers are needed to shape their radiation pattern and prevent exceeding the eye-safety radiation limits.

Diffusers could be simple glass diffusers or sophisticated computer generated holograms. New holography techniques have been proposed for these purposes [75-113]. The holographic diffusers can change the radiation pattern of an infrared source and result in a more efficient optical link. They are also less bulky and could be mass-produced very inexpensively. The last chapter of this thesis is devoted to the discussions about the design and implementation of holographic diffusers that increase the coverage of the source, make it eye-safe and make the optical link more resistant to shadowing.

2.3 INDOOR INFRARED CHANNEL

Consider a non-directed infrared transmission system as shown in Figure 2. This system contains an optical source that converts electrical signals into optical intensity, a photodiode

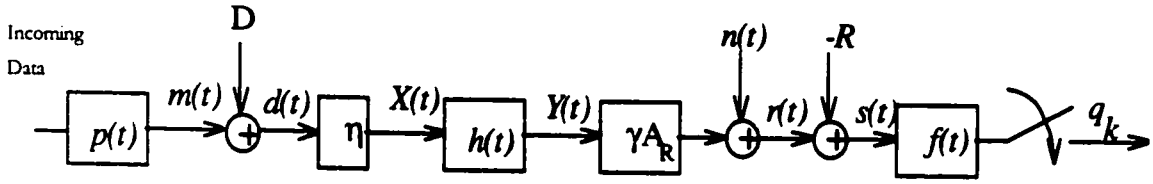

Figure 2. Block diagram of an infrared transmission system (from [60])

receiver that detects the optical signal and converts it to an electrical signal. Generated optical signal passes through the media between the transmitter and the receiver. The media attenuates the signal and spreads its energy in time.

In this thesis, the focus of the analysis is on systems that employ wide FOV photodetectors that collect the light from all directions, converting the optical intensity of the received signal to an electrical current. This is a process called Direct Detection (DD). In addition, the optical source in this discussion modulates the intensity of the transmitted optical signal to carry information. Intensity modulation at the transmitter and direct detection at the receiver, (IM/DD), is the most feasible choice for non-directed optical communications [12].

Transmission of a digital stream from the transmitter to the receiver is summarized in Figure 2 [60]. An analog signal, $m(t)$, is generated by applying a proper modulation scheme, $p(t)$, to an incoming stream of digital information. This can be any digital modulation. Some possible examples are Pulse Amplitude Modulation (PAM), Frequency Shift Keying Modulation (FSK), Multiple Sub-carrier Modulation, or Pulse Position Modulation (PPM). One of the simplest modulation techniques used in IR systems is 2-level PAM also known as On-Off-Keying (OOK) [12]. This signal is used to modulate the current of an optical signal generator device such as a laser diode (LD) or a light emitting diode (LED).

These devices should be driven with a positive current to generate an optical signal. To insure this, a proper dc bias, D should be added to the signal before modulating the optical device with it. Changing the driving current of the optical device changes the intensity of the generated optical signal, with a conversion ratio, η. Therefore, $X(t)$, the intensity of the optical signal (optical power) is related to $d(t)$, the driving current, by: $X(t)=\eta d(t)$.

The transmitted optical power $X(t)$ is reflected by the objects of the environment and the direct and reflected light rays reach the receiver. As it is shown in the next section, the received photocurrent is related to the transmitter optical power through a real valued impulse response.

2.4 LINEAR MODEL OF THE INFRARED CHANNEL

In this section, it is shown that in a non-directed infrared link using IM/DD, the total received optical photocurrent $Y(t)$ is related to the total transmitted optical power by $Y(t) = X(t) \otimes h(t) + n(t)$ where $h(t)$ is the real valued impulse response of the channel [21]. To simplify the derivation, the noise term is neglected and the detector is considered as it is shown in Figure 3. At detector position (x,y), the total incident electric field $\vec{E}(x, y)$ can be written as the sum of electric-field components arriving along direction (φ,θ) after undergoing k bounces en route from the source, denoted here by $\vec{e}(x, y,\theta,\varphi)$:

$$\vec{E}(x, y) = \sum_{k=0}^{\infty} \int_{2\pi} \vec{e}(x, y,\theta,\varphi) dA$$

The integration is performed over the entire solid angle above the detector. Assuming that the transmitted signal is narrow-band, the electric-field components can be expressed as:

$$\vec{e}(x, y,\theta,\varphi) = \vec{\alpha}_k(x, y,\theta,\varphi)\sqrt{X(t-\tau_k(x, y,\theta,\varphi))}e^{j[\psi_0(t)+\psi_k(x,y,\theta,\varphi)]}$$

Here, $\vec{\alpha}(x, y,\theta,\varphi)$, assumed to be real, describes the magnitude and polarization of the field component arriving along direction (φ,θ) after undergoing k bounces. All attenuation along the propagation path or within the receiver collection is described by this parameter. The quantity $\tau_k(x, y,\theta,\varphi)$ describes the group delay of intensity modulated envelope. The phase factor includes the propagation phase $\psi_k(x, y,\theta,\varphi)$ in addition to the path-independent carrier phase $\psi_0(t)$.

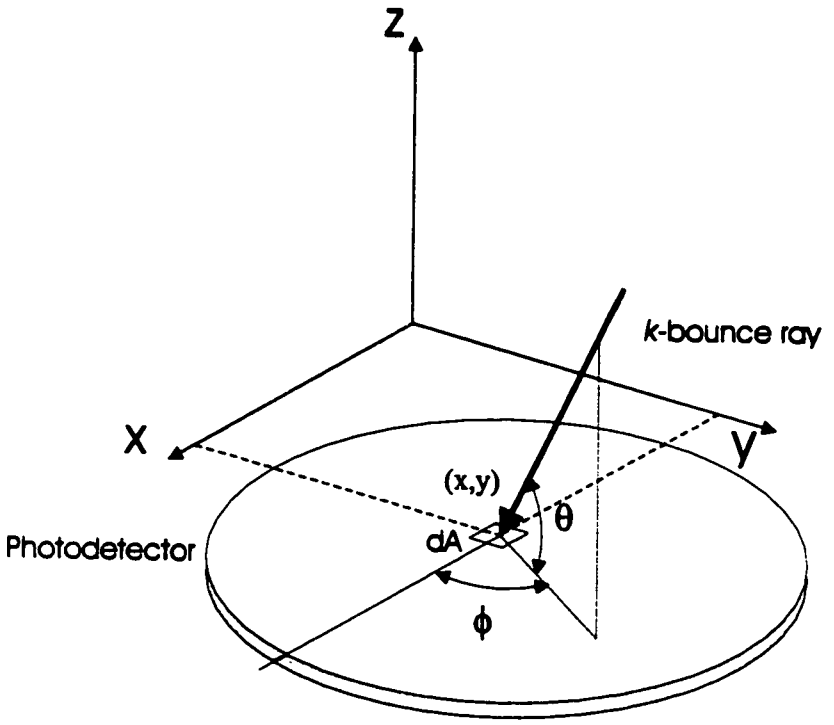

Figure 3. Geometry used in the derivation of the channel model

Neglecting the shot noise, the total photocurrent is given by:

$$Y(t) = \frac{c\varepsilon_0 \gamma}{2} \int_{detector} dA \, | \vec{E}(x,y) |^2$$

where γ is the detector responsivity and the integral is over the detector surface. A simplifying assumption is made that $\vec{\alpha}(x,y,\theta,\varphi) \approx \vec{\alpha}(x,y)$ and $\tau_k(x,y,\theta,\varphi) \approx \tau_k x,y)$, i.e., along a given path the attenuation and delay are the same to all points on the detector surface. Clearly, the same is not true for the phase. The total photocurrent becomes:

$$Y(t) = \frac{c\varepsilon_0 \gamma}{2} \sum_{k=0}^{\infty} \sum_{k'=0}^{\infty} [\int_{detector} dA e^{j[\psi_k(x,y,\theta,\varphi) - \psi_{k'}(x,y,\theta',\varphi')]} \times$$

$$\int_{2\pi} d\Omega \times \int_{2\pi} d\Omega' \vec{\alpha}_k(\theta,\varphi) \vec{\alpha}_{k'}(\theta',\varphi') \sqrt{X(t-\tau_k(\theta,\varphi)) X(t-\tau_{k'}(\theta',\varphi'))}$$

Examining this integral that is taken over the detector surface, it is obvious that when $k \neq k'$ or (φ,θ) differs even slightly from (φ',θ'), the phase term $\psi_k(x,y,\theta,\varphi) - \psi_{k'}(x',y',\theta',\varphi')$ undergoes changes of the order of 2π radians as x or y changes by a distance of the order of

the wavelength. Since the integral is taken over a region whose dimensions are much larger than the wavelength, the integral vanishes. When $k=k'$, the integral and $(\varphi,\theta)=(\varphi',\theta')$, the integral takes on a value equal to the detector surface area A_R. Hence, this integral can be expressed approximately as:

$$\int_{\text{detector}} dA e^{j[\psi_k(x,y,\theta,\varphi)-\psi_{k'}(x,y,\theta',\varphi')]} \approx A_R \delta_{kk'} \delta(\cos(\theta)-\cos(\theta'))\delta(\varphi-\varphi')$$

where δ_{mn} is the Kronecker delta and $\delta(x)$ is the Dirac delta function. Substituting this expression into the $Y(t)$ expression, integrating it over Ω' and summing it over k' results in:

$$Y(t)=\frac{c\varepsilon_0\gamma}{2}\sum_{k=0}^{\infty}\int_{2\pi} d\Omega X(t-\tau_k(\theta,\varphi))\,|\vec{\alpha}_k(\theta,\varphi)|^2$$

This expression can be written as $Y(t)=X(t)\otimes h(t)$ where

$$h(t)=\frac{c\varepsilon_0\gamma A_R}{2}\sum_{k=0}^{\infty}\int_{2\pi} d\Omega \delta(t-\tau_k(\theta,\varphi))\,|\vec{\alpha}_k(\theta,\varphi)|^2$$

It is seen that the impulse response $h(t)$ can be viewed as the sum of separate impulse responses $h^{(k)}(t)$, each describing the contribution from the light that has undergone exactly k reflections en route from the source. Each k-bounce impulse response $h^{(k)}(t)$ is a collection of unit impulses arriving from direction (φ,θ), delayed by the propagation delay $\tau_k(\theta,\varphi)$ and scaled by the power attenuation factor $|\vec{\alpha}_k(\theta,\varphi)|^2$. It should be noted that these two quantities depend only on the macroscopic features of the propagation paths. When the propagation path lengths are changed by a wavelength, there are no observable changes in $|\vec{\alpha}_k(\theta,\varphi)|^2$ and $\tau_k(\theta,\varphi)$. Thus, there is no measurable change in the channel impulse response, i.e., no "multipath fading".

The receiver photodiode converts the received optical signal intensity to an electrical signal (current) with a conversion ratio γ that is sometimes referred to as the photodiode efficiency. The amplitude of the generated current is also proportional to the area of the photodetector, A_R. Background light is also detected by the photodiode and generates a dc current plus an additive white noise, $n(t)$. The dc component of the photodiode output is removed by subtracting R from $r(t)$ and the result is passed through the receiver matched filter $f(t)$. Decisions are made based on the samples of the output of this filter.

For some types of office background light sources such as fluorescent lamps and ballast type lamps, the induced background noise varies in time and the resulting noise signal at the receiver has harmonics that could range up to 1 MHz [3]. High pass filtering of the received signal could be employed to reduce the effects of noise in these environments.

2.5 INFRARED CHANNEL AND RADIO FREQUENCY CHANNEL : A COMPARISON

There are some major differences between an infrared channel and a conventional radio frequency (RF) channel [86][87]. In RF channels, the wavelength of the carrier is in the order of millimeter[1] (GHz range of frequencies) or centimeter (UHF range) while in the infrared, the wavelength is in the 700-900 nm range. In addition, in IM/DD systems, the intensity of optical signal carries information while in radio the amplitude and phase of the radio wave carry the information. Consequently, multipath effects in radio channels are different from optical channels. In radio, carrier signal cancellation due to multipath induces fading in the received signal. These fades occur in space, time or frequency and can potentially cause deep nulls in the frequency response of the received signal or huge reduction in the level of received signal. In an optical channel, the size of photodiode is in the mm-range, thousands of times larger than the infrared wavelength. There is a built-in averaging process in the photodiode which, adds up the peaks and nulls due to cancellation in the optical carrier frequency range. Therefore, the output of the photodiode will never go to zero because of the fades due to multipath. An illustration of this phenomenon is presented in Figure 4. This is why an infrared channel is a baseband channel. Note that, the averaging process averages out space-domain nulls while there are still frequency-domain nulls due to multipath effect in infrared channels. In other words, regardless of the dimension of the detector, the frequency response of an infrared channel may have nulls and peaks. In the following chapters, some samples of the frequency response of infrared channels with nulls and peaks are shown. These nulls and peaks are a result of multipath dispersion caused by reflection of optical signals from reflectors.

---

[1] As an example, a sine wave radio signal with a frequency of 10 GHz has a wavelength of $\lambda = c/f = (3\times10^8)/(10\times10^9) = 0.03$ m = 30 mm

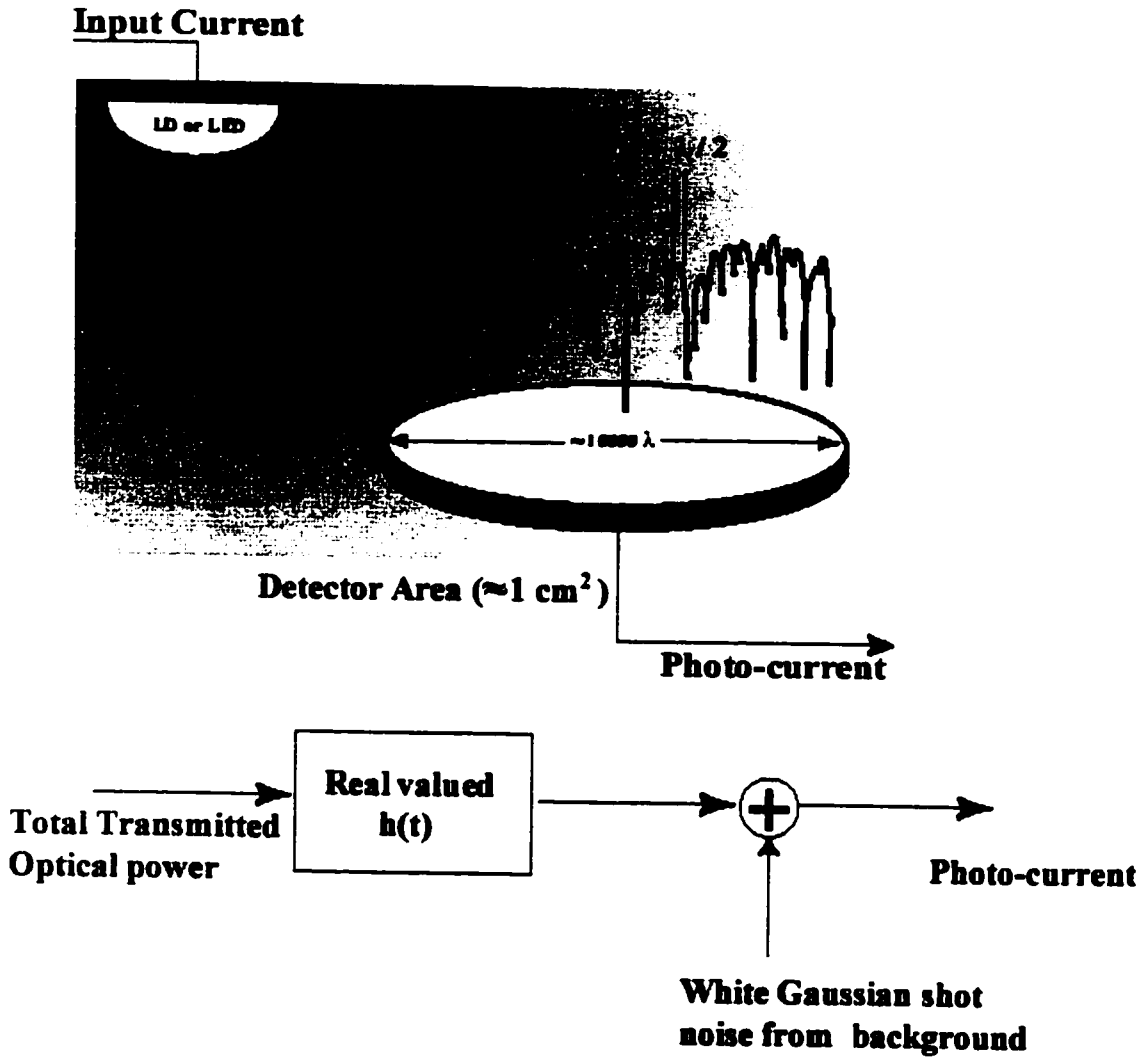

Figure 4. Size of a photodetector is several thousands times larger than the infrared wavelength. Therefore, the photodiode averages out peaks and nulls resulting from cancellation of the carriers in the optical frequency range. The counterpart to this process in conventional radio communications is like when several thousands of antennas are used and the outputs of the antennas are squared and fed into the receiver. (top figure modified from [53])

The process of averaging in a photodiode is as if thousands of antennas, each with a size smaller than the wavelength, are placed in the receiver. Then non-coherent square law detectors for each antenna branch is used and the results are added to produce the output. It is evident that there won't be any nulls due to carrier-level signal cancellation in this

configuration. Another view of a photodiode in DD systems is to consider it as a photon counting device that generates electrical current from detected photons. It is obvious that fading and cancellations can not reduce the number of received photons to zero. That will happen only if the receiver is blocked from receiving optical energy.

As a conclusion, processes like flat or Rayleigh fading in radio channels, which distort the incoming signal regardless of bit-rate, are effectively not present in the IM/DD optical channels. Distortion of the signal in an infrared channel is a result of intersymbol interference (ISI) which is caused by the spread of the signal energy in time. This kind of distortion is related to the signaling rate over the channel. A system operating at low baud rates will not experience such distortions while high bit rate systems need to use equalizers to reduce ISI. In addition, this averaging process makes infrared detectors less sensitive to location than a radio detector. In RF channels, huge differences in the received power can happen with small movements of the receiver. In infrared, noticeable change in the channel characteristics happen only when there is considerable movements of the receiver in the order of tens of centimeters or when there is shadowing.

RF antennas are sometimes omni-directional, making them almost direction insensitive, but an infrared photodiode can have a maximum Field of View (FOV) of 90°. Receiver Field of View (FOV) is defined to be the angle between the photodiode surface normal and the maximum angle from which the receiver can detect light. This is illustrated in Figure 5. In general, infrared systems are much more sensitive to rotation than RF systems. Although, channel characteristics do not change in an infrared system with small spatial movements, they could change considerably with rotation. The effect of rotation on the channel transfer function are investigated in subsequent chapters.

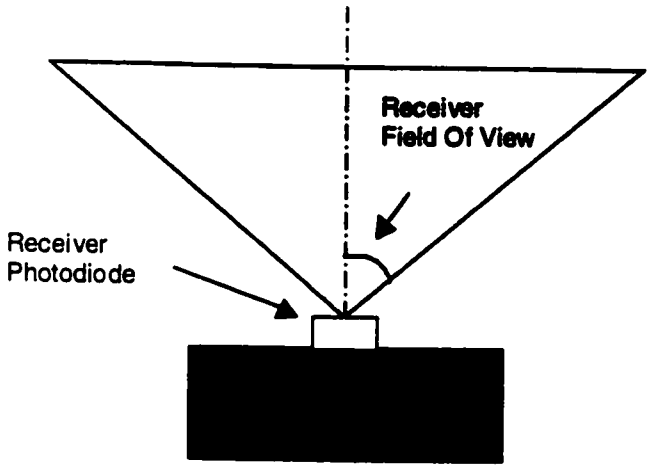

Figure 5. An infrared receiver has a limited range of detection angles. Receiver Field of View (FOV) is defined to be the angle between the photodiode surface normal and the maximum angle from which the receiver can detect light.

2.6 NOISE

Figure 6 shows the power spectral density of three common illumination sources: fluorescent light, sunlight, and incandescent light [39]. It is seen that the sunlight and the incandescent light both have strong components in the operating wavelength of infrared systems. The power of the background light can be tens of times more than the received signal. For example, IrDA-compatible infrared systems should be able to tolerate sunlight signal intensity of 490 $\mu W/cm^2$. Noting that the minimum value of the received signal intensity from an IrDA infrared source is around 4 $\mu W/cm^2$, it is clear that the background sun light is about 100 times more powerful than the received information signal. When detected by the photodetector, this ambient light generates a dc current plus shot noise. This shot noise is proportional to the detected ambient light power and is the major source of noise in infrared systems. This clearly shows the need for optical bandpass filters to reduce the amount of background radiation detected by a photodiode. Reduction of ambient light by a filter is very important in achieving the desired SNR in practical systems.

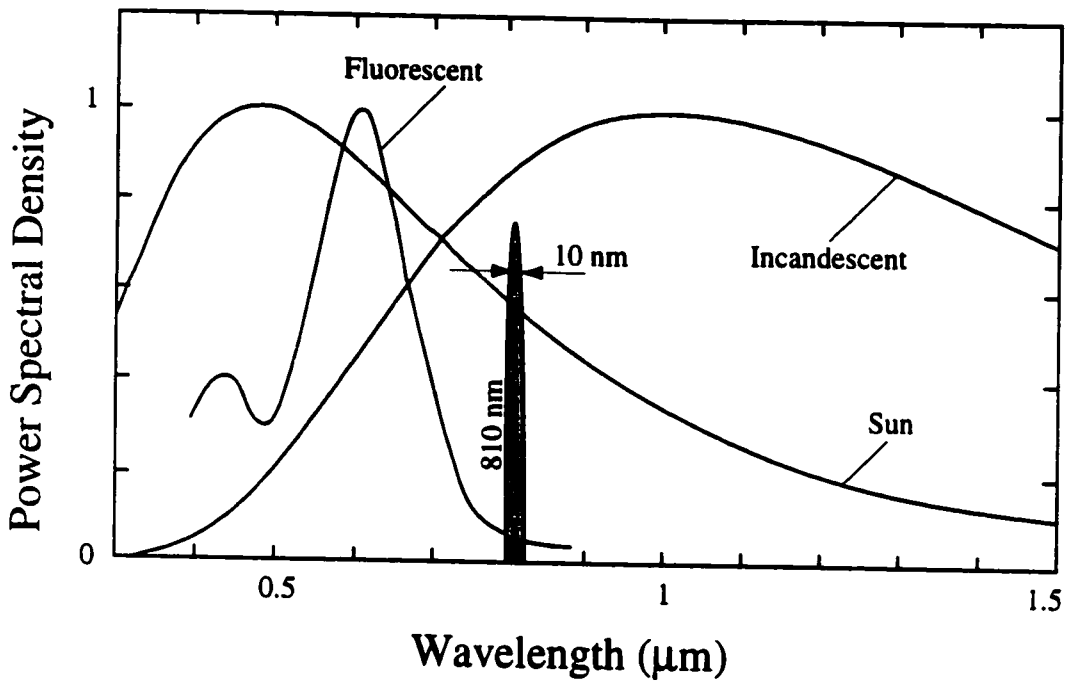

Figure 6. Power Spectral density of three major noise sources for infrared receivers. The infrared system is assumed to work at 850nm wavelength. (from [12])

The background induced shot noise is modeled as an additive white Gaussian noise (AWGN) with a one-sided power spectral density (PSD) given by [12]:

$$S_n(f)=P_{bg}A_R\gamma q \equiv N_0 \quad (A^2/Hz) \tag{2.1}$$

where P_{bg} is the level of background radiation per unit area detected by photodiode, γ is the photodiode efficiency and q is the charge of an electron (1.6×10^{-19} Coulombs).

In a typical lighting condition, P_{bg} is much more than the power of the received signal. This is a major difference between infrared receivers and optical fiber receivers. In the latter, the dominant source of noise is the noise generated by electronic components.

In this model, the received signal $r(t)$ is represented as the convolution of $d(t)$ and $\gamma A_R h(t)$. Therefore, signal power is proportional to $Y^2(t)$. Increasing the amount of received light in the receiver increases both the signal and the noise power due to ambient light. Noise power is proportional to the detected background light power, P_{bg}, while signal power is proportional to the square of the detected optical signal power. Therefore, increasing the size of the detector

or using concentrators or lenses to collect more light at the receiver improves the signal-to-noise ratio (SNR).

2.7 CHANNEL PARAMETERS

The primary objective of the designer of an infrared link is to achieve a high SNR at the receiver. This is a challenging objective because the SNR of an IM/DD link depends on the square of the received average optical power. The transmitted optical power is limited by the considerations of eye-safety and transmitter power consumption. Therefore, the infrared link is mainly a power-limited link and the average received optical power or the channel path loss is the most important parameter of this channel.

Path loss is defined as the "inverse value of the dc gain of the frequency response of the channel". The dc gain of the frequency response of the channel, a measure of the received optical power, can also be used to find the path loss. That is, the path loss can be represented by $1/H(0)$ on a linear scale or $-10\ \log_{10}(H(0))$ on a logarithmic scale in units of dBo (optical dB). As it was stated before, the received electrical signal is proportional to the area of the receiving photodiode. Therefore, for a given configuration, increasing the receiver photodiode area increases the received signal power and decreases the channel path loss. To remove this dependency and make the path loss a parameter that describes the channel rather than the combination of channel and receiver, the path loss could be normalized for a given receiver area. As an example, a receiver area of $1cm^2$ can be used as the basis for this normalization. This would make this parameter a universal parameter for comparing different channel conditions and different optical receivers. Throughout this thesis, the values of the path loss are all normalized for a receiver area of $1cm^2$.

The other important parameter of the infrared channel is the result of multipath propagation of light waves. Reflection of light by objects causes a distortion called the *multipath-induced temporal dispersion* or simply *multipath dispersion* in an infrared channel. For each transmitted impulse, a widened pulse is detected at the receiver. Optical impulse undergoes several reflections and attenuated replicas arrive at different times causing the transmitted impulse to be received as an attenuated, widened pulse. Examples of impulse response of an infrared channel are presented in Chapter 3. Based on our measurements, in an indoor environment, the spread of impulse response is usually much less than 100 ns. The exact value of spread

depends on the physical configuration. This spread causes a distortion that is baud rate dependent. Higher baud rate signaling over this channel results in more distortion. This distortion causes ISI in the received signal. ISI causes the tails of previous symbol(s) to overlay the current symbol. This added component reduces the noise margin, i.e. increases the possibility of wrong decisions by closing the eye of the received signal. To compensate for the reduced margin, the transmitted power should be increased to keep the system performance similar to an ISI-free system. This added power opens the received signal eye pattern. The amount of extra power needed to provide the same performance is called ISI power penalty. If the sum of the tails of the previous pulses is more than the value of the current pulse, then there is an irreducible error rate. In this case, increasing the transmitted power doesn't solve the problem because the amplitude of the tails also increases. In this case, equalizers are used to compensate for ISI.

A useful parameter that quantifies the spread of $h(t)$ is the *root mean square delay spread* or simply *r.m.s. delay spread* defined by [60]:

$$\sigma = \sqrt{\frac{\int_{-\infty}^{\infty}(t-\mu)^2 h^2(t)dt}{\int_{-\infty}^{\infty}h^2(t)dt}} \qquad (2\text{-}2)$$

where μ is defined by:

$$\mu = \frac{\int_{-\infty}^{\infty}th^2(t)dt}{\int_{-\infty}^{\infty}h^2(t)dt} \qquad (2\text{-}3)$$

This definition accounts for the distribution of $h(t)$ in time and therefore is a suitable definition for the spread of impulse response. The r.m.s delay spread is defined in radio channels as the square root of the second central moment of the ensemble average of the magnitude squared channel impulse response. In deriving this definition, the channel is assumed a slowly varying, zero-mean, wide sense stationary, random function of spatial location or time. It has also been assumed that the values of $h(t)$ are uncorrelated in time, namely $E[h(t)h(t')]=0$ for $t \neq t'$. These assumptions are not valid for an infrared channel and so the relations between the channel

r.m.s. delay spread and the channel performance which are derived for conventional RF channels are not directly applicable here.

For infrared systems, the relation between multipath power penalty and the value of the channel r.m.s delay spread depends on the modulation and equalization scheme. However, it has also been shown that there is a strong relationship between σ and the power penalty due to ISI for most of the commonly used infrared digital modulation schemes [52]. Throughout this thesis, the value of the channel r.m.s. delay spread or simply the channel delay spread is used as a mean to compare the width of the channel impulse response and its effects on the transmission system for different configurations.

Once the impulse response or the frequency response of the channel is known, one can extract other useful parameters. The 3-dB and 10-dB channel bandwidths are among them. These are points in frequency where the channel frequency response drops 3-dB or 10-dB below its dc value. They represent the flatness of the transfer function and could be indirectly related to the maximum transmission rate over the channel without equalization. In addition, the peak amplitude of the impulse response and the total length of the impulse response in time domain, which is called the excess delay of the channel, can also be extracted.

2.8 MODULATION AND DEMODULATION

Modulation of the signal for indoor infrared application has been the subject of many research projects. Based on the published results [55] the digital modulation techniques that are feasible for infrared communication systems are:

- On-Off Keying (OOK)
- Pulse Position Modulation (PPM)
- Multi Sub-carrier Modulation (MSC)

Each of these modulation schemes has some advantages and some disadvantages. The final choice of the modulation scheme depends on the specific requirements of a given system.

The OOK modulation scheme is the simplest scheme. The infrared source is turned on for a "1" and turned off for a "0" (or vice versa). The pulse shaping is usually used to avoid sharp edges of the pulses fed to the infrared source. The power spectrum of OOK signal contains significant amount of power near dc. This can be considered both as an advantage and as a disadvantage. The frequency response of infrared has a low pass shape and therefore the

presence of signal energy near dc makes it less susceptible to the nulls and attenuation of $H(f)$ in high frequency. In typical office environments, usually there is a strong interference from the fluorescent light sources. This interference should be removed by high-pass filtering of the received signal. This is a disadvantage for the OOK modulation scheme since it causes some higher power penalty for OOK compared to other proposed modulation schemes. OOK is relatively simple and for the multipath infrared channel, adaptive equalizers could be used to mitigate the multipath effects for this modulation scheme.

PPM and its variants are considered very suitable for infrared systems. In PPM, the symbol period is divided into L non-overlapping slices. A pulse is sent in each interval to indicate the transmitted symbol. For example in a 4-PPM, the duration of symbol is divided into 4 parts and the presence of a pulse in each of these positions indicates one of the four possible combinations of {00,01,10,11}. Therefore, the number of bits that are carried by a simple L-PPM is $\log_2 L$. It could be easily seen that because of the confinement of the pulses to a shorter duration of time, the required bandwidth of L-PPM signal is higher than OOK. The bandwidth requirement of an L-PPM signal is given by $(L/\log_2 L)R_b$ where R_b is the required bit rate. On the other hand, the amount of required power in L-PPM is smaller compared to OOK. This is one of the most important advantages offered by PPM systems. Severe restriction of power budget for indoor infrared links because of eye-safety requirements and also limited battery power has forced many manufacturers to use PPM as their modulation scheme for infrared communications products. PPM contains little energy near dc, permitting high pass filtering to further mitigate the fluorescent interference. There could be other useful variations of PPM for this application. One can think of choosing to send k pulses in L positions to represent more bits per symbol duration. The positions of those k pulses in L positions could be chosen such as to minimize the probability of error by considering the effects of intersymbol and intrasymbol interference due to the multipath of the channel. The detection and equalization of PPM is more complex compared to OOK. The equalizer could be implemented as a chip-rate equalizer or a symbol-rate equalizer. Each of the two has its own advantages and disadvantages. A detailed discussion of this subject could be found in [9].

In a multiple sub-carrier modulation scheme, the band of operation is divided into N sub-channels. Each channel carries a separate bitstream using QPSK or multi level QAM modulation scheme. Since the signal that drives the infrared source should always be positive, there should be a dc component added to the signal fed into the optical source. In this

modulation scheme, each bitstream (the contents of each sub-channel) could be modulated or demodulated regardless of the other streams. This allows for simpler implementation of the receiver electronics. At the receiver, there is no need to de-modulate all the data. The particular bitstream, which is intended for that particular user, could be extracted. This implies reducing the required speed for the electronics of each of the receiver circuits. Also, using a proper channel monitoring technique, the transmitter can avoid transmitting data on the faded sub-channels and use the best parts of the channel frequency response to send their data. This is achieved by dynamic channel allocation in the physical layer. The interference of the fluorescent light could also be avoided by choosing a proper center frequency for the first sub-channel. Since the data for each bitstream has a much smaller bandwidth, there is no need for equalization in this technique if the sub-channels are operating at low bit rates.

There are some disadvantages with this modulation technique. The most important one is the power penalty associated with this method because of the requirement of adding a dc component to keep the signal level above zero all the time. Comparing the power requirement of these methods show that in general and for the real measured infrared channels, the performance of this scheme is worse than equalized PPM or OOK [20].

2.9 CONCLUSIONS

Infrared light can be used for high speed indoor wireless communications. Systems employing infrared can benefit from the compactness and availability of in-expensive transceiver components. A very successful industry initiative for using infrared, called IrDA is widely accepted and employed in all portable computers and many new communication devices such as palm pilot and similar handheld computers.

Infrared channel can be used in many different configurations, each with its own applications and limitations. The most feasible method of data transmission over a free space infrared link is the use of intensity modulation and direct detection (IM/DD). For such systems, it is shown that the infrared channel can be characterized by a real-valued impulse response. The major differences between the infrared channel and the radio channel were briefly explained.

The basic system-level model of a communication system employing infrared transmitter and infrared receiver was described and the important channel parameters that can be extracted

from the channel impulse response were defined. Finally, a brief overview of the common modulation schemes for digital communication over this channel concludes this chapter.

CHAPTER THREE

3 INFRARED CHANNEL, SIMULATION AND MEASUREMENTS

3.1 INTRODUCTION

Modeling and simulation of indoor infrared channel has been addressed in literature with the first steps taken by Gfeller *et al.* [39] who pioneered the idea of using infrared for indoor wireless communications. He analyzed the dispersion property of this channel using a simple model and demonstrated a baseband PCM at 125 kbps over this channel. Barry *et al.* [13] presented a general computer simulation method for infrared channel characterization. Experimental measurements of indoor infrared channel were performed at the University of Ottawa [43] over a 40 MHz band. Later, Krause, *et al.* [52] measured infrared channel over a 150 MHz 3-dB band and the measurements at the University of Ottawa continued with a higher bandwidth of 400 MHz for many different configurations [94][96].

The radiation pattern of a diffused infrared source could be modeled by a Lambertian pattern (see Figure 7). It has also been shown that the reflections of infrared light from the surface of most indoor materials can be approximately modeled by a diffused Lambertian pattern [39]. The reflection coefficient, ρ, of a unit area of the surface can be defined as the ratio of the light power reflected from the surface to the light power received by that area. Parameter ρ was measured in [39] for many materials used in building construction and it was noted that most of these materials are good reflecting objects with a reflection coefficients ranging from 0.4 to

0.9. The relatively high value of ρ is a major motivation behind using the diffused configuration that relies on reflections from reflectors inside a room. The Lambertian pattern is also observed when the infrared light that is generated by a narrow-beam source such as a laser diode (LD) passes through a glass diffuser. The analysis by Gfeller *et al.* [39] was meant for power-budget calculations, so they were interested in calculating the total received power at the detector. They accounted only for single reflections of light. Hash *et al.* [42] extended their work to account for double reflections, as well. These analyses did not consider temporal dispersion of the channel. In other words, the only interest was in the total received optical power, which can be expressed as the dc component of the frequency response of the channel, $H(0) = \int_{-\infty}^{\infty} h(t)dt$. For power-budget analysis, two reflections are usually enough because of the safety margins usually included in the calculations. However, for a complete system design, more comprehensive information about channel characteristics is required. Hortensius, *et al.* [46] simulated impulse response of the channel for the first time, accounting for a single reflection. Barry, *et al.* [12][13] presented an algorithm to calculate the impulse response of this channel, taking into account an arbitrary number of reflections. This algorithm was verified by a set of channel measurements by Krause *et al.* [60] showing a good agreement between the estimated and the measured channel impulse responses.

Although their simulation algorithm was implemented for a rectangular empty room, the algorithm is general and can be applied to more complicated environments. Abtahi, *et al.* [2] extended this simulation work and reported the effects of furniture and people in the room on the channel properties. It was shown that office furniture or movement of people near the receiver or transmitter can have considerable impact on the channel characteristics. In this chapter, the fundamentals of the simulation algorithm are briefly described and some of its implementation details are presented.

There are practical limits on the accuracy of simulation models. There are always effects that could not be modeled properly or their modeling is more difficult than measurement of the real-life event. Indoor infrared channel is not an exception to this rule. There are many parameters that affect the channel impulse response and can't be modeled properly or require lots of added complexity. For example, Chapter 8 reports on using holograms for diffusing the infrared light. A simulation model that combines the diffusion pattern of a given hologram in the simulation program proves to be very complex. Therefore, a wide-band measurement

system was developed and used to measure the characteristics of this channel under different circumstances [49][92][93][94]. The set up was used to investigate the effects of displacement, rotation, shadowing and different diffusion mechanisms on the characteristics of the infrared channel. A brief description of the measurement setup as well as the data processing that is required for the measurements is presented in this chapter.

3.2 SIMULATION MODELS

In this section, models for source, receiver and reflector are presented and line-of-sight impulse response is defined [13]. Based on the LOS impulse response, multiple reflections impulse response will be derived and the implementation issues will be discussed.

3.2.1 Source and receiver model

The radiation pattern of a wide beam optical source can be described by a generalized Lambertian law [39]:

$$R(\phi)=\frac{n+1}{2\pi}P_s\cos^n(\phi) \qquad \text{for} \quad \phi\in\left[-\pi/2,\pi/2\right]$$

Here, n is the mode number of the radiation lobe defined by:

$$n=\frac{\ln(0.5)}{\ln[\cos(HPBW)]}$$

where $HPBW$ is the half power emission angle of the infrared source. The higher value of n corresponds to more directive radiation pattern of the source. Effect of n on the radiation pattern of an infrared source can be seen in Figure 7. Note that, $(n+1)/2\pi$ is a normalizing factor used to ensure the total radiated power of the source over the hemisphere equals P_s.

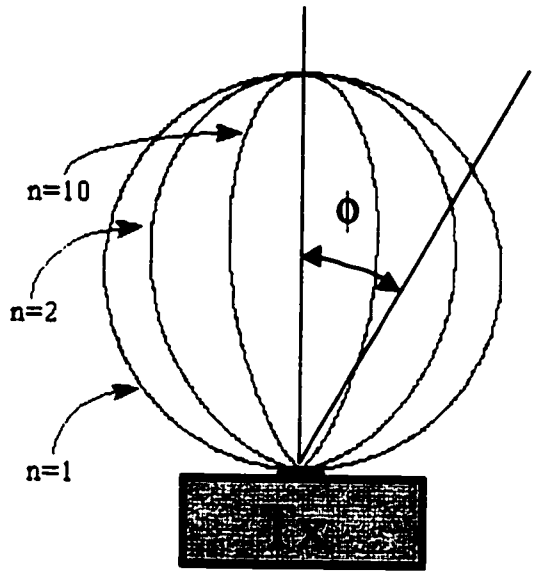

Figure 7. Normalized radiation pattern of a generalized Lambertian source for several values of n.

A point source S can be described by a set of scalars and vectors:

$$S \begin{cases} \vec{r}_s : \text{A three element vector describing the location of transmitter.} \\ \hat{n}_s : \text{A three element normalized vector describing orientation of transmitter.} \\ P_s : \text{Total optical power radiated from the source.} \\ R(\phi,\theta) : \text{Radiation pattern of the source.} \\ FOV_S : \text{Source Field - Of - View.} \end{cases}$$

A receiver of the light can also be described by a set of scalars and vectors:

$$\Re \begin{cases} \vec{r}_R : \text{A three element vector describing the location of receiver.} \\ \hat{n}_R : \text{A three element normalized vector describing orientation of receiver.} \\ A_R : \text{Receiver area.} \\ FOV_R : \text{Receiver Field - Of - View.} \end{cases}$$

3.2.2 Line-of-sight impulse response

Assume an environment without any reflectors. The impulse response between a source S and a receiver $\Re$, is given by:

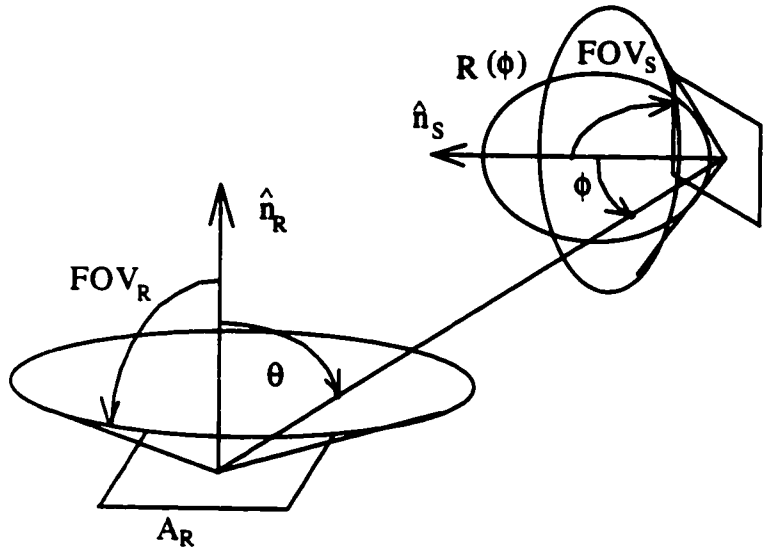

Figure 8. Geometry of infrared transmitter and receiver

$$h^{(0)}(t;S,\Re) \approx \frac{n+1}{2\pi}\cos^n(\phi)d\Omega\,\mathrm{rect}(\theta/FOV_R)\mathrm{rect}(\phi/FOV_S)\,\delta(t-R/c) \qquad (3\text{-}1)$$

where c is the speed of light, $d\Omega$ is the solid angle subtended by the receiver's differential area

$d\Omega = \cos(\theta)A_R/R^2$,

R is the distance between the source and the receiver:

$R = \| r_s - r_R \|$,

θ is the angle between $\hat{n}_R$ and $(r_s - r_R)$:

$\cos(\theta) = \hat{n}_R \cdot (r_s - r_R)/R$,

ϕ is the angle between $\hat{n}_s$ and $(r_R - r_S)$:

$\cos(\phi) = \hat{n}_s \cdot (r_R - r_s)/R$

The rectangular function is defined by:

$$\mathrm{rect}(x) = \begin{cases} 1 & |x| \le 1 \\ 0 & |x| > 1 \end{cases}$$

In deriving the impulse response between the source and the receiver (3-1), it is assumed that the receiver area is much smaller than the distance between transmitter and receiver.

Therefore, the received optical power is constant over the photodetector area and all optical energy reaches the receiver at the same time.

3.2.3 *Multiple bounce impulse response*

In a room with a receiver $\Re$ and a transmitter S, one can write the impulse response of the channel as the sum of the impulse responses from the light rays reflected just once, plus those that are reflected twice and so on. In other words, impulse response of the channel can be written as:

$$h(t;S,\Re)=\sum_{k=0}^{\infty}h^{(k)}(t;S,\Re) \qquad (3\text{-}2)$$

where $h^{(k)}(t;S,\Re)$ represents the light undergoing exactly k reflections to reach the receiver $\Re$ from the source S. The line-of-sight path, the path without any reflection, is given by ((3-1)). Higher order reflections can be calculated recursively using:

$$h^{(k)}(t;S,\Re)=\int_{A}h^{(0)}(t;S,\{r,\hat{n},\pi/2,dA\})\otimes h^{(k-1)}(t;\{r,\hat{n},1\},\Re)dA \qquad (3\text{-}3)$$

where symbol $\otimes$ denotes convolution and A is the receiver area. Source and receiver are specified by grouping their parameters in a set. For example, S:{r,n,1} means a source with location r, normal vector n that transmits 1W power. In this analysis, the FOV_r is always assumed to be $\pi/2$ and is dropped from the set for simplicity. Here, the LOS impulse response from source S to the an element of size dA (as the intermediate receiver/transmitter) is convloved with the $(k\text{-}1)^{th}$ bounce impulse response from that element to the receiver $\Re$ and integrated over all the reflector areas. Substituting (3-1) in (3-3) will result in:

$$h^{(k)}(t;S,\Re)=$$
$$\frac{n+1}{2\pi}\int_{R}\frac{\rho_r\cos^{n}(\varphi)\cos(\theta)}{R^{2}}\,rect(2\theta/\pi)\,h^{(k-1)}(t-R/c;\{r,\hat{n},1\},\Re)\,dA \qquad (3\text{-}4)$$

These integrations are performed with respect to the position r on the surface S of all reflectors and the notation used in the integration is as follows:

$\hat{n}$: Normal to the reflector surface S at position r.

dA: Differential area of the reflector surface at position r.

ρ_r : Reflectivity at position r.

R: Distance between differential area and receiver, ($R = \| r - r_R \|$)

ϕ: Angle between source normal and the line connecting source and differential area, so $\cos(\phi) = \hat{n}_s \cdot (r - r_s)/R$.

θ: Angle between differential area normal and the line connecting source and that area., so $\cos(\theta) = \hat{n} \cdot (r_s - r)/R$.

From this integration, it is clear that the k-bounce impulse response depends on the (k-1)th bounce impulse response. In other words, to find the k-bounce impulse response from source S, the distribution of power and its timing over all reflectors should be found. Then, each differential area can be assumed as another source that is emitting a portion of its received power back to the medium. From each of these secondary sources, the (k-1) bounce impulse response can be calculated.

3.2.4 Implementation

To calculate the integral in (3-3), reflecting surfaces should be divided into smaller elements, each with area ΔA. Each of these elements receive an amount of power with a certain delay and then acts as a transmitter with a Lambertian pattern by reflecting a portion of its received optical energy back into the media. Assuming total number of elements to be N and noting the i^{th} element with E_i the $h^{(k)}(t)$ can be approximated by:

$$h^{(k)}(t;S,\Re) \approx \sum_{i=1}^{N} h^{(0)}(t;S,E_i) \otimes h^{(k-1)}(t;E_i,\Re)$$
$$= \frac{n+1}{2\pi} \sum_{i=1}^{N} \frac{\rho_i \cos^n(\varphi)\cos(\theta)}{R^2} rect(2\theta/\pi) h^{(k-1)}(t - R/c;\{r,\hat{n},1\},\Re)\Delta A \quad (3\text{-}5)$$

It is obvious that E_i plays the role of a source in calculating the (k-1) bounce impulse response while acting as a receiver in the first bounce (power directly from source). Approximating the integral by a discrete sum results in a piece-wise continuous function $h^{(k)}(t)$. In fact, the resulting $h^{(k)}(t)$ would be a finite sum of scaled and delayed delta functions. The time axis can be divided into bins of width Δt and the total power received in each bin can be added up. The result would be a histogram that closely represent $h(t)$. For more accurate representation of $h(t)$ the time and spatial resolution should be increased.

For reflection orders greater than one, it is not efficient to implement (3-5) directly. It can be seen that a direct implementation would require identical operations to be performed several times. It is obvious that for a specific room with N differential reflector elements, all that is needed to calculate impulse response is the delay between i^{th} element and the j^{th} element, $\tau(i,j)$, and the power received from i^{th} element to the j^{th} element, $\Delta P(i,j)$. A direct implementation, calculates each of these, k times, and therefore is very time consuming. Instead, these elements can be stored in two table look-ups to be retrieved as they are needed in the calculations. The procedure for calculation of impulse response using table lookup method is given by [13]:

```
function h(t;i,j,k)
begin
        f(k=0)
                return ΔP(i,j) * delta(t-τ(i,j))
        else
                return sum from e=1 to N
                rho(e) * ΔP(i,e) * h(t-τ(i,e);e,j,k-1)
        end if
end
```

Although the table lookup method reduces the computation time, it increases the memory requirements. Assuming 4-byte space is required for the storage of a floating-point number, table look-up method would require $8N^2$ bytes of memory. For example, considering a 5 m × 5 m × 3 m room with ΔA=10 cm × 10 cm, there will be N=11000 small elements. To create a look up table for these elements, 968 Mbytes of memory is required which is not normally available. For this example, assuming 32 Mbytes of available memory, the size of elements should be greater than 25 cm × 25 cm that would considerably reduce the accuracy of the results.

Clearly there is a trade-off between the speed and the available memory in practical implementation of this algorithm. When more accuracy is desired, a smaller size for the elements should be chosen, which in turn will increase N and therefore the direct calculation should be used. With small values of N, table lookup is practical and faster. Running the program on a SUN SPARC STATION 20™, the time required for estimation of impulse

response using the direct algorithm was approximately $4N^k$ μsec. This means that for the same size room with element size of 10 cm × 10 cm, and k=2 approximately 9 minutes were required. Increasing the number of bounces, k, to 3, the required time would be approximately 64 days. This shows the effect of k on the computing time.

3.3 INFRARED CHANNEL MEASUREMENTS

The design of wireless communication systems using infrared as their carrier requires extensive knowledge about the behavior of the indoor infrared channel. This requires measurement of this channel under different conditions and using different optical configurations. Such measurements could eventually lead us to an in-depth understanding about the behavior of the channel under different circumstances. Measurements are also essential in providing the required knowledge about the distortions and noises that are generated in a real-life implementation of these systems. For example, rotation of the receiver has an important effect in the performance of an indoor infrared link. The effect of receiver rotation for an infrared system would be an interesting subject to study in infrared channel measurements. Displacement of the receiver as well as receiver shadowing are other important events that impact the infrared channel and their effects should be investigated.

A wideband measurement system has been developed to investigate the effects of different parameters on the characteristics of the indoor infrared channel [49]. Techniques commonly used in radio channel measurements can be adapted to the characterization of this channel. One of the common techniques suitable for characterization of communication channels is the continuous-wave swept-frequency technique. This technique can be implemented easily and accurately using a network analyzer. The technique uses a constant-amplitude, swept-frequency sinusoid to probe the channel. The received signal is multiplied by the transmitted signal and by a 90° phase-shifted version of the transmitted signal. The product signals are low-pass filtered and normalized to the transmitted signal amplitude, yielding estimates of the real and imaginary parts of the channel frequency response. Therefore, the attenuation and phase shift (caused by the propagation medium) is obtained for each frequency component. An HP8751A network analyzer was used for generating the swept frequency signal and calculating and recording the channel transfer function. This network analyzer is a high throughput instrument with lab precision that covers 5 Hz to 500 MHz. The HP 8751A provides resolution of

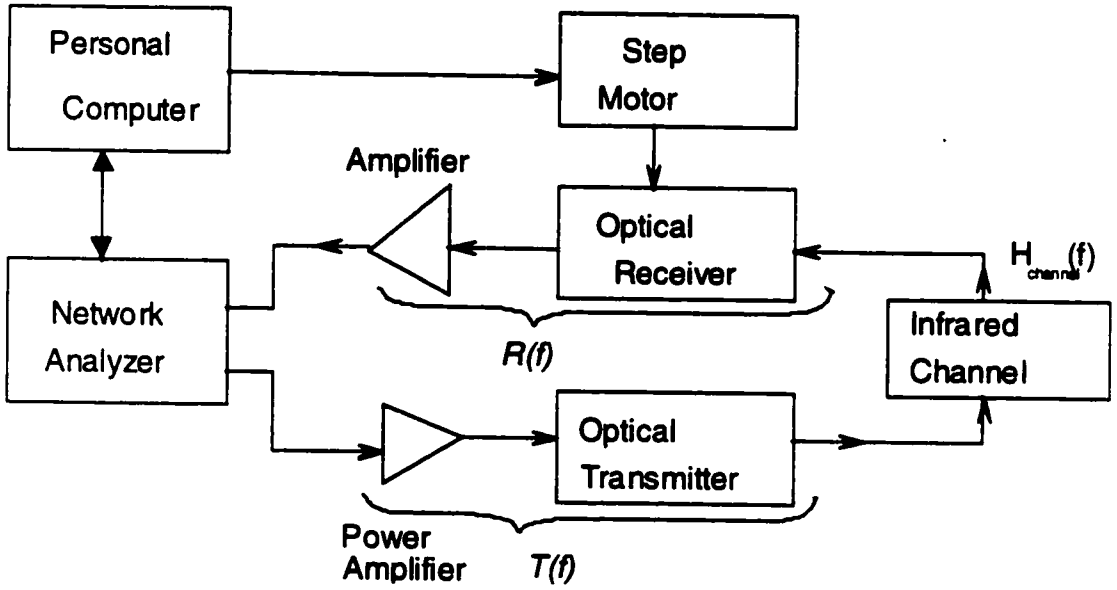

Figure 9. Block Diagram of the indoor infrared channel measurement system

0.001Hz, 0.001dB, 0.001 degree, and 10ps for characterizing the linear behavior of either passive or active networks, devices, components or systems in the lab and the production test areas. It has a built-in 1.44MB disk drive for direct save and recall of instrument state, calibration data, and application programs and it also supports HPIB bus for data input and output. This bus has been used to transfer the recorded channel transfer functions to a personal computer for further data processing.

Figure 9 shows the block diagram of the measurement system. The sinusoidal signal from the network analyzer is amplified and converted to the optical domain with an optical transmitter. The lightwave propagates in an indoor environment and is received by a portable optical receiver. The received signal is amplified and fed back to the network analyzer via a coaxial cable. The measurement system requires a high-power optical transmitter and a wideband optical receiver with a large area photodiode. Because of the special requirements, the transmitter and the receiver were not available off the shelf.

The optical transmitter and optical receiver circuits were designed and built in the broadband communication research laboratory (BCRL) at the University of Ottawa [49]. The optical transmitter uses an 808-nm laser diode. The laser diode is impedance-matched with a 47Ω resistor. A bias tee circuit combines the sinusoidal signal from the network analyzer with the dc current from a power supply. The signal level from the network analyzer is boosted by a

wideband power amplifier. The modulation bandwidth of the transmitter is from 1 kHz to 500 MHz and the laser diode is biased such that its average output power is 180 mW. Lower levels of output power can be obtained by changing the bias point of the laser diode. The laser diode is considered to be fairly linear for this range of operation.

The optical transmitter is packaged in an aluminum box to minimize the RF leakage. The operating bias and temperature of the transmitting laser diode is controlled by a series-120 laser driver made by Lightwave Electronics Co. The bias point of the laser is chosen to operate the laser in its linear range of operation and avoid introduction of higher order harmonics into the measurement results.

An external optical diffuser can be attached to the transmitter box. The external diffuser can be a simple glass diffuser that shapes the radiation pattern of the laser as a first order Lambertian pattern. It can also be a more complex diffuser such as a holographic diffuser as it will be discussed in Chapter 8. To measure the channel using a non-directed LOS configuration, a Nikkor 50mm f/1.4 lens is mounted on top of the transmitting laser source. The lens is then adjusted to create a focused laser beam on a diffusing surface on the ceiling. A white sheet of paper that has a reflectivity coefficient close to unity is placed on the ceiling so that the focused laser beam can be reflected without loosing lots of its energy. Therefore, the spot on the ceiling acts as a single point Lambertian source of infrared energy that illuminates the measurement site. This method allows us to measure the characteristics of the channel in LOS mode without having to mount the transmitter on the ceiling.

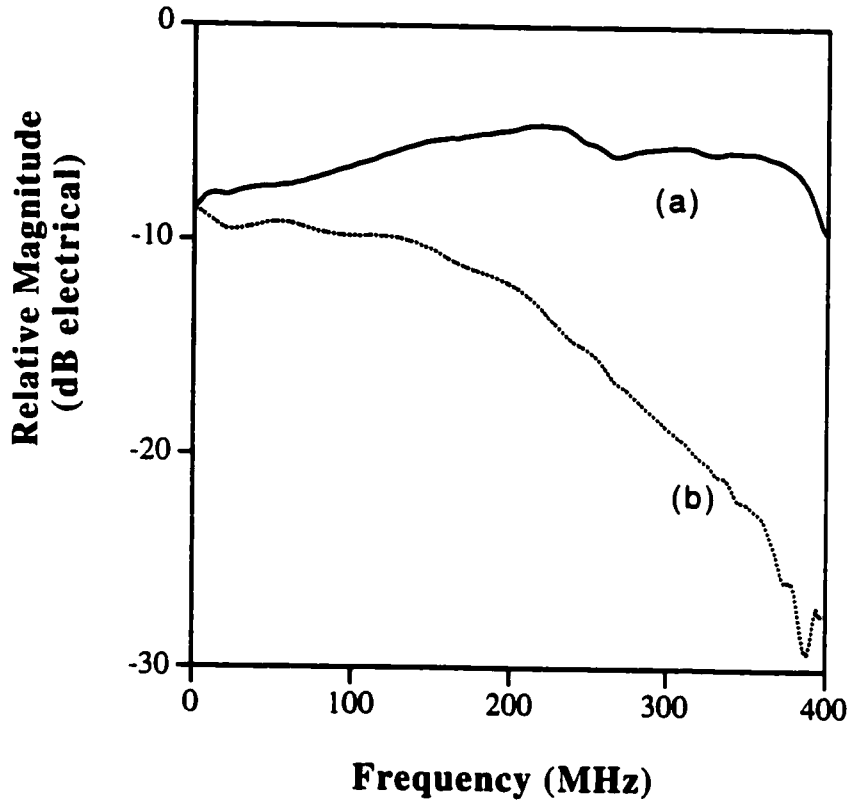

Figure 10. Frequency response of the receiver (a) with the equalizer and (b) without the equalizer.

The developed optical receiver uses a large-area (25 mm^2) silicon APD (avalanche photodiode). The packaged APD has no lens in front of the detector surface. Therefore, the optical receiver has a wide field-of-view (about 60 degrees). For the front-end amplifier, a transimpedance receiver scheme is chosen to achieve a large dynamic range. The major challenge in the receiver design is that the APD has a large capacitance (30 pF) and its bandwidth is limited by its transit time. The transit time is 5ns and it limits the 3 dB bandwidth of APD to 200 MHz as shown in Figure 10 (b). The frequency response drops by about 20 dB at 400 MHz. A resonant-type analog equalizer was designed to extend the receiver bandwidth to 400 MHz. Figure 10 shows the frequency response of the optical receiver with the equalizer. The overall bandwidth extends approximately from 10 kHz to 400 MHz.

The APD is biased at 410 V resulting in a multiplication factor of 110 at room temperatures. To avoid the use of optical filters for rejecting ambient light, the measurements were conducted in dark rooms. Otherwise, the ambient light would saturate the receiver. Optical

filters should be used to allow proper operation of the receiver in the presence of strong background light. The drawback of using optical filters is that off-the shelf filters severely limit the receiver FOV and this is not desired for our measurement objectives. Therefore, most of our measurements were performed without an optical filter. A summary of the measurement setup parameters is presented in Table 1.

The noise level appearing at the network analyzer can be reduced by choosing a small IF (intermediate frequency) bandwidth which in turn increases the required time for recording a frequency response. The minimum IF bandwidth of 8751A network analyzer is 2 Hz. When choosing a small IF bandwidth, the RF interference, due to RF leakage from the transmitter and pickup by the receiver becomes the major factor limiting the receiver performance. When operating at a distance of approximately 3 m from the transmitter, the received interference levels are about -160 dB at 300 MHz and -140 to -150 dB at 400 MHz. Therefore, the ratios of the transmitter power to the receiver interference-equivalent-power are about 80 dBo at 300 MHz and 70 to 75 dBo at 400 MHz.

For each desired frequency response, a set of 128 samples was chosen. The signal frequency response on a network analyzer is swept from 30 kHz to 400 MHz in steps of 3.125 MHz. The start frequency is chosen to avoid the effects of dc-blocking capacitance that is used in the receiver circuit. The IF bandwidth of the network analyzer is set to 20 Hz to reduce the noise level recorded by the network analyzer.

Measurement Setup Important Parameters	
Operating wavelength	808 nm
Frequency range of the measurement system	1 kHz to 400 MHz
Average optical output power of laser diode	180 mW
Area of the receiver APD	25 mm^2
Receiver field-of-view	≈60°
APD Gain at operating voltage	110

Table 1. Important parameters of the infrared channel measurement setup.

3.4 CALIBRATION OF THE MEASUREMENT SYSTEM

The measurement system is calibrated by putting the transmitter and the receiver together in a back-to-back configuration. Let's assume that the transmitter side of the system has a frequency response of $T(f)$ and the receiver side has a frequency response of $R(f)$ (see Figure 9) The recorded frequency response by a network analyzer can be expressed as:

$H_{rec}(f)=T(f)R(f)H_{channel}(f)$

where $H_{channel}(f)$ is the desired channel frequency response. A normalization curve is recorded by putting the transmitter and the receiver in a back-to-back configuration. In this configuration, the receiver and source are placed such that the receiver is looking directly at the receiver from a distance of a few centimeters. To avoid the saturation of the APD due to the high amount of the received optical power, some optical attenuators (like sheets of white paper) are placed between the transmitter and the receiver. Recording the back to back frequency response yields

$H_{back2back}(f)=T(f)R(f)K_{back2back}$

Here, $K_{back2back}$ is the unknown attenuation caused by the sheets of paper between the source and the receiver. This attenuation is frequency independent and therefore it can be assumed as a constant. To find the $K_{back2back}$ the current that is passing through a resistor which is in series with the APD is measured. First the bias voltage across the APD is reduced to a nominal value of 8 volts which in turn reduces the APD gain to unity. Therefore, the APD is functioning as a photodiode. Then the current that is passing through the APD is measured by observing the voltage across a 10 kΩ resistor that is in series with the APD. The actual received optical power could be determined by using the following formula

$P_{optical}=I_{photodiode}/(\gamma A_R)$

where γ is the responsivity or efficiency of the photodiode and A_R is its area. Based on the manufacturer's specifications, the APD in the receiver of the measurement setup has a responsivity of $\gamma=0.5$ and an area of 0.25 cm^2. Knowing the current passing through APD the $P_{optical}$ can be found. The amount of transmitted optical power from the laser diode is then measured by using an optical power detector and without changing the transmitter electrical configuration. Dividing these two values, results in the desired $K_{back2back}$.

$K_{back2back}$=Transmitted optical power/Received optical power

Knowing $K_{back2back}$, all the recorded frequency responses can be normalized to find the desired channel transfer function, $H_{channel}(f)$.

$H_{channel}(f)=H_{rec}(f)K_{back2back}/H_{back2back}(f)$

The following are the measured values of the transmitted optical powers from the source:

- Received optical power for back-to-back system: 680 nW (back-to-back system uses the lens on top of the laser).
- Transmitted power from source: 180 mW.
- Transmitted power from the diffused source: 60 mW.
- Transmitted power from the lens (LOS): 95 mW.

3.5 DATA PROCESSING

As was mentioned before, the frequency response of the receiver APD looks like a low-pass filter with a cut-off at about 200 MHz. To flatten the spectrum up to 400 MHz an analog equalizer is used in the receiver. The frequency response of the equalizer compensates for the low-pass filtering of the APD by enhancing the frequency components in the 200-400 MHz range. As a results, the end-to-end transfer of the transmitter and the receiver is flat with variation of less than 2 dB across the band. The noise and interference components in high-frequency range are enhanced by the equalizer. Therefore when the received optical signal is weak, there is a noticeable strong interference component in high frequency ranges which sometimes dominates the channel frequency response in that band. The effect of interference is dominant when the received optical signal is very weak. This happens mostly during the measurements of shadowing and rotation effects.

An important aspect of data-processing is discrimination between the channel frequency response and the interference effects. Since the recorded frequency response could be considered a sum of both, there is a need to somehow specify the frequency ranges or frequency responses in which the interference is dominant. This seems to be a complex problem because the interference is not fixed and depends upon the environmental conditions. The effect of interference is particularly strong in high frequency bands and in cases where the received signal is weak. The question is:

What is the range of frequencies in which the recorded $H(f)$ is not a good representative of the infrared channel ?

One answer could be the use of the shape of $|H(f)|$. When the interference is dominant, $|H(f)|$ has a high-pass shape with several peaks and nulls. This method is not reliable since it does not provide an algorithm to define where the $H(f)$ should be truncated. Which peaks and nulls correspond to the channel and which correspond to interference? Note that the infrared channel can have frequency nulls and peaks too. This is a qualitative method and is good if a one by one study of the frequency responses is concerned.

Observing the results of the measurements and applying different techniques, an appropriate algorithm has been chosen to address this issue. It was found that the group delay of the recorded $H(f)$ can be used effectively to distinguish the interference from the channel. It is observed that the interference signal introduces a noticeable change in the shape of the channel group delay. Simulation results for similar indoor environments show that the group delay of the infrared channel is relatively flat with variations of around +/- 20 ns from its average. However, in the frequency bands in which the interference is dominant the group delay has much larger fluctuations. The available results show that the start of fluctuations is a good indicator of the end of the useful band. In cases where the received optical signal is strong enough, the group delay does not have huge fluctuations and almost all the 400 MHz band is useful. When the received signal is weak, the fluctuations begin at high frequencies and the weaker the signal, the smaller is the useful band. Considering the available data, a threshold of 50 ns was chosen and the first time the group delay curve exceeds its average value by more than 50 ns, the $H(f)$ is set to zero. The average value of the group delay curve is calculated for the 30 kHz to 160 MHz band where the analog equalizer does not enhance the interference.

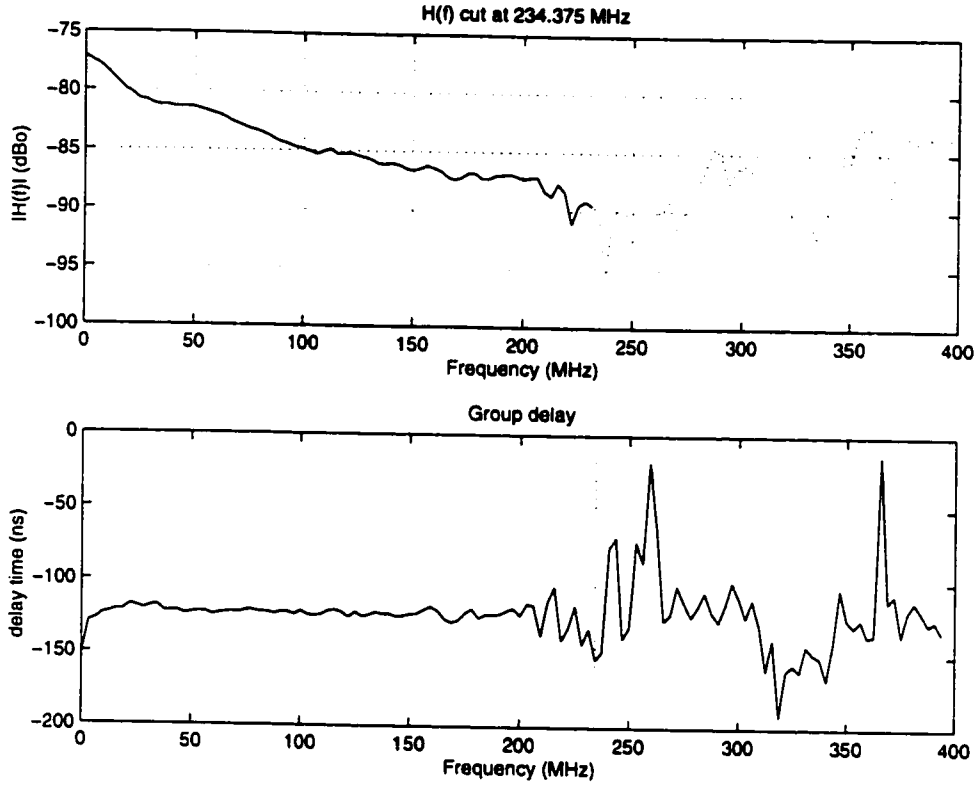

Figure 11. The recorded frequency response contains an added interference component. The interference component causes distortions in high frequency portions of the recorded signal. The group delay of $H(f)$ can be used to specify the frequency ranges where the interference is dominant and the recorded $H(f)$ is not representing the infrared channel appropriately. In this figure, $H(f)$ above 234 MHz is not useful since the group delay exceeds its average by more than 50 ns at this frequency.

Figure 11 shows an example of a recorded frequency response where the interference becomes the dominant received signal at high frequencies. The top graph shows the recorded $H(f)$ and the bottom graph shows the corresponding group delay. The group delay curve exceeds its average by more than 50 ns at f=234 MHz. Therefore, this frequency is used as the end of useful band for the recorded $H(f)$.

After truncating the frequency response, the result is padded with zeros to fill it to a vector of 128 points. Then the right half of a Hamming window of length 256 is applied to the $H(f)$. The result is like a low-pass version of $H(f)$. Then, the complex conjugate of the result is padded to itself and vector with 256 elements is generated. The channel impulse response is the inverse discrete Fourier transform (DFT) of the above vector. The impulse response $h(t)$ is a vector of length 256 points. Therefore, the time resolution and the time span of the resulting impulse response would be $1/(2\times400\times10^6)=1.25$ ns and $256*1.25=320$ ns respectively.

3.6 EXTRACTED CHANNEL PARAMETERS

There are frequency domain and time domain parameters of interest for each set of the recorded data. The following parameters of the channel have been chosen and they are extracted from the measured data:

- Frequency domain parameters
- 3-dB bandwidth of the frequency response
- 10-dB bandwidth of the frequency response
- Received optical power (or alternatively the channel path loss)
- Total power of $|H(f)|$
- Time domain parameters
- Peak of the channel impulse response
- R.m.s. delay spread of the impulse response
- Excess delay of the impulse response

These parameters are calculated after normalizing the frequency responses to the back-to-back frequency response and before truncating the $H(f)$. The value of the frequency response at the edge of 3-dB (10-dB) band is found by subtracting 3-dB (10-dB) from the dc gain of the channel, $H_0=10\log_{10}(|H(0)|)$. Whenever this value is between two points of the available $H(f)$ vector, a linear interpolation between the two neighbor points is used to find the exact frequency of the 3-dB (10-dB) band. For example, for the 3-dB bandwidth, if

$$H_1 = 10\log_{10}(H(f_1))$$

and

$$H_2 = 10\log_{10}(H(f_2))$$

such that

$$H_0 - H_1 < 3 < H_0 - H_2$$

then, the 3-dB bandwidth is given by:

$$f_{3dB} = f_1 + (f_2 - f_1)\frac{H_0 - H_1 - 3}{H_1 - H_2}$$

similar method is applied to find the 10 dB bandwidth of the channel. This approximation is based on the observation that almost all measured peaks and nulls of the transfer function have a span of more than 10 MHz in the frequency domain. Therefore, it is not expected that the transfer function has a peak or null between two points that have a separation of only 3.125 MHz.

Another extracted parameter is the power of $H(f)$ that is defined by:

$$H_{Power} = \sum_{n=1}^{128} |H(n)|^2$$

This parameter can be used to compare to total power under the curve $|H(f)|$ for different configurations.

To find the delay spread and the excess delay of the impulse response, $h(t)$ is truncated using a threshold. Any $h(t)$ which is below a certain level is assumed to be zero. Excess delay is then defined as the time span in which $h(t)$ has non-zero components. Using the empirical judgment of the available data, it was found that a good threshold value is found by noting the average energy in the tail of the impulse response. The average value of the impulse response in its last 60 ns is found and the threshold is set to be 6 dB above this value. Therefore, any value below this threshold is set to zero for the purpose of delay spread and excess delay measurements. Note that the length of the collected impulse response is around 320 ns and the delay spread of the channel is usually much less than 100 ns. Therefore, the last 60 ns of the impulse is expected to contain negligible energy from the transmitted infrared impulse. However, interference from the source, other electromagnetic interferers and the noise of the receiver would determine a noise floor for the impulse that should not be mixed with the channel characteristics.

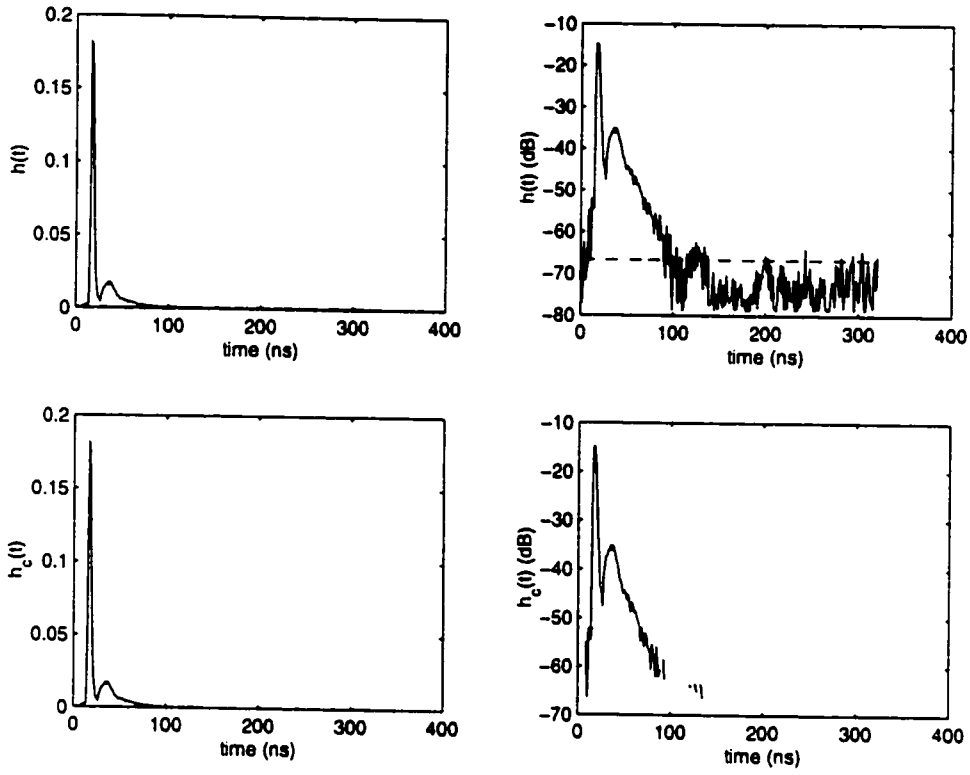

Figure 12. This figure shows the process of truncating the measured impulse response for calculating the values of the channel delay spread. The top figures show the impulse response derived from the recorded channel transfer function in linear (left) and dB (right) scale. The threshold for truncating the impulse response is derived by averaging the last 60ns of its tail and setting the threshold to be 6 dB higher than this average. The bottom graphs show the results of truncation in linear and dB scale.

This process is shown in Figure 12 where the top two graphs show the impulse response in linear and dB scale. The dashed line in the top right graph shows the threshold value. The result of applying this algorithm for truncating the impulse response is shown in the bottom two graphs. This procedure reduces the effects of residual noise and interference on the calculated value of the channel delay spread.

3.7 SUMMARY AND CONCLUSIONS

To design an infrared system, knowledge about the infrared channel is required. Infrared channel can be characterized by a real valued impulse response. Section 2 of this chapter described an algorithm that can be used to simulate this impulse response. Implementation aspects of the algorithm as well as its limitations were discussed. It was noted that computational complexity of the algorithm remains within reasonable limits when 1 or 2-bounces are considered. To track more bounces, the spatial resolution should be drastically decreased or powerful computing resources should be utilized.

Measurement of the channel characteristics is another important tool that can be utilized to increase our knowledge about the behavior of the infrared channel under different circumstances. Section 3 of this chapter described a wide-band measurement setup that has been designed and at BCRL Labs at the University Of Ottawa. A summary of the measurement setup specifications and parameters was presented. The method that has been used to calibrate the results was also described in details. This measurement setup has been used to collect information about the characteristics of infrared channel in many different configurations. The measurement procedure, results and conclusions of these measurements are reported in the subsequent chapters of this thesis.

Section 4 describes the data processing aspects of the results obtained from the measurement systems. A novel method to discriminate between the channel transfer function and the interference contribution to the recorded data was presented. The method has been used for data processing through this thesis and has proved to be effective. The most important parameters that are extracted from the collected data are the channel path loss and the channel delay spread. There are other useful channel parameters that have been extracted from subsets of the recorded transfer functions such as 3-dB and 10-dB channel bandwidths and were discussed in this section.

CHAPTER FOUR

4 DESIGN CONSIDERATIONS FOR INFRARED WIRELESS COMMUNICATION SYSTEMS

4.1 INTRODUCTION

Design and implementation of a broadband indoor infrared communication system needs careful attention to the problems facing this type of transmission [86]. One of the important challenges in designing a wideband indoor infrared communication system is providing a link with a high Signal-to-Noise Ratio (SNR). In doing so, it is very important to increase the received optical power by designing an efficient transmission system.

The sensitivity of an infrared receiver to the direction of reception is another important point that has to be considered. Dependence of the channel characteristics upon the transmitter and receiver field of view (FOV) is a property of optical atmospheric communication system and can be used properly to combat distortions over this channel [86][85]. An infrared receiver can have a maximum FOV of 90° and in practical implementations, this value can be much smaller. Therefore, rotation of the receiver may result in considerable changes in the channel characteristics. The effects of rotation on the characteristics of the channel are studied in the next chapter. Direction diversity reception techniques can be employed to take advantage of the independent signals received from different directions. The idea of direction diversity for indoor infrared communications which is first proposed in [123] and [43] and then in [88] is based on using separate receivers looking in different directions to detect the incoming optical

signal. The outputs of these receivers can be combined properly to increase the quality of the received signal. Direction diversity is one of the best techniques that could be used to achieve a high bit rate indoor infrared communications link [22].

4.2 CHANNEL PARAMETERS

There are two major impairments for an indoor infrared communications link. Attenuation of the received signal (path loss) which decreases the SNR at the receiver and the channel delay spread of the impulse response $h(t)$ that limits the maximum transmission rate for a given configuration.

Since optical signal is subject to shadowing and the path loss is relatively high, the indoor channel is a power limited channel. On the other hand, the transmitted optical power from the infrared source is limited by eye safety regulations. Therefore, efficient use of optical power is very important in providing a reliable infrared link for high-speed communications. In this chapter, alternative methods in achieving higher efficiencies in using optical power through proper use of physical arrangements of transmission system are shown.

As it was stated before, the channel delay spread is another important channel parameter. The spread of signal due to multipath propagation causes ISI that degrades the bit error rate as the bit rate increases. It has been shown that without using proper equalization techniques, the bit rate is limited to about 30 Mbps for a non-directed infrared link in typical indoor environments [53]. Therefore, for higher speeds, the use of equalizers seems unavoidable. However, this adds to the price and complexity of the system. Even with the use of equalizers, more power is needed to achieve the same bit error rate (BER) of an additive white Gaussian noise channel without any multipath distortion. Therefore, an optimized optical link design should try to maximize the received optical power and at the same time minimize the channel delay spread.

Characteristics of the receiver such as its FOV and direction of reception are also among the important factors determining the quality of the received signal. For indoor environment, the background noise is directional. In other words, the most important portions of background radiation from office lamps or skylight are detected from certain directions. Having a multi-branch receiver enables the receiver to implement proper combining methods to decrease the effective noise and reduce ISI in the received signal. For proper design of multi-branch receivers employing direction diversity, the effects of receiver FOV and its direction should be studied. A brief overview of these effects is presented in [86].

The received optical power and the channel delay spread of the impulse response will be used to compare the effects of transmission and reception configurations on the received signal. Sometimes it is important to have information about spatial variations of the channel. Distribution of the received power and the channel delay spread over the area of a room and sensitivity of these distributions to environmental conditions are among important information required for an optimized optical link design. The probability distribution function (PDF) and cumulative distribution function (CDF) for the simulation results can be used to compare the coverage area of the given configuration. For example, assuming one simulation per each 10 cm×10 cm block all over the room, the channel parameters can be calculated for 1200 locations in a 3 m×4 m×3 m room. This will generate a vector of size 1200 for the calculated parameter. The PDF(x) and CDF(x) can be used to provide more information about the spatial distribution of the values of the desired parameter. Average of the measured values as well as their minimum, maximum, variance and also the 10^{th} and 90^{th} percentile of the CDF curve are other measures used for comparison of the proposed configurations. $P_{10\%}$ is defined as the received optical power that is received in more than 90% of the room area at a desktop level. In other words, only 10% of the area in a room receive optical power that is less than $P_{10\%}$. Considering the spatial distribution of the channel delay spread, 90% of the area have a channel delay spread smaller than $d_{90\%}$. In the following sections, the difference between the minimum and maximum of a particular parameter is termed its dynamic range. It is desired that the dynamic range of the channel delay spread and the received optical power be as small as possible.

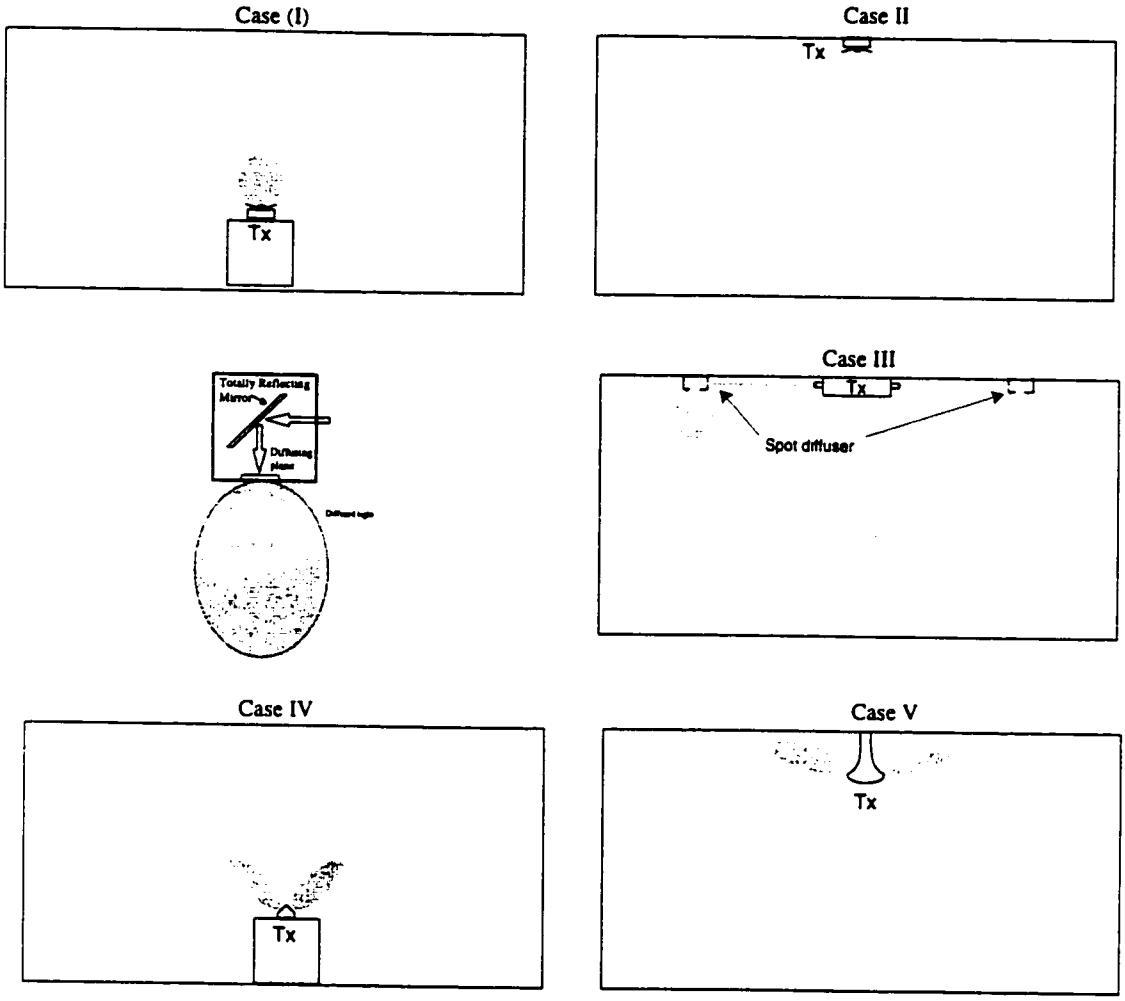

Figure 13. An optical signal could be transmitted using different configurations. Some of these configurations show considerable advantages in terms of uniform coverage and resistance to shadowing. The configurations that are proposed, simulated and compared are shown in this figure.

4.3 POWER EFFICIENT TRANSMISSION DESIGN

To demonstrate the link design alternatives, the simulation software is used to calculate the spatial and numerical distributions of the received optical power and the channel delay spread for a typical conference room under different transmission configurations. The simulation is conducted considering the first two reflections for each impulse response. Five different configurations were used for comparison purposes. The physical arrangement of the

transmission systems is illustrated in Figure 13. For each configuration, 1200 impulse responses were calculated and the received optical power and the channel delay spread of these responses were used to sketch the spatial and numerical distributions presented in Figure 14 to Figure 18. The receiver is assumed a wide field-of-view receiver with a detector size of 1 cm^2 located at the height of 1 m from the ground and looking towards the ceiling. To measure the spatial distribution of channel parameters in each room, the receiver is moved in steps of 20 cm and the whole room is covered by this movement (25 measurements in each square meter). Reflection coefficients of walls, ceiling and floor are assumed 0.7, 0.8 and 0.2, respectively. In all cases, the transmitted power is 1W and the received power is measured in optical dB (dBo).

4.3.1 Case I: Table-mounted single diffused source

This is the simplest diffused configuration in which the base station is located in the center of a room looking directly towards the ceiling and the transmission pattern of the diffuser is a first order Lambertian pattern. This is a very common configuration which can be used for example in the ad-hoc connection of infrared transceivers between two mobile computing devices in a conference room.

Figure 14 shows the spatial distribution and numerical distribution of the received optical power as well as the channel delay spread in plots (a) through (d).

This architecture is fairly simple and robust to shadowing, since the entire ceiling is contributing to the received power at the receiver and it is very difficult to be blocked. The path loss is high in this configuration and it has a large dynamic range that shows sensitivity to receiver movements. In other words, displacement of the receiver in this configuration can change the received optical power from –58 dBo near the room center to less than –62 dBo near the room corner. The channel delay spread is also moderately high which adds to the power requirements of the system.

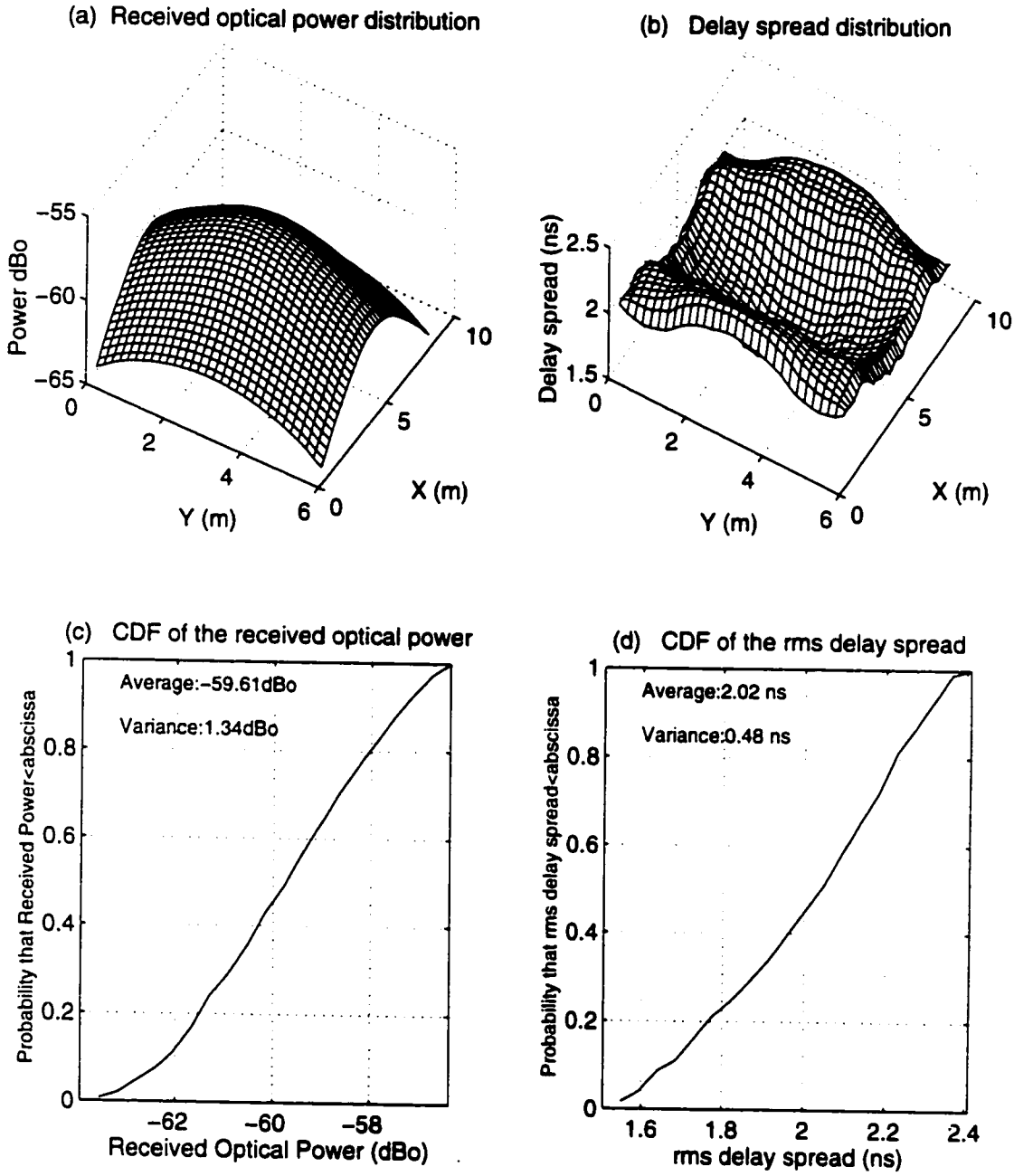

Figure 14. Spatial and numerical distribution of a fully diffused configuration (Case I).

4.3.2 *Case II: Ceiling mounted LOS*

In this configuration (which is sometimes called quasi-diffused configuration) the transmitter is mounted on the ceiling and radiates the optical power by a Lambertian pattern. This configuration is suitable for applications that require asymmetric communications links in which the downstream has a higher data rate compared to the upstream data rate. The base station is mounted on the ceiling to generate the signal for multiple users of the system in a given area. Examples of these applications could be found in high-quality multimedia broadcast of signals to many users in a small area such as museums or theaters. In general, all configurations that use a ceiling mounted device are more suitable for applications in which the link is not symmetrical. This assumes that the receivers are operating in a non-directed environment in which the alignment of the receiver to the source is not required. Therefore, the receivers need to generate the upstream signal using a diffused configuration that would limit the achievable upstream capacity, resulting in an asymmetrical link.

The received impulse response in this case consists of a very strong impulse plus a tail of relatively weak residual signals coming later. This is because of the fact that there is a line-of-sight between the transmitter and the receiver, which carries a lot more power than the reflected rays from objects in the room. The strong contribution of this line-of-sight (LOS) impulse to the total impulse response results in a very low channel delay spread in the overall impulse response as it can be seen from plot (c) and (d) on Figure 15. It is also seen from this figure that the average received optical power is much higher in this configuration compared to the configuration of case I. However, it should be noted that this configuration is highly-sensitive to shadowing. Any blockage of the LOS path by shadowing causes a severe decrease in the received power and an increase in the channel delay spread.

This is intuitively justified, as well. It can be seen from the physical configuration that in the absence of LOS path, the received signal to the receiver is mainly through first-bounce reflections from walls and second-bounce reflection from ceiling. Both of these energy sources are weaker than first-bounce reflections from the ceiling as in the pure diffused case.

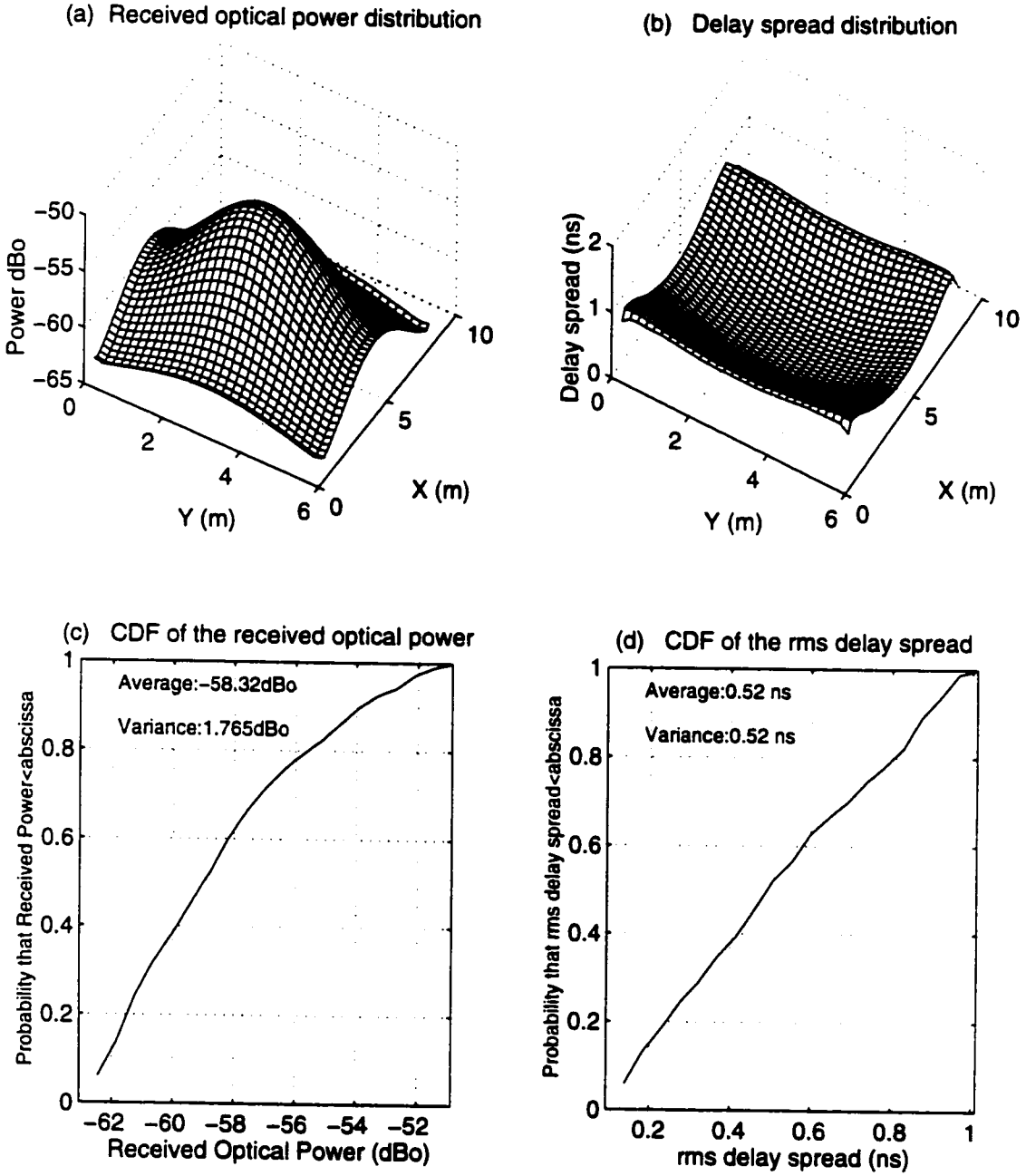

Figure 15. Spatial and numerical distribution of a quasi-diffused configuration (Case II).

4.3.3 *Case III: Ceiling mounted LOS using spot diffusers*

Passive optical components such as a simple reflector and a diffuser can be used to provide an efficient distribution of optical power for the desired coverage area [123][85]. An example of this is illustrated in Figure 16, plot (c) and (d). In this configuration, the base station is mounted at the center of the ceiling and uses collimated optical beam to pass the signal to four passive optical components (spot diffusers) mounted in different parts of the ceiling. The passive optical components are used to diffuse the infrared signal into the designated coverage area. Each diffuser covers a quarter of the room, but since the transmission pattern is Lambertian, there is no limitation on the FOV of the transmitter. In other words, in any location, there is a signal coming from each spot diffuser. The presence of a LOS between the sources and the receiver results in higher power efficiency and lower channel delay spread for this configuration. At the same time, since there are multiple sources of optical signal, the shadowing probability is lower which means that this configuration is much more robust to shadowing compared to the configuration of case II. It can be seen from the results plotted in Figure 16 that the received average optical power is the highest in this case compared to all other configurations. Note also that the channel delay spread is very small in this case.

This configuration requires some installation works that might be problematic for some business applications. In addition, this configuration is not as robust to shadowing as the other diffused cases.

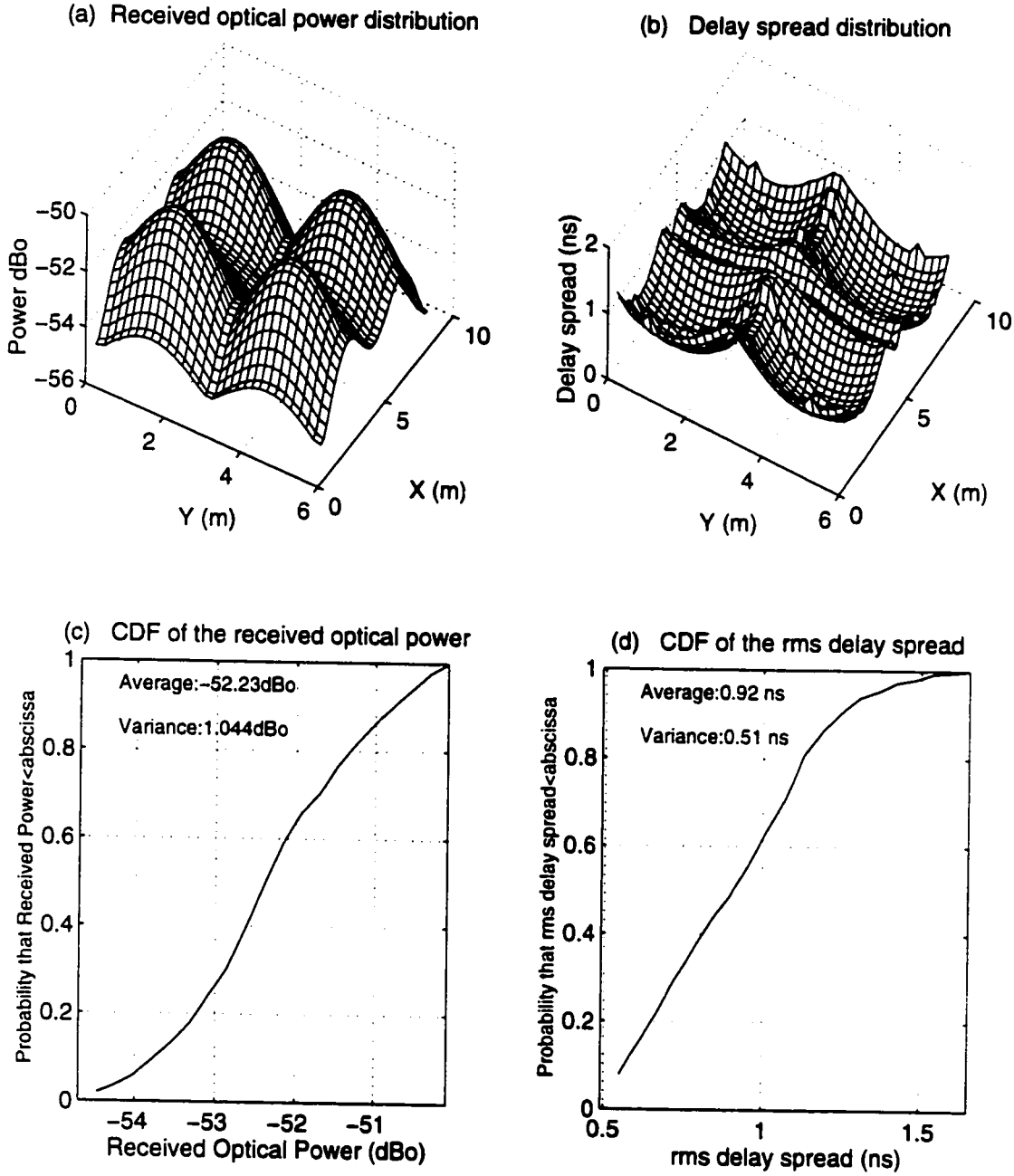

Figure 16. Spatial and numerical distribution of a diffused configuration using spot diffusers (Case III).

4.3.4 *Case IV: Four sources, different directions, table mounted diffused*

This configuration uses four transmitters looking into four different directions to illuminate the different parts of the ceiling of the room. Each transmitter has an elevation angle of 30° and a 5th order Lambertian radiation pattern. This results in a more directed form of transmission compared to a first order Lambertian pattern. The total transmitted power of 1 W is divided between the four transmitters. Having several lower power lasers at the base station enables the designer to have control over which area of the room should be illuminated. A proper mechanism can be used to scan the presence of receivers in different directions based on the strength of the received signal. The base station then can send the signal only in that direction and save some power. This is the basic idea of the so-called transmission diversity for indoor infrared communications.

Since the main source of power for the receivers is from the reflections on the ceiling, this configuration is also very robust to shadowing. The drawback for this configuration is the higher channel delay spread as it can be seen from the graphs in Figure 17. However, the power penalty due to the higher channel delay spread is much less than the gain in the received power. So overall, this configuration uses the transmitted optical power more efficiently.

The variation range of the received optical power and the channel delay spread is very small showing a uniform distribution of power across the room and a small sensitivity to the movement of the portable receiver.

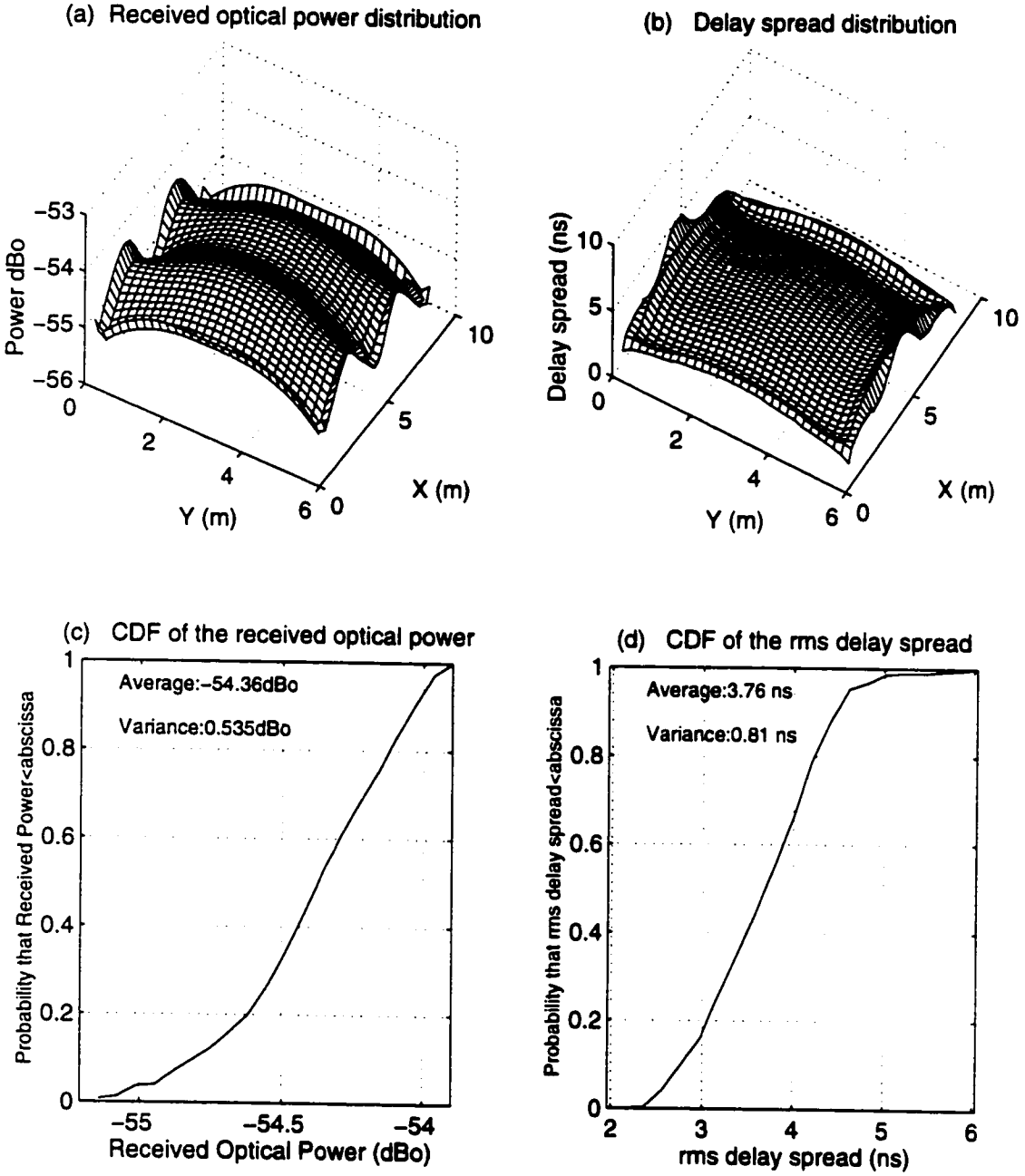

Figure 17. Spatial and numerical distribution of a fully diffused configuration using four transmitters at a desktop level (Case IV).

4.3.5 *Case V: Ceiling mounted diffuse using multiple diffused transmitters.*

In this last configuration, there are four transmitters each with a 5th order Lambertian pattern looking toward four quarter of the ceiling. The base station is mounted on the ceiling and the transmitters are about 30 cm below the ceiling looking toward the ceiling at an elevation angle of about 10°. This configuration is very similar to the configuration of case IV, but as it is seen in the results of Figure 17, the power efficiency is higher and the channel delay spread is smaller. Since the whole ceiling is used as the reflector and power source for receivers, the shadowing is not a major problem in this configuration.

The smaller distance between the base station and the ceiling results in higher power efficiency as it can be seen in Figure 18. The presence of base station on the ceiling while providing a ceiling reflected transmission pattern makes this configuration a good choice for areas in which a desktop mounted base station is not practical. For example, in some office environments, partitions create serious shadowing problems for a desktop mounted base station. In those cases, such configurations provide a highly efficient power distribution, small delay spread values and less sensitivity to shadowing.

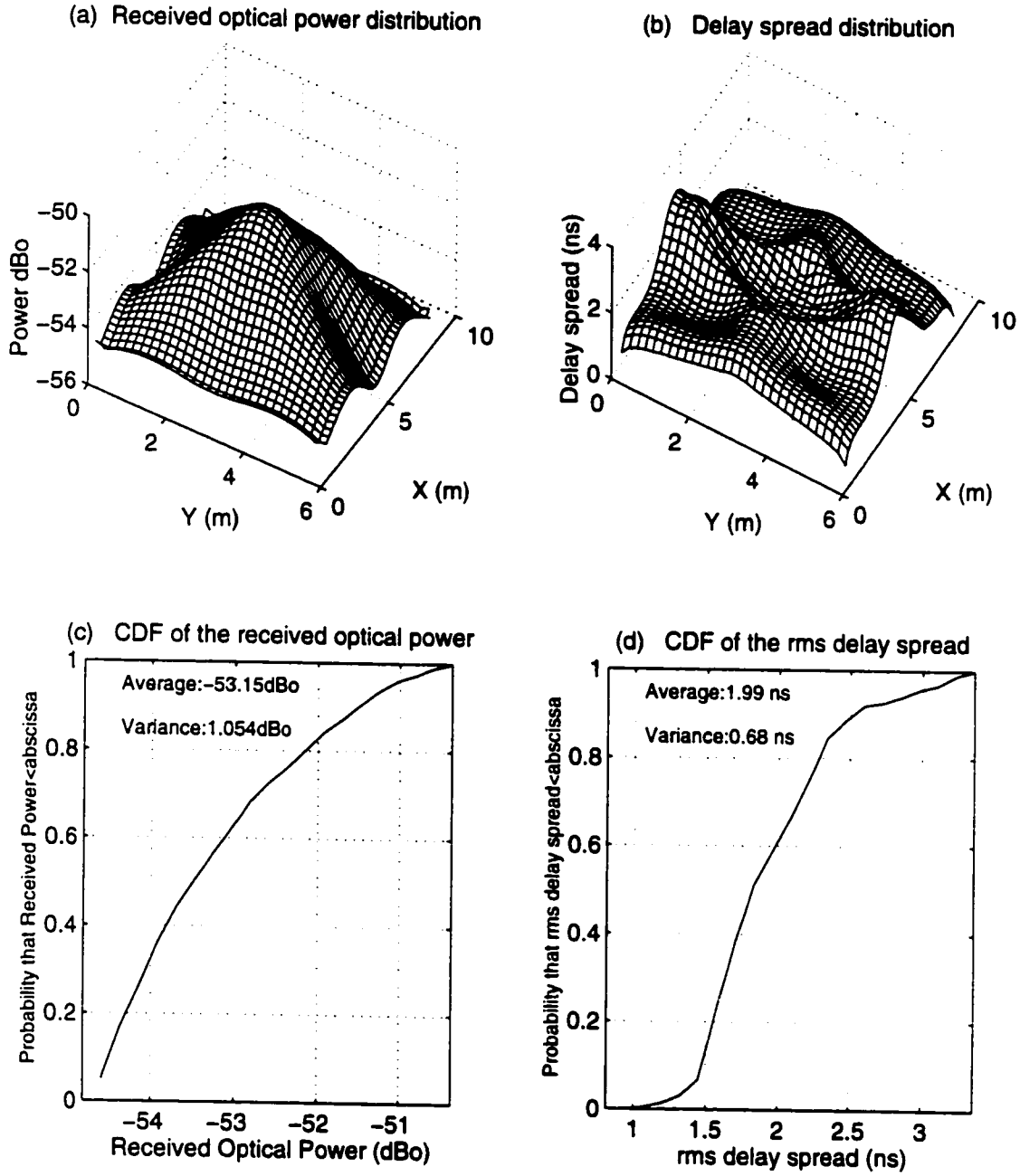

Figure 18. Spatial and numerical distribution of a fully diffused configuration using four transmitters on the ceiling (Case V).

	Received Optical Power (dBo)				Channel delay spread (ns)			
	Average	P90%	Max	Variance	Average	d90%	Max	Variance
Case I	-59.61	-62	-63.7	1.34	2.02	2.3	2.41	0.48
Case II	-58.32	-62	-62.5	1.76	0.52	0.9	1.03	0.52
Case III	-52.23	-53.7	-54.6	1.04	0.92	1.31	1.52	0.51
Case IV	-54.36	-54.8	-55.3	0.53	3.76	4.2	6	0.81
Case V	-53.15	-54.5	-54.7	1.05	2	2.5	3.4	0.68

Table 2. A summary of the simulation results showing the received optical power as well as the channel delay spread when different transmission configurations are used.

4.4 SUMMARY AND CONCLUSIONS

Design of an indoor broadband wireless system using infrared needs careful attention to the details of transmission and reception subsystems.

It is shown that a proper design of such a system involves proper design of the transmission subsystem and proper arrangements of the transmitters and/or diffusers. Table 2 shows a summary of the simulation results. Overall, it is shown that an improvement of 4 to 8 dBo in the received optical power can be achieved by using proper design and implementation of the transmission system. Also, the channel delay spread and the dynamic range of power can be made smaller by choosing proper configurations. The proposed configurations are just samples of possible choices and they just introduce the fact that "a proper link design includes optimization of transmission arrangements". Depending on the applications and the environment type, case III to V show better characteristics as compared to case I and II which are the usual candidates for employing an indoor infrared link. Furthermore, when more than one transmitter is used, a proper power control algorithm can be used to turn-on only the desired lasers. This can be thought as a transmission diversity that can save transmission power and reduce the risk of the shadowing.

CHAPTER FIVE

5 EFFECTS OF RECEIVER ROTATION ON INFRARED CHANNEL

5.1 INTRODUCTION

Infrared transmission is very sensitive to the direction of the source and the receiver. Infrared systems employing diffuse configuration are less sensitive to this effect. However, there are still considerable variations in the channel characteristics as the receiver or transmitter rotates.

This chapter contains the measurement procedure and results obtained from a large set of measurements performed at the University Of Ottawa in Colonel By Hall (CBY), 770 King Edward. These measurements were conducted to investigate the effects of receiver rotation on the channel characteristics. In the following sections, the measurement setup, the measurement plans and results for rotation measurements are presented. The measurement results are used to describe the general characteristics of the channel transfer function using a piecewise linear method. It is shown that the variation of the channel path loss is smooth and predictable. A method to predict the angle of minimum path loss along a rotation path is suggested and verified by comparing against simulation results. Also, the results of these set of measurements have been used to define an algorithm that can be used to predict the variation of path loss in any given transceiver configuration

5.2 RECEIVER ROTATION

As mentioned before, the objective of measurements included the investigation of the effects of receiver rotation and receiver shadowing. This section describes the results obtained from the receiver rotation measurements and general conclusions obtained from them.

The receiver direction is an important parameter that has a major impact on the infrared channel characteristics. It is obvious that an infrared receiver with small FOV that is operating in a LOS configuration is subject to severe channel changes when it rotates. When the diffuse configuration is used, the system is less sensitive to rotations. As the receiver FOV increases, the changes in the channel properties become smaller. However, even a wide FOV receiver is subject to major channel degradation because of receiver rotation. This is clearly shown in the results of the following sections.

5.2.1 Measurement objectives and procedure

To investigate the effects of receiver rotation on the channel characteristics, 9 measurement sites in Colonel By Hall (CBY), are chosen. The rooms have different sizes and shapes and contain different objects. For each room, one or two positions for the transmitter and the receiver were chosen. For each position, the measurements were performed in both LOS and diffuse configurations.

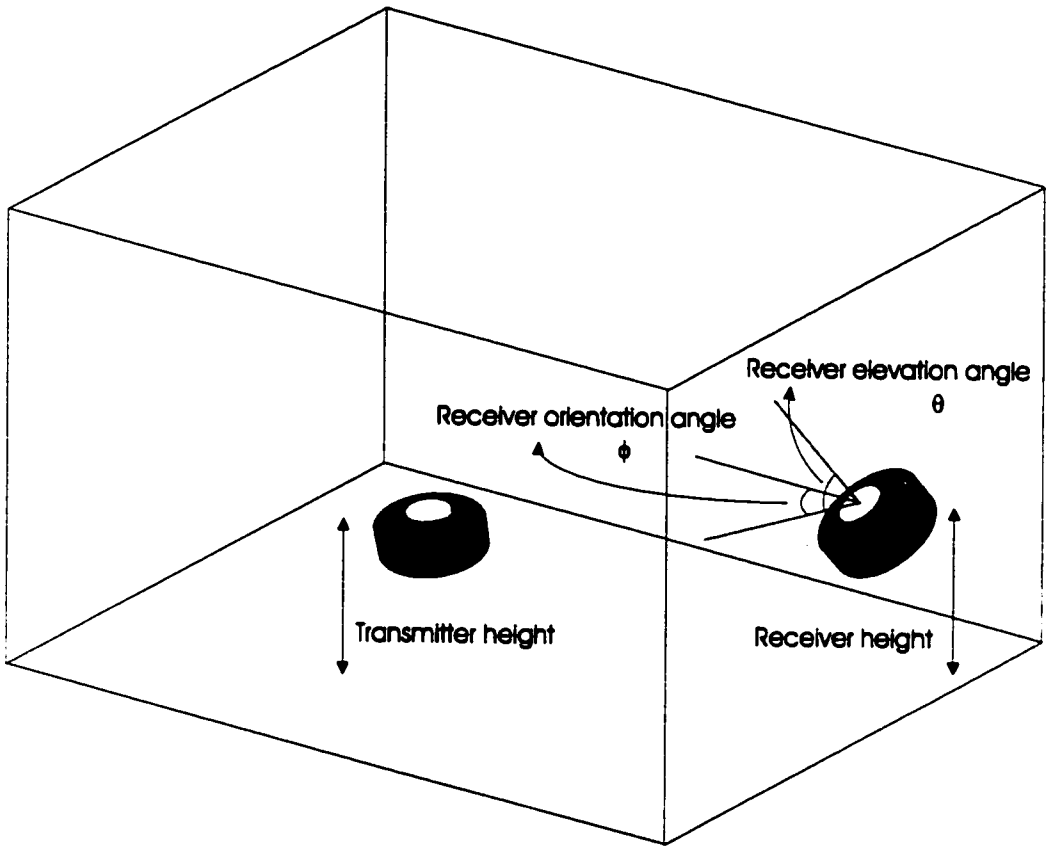

Figure 19. For each measurement location, the elevation angle of the receiver (θ) is varied from 0° to 180° in steps of 5° and the channel transfer function is recorded in each step. Then the receiver orientation angle (ϕ) is changed by 45° and the elevation angle is set to 0° and the same set of measurements is repeated. This process is performed 4 times in each location. Therefore, the orientation angle takes the values of 0°, 45°, 90° and 135° and the elevation angle takes 0°, 5°,...,180°. This way, the entire hemisphere above the receiver is covered with 148 recorded transfer functions.

To measure the channel frequency response in a LOS configuration, the optical beam from the laser diode is collimated with a Nikkor 50mm/f1.4 lens and points to a white flat reflector mounted on the ceiling. The reflector is placed directly over the transmitter on the ceiling and the transmitter is to the ceiling. Light is diffusely reflected with a Lambertian radiation pattern

from the ceiling towards the floor. This is as if there is a Lambertian source in a desired point on the ceiling. This method is called spot diffusing [123]. In our set-up, the lens introduces a 2.7dB optical loss. For measurements in a diffuse configuration, a glass diffuser is attached to the laser diode, generating a Lambertian radiation pattern. The diffuser introduces a 4.7dB optical loss. For both cases, the infrared source is mounted on an adjustable stand and is looking straight up towards the ceiling.

The receiver is mounted on a step motor that is fixed to a stand. The step motor is a dc motor made by American Precision Co. and is controlled by a personal computer. It enables the receiver to rotate by 180 degrees in programmable steps to detect signals from different directions. Custom computer software controls the step motor and collects data from the network analyzer. The computer, the network analyzer and the power supplies are all placed on a cart. In the measurements, the locations of the transmitter and receiver are first chosen. Then, the computer program automatically rotates the receiver by 5° per step, collects the frequency response data from the network analyzer and stores the data on the computer hard disk.

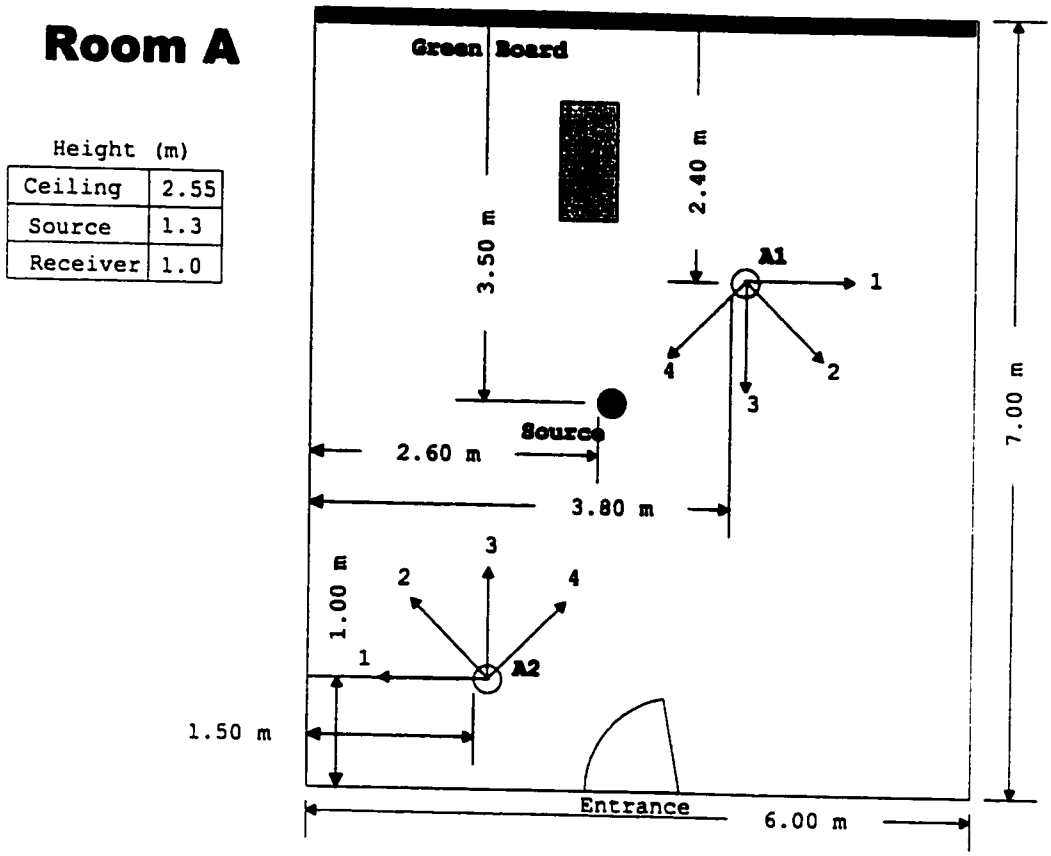

Figure 20. Location of the receiver and transmitter in one of the measurement rooms (CBY: E015). Arrows at the receiver locations show the major directions of rotation for each position.

For each desired location/configuration, four sets of data are collected. Each set corresponds to a full 180° rotation of the receiver and since the rotation is done in steps of 5°, there are 37 recorded frequency responses in each turn. This rotation is done to change the elevation angle of the receiver as illustrated in Figure 19. The receiver is looking towards one of the walls of the room at angle zero and as the elevation angle increases, the receiver rotates towards the ceiling. When the elevation angle reaches 90°, the receiver is looking directly towards the ceiling. As the elevation angle increases again, the receiver turns towards the opposite wall of the room and at 180° the receiver is facing directly towards the opposite wall. The receiver is rotated 3 times and by 45° each time to record another set in the same position. This rotation simply changes the orientation of the receiver in the room to change its starting point from being towards one of the walls to face to a room corner and then the other wall and so on.

Figure 19 shows the orientation and elevation angle of the receiver. Figure 20 shows one of the measurement sites called room A (Room E015, CBY building). For each of the two locations in the room, the four orientation angles are clearly marked by numbered arrows.
For each configuration at each point, four sets of 37 frequency responses are recorded. The same procedure is followed for both LOS and diffuse configurations. Therefore, for each location in each room, there are 148×2=296 recorded frequency responses. For our measurements concerning the effects of rotation, 17 positions in the rooms were chosen resulting in a database of 296×17=5032 frequency responses of the channel. This is a very large database of indoor infrared channel measurements and gives us a good base for statistical analysis of the recorded data and its parameters. Appendix B contains the shapes and dimensions of all the measurement sites. It also shows the locations and directions of rotations for the receivers in the measurement sites.

5.2.2 Measurement results and observations

In this section, parts of the results obtained from the measurements are described. Figure 20 shows the location of the source and the receiver in room A. This is a typical classroom of size 5.3 m×7.0 m with 5 rows of chairs, a total of 33 chairs for students. Walls are rough concrete type with yellowish color. Ceiling is flat with the same color. Green board extends over the entire width of the class. There are 16 flourescent lamps with transparent plastic covers on the ceiling each is 1.2m by 0.3m. In the diffuse measurements where the ceiling is illuminated by the infrared radiation, it seems that little energy is reflected from these covers and most of the received energy passes through the covers and is being absorbed. All other office and class environments that are used for measurements have the same type of ceiling unless otherwise specified in the room description in Appendix B. The source is at the center of the room with a height of 1.3 m. The source is placed at coordinates A_1={1.5 m, 2.5 m} and has a height of 1 m. The receiver is at the center of the room. Figure 21 shows the effect of receiver rotation on the amplitude of the channel frequency response in room A. It can be seen that the shape of the transfer function changes when the receiver rotates. The rotation may cause some nulls in the frequency response and changes its dc value representing the channel path loss. This figure also shows the effects of receiver rotation on the channel impulse response.

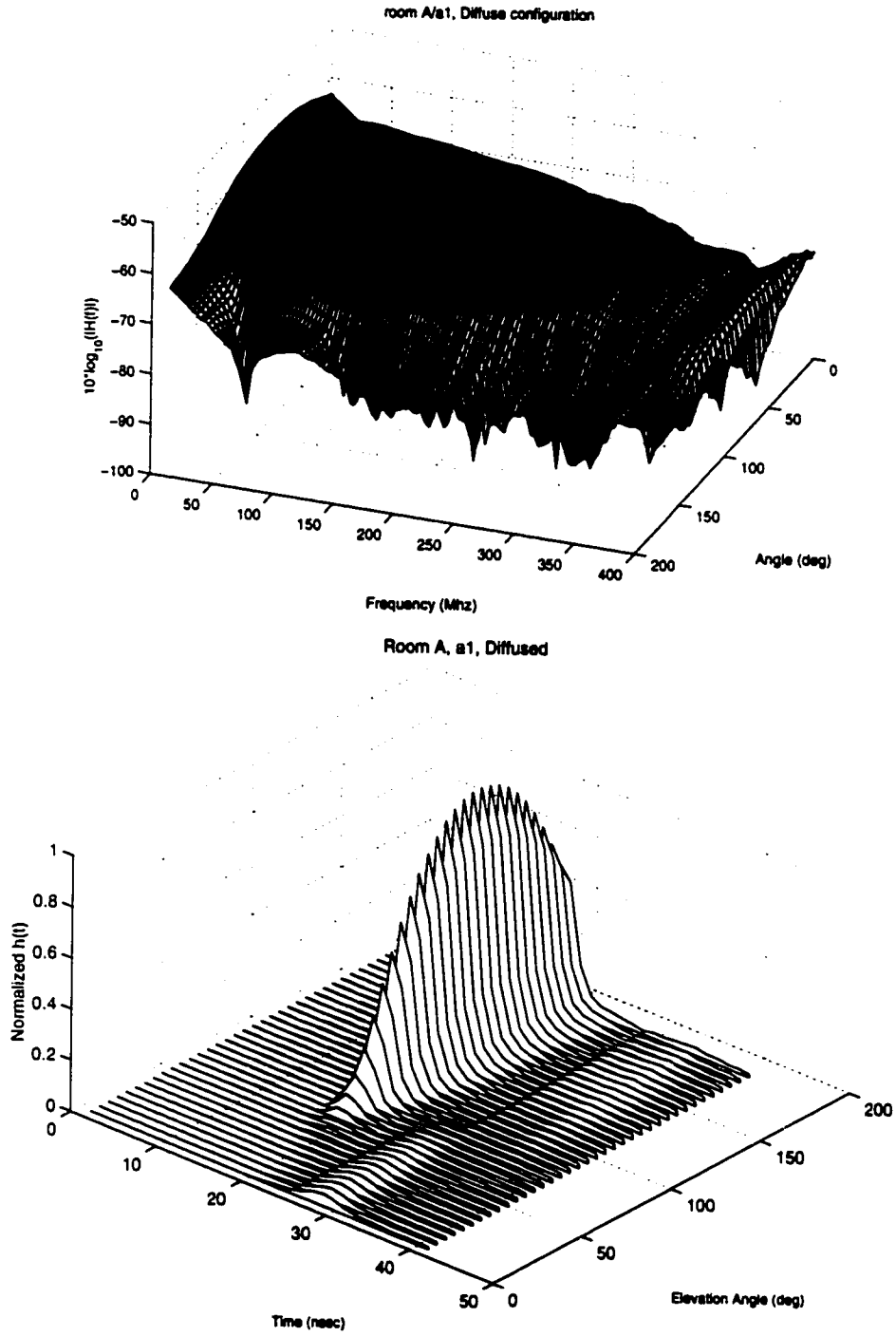

Figure 21. Effect of receiver rotation on the magnitude of the channel frequency response (top) and the channel impulse response (bottom).

Although the details of the transfer function shape and the change in the path loss are different in each room, the same trend is observed in all the measurement results. The path loss and the delay spread of the channel change with receiver orientation such that the high values of the received optical power correspond to low values of delay spread. The relation between the channel path loss and channel delay spread is studied with more details in subsequent sections. Figure 23 shows an example of these changes for both LOS and diffuse configurations in that same location of room A. As the receiver elevation angle, θ, increases from zero toward 90° the PL and delay spread decrease. When θ is between 50° and 130°, the channel delay spread is usually very low and also the PL has its lowest value somewhere in between. Increasing θ after 130° would increase the path loss and the delay spread again. By observing similar curves for other locations, it is clear that the rotation has an almost deterministic effect on the variation of the path loss and the delay spread. The lowest value of the PL and the angle of lowest PL seem to be quite related to the physical location of the source and receiver. It will be shown that these two important parameters can be predicted by using the information about the physical location and relative rotation angle of the receiver.

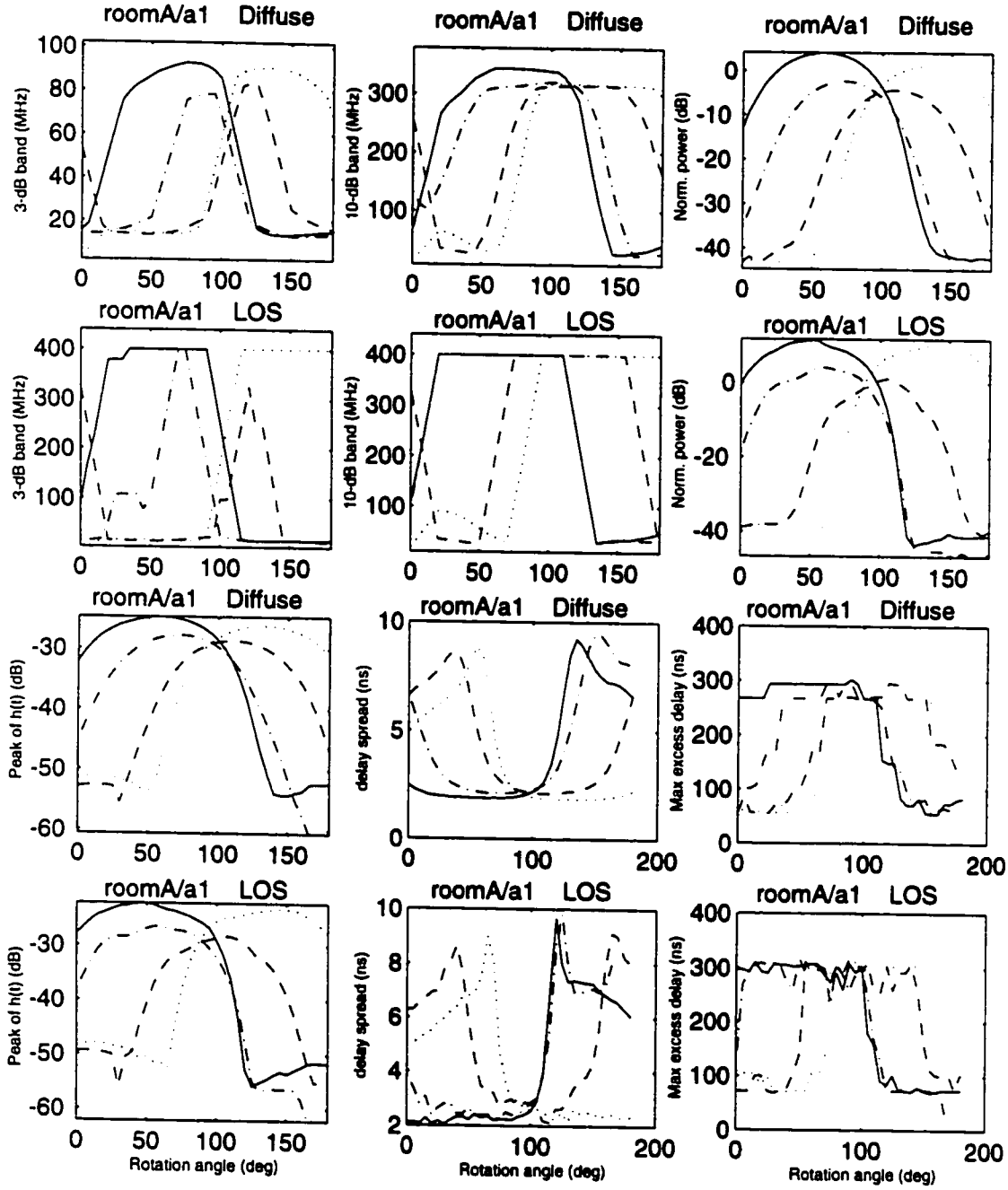

Figure 22. Variation of the extracted set of parameters for a rotated receiver in location a1, room A. Each plot shows the variation of a parameter for 4 sets (4 curves) of 180° rotations in a given location. Results of the diffused and LOS configurations are presented separately for comparison purposes.

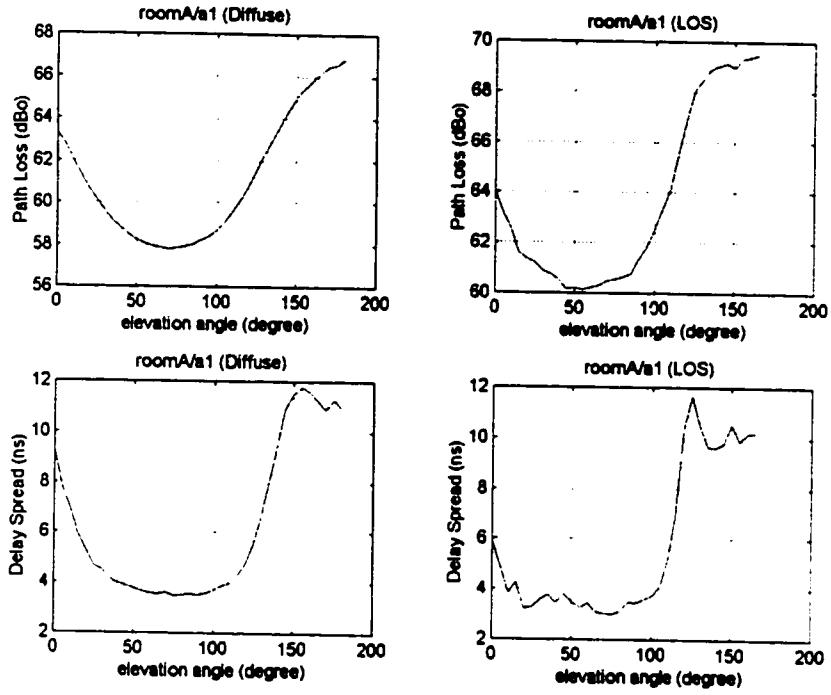

Figure 23. The channel path loss and its delay spread change when the receiver rotates. Graphs show these changes for both LOS and diffuse configurations for location a1, direction (2).

Figure 22 shows a set of graphs showing the desired parameters and their change due to the rotation of the receiver. The extracted sets of parameters are from the recorded set of frequency responses in one of the locations in room A. The change of each parameter with respect to the angle of the receiver is clearly seen in the graphs. The graphs are also useful for comparing the LOS and diffuse configurations.

It is also interesting to note that the fall and rise of the path loss and the delay spread in Figure 23 seem to have some correlation. This is an interesting fact that is observed more clearly by plotting the path loss versus the delay spread for any given location.

Figure 24 shows this plot for the room A, location a1. The two plots show the relationship between these two parameters for the LOS and diffuse configurations in the same location. It can be seen that the two parameters are linearly dependent on each other when they are plotted on a log scale. Note that the channel path loss is usually reported in log scale by dBo, but the delay spread is usually reported by its value and not its log value. In other words, when

the two variables are expressed in a log scale, the value of the correlation coefficient for the linear regression between them is very close to unity. It should be noted that this relationship is a statistical measure of dependence of these two variables. That means for most cases, a high value of delay spread corresponds to a high value of path loss. Figure 24 also shows the result of a linear regression between the two parameters as a solid line on the plot. This relationship can be represented by

$$PL = \alpha \log_{10}(\sigma) + \beta$$

where PL is the path loss and σ is the delay spread.

This relationship was also observed for in all other measurements. The values of α and β are not the same in all cases and they depend on the location and configuration. However, for most of our results, the values are very close as it can be seen in Table 3. This table shows the correlation coefficient between path loss and delay spread values for different configurations and in some of the measurement sites. The parameters of the linear fit, α and β are shown. It is seen that the correlation coefficient ranges between 0.89 to 0.97 for both configurations in all the rooms. On the average, the correlation is high (around 0.93) and one can conclude that these two variables are dependent as far as the receiver rotation is concerned.

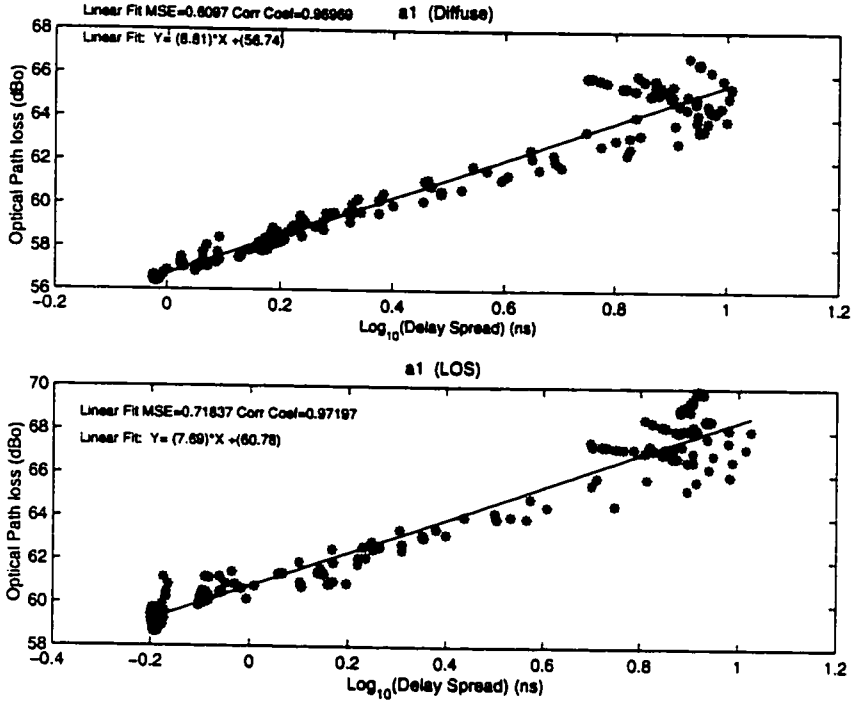

Figure 24. The channel delay spread and the channel path loss have a strong correlation when the receiver rotates. These two plots show this relationship in one of the measurement locations (room A, a1).

From the numerical results obtained, it is seen that the average value for α and β are noticeably different for LOS and diffuse configurations. The variances of these variables are also smaller for the LOS case. Using the numerical results reported in this table, it can be concluded that when the receiver rotates, the channel delay spread can be approximately estimated from its path loss by using:

$$\sigma \approx 10^{\left(\frac{PL-\beta_{avg}}{\alpha_{avg}}\right)}$$

The value of α_{avg} is approximately 9 (dBo/ns) for the diffuse configuration, 8 (dBo/ns) for the LOS configuration. The value of β_{avg} is approximately 57 dBo for the diffuse configuration and 61 dBo for the LOS configuration.

The mean-squared-error (MSE) for the linear fit in all locations has also been included it in the table. The small value of the MSE, which is less than 1.5 dBo in most cases, shows that usually, the suggested linear relationship is a very good approximation.

5.3 VARIATIONS OF THE TRANSFER FUNCTION

The channel transfer function varies in all frequencies when the receiver rotates. In this section, the variations of $H(f)$ are studied and some general conclusions about the effects of rotation on the channel transfer function are provided.

As it was mentioned before, the collected data for each point consists of 4 sets of frequency

Room	α_{nlos}	β_{nlos}	MSE_{nlos}	$X_{corr_{nlos}}$	α_{LOS}	β_{LOS}	MSE_{LOS}	$X_{corr_{LOS}}$
A1	8.81	56.74	0.6097	.97	7.69	60.78	0.7184	.97
A2	9.11	56.68	1.2237	.89	7.89	60.04	0.9839	.94
B1	10.17	55.92	0.6507	.92	7.42	61.37	0.6157	.94
B2	8.51	55.01	0.6672	.95	8.41	58.84	0.8469	.95
C2	4.62	64.87	0.2960	.97	4.79	65.02	0.7690	.92
C3	7.99	58.94	1.1574	.97	9.46	60.47	2.3529	.96
D1	9.06	58.65	1.1756	.94	8.39	61.89	2.0323	.91
D2	8.39	58.35	1.5362	.93	7.34	61.37	1.4281	.93
E1	8.03	58.75	0.7282	.97	7.45	61.95	1.0827	.95
E2	7.88	57.85	1.4376	.94	9.79	59.80	2.1768	.94
F1	8.79	57.33	0.7521	.90	5.85	62.73	1.0284	.86
F2	9.93	57.66	0.8604	.96	7.18	63.01	0.5315	.98
G1	15.59	50.86	1.2283	.89	10.89	58.45	1.3423	.89
I1	9.89	58.43	0.3857	.98	6.97	63.09	0.9751	.93
I2	7.46	61.68	0.5509	.93	7.42	64.66	0.6905	.93
J1	11.27	51.66	1.0070	.91	10.12	54.25	1.2883	.91
Mean	9.0938	57.461	0.8917	0.9388	7.9412	61.107	1.1789	0.9319
Var.	2.2649	3.333	0.3709	0.0303	1.5626	2.6098	0.5645	0.0299

Table 3 Correlation coefficient between the channel path loss and the delay spread in different rooms and in different configurations is shown here (Xcorr). The coefficients of the linear fit as well as the MSE of the fit are also shown in this table. Note that, the corresponding values depend on the transmission configuration (LOS vs. diffuse).

responses each corresponding to a different starting angle. Each of these four sets consists of 37 different frequency responses collected at different elevation angles. The receiver starts from angle $\theta=0°$ and continues up to $\theta=180°$ in steps of five degrees. Therefore, in each rotation of the receiver, 37 frequency responses are collected. These frequency responses cover a frequency band of 400MHz. For each $H(f)$, 128 complex samples are stored and used for processing. Therefore, each set could be considered as a matrix of size 128×37. Each column represents the transfer function at a given angle and each row represents the changes in the frequency response at a given frequency. Since the objective is to study the effects of rotation on the channel transfer function, the changes in rows of these matrices are considered.

Each row represents the changes of the transfer function at a given frequency with respect to the receiver direction. These functions can be represented by $G(f,\theta,P,C)$ where P is a set of parameters that affect the channel transfer function except the elevation angle, θ, and C is a parameter specifying the configuration (diffuse or LOS). By observing the shape of G at different frequencies, it is seen that G could not be considered as a random process. In other words, it exhibits a predictable shape. A simple and straightforward method of characterizing the shape of G is to apply a piecewise linear approximation to each G and recording the parameters of the fitted curve.

5.3.1 Piecewise linear approximation

Figure 25 shows a sample of the G function. The piecewise linear approximation to the curve is also shown in this figure. The developed fitting algorithm that is used to process the results is as follows:

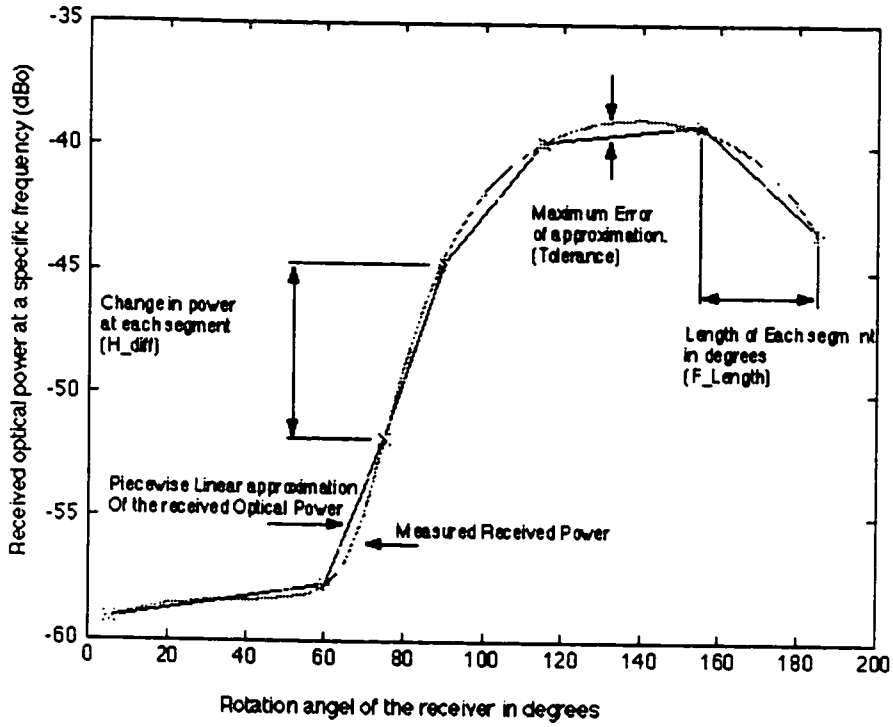

Figure 25. A sample of the changes in the transfer function of the indoor infrared channel at a given frequency with respect to the orientation of the receiver.

Given a curve $G(\theta)$, it is desired to fit a piecewise linear curve with an unknown number of pieces to it. The parameter "tolerance" specifies the maximum square error between the fitted curve and the actual curve. The curve $G(\theta)$ consists of a finite set of points (37 points in our case). The algorithm starts from the first point and passes a best approximate line from the first three points. The best approximate line is specified by using a mean-squared fitting algorithm, which is a widely used linear fitting algorithm. Then the maximum squared value of the difference between each and every one of the points on the $G(\theta)$ curve from the fitted line is calculated. If this error is more than the tolerance, then the linear fit would only be a line passing from the first two points and the algorithm starts this procedure again from the second point. If this error is less than the tolerance, one more point is added to the set and again the best linear fit is passed through these four points. This would go on until adding the K^{th} point results in an error, which is more than the tolerance. Then, the first piece is fixed from point 1 to K-1. The algorithm starts again from point K and repeats the procedure until it reaches the last point of the curve $G(\theta)$. The tolerance value is set to 0.5 dBo which means that each and

every point of the curve has a squared distance of less than $0.707=0.5^{½}$ dBo from the actual curve.

The fitted curve has a maximum deviation from the actual curve that is specified by the tolerance of fitting. The piecewise linear curve has H_nonzero pieces and the lengths of those pieces are specified by the parameter F_Length. The length of each piece could be different from another one. The slope of each of these linear pieces is also a useful parameter. This slope is specified by the parameter H_Diff that is the change of G in each piece divided by the length of that piece. This is effectively the slope of that piece. Clearly, more fluctuations in G results in a larger H_nonzero since more linear pieces are required to approximate a non-smooth curve. F_Length is a parameter that specifies how long G maintains its linearity when θ is changing. A large value of F_Length means a linear curve. H_Diff specifies how fast $G(\theta)$ changes by changing θ. A large value of H_Diff means more sensitivity of the received optical power to rotations.

5.3.2 Parameters

There are about 18,000 G curves in the database (128 curves for each rotation set that consists of 37 transfer functions). For each of these curves, two sets of parameters, H_Diff and F_Length, plus a single number, H_nonzero are derived. It is obvious that depending on the shape of G, the H_Diff and F_Length sets may contain different number of elements. In other words, a smooth G results in a small H_nonzero and two sets with a few elements for H_Diff and F_Length. However, a non-smooth curve may result in a high value for H_nonzero and two large sets of data for H_Diff and F_Length. For each of these parameters, the following statistical parameters can be obtained:

- Mean.
- Variance.
- Median.
- 10^{th} percentile.
- 90^{th} percentile.

There would also be an interest in estimating the probability distribution function (PDF) and cumulative distribution function (CDF) of these parameters. This would give a statistical

description for each of these parameters. The change of these parameters with respect to the frequency and the transmission configuration (LOS and diffuse) are also important.

5.3.3 Results and observations

The desired statistics are collected by adding all the available G functions from all the available rooms and locations. The LOS case and diffuse case are considered separately to let us compare between the statistics of the two different configurations. Figure 26 to Figure 32 show the graphs of the extracted parameters and their distribution with respect to the frequency and the configuration. The results for each parameter are described individually.

5.3.3.1 Parameter F_Length

As it was mentioned before, this parameter specifies the length of each linear piece. It has a unit of degrees. Figure 26 and Figure 27 show the parameters for F_length. Figure 26 contains two columns. The second column represents the PDF of F_Length at different frequencies. In each column, the top row represents the distribution for the diffuse configuration and the second row represents the distribution for the LOS configuration. The first column is a top view of the PDF curves with the shades corresponding to the amplitude of the PDF. In this graph, the mean of the F_Length is also superimposed to give a better understanding about the changes of this parameter with respect to frequency. It could be seen from the graphs that the average length of linear pieces, F_Length, is decreasing by increasing the frequency. In other words, at low frequencies, the G curve is smoother than in high frequencies.

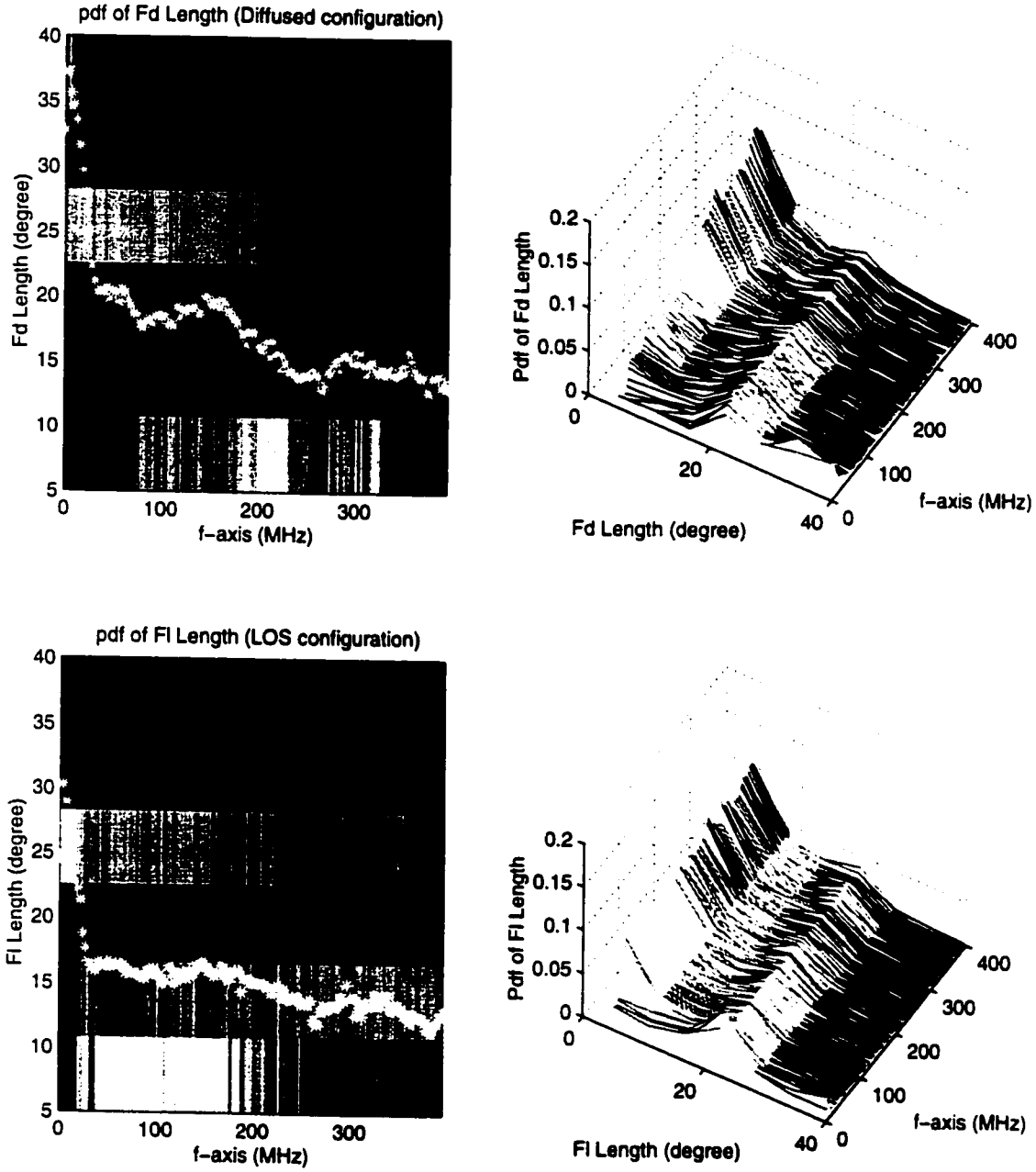

Figure 26. This graph shows the probability distribution function of the F_Length parameter for diffuse case (first row graphs) and LOS case (second row graphs). The left column graphs are a top view of the PDF graphs with average of the parameter superimposed on them.

It is also seen that the PDF of F_Length for the diffuse case is more uniform near dc compared to the LOS case. In the LOS case, it seems that the PDF has a constant shape across the frequency band except in the first few MHz of the band. In other words, its statistics seem quite stable with respect to frequency. This is more clearly seen in Figure 27 where all five statistical parameters of the F_Length are plotted for the two configuration cases. The average of F_Length is almost constant from 30 MHz to 400 MHz in the LOS case while in the diffuse case it has more variations. This average ranges from 20° to 30° at low frequencies and is around 15° from 50 MHz up, for the LOS case. For the diffuse case, at high frequencies, the average F_Length is around 15°, but for low frequencies, it ranges from 15° to 35°. For both cases, the average of F_Length is sharply decreasing from dc to 50 MHz.

The variance of the F_Length is almost constant across the frequency band. Note that the graphs in Figure 27 represent the mean minus variance and the mean plus variance to give a good idea about the spread of the parameter's value.

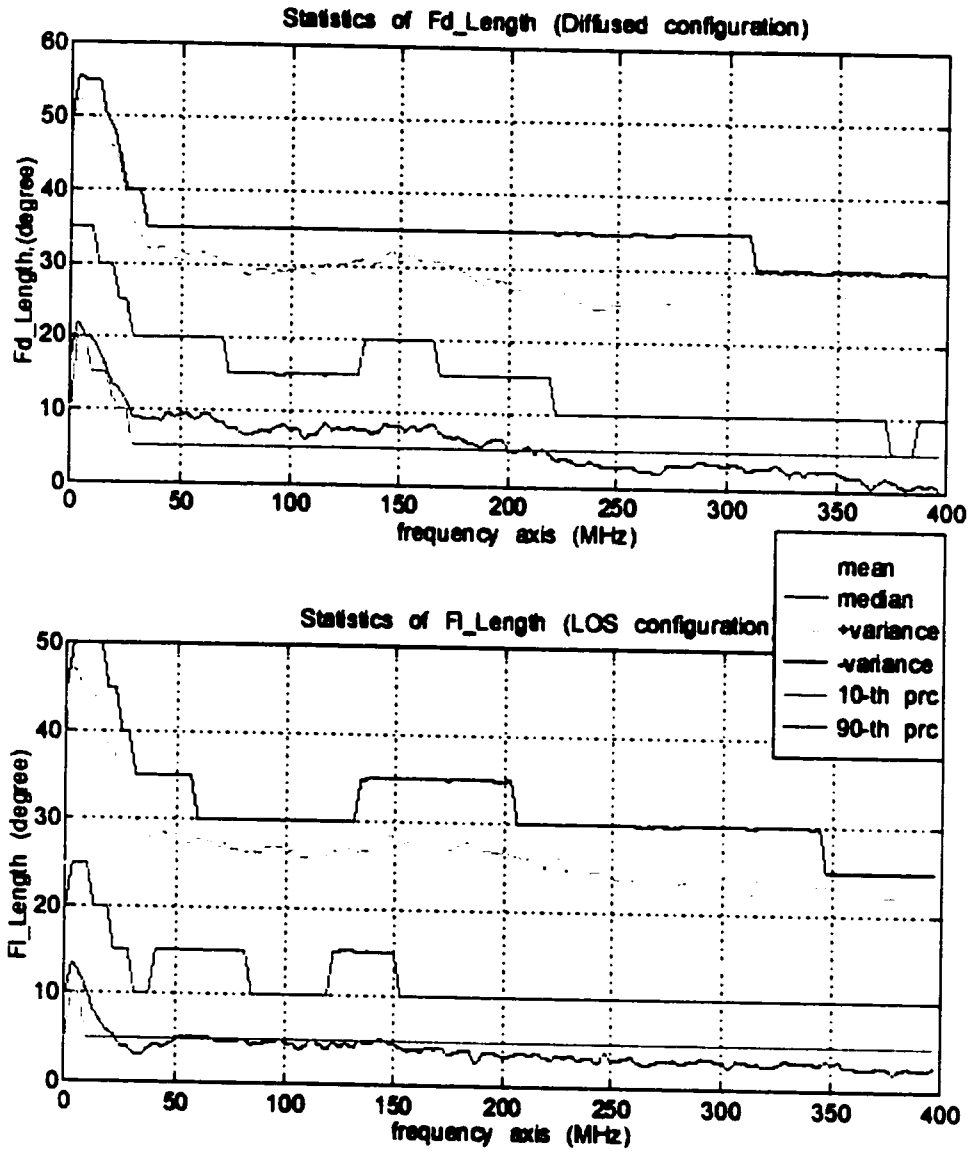

Figure 27. Statistics of F_Length for the diffuse (top) and LOS (bottom) configurations are shown in this figure. These statistics include average, median, 10^{th} percentile, 90^{th} percentile and mean plus and minus variance.

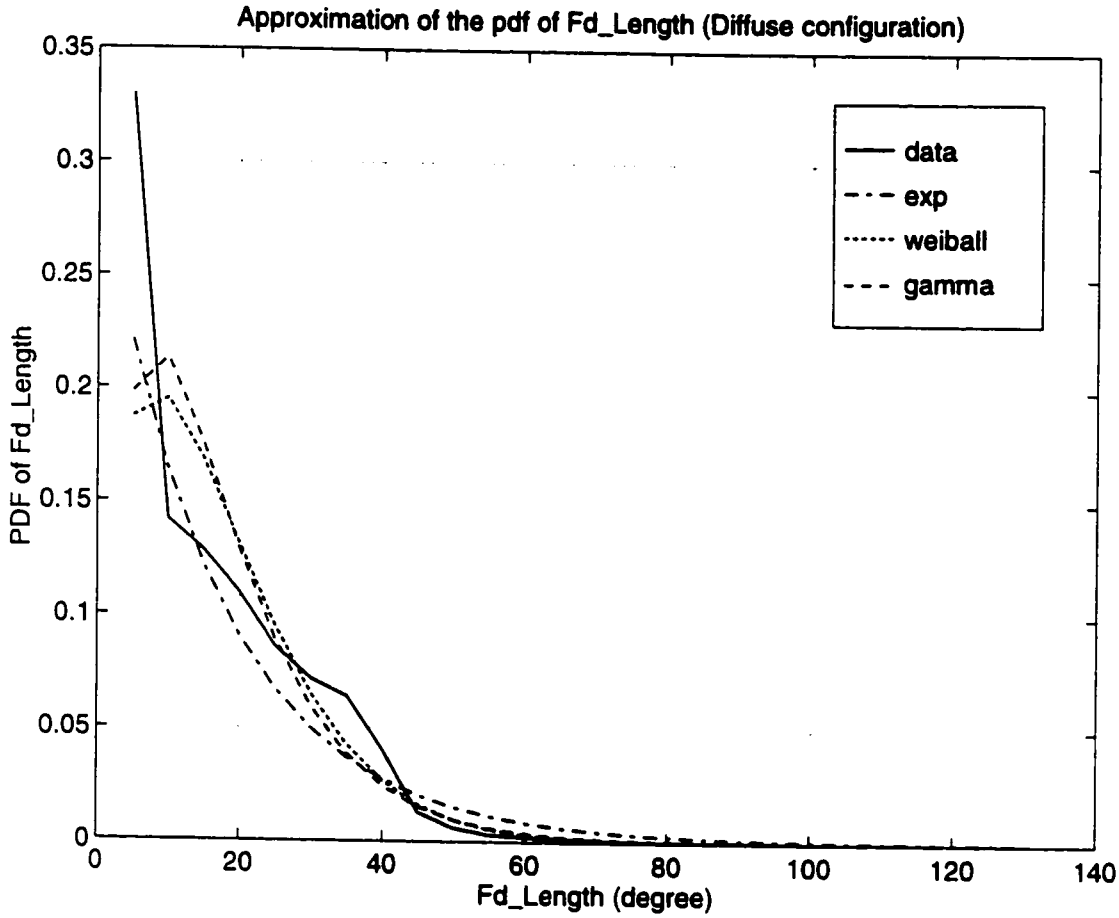

Figure 28. The probability distribution function of F_Length closely matches some well-known distributions such as gamma, Weibull and exponential distribution. This graph shows a sample of the PDF of F_Length and the corresponding fit of these three well-known distributions to it.

Another notable point here is the shape of the PDF for the F_Length. These shapes are quite similar to some well-known distributions such as Weibull, exponential or gamma distribution. This similarity is clearer at higher frequencies. A graph showing an optimized fit of these three distributions to the PDF of F_Length is shown in Figure 28. The gamma distribution provides the best fit.

5.3.3.2 *H_nonzero*

This parameter specifies the number of linear pieces that is required to fit the G curve with a piecewise linear curve. It can be considered as a measure of smoothness of the G curve. From Figure 29, the PDF of H_nonzero does not have a stable shape across the frequency band. Near dc, it is more concentrated around small numbers between 6 to 10. Increasing the frequency seems to distribute this PDF with an increasing average towards higher frequencies. In other words, increasing the frequency, the shape of G curve is getting more nonlinear. From Figure 30, the average of 6 to 10 pieces is enough to approximate the G curve from dc to around 40 MHz. From 40 MHz to 400 MHz, 10 to 15 pieces exhibit a reasonable approximation for the G curve. On the average, the LOS case has a larger H_nonzero compared to the diffuse case. This average also steadily increases with frequency for both the LOS and diffuse configurations. The variance of H_nonzero also steadily increases with frequency.

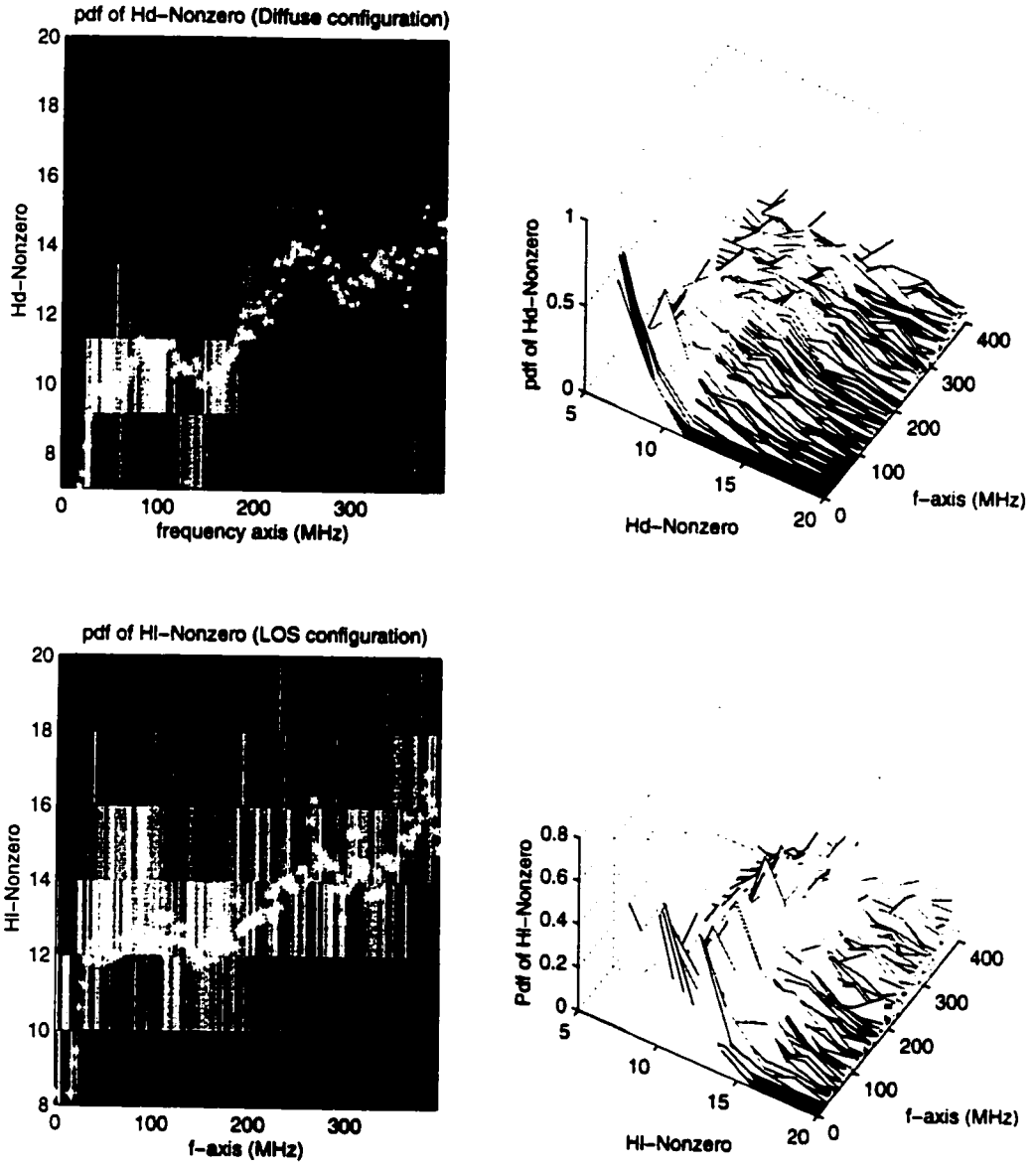

Figure 29. This graph shows the probability distribution function of the H_nonzero parameter for diffuse case (first row graphs) and LOS case (second row graphs). The left column graphs are a top view of the PDF graphs with average of the parameter superimposed on them.

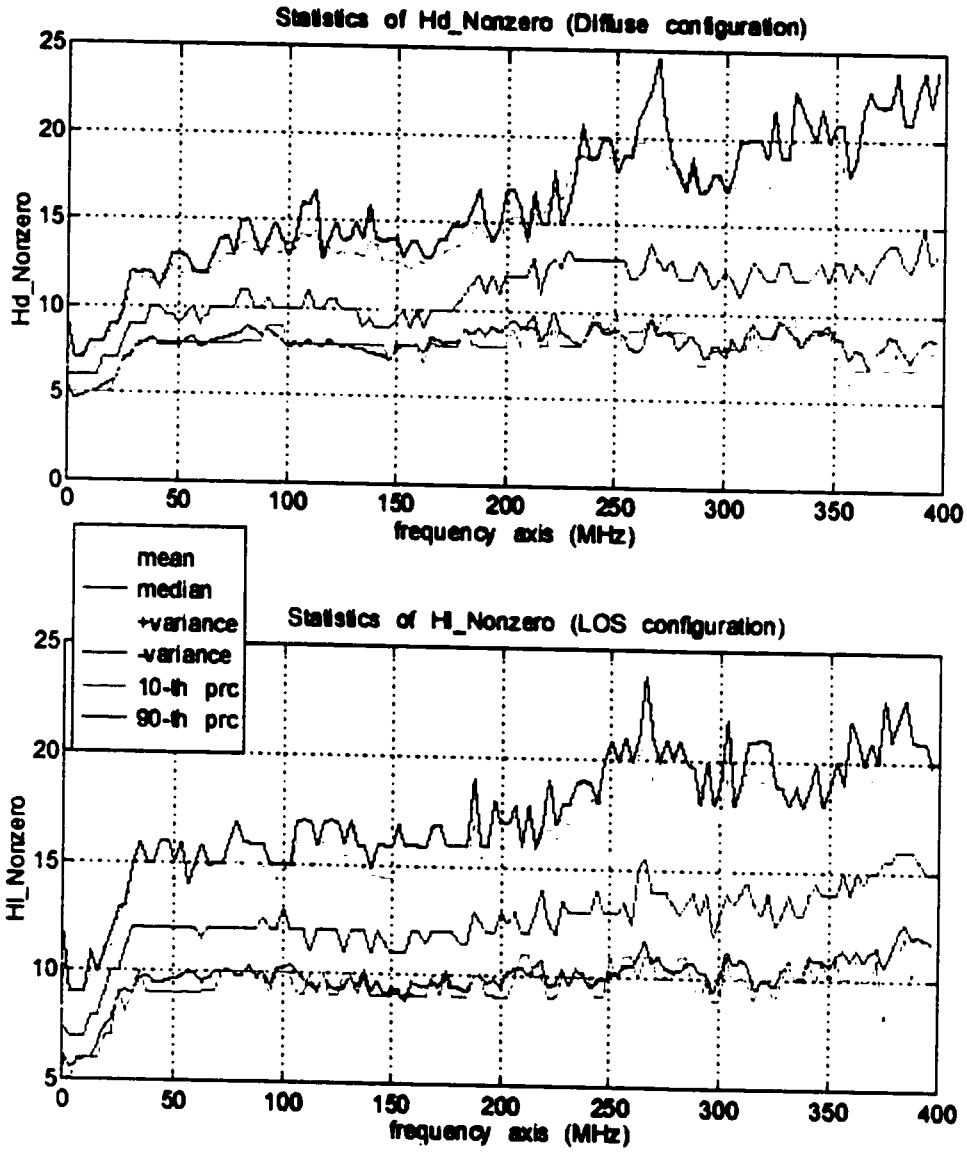

Figure 30. Statistics of H_nonzero for the diffuse (top) and LOS (bottom) configurations are shown in this figure. These statistics include average, median, 10^{th} percentile, 90^{th} percentile and mean plus and minus variance.

5.3.3.3 H_Diff

Figure 31 and Figure 32 show the PDF and the statistical distribution of the H_Diff parameter. This parameter as it was mentioned before, specifies the rate of change in the G in each step. Considering the results, it is clear that the average of H_diff is very close to zero across the frequency axis. This shows that the probability of increasing or decreasing the received magnitude of $H(f)$ at a certain frequency by rotating the receiver is almost the same. It is also clear that the variation of H_diff is smaller near dc. It increases sharply from dc to 40 MHz. It remains almost constant from 40 MHz to 300 MHz.

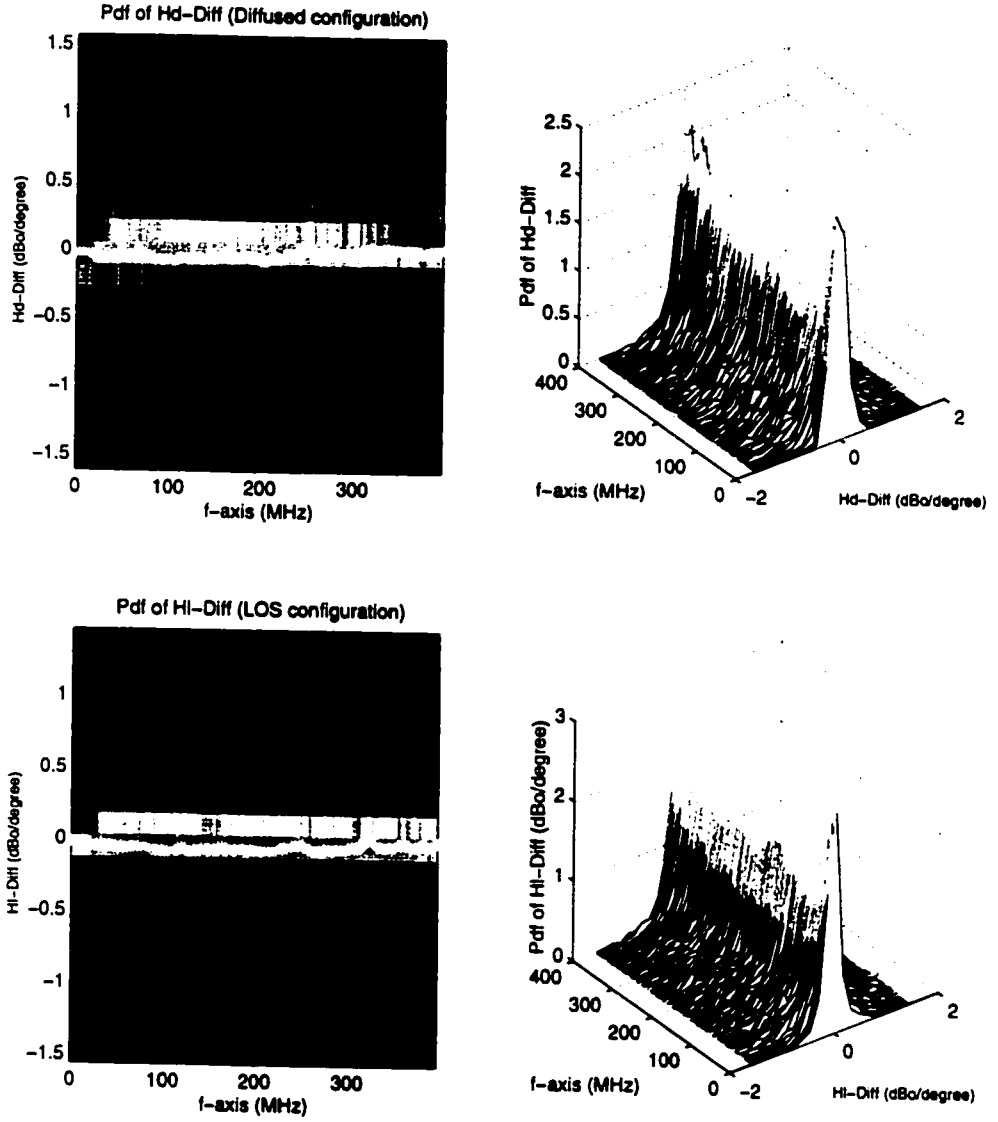

Figure 31. This graph shows the probability distribution function of the H_Diff parameter for diffuse case (first row graphs) and LOS case (second row graphs). The left column graphs are a top view of the PDF graphs with average of the parameter superimposed on them

This shows that $G(\theta)$ is flatter near dc. In other words, there are smaller chances of large variations in $|H(f)|$ due to rotation at low frequencies. This illustrates that the low frequency components of $|H(f)|$ are less susceptible to rotation effects. It is also seen that the PDF of H_Diff has a uniform shape across the frequency axis that looks like a two-sided exponential distribution.

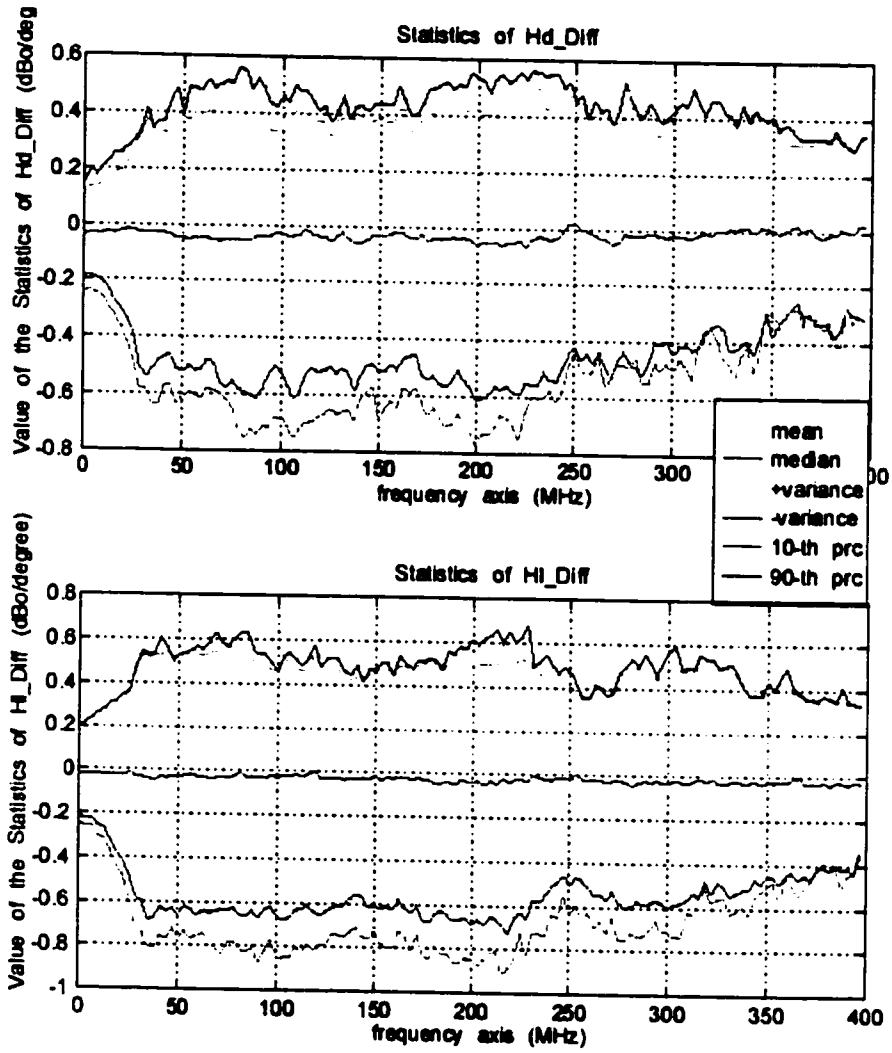

Figure 32. Statistics of H_Diff for the diffuse (top) and LOS (bottom) configurations are shown in this figure. These statistics include average, median, 10^{th} percentile, 90^{th} percentile and mean plus and minus variance.

5.4 PATH LOSS VARIATIONS PROPERTIES

Channel path loss, PL is the most important parameter of the infrared channel. Noting the variation of the curve $PL(\theta)$ for all our measurements, it was observed that the variation of this curve has some general properties. For example, the location of the minimum of $PL(\theta)$ can be predicted by knowing the physical location of the source, and the receiver in the room. In addition, it was found that the variation of this curve is such that it can be approximated by a curve-fitting model. This section describes these general characteristics of the variation of the received optical power or channel path loss for a rotating receiver.

5.4.1 Peak angle estimation algorithm

Figure 33 shows the physical configuration of an infrared transmitter and an infrared receiver. The line RM is the surface normal line for the receiver and AT is the receiver surface normal line for the transmitter. The receiver R is rotating such that the angle θ changes from 0° to 180° in steps of 5°. M is the point on the ceiling that is right in front of the receiver. In other words, M is the intersection of the receiver R surface normal line and the ceiling. Point B is the origin of a normal line to the ceiling that passes the receiver. When the receiver rotates, location of M changes on the ceiling.

The light is emitted from the transmitter and is diffusely reflected by the ceiling, walls and floor to reach the receiver. Each reflection re-transmits the optical power with a Lambertian pattern. The reflections are lossy and therefore, among the received optical rays, the set of rays which are bounced just once carry most of the received optical power.

The channel transfer function is a function of frequency and the receiver elevation angle θ and it can be denoted by $H(f,\theta)$. The received optical power is the dc component of the transfer function or $H(0,\theta)$. Observing the results of the measurements, it is seen that $H(0,\theta)$ has one peak which corresponds to angles in which the receiver is looking towards the ceiling. It decreases almost monotonically as θ changes from the peak angle. This characteristic of the transfer function guides us to find a simple mathematical model to find the angle of the received peak power using the room coordinates. To simplify the calculations, the ceiling is assumed to be an infinite plane with a uniform reflection coefficient.

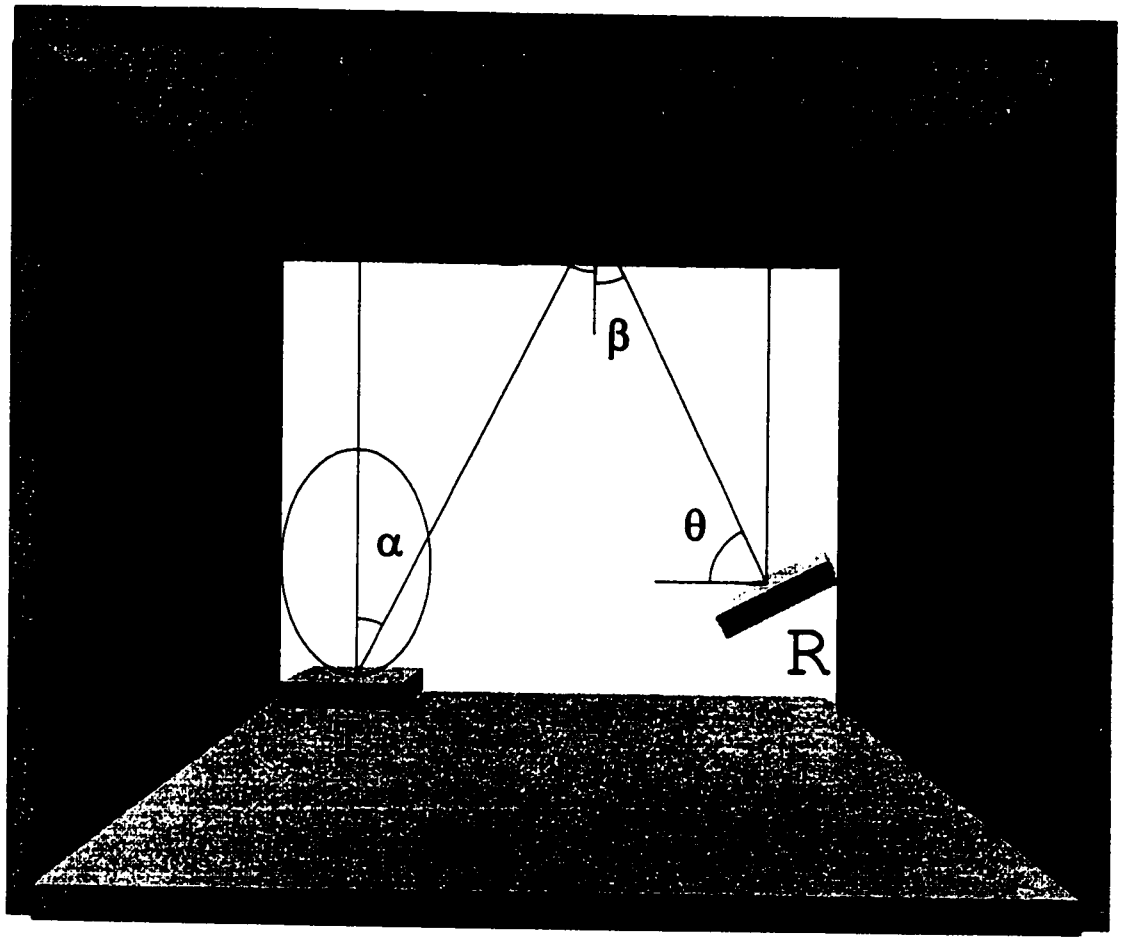

Figure 33. Geometry of a transmitter and a rotating infrared receiver.

Assume that the receiver has a very narrow FOV. Such a receiver would only receive the optical power that is transmitted from a small surface area near point M as shown in Figure 33. Assuming a Lambertian reflection pattern, the received optical power at receiver R from the source could be written as follows:

$$P_R \propto P_M \cos^n(\beta) d\Omega_R$$

where P_R and P_M are the received optical power at R and M respectively, n is the Lambertian reflection order of the ceiling. The angle between the receiver normal vector and the normal vector of element M on the ceiling is denoted by γ and is shown in Figure 33. Since the source and ceiling are in parallel, $d\Omega_R$ is given by:

$$d\Omega_R = \cos(0)\frac{A_R}{(RM)^2} \qquad (5\text{-}1)$$

Now considering the P_M,

$$P_M \propto P_T \cos^m(\alpha) d\Omega_M$$

$$d\Omega_M = \cos(\alpha)\frac{A_M}{(TM)^2} = \cos(\alpha)\frac{(RM)^2 d\Omega_{FOV}}{(TM)^2 \cos(\beta)}$$

where A_M is the small area in the vicinity of M that is seen by the receiver, P_T is the transmitted power from the source, m is the Lambertian order of the source and $d\Omega_{FOV}$ is the small receiver FOV. Noting that, TA and RB are fixed for a given set of measurements and don't change with θ, it follows:

$$TM = \frac{(TA)}{\cos(\alpha)}$$

These results can be combined as follows:

$$P_R \propto P_T \cos^m(\alpha)\cos^n(\beta) d\Omega_R d\Omega_M = P_T \frac{A_R d\Omega_{FOV}}{(TA)^2}\cos^{m+3}(\alpha)\cos^{n-1}(\beta)$$

The values of P_T, A_R, $d\Omega_{FOV}$, RB and TA are known and fixed for a given measurement configuration. Therefore, noting that β=90°-θ, it follows that:

$$P_R \propto \cos^{m+3}(\alpha)\sin^{n-1}(\theta) \qquad (5\text{-}2)$$

For most office environments, n=1 and therefore, the received power would be proportional to $\cos^{m+3}(\alpha)$.

The assumption of a narrow field-of-view receiver doesn't hold for receivers designed for diffuse configurations including the receiver that was used for our measurements. However, the strongest set of rays that are reflected just once and reach the receiver are passing the path of $T \rightarrow M \rightarrow R$. This is evident by noting that other small areas on the ceiling that receive the optical power and have a Lambertian reflection, will have an angle with respect to the RM line (The receiver surface normal) and therefore, their power would be multiplied by the cosine of that angle before it gets added to the received power. As the distance between this area and M increases, the reduction will be increased and those areas will contribute less to the first-bounce received power.

Therefore, this simplification is expected to be valid for estimating the peak angle for the H curve and as the results show, the expectation is justified. It should be noted that this approximation is valid to find only the peak of the received power and not all variations of $H(0,\theta)$. As M moves away from the point of maximum, the effects of reflections from other parts of the ceiling and walls become more and more important and a narrow-FOV receiver doesn't provide a good model to predict the variation in the received optical power for those cases. The peak of the $H(0,\theta)$ curve would be at a point where $\cos(\alpha)$ is maximized. This point will be along the line of intersection between the ceiling plane and the surface specified by the triangle RBM. It is therefore very easy to find M for any given configuration by just following this procedure.

1. Pass a plane from the receiver that contains the direction of receiver rotation and is normal to ceiling.
2. Find the intersection of this plane with the ceiling plane. Name that line BB'.
3. Pass a line from A to be orthogonal to BB' and find the intersection. Call that point M.
4. Connect M to R and measure the θ corresponding to RM.

The rationale behind the scheme is that $\cos(\alpha)$ is maximized when AM has its smallest value and the smallest possible AM for a rotating receiver could be found using the above algorithm. For implementation of the algorithm, the desired point on the ceiling can be found by tracing the loci of M and finding the point in which equation(5-2) is maximized.

5.4.2 Peak angle estimation results

The measurement results are recorded for 17 different locations in 9 rooms and at each location, 4 sets of rotational results are collected. Using the simulation program, the transfer functions corresponding to all measurement sets have also been calculated.

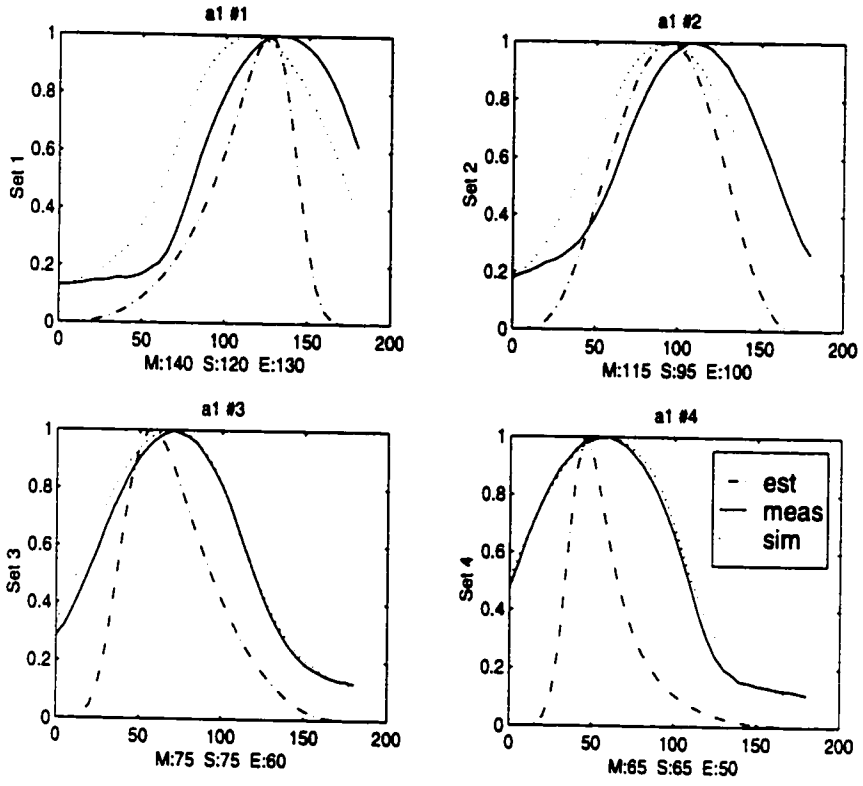

Figure 34. These graphs show the variation of the normalized curve $H(0,\theta)$. Solid lines are measurement results. Dotted lines are results obtained from the simulation program. Dash-dot lines are the curves generated by using the peak angle estimation algorithm. Note the close locations of the peak for the estimation curves and the measurement curves.

The above algorithm has been applied to generate a power estimate curve for each set of collected data. A unity value for n and m are assumed. To generate the results, the $H(0,\theta)$ curves from simulation, measurement and estimation were all normalized to a maximum of one to show the location of peak. Figure 34 shows the location of the peak for measurement, simulation and estimation results. As it can be seen from the generated results, the estimation method provides very good results for the peak of these curves.

In addition, the graphs in Figure 34 show very good agreement between the simulation results and measurement results. Not only the peaks are matching in almost all cases, but also the

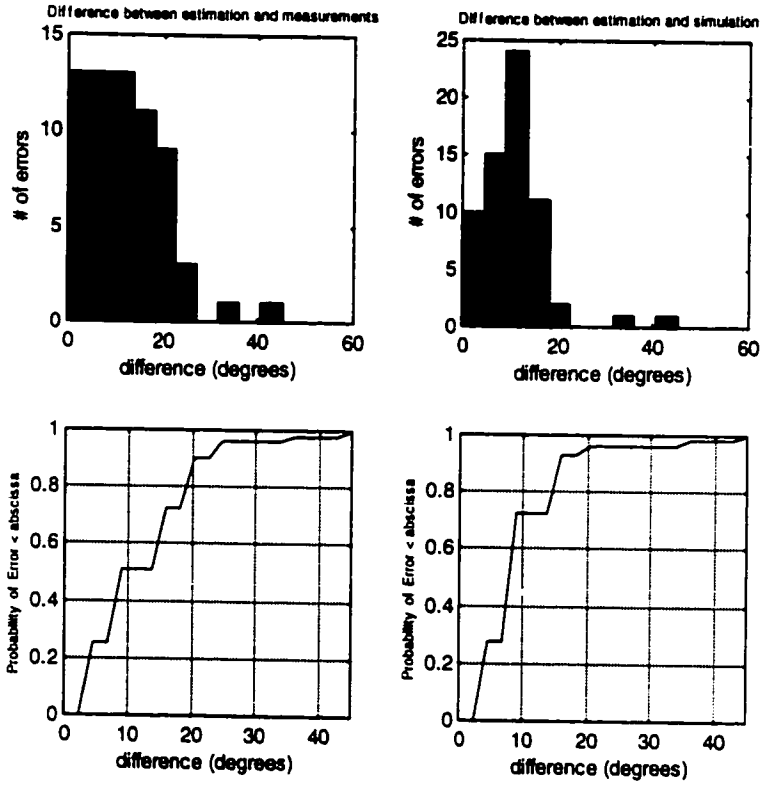

Figure 35. Graphs showing the estimation error when compared to the measurement (right column graphs) and simulation results (left column graphs). The top graphs show the distribution of error value and the bottom graphs show the cumulative distribution of errors. The difference between the estimation algorithm and the measurement is less than 20 degrees in more than 90% of all the results (left bottom graph). The error is smaller than 20 degrees 95% of the time when compared to the simulation results (right bottom graph).

shape of the curves are very similar. It should be noted that for the simulation results, only two bounces were used. Increasing the number of bounces used in the simulation would result in excessive computation time and doesn't change the results drastically.

Figure 35 shows the error distribution for the estimation method with respect to measurement results as well as the simulation results. It can be seen that in almost 90% of the cases, the estimation has an error of less than 20° when compared to the measurement results. Compared to the simulation results, the error is less than 20 degrees for 62 sets of results out

of 64 simulated cases. That shows a good agreement between the peak angle estimation algorithm and the simulation results for more than 95% of all the results.

5.4.3 *Estimation of the received optical power using curve fitting*

Variation of the received optical power with respect to the elevation angle seems to be following a predictable pattern. Traditional curve fitting algorithms have been used to estimate the variations of these curves and have achieved very good results. The idea is to estimate the path loss of the infrared channel at all angles in a rotation set (θ ranging from 0° to 180°) by knowing a few samples of the dc value of the transfer function measured at some given values of θ. These samples could be obtained from actual channel measurements or using the simulation program. The measurement database contains more than 130 sets of $H(0,\theta)$. For each curve in the database, N samples are chosen. A fitting algorithm is then used to fit a $G(\theta)$ curve to these samples. The samples are chosen uniformly from θ=0° to θ=180° and the distance between them is 180/(N-1) degrees. Several different curve fitting algorithms including polynomial curve fitting, spline curve fitting, piecewise linear approximation fitting and nearest neighborhood curve fitting have been tried [72]. The error of curve fitting is defined as the difference between $G(\theta)$ and $H(0,\theta)$ on a dBo scale.

Results show that as N increases, the error decreases. In addition, simple curve fitting algorithms such as polynomial curve fitting seem accurate enough for the precision requirements of most communication applications. The best results are obtained when the spline curve fitting algorithms are employed. The figure of merit for comparing different fitting algorithms is the average of the difference between the fitted curve and the measured $H(0,\theta)$ for all the measurement results.

Figure 36 shows examples of the curve fitting results. The left figure shows a case with an average curve fitting error of less than 0.1 dBo and the right curve corresponds to one of the poor cases with about 0.5 dBo of average error. These curves are obtained by using a polynomial curve fitting algorithm and using N=5. It is found that using this value and a polynomial curve-fitting algorithm is simple and provides a very good approximation for all our measurements.

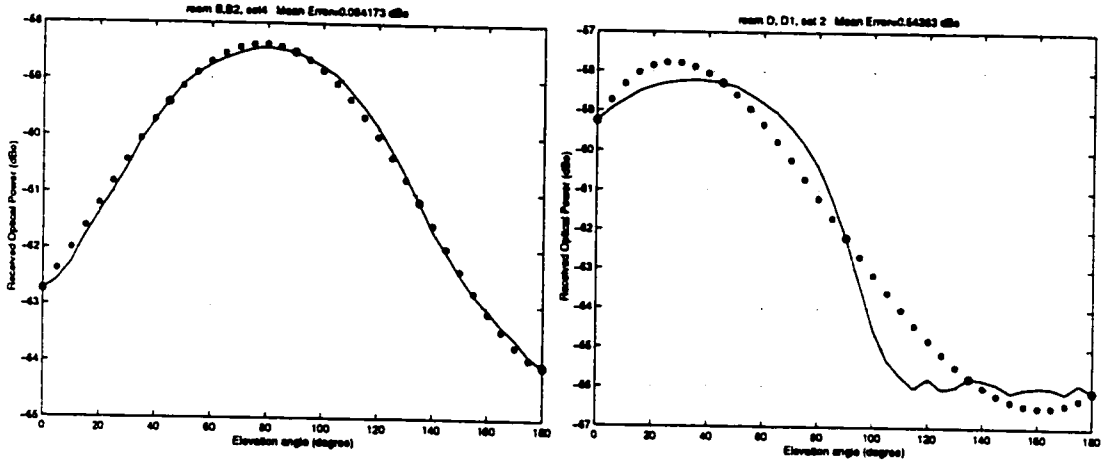

Figure 36. The above two graphs show the accuracy of a curve fitting to predict the variation of the $H(0,\theta)$ curve. Solid line represents the actual measurement results. Star dots represent the estimated curve which is obtained by a polynomial curve fitting of order 4 to the sample points obtained from the measurement results. Sample points are chosen uniformly from θ=0° to θ=180° in steps of 45° and are specified by a circle around the star on the graphs.

The worst case average error when the curve fitting of order 4 with N=5 was applied to the entire collected database of $H(0,\theta)$'s was about 0.6 dBo. Similar results can be obtained by using a spline curve fitting algorithm. For N=4, the results of the spline curve fitting algorithm provide better accuracy compared to the polynomial curve fitting. For N=3 or less, the fitting does not provide acceptable results for all cases.

Therefore, it can be concluded that the variations of the channel path loss for a receiver that changes its elevation angle from 0° to 180° can be accurately estimated by measuring (simulating) only five points along the entire rotation path. Applying a 4th order curve fitting algorithm to the measured (simulated) results, the variation of path loss versus elevation angle is found with errors of less than 0.5 dBo. This curve can be used to estimate the path loss for any arbitrary elevation angle θ between 0° and 180°.

5.5 MODELING PATH LOSS VARIATION

For system level analysis of the infrared communication systems, the variation of channel parameters such as the channel path loss or the channel delay spread may be required. The simulation algorithms described in Chapter 3 provide good initial estimates for the value of these parameters. If results with more accuracy are desired, the spatial resolution of the model as well as the tracked number of bounces should be increased. This increases the computational complexity of the model and in some cases makes it impractical for engineering purposes.

Measurement results can be used to enhance the accuracy of the simulation algorithm as was shown in the case of receiver displacement modeling. In this section, the objective is to show that the results of the rotation measurements can be used to provide means of increasing the accuracy of the channel path loss estimate for a rotating infrared receiver.

The starting point for estimating the channel path loss is using the simulation algorithm that was described in Chapter 3. For any given room, knowing the physical parameters of the source and the receiver, the algorithm given in Chapter 3 can be used to estimate the channel impulse response. The calculation of the channel path loss can be done very fast if the number of bounces (k) is less than 2. The initial estimate of the channel path loss in this section is derived with this setting, i.e., tracking only the rays that are reflected just once. Therefore, for each major rotation direction of a given location, a curve $PL_i(\theta)$ can be generated. This curve represents the estimated value of the channel path loss when the receiver changes its elevation angle from 0° to 180° in steps of 5°. The measurements provide a similar curve, $PL_m(\theta)$ that shows the actual value of the channel path loss for the same conditions.

Figure 37 shows some samples of these curves for one of the measurement locations in room J, location j1 (See Appendix B for location specifications). The top four graphs show the curves $PL_i(\theta)$ and $PL_m(\theta)$ for each of the major measurement directions in this room. It can be seen that the two curves have considerable differences when the elevation angle is close to 0° or 180°. In other words, the accuracy of the one-bounce estimate decreases when the receiver is facing towards the walls. The bottom graph in Figure 37 shows the path loss estimation error, $PL_m(\theta)$-$PL_i(\theta)$ for each of the top four graphs. It can be seen that the error values range from close to 0dBo to around 10dBo. Note that, the error curve has higher values at both its ends and goes lower in the middle.

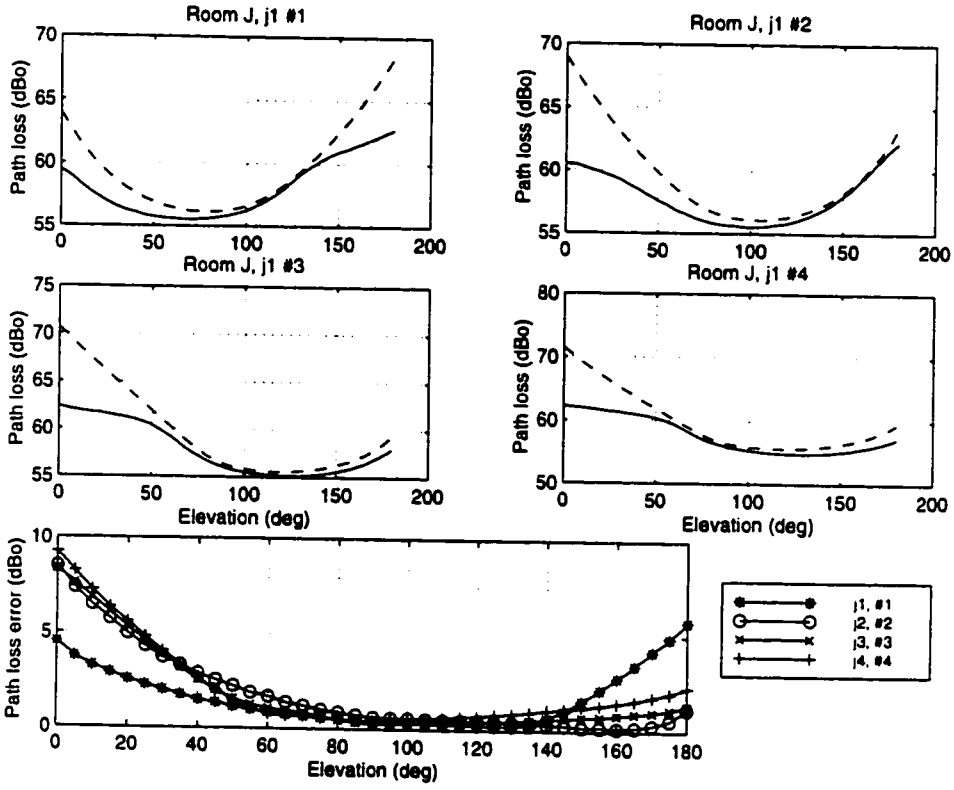

Figure 37. Variation of the channel path loss in room J, when the elevation angle is changed from 0° to 180° in steps of 5° shown in the top four graphs. The graphs also show the estimated value of the channel path loss using the simulation algorithm with dashed lines. Bottom graph shows the error in the estimation of channel path loss using the simulation.

The estimation error generally reaches its minimum when the channel path loss is minimum. This happens when the elevation angle is such that the received optical power is at its maximum level for that rotation. In other words, the error reaches its minimum when the curve $PL_{\omega}(\theta)$ reaches its minimum. The corresponding angle, θ_{min} can be estimated as described in Section 1.4. The value of error at θ_{min} is usually small and varies between 0.5dBo to around 2dBo. The small error value at the dip of $PL_{\omega}(\theta)$ compared to the error values at the two ends suggests that the simulation results are close to the actual value for this range of elevation angles. Therefore, the focus would be to find methods of reducing the estimation error at angles that are not close to θ_{min}. Consequently, a simplifying assumption is made that

the two curves are equal at θ_{min} and the objective is to find an algorithm that minimizes the distance between the two curves for all angles.

The error value increases as the elevation angle moves away from θ_{min}. The error ranges from a few dBo to as high as 15dBo for some measurement configurations. The error is a monotonically increasing function of the difference between the receiver angle and θ_{min}, i.e. $|\theta-\theta_{min}|$. Obviously, the amount of error depends on many parameters that relate to the properties of the room as well as the location of the transmitter and receiver. However, the purpose of the effort is to see if it is possible to relate the estimation error to one or two known variables for a given configuration. To answer this question, many different parameters that relate to the physical properties of the system as well as the estimated path loss curve have been studied and two appropriate candidates have been identified. These two parameters can be easily found for a given configuration. By applying a simple algorithm as described below, the accuracy of the path loss curve, $PL_s(\theta)$ can be considerably increased

5.5.1 Modeling parameters.

Figure 38 shows the normalized path loss curves for room A, location a_2. Both curves are normalized and have a dip of 0dBo. Define

$$\begin{aligned} u_1 &= PL_s(\theta_{\min}) - PL_s(0) \\ u_2 &= PL_s(\theta_{\min}) - PL_s(180) \\ Err_1 &= PL_m(0) - PL_s(0) \\ Err_2 &= PL_m(180) - PL_s(180) \end{aligned} \qquad (5\text{-}3)$$

where u values are the differences between the dip of the $PL_s(\theta)$ curve and its two ends in dBo scale and Err values are the differences between the measured and the estimated curves at their two ends.

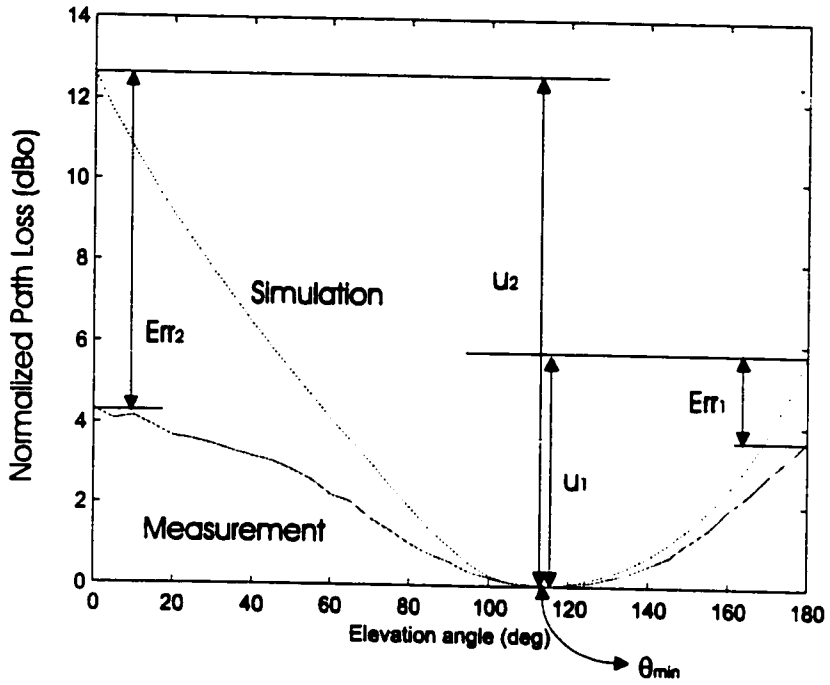

Figure 38. The normalized values of the estimated path loss and measured path loss for location a2 are shown in this figure. The error values Err_1 and Err_2 curves are proportional to the values u_1 and u_2. That is as the estimated value from the simulation algorithm drops from its peak, its error increases proportionally.

These values are all shown in Figure 38. Based on the results of the measurements, a close relation between the values u_1 (u_2) and Err_1 (Err_2) is observed. The error value at each end of the curve, Err_1 (Err_2) increases as the difference between the estimated path loss and its peak increase. This is an important observation that is used to estimate Err_1 (Err_2) by only knowing the values of u_1 (u_2). Note that, u_1 (u_2) could be simply derived from the first-bounce simulation curve, $PL_1(\theta)$.

It was also found that the amount of the estimation error depends on the distance between the receiver and the closest wall in front of the receiver. Figure 39 illustrates this distance that is shown by the variable $RV(\theta)$. As this distance increases, the estimation error becomes smaller and as the receiver moves to face a closer wall, the estimation error becomes larger. This could be intuitively verified by noting that the single bounce estimation does not consider the second, third and higher order reflected rays that are received from walls. When the receiver is

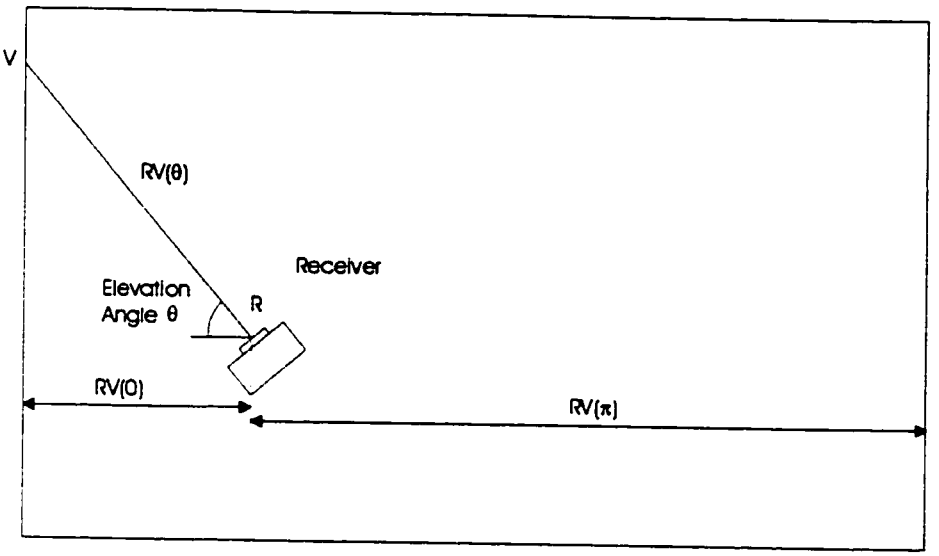

Figure 39. As the receiver changes its elevation angle from 0° to 180°, the distance of the line $RV(\theta)$ changes. Point V is the intersection of the receiver surface normal and the closest wall of object inside the room. The length of RV at $\theta=0°$ and $\theta=180°$ has a good correlation to the error in the path loss estimation.

facing a close wall, a considerable amount of the received energy is coming from the wall that is in its front. This energy is much smaller than the energy of the reflected light off the ceiling and it consists of the energy of the rays that are reflected once, twice and more. Since the simple one bounce model does not consider the rays that are reflected twice and more, the amount of error in the estimation increases. As an example, in room A location a1, as shown in Figure 20, when the receiver is rotating along the major direction (1), the one bounce model has a better prediction at $\theta=180°$ than $\theta=0°$. This is because the distance of the receiver to its opposite wall is larger at $\theta=180°$.

Concluding from these observations, the two variables RV and u are chosen to predict the estimation error at the edges of the error curve. The objective is to find a simple formula that matches the value of Err for the measured cases. For each measurement location and along each of the major rotation directions, the measured $PL_m(\theta)$ is compared against the simulated curve $PL_s(\theta)$ to find two estimation error values, Err_1 and Err_2. These two values are added to a target set $\underline{\mathbf{Err}}$. Then the curve $PL_s(\theta)$ is generated and used to find u_1 and u_2 that are added to a set of all simulated u values, $\underline{\mathbf{U}}$. The room configuration is used to find two variables $RV(0°)$

and $RV(180°)$ that are added to a measured set of all receiver to wall distances, **RV**. Observing the relation between the values in these three sets, a second order function of $\{u, RV\}$ seemed a simple and yet effective fit to the recorded Err values.

Define

$$g(RV,u) = a_1 RV^2 + a_2 u^2 + a_3 RV + a_4 u + a_5 uRV + a_6$$

The objective is to find the set of $\{a_1, a_2, a_3, a_4, a_5, a_6\}$ that minimizes the distance between g and the elements of the set **Err** for all $\{(RV,u) \mid u \in \mathbf{U}, RV \in \mathbf{RV}\}$. To solve this problem, a Nelder-Mead type simplex search algorithm is used. This is a method used to minimize a given function using a set of known data. The method is a direct search method that does not require gradients or other derivative information. The details of the search method could be found in [72].

5.5.2 Modeling results

Figure 40 shows the results of applying the optimization method to find a good approximation for the target set **Err**. The top graph in this figure shows the relation between the value RV and the estimation error. As it was mentioned before, the error in estimating the path loss has a larger value when the receiver has a shorter distance to the wall or object that is in front of it. For RV values less than 2m, the error ranges from 2 to 18 dBo. The error decreases as the RV increases and for RV values above 4 m, the estimation error is smaller than 2dBo. Note that, for a small RV value, the error has a large range and therefore, the parameter RV can not uniquely specify the error. That's why the parameter u has also been used to approximate the error values.

The bottom graph shows the error value vs. u as defined in equation (5-3). Again, it is clear that the error is a monotonically increasing function of u. Note that, the error has a larger range for larger u values. When the edge of the curve $PL_r(\theta)$ is 25dBo or more below its peak value, the actual path loss could be 2 to 18 dBo away from the path loss estimated by the single bounce model.

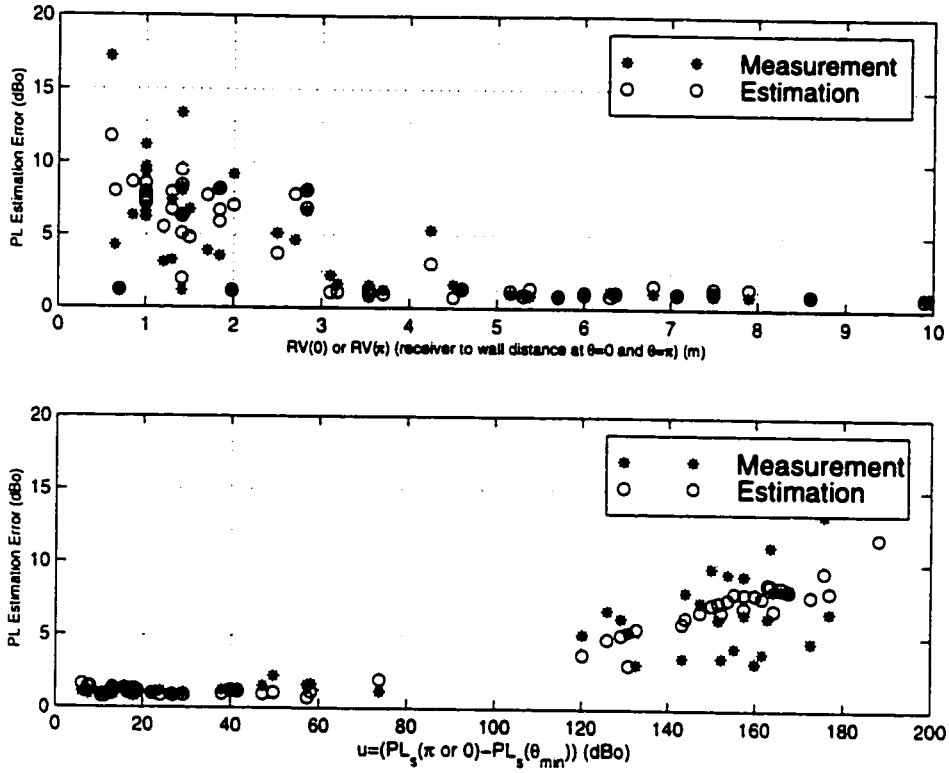

Figure 40. Top graph shows the relation of RV (receiver to wall distance at the elevation angle of 0° and 180°) to the estimation error, *Err*. Bottom graph shows the relation of the variable u (drop of the estimated path loss, *PL*, from its peak at elevation angle of 0° and 180°). The circles in the graph represent the estimated error value using the second order curve fitting method.

Applying the optimization algorithm, the error estimating function is found to be:

$$g(RV,u) = -0.06RV^2 + 0.02u^2 + 0.97RV + 0.38u - 0.11uRV - 2.12 \qquad (5\text{-}4)$$

The circles in both graphs of Figure 40 show the results of applying this second order polynomial to the set of known $\{u,RV\}$. It is clear from these graphs that the circles have a relatively good match with the error points especially in the cases where the error values are less than 7dBo. When the value of error has a larger range (small RV values and large u values), the circles do not match all the error points. In some cases, the estimated value by the

approximation function is too optimistic and in some cases, it is too pessimistic. Note that, the one-bounce simulation results are generated assuming a reflection coefficient of 0.7 for the ceiling and 0.5 for all the walls. Also, the radiation pattern of the source is assumed a first order Lambertian pattern and the receiver is assumed to have a uniform 60° FOV. These are all simplifying assumptions that can contribute to the in-accuracy of the curve fit model. Note that the objective of this exercise is to find a method of enhancing the accuracy of the path loss estimation for a rotating receiver and not predicting the exact value. If the exact value for a given system is desired, simulation of the type described in Chapter 3 with 4 or more bounces should be performed.

For each of the measured and simulated pair of path loss versus elevation angle curves, a corresponding ratio curve can be defined by:

$$Ratio(\theta) = PL_m(\theta) / PL_s(\theta)$$

where the values of $PL_s(\theta)$ and $PL_m(\theta)$ are presented in a linear scale. It is clear that the previously defined Err_1 and Err_2 values correspond to the two ends of this curve represented in dBo scale. Figure 41 shows an example of a ratio curve for room B location b1, direction (2). So far, the effort has been focused on estimating the two ends of the ratio curve, or Err values. The desired objective is to estimate the path loss for the entire set of elevation angles ranging from 0° to 180°. In other words, it is desired to model the behavior of the ratio curve as defined above. Having an appropriate model of this curve would lead to appropriate scaling of the simulated one-bounce path loss curve, $PL_s(\theta)$ to result in a more accurate representation of the curve $PL_m(\theta)$.

Note that, to model the curve $Ratio(\theta)$, only three points are available. Two points are the end points of the curve at angles 0° and 180° as estimated by the function g. The other known point is the point where $Ratio(\theta_{min})=1$. This middle point is simply stating that the path loss estimate is approximately equal to the measured estimate for the elevation angle $\theta=\theta_{min}$. Noting the results of the measurements and investigating the properties of the curve $Ratio(\theta)$, the following properties have been observed.

- $Ratio(\theta)$ monotonically increases as the elevation angle moves away from $\theta=\theta_{min}$.
- $Ratio(\theta)$ has only one minimum in the span of $\theta \in [0° \ 180°]$.
- $Ratio(\theta)$ does not have the same rate of increase on the left and right hand side of $\theta=\theta_{min}$.

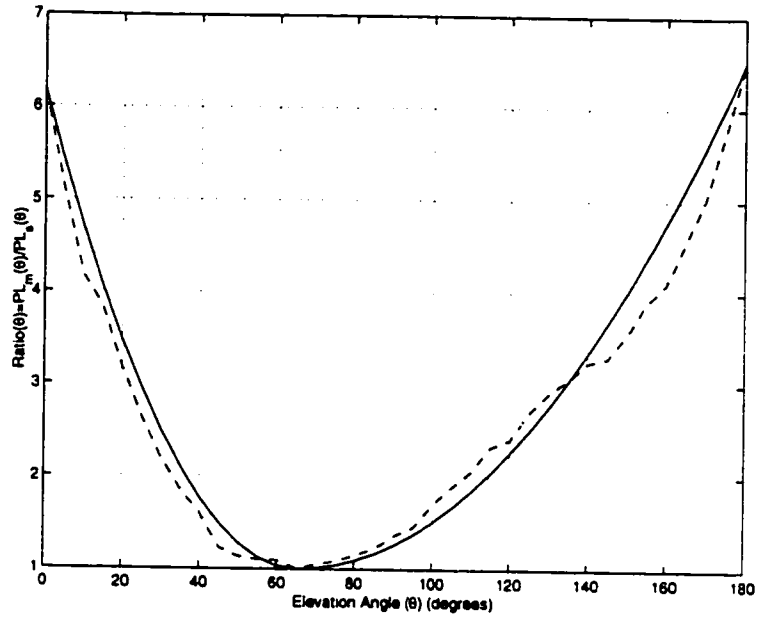

Figure 41. Ratio of the measured path loss to the simulated path loss for a rotating receiver is shown with dashed line. A 4th order curve fit to the ratio curve is also shown with a solid line.

All these properties can be clearly seen in Figure 41. Concluding from these observations, it was found that the best fitting algorithm for this curve is to divide it into two sections, $Ratio_1(\theta)$ and $Ratio_2(\theta)$ where $Ratio_1(\theta)=Ratio(\theta)$ for $\theta\in[0^\circ\ \theta_{min}]$ and $Ratio_2(\theta)=Ratio(\theta)$ for $\theta\in[\theta_{min}\ 180^\circ]$. For each of the two, the curve that has a very good fit with a simple 4th order function of θ-θ_{min}.

Therefore, the overall fit to the ratio curve can be written as:

$$Ratio(\theta)\approx Rf(\theta)=\frac{Err_1}{\theta_{\max}^4}(\theta_{\max}-\theta)^4\{u(\theta)-u(\theta-\theta_{\max})\}+ \frac{Err_2}{\theta_{\max}^4}(\theta_{\max}-\theta)^4\{u(\theta-\theta_{\max})-u(\theta-\pi)\}+1 \tag{5-5}$$

where $u(\theta)$ is the step function, Err_1 and Err_2 are the values of the ratio curve at its ends and the constant 1 is added to make sure that $Rf(\theta_{min})=Ratio(\theta_{min})$. It is easy to verify that $Rf(\theta)$ satisfies all the observed properties of the ratio curve as mentioned above.

Applying this function as an approximation to the ratio curve provides a simple and effective method of enhancing the accuracy of the one-bounce model results. Therefore, the proposed method for estimating the variation of the path loss curve versus the receiver elevation angle can be summarized as follows:

1. For the given room, transmitter and receiver configuration, apply the one-bounce model as described in Chapter 3 to calculate the initial estimate of the path loss curve, $PL_1(\theta)$ for $\theta \in [0°,180°]$.
2. Find the two ratio values u_1 and u_2 as described by equation (5-3).
3. Find the distance of the receiver to the closest wall at the beginning (RV_1) and at the end of the rotation (RV_2), i.e., when θ=0° and θ=180°.
4. Use equation (5-4) to estimate the amount of path loss error at the two ends of the rotation path, Err_1 and Err_2.
5. If $Err > u$, set Err=1 at both ends. This step is needed to make sure that the corrected curve does not exceed the peak of $PL_1(\theta)$ curve.
6. Find the angle of minimum path loss θ_{min} by following the procedure outlined in Section 4 of this chapter.
7. Apply equation (5-5) to approximate the ratio curve.
8. Multiply the ratio curve with $PL_1(\theta)$ to find the enhanced path loss curve that is a better match to $PL_m(\theta)$.

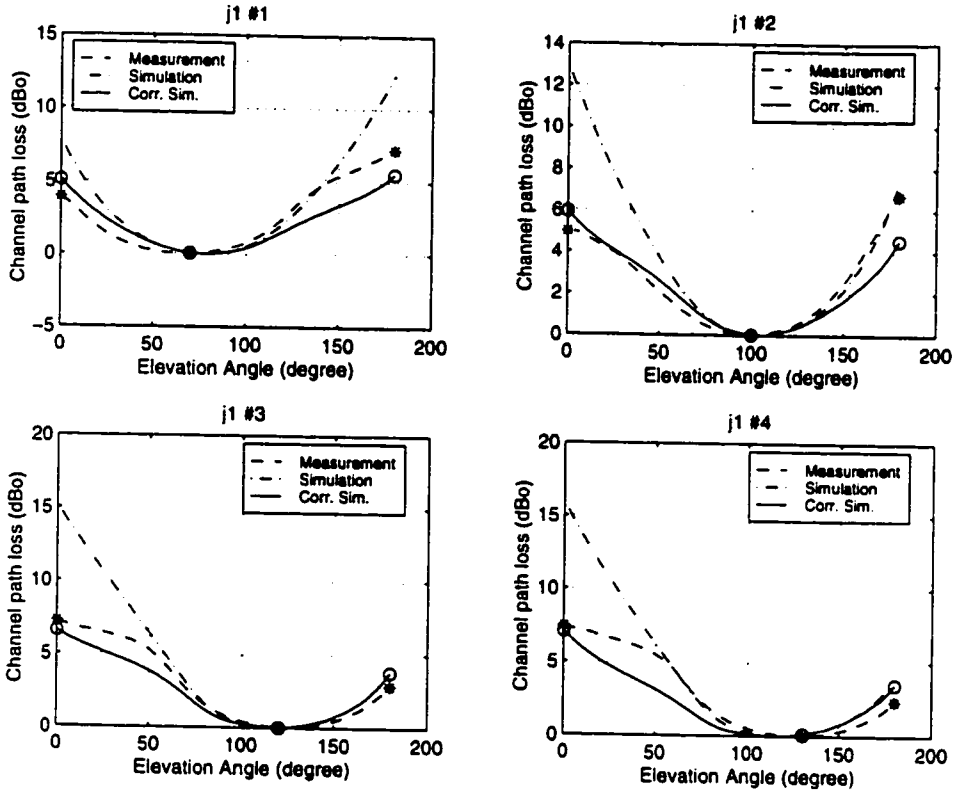

Figure 42. The measured path loss for a rotating receiver, the one bounce simulated curve and the corrected curve are shown in this figure. Note the increase in the accuracy of the estimation by applying the correction algorithm.

Figure 42 shows the results of applying the correction algorithm for measurements performed in room J, location j1. Each of the four graphs in this figure present the results of rotation along one of the four major directions at location j1. In each graph, the dashed line represents the measured value of the path loss change, $PL_m(\theta)$. The dash-dot line represents the estimated path loss curve using the one-bounce model, $PL_s(\theta)$ and the results of applying the correction algorithm on $PL_s(\theta)$ is shown with a solid line. Each graph also shows the measured values of Err_1 and Err_2 with stars (*). The estimated values of Err as a result of applying equation (5-4) are shown with small circles (o). It is clear that the correction algorithm provides an effective way of reducing the errors of the simplistic one-bounce model.

Applying this correction algorithm to measurement data resulted in same kind of reduction in the path loss error. Overall, considering the results of all measured sites, the average error in the first and last 30° of rotation (where errors are much larger) was reduced from 3.2dBo to less than 1dBo. The maximum error was reduced from 18dBo to less than 5dBo.

5.6 SUMMARY AND CONCLUSIONS

Infrared links are very sensitive to the direction of the transceivers. A set of measurements have been designed and performed to investigate the effects of rotation on the characteristics of the indoor infrared channel. The results of these measurements have been reported. A piecewise linear model was developed to describe the general behavior of the channel transfer function for a rotating receiver. The model reveals the rate of change as well as the continuity properties of the transfer function in different frequency bands.

The variations of the channel path loss are particularly important and useful. An algorithm was developed to predict the angle of minimum path loss for a rotating receiver. Measurement results have been used to show the validity of the proposed method.

Using the measurement results, it was shown that the variations of the channel path loss are smooth and a simple curve fitting algorithm can be used to accurately interpolate the intermediate values. It was shown that for a receiver changing its elevation angle from 0° to 180°, five points along the entire path is sufficient to predict the variation of the channel path loss for the entire rotation range.

Last section of this chapter provides an algorithm that can be used to estimate the variation of the channel path loss of a rotating receiver by improving the accuracy of the results obtained from the simulation algorithm. The results of the measurements have been used to define an algorithm that can reduce the errors of the simplistic simulation method and provide a much more reliable estimate for the path loss variation of a rotating receiver.

CHAPTER SIX

6 RECEIVER DISPLACEMENT

6.1 INTRODUCTION

As it was discussed before, characteristics of the indoor infrared channel vary depending on the physical properties of the receiver, transmitter and the environment in which they operate. Simulation of the channel as discussed in Chapter 3, can provide an estimate of the channel properties for a given configuration. However, the simulation suffers from a few drawbacks. For accurate estimation of the important channel parameters such as path loss and delay spread, five or more bounces need to be included [119]. This would exponentially increase the time requirements of the simulation algorithm and make it impractical to run on ordinary computers. Furthermore, the simulations can not accurately include all physical properties of the environment such as furniture and office equipment.

For system level simulation of communication systems, the communication channel should be represented as accurately as possible. In this section, the results of the measurements are used to enhance the results of the channel simulation algorithm. It is shown that combining the channel simulation results and the enhancements that are derived from the measurements could provide more reliable channel estimation. Such a modeling work can be used to simulate the performance of infrared communication systems more accurately.

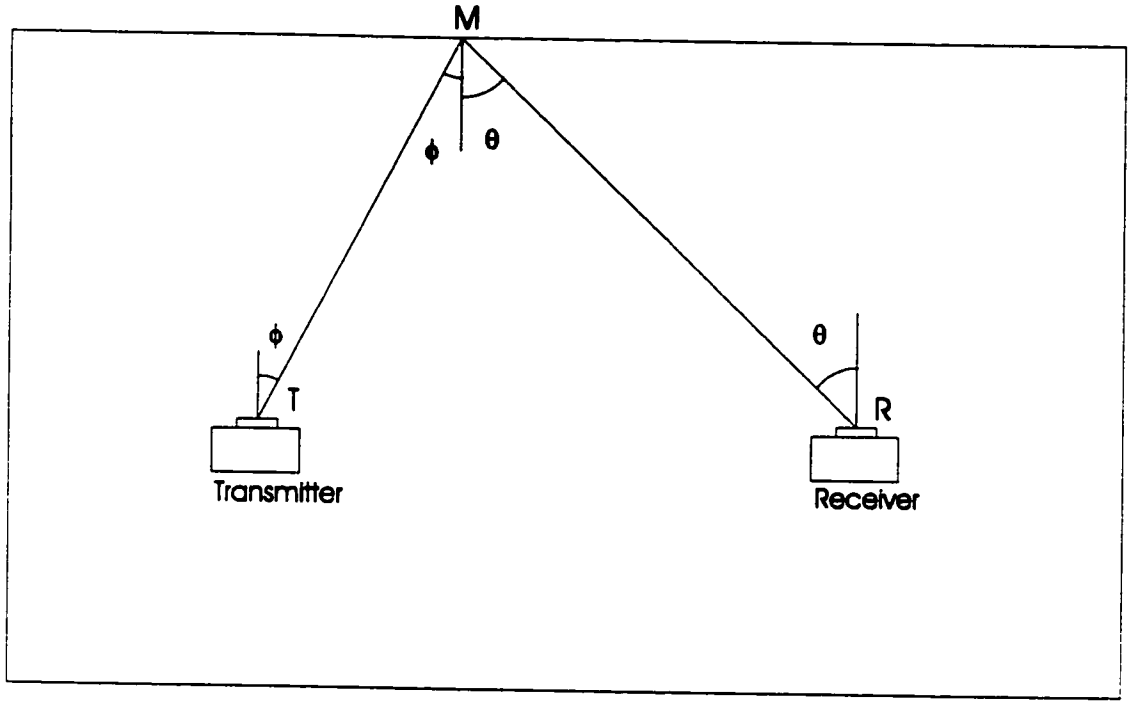

Figure 43. A diffused infrared transmitter illuminates the ceiling and the wide FOV receiver collects the received optical power from the ceiling.

6.2 RECEIVER DISPLACEMENT

Figure 43 illustrates a room with an upward looking diffused infrared transmitter T and a wide FOV infrared receiver R. The model described in Chapter 3 can be used to calculate the total received optical power from the light rays that are reflected just once from the ceiling. Using (3-5), the impulse response from the source T to a differential element M on the ceiling is given by:

$$h^{(0)}(t;T,M) \approx \frac{n+1}{2\pi}\cos^n(\phi)d\Omega_{TM}\,\delta(t-(TM)/c) \qquad (6\text{-}1)$$

where $d\Omega_{TM}$ is given by $d\Omega_{TM} = \cos(\theta)\Delta_M/(TM)^2$

Δ_M is the differential area on the ceiling that directly receives the optical power from the source and has a distance of TM to the source T. In writing the above equation, it is assumed that the differential element has a 90° FOV and a reflection coefficient ρ.

The differential area acts as a Lambertian source of infrared radiation and the impulse response from M to R can be written as:

$$h^{(0)}(t;M,R) \approx \frac{1}{\pi}\cos(\theta)d\Omega_{RM}\ rect(\theta / FOV_R)\,\delta(t-(RM)/c) \qquad (6\text{-}2)$$

where $d\Omega_{RM}$ is given by

$$d\Omega_{RM} = \cos(\theta)A_R/(RM)^2$$

A_R is the effective receiver area that has a FOV given by FOV_R. Based on the measurement of the reflectivity of typical office surfaces, it can be assumed that these reflect the light as a first order Lambertian source.

Convolving the above two impulse responses and integrating over the ceiling area results in the impulse response of the channel from source T to receiver R using the rays that are reflected just once.

$$h^{(1)}(t;S,R) \approx$$

$$\frac{\rho A_R(n+1)}{2\pi^2}\iint_{ceiling}\left[\frac{\cos^2(\theta)}{(RM)^2}rect\left(\frac{\theta}{FOV_R}\right)\delta\left(t-\frac{(RM)}{C}\right)\right]\otimes\left[\frac{\cos^n(\phi)}{(TM)^2}\delta\left(t-\frac{(TM)}{C}\right)\right]d\Delta_M \qquad (6\text{-}3)$$

This integral can be numerically calculated and it provides a first order estimate of the channel transfer function between the source and the receiver. If there is a direct line of sight path between the two, the channel impulse response should include a LOS component as well. However, in diffuse configurations such as the one depicted in Figure 43, the LOS component usually doesn't exist or its energy is negligible due to the limited receiver FOV and Lambertian radiation pattern of the source.

If the channel path loss or alternatively the total received optical power is required, the above integral could be simplified to provide a closed form expression. The temporal dispersion of the received power that is represented by delta functions in the above expression can be removed by integrating it over time. This would yield the sum of all the time-dispersed received optical energy which is identical to the received optical power. It could also be assumed that all the ceiling area is within the receiver FOV. This may not be a realistic assumption for some narrow FOV receivers. However, single branch receivers are usually designed to have a wide FOV and this implies that the ceiling is within their FOV. As an example, a receiver at a height 1m with 70° FOV placed in a room of height 3m receives the

reflected light from an area on the ceiling with a diameter of around 11m. That covers the ceiling of most typical office environments. This assumption would simplify the expression for the boundaries of the integral. Using these assumptions, the total received optical power at the receiver for 1 W of transmitted optical power can be written as:

$$P_{diffused}(T,R) = \int_{-\infty}^{+\infty} h^{(1)}(t;T,R)dt \approx \frac{\rho A_R (n+1)}{2\pi^2} \iint_{ceiling} \frac{\cos^2(\theta)\cos^{n+1}(\phi)}{(RM)^2(TM)^2} d\Delta_M \qquad (6\text{-}4)$$

Note that, the value of P can also be interpreted as the inverse of the channel path loss in linear scale. On dBo scale,

$$PL(T,R) \ \ (\text{optical dB}) = -10\log_{10} P(T,R)$$

Without loss of generality, T could be assumed to be at {0,0,0} coordinates. Let $R:\{x_R, y_R, z_R\}$ specify the receiver coordinate and $M:\{x, y, z_M\}$ specify the coordinate of the differential reflecting element on the ceiling. Defining H_s as the distance between the source and the ceiling and H_r as the distance between receiver and the ceiling, It follows that:

$$TM^2 = x^2 + y^2 + H_s^2$$

$$RM^2 = (x - x_R)^2 + (y - y_R)^2 + H_r^2$$

$$\cos(\varphi) = \frac{H_s}{(TM)}$$

$$\cos(\theta) = \frac{H_r}{(RM)}$$

If the source is a first order Lambertian source, the integral simplifies to:

$$P_{diffused}(T,R) \approx \frac{\rho A_R H_s^2 H_r^2}{\pi^2} \iint_{ceiling} \frac{dxdy}{((x-x_R)^2 + (y-y_R)^2 + H_r^2)^2 (x^2 + y^2 + H_s^2)^2} \qquad (6\text{-}5)$$

It is instructive to solve this integral for a case where the ceiling is extended to infinity and the transceivers are at the same height (z_R=0). This provides a simple formula that relates the normalized received optical power to the location of the transceivers. The expression is then simplified to

$$P_{diffused}(T,R) \approx \frac{\rho A_R z_M^4}{\pi^2} \iint_{R^2} \frac{dxdy}{((x-x_R)^2 + (y-y_R)^2 + z_M^2)^2 (x^2 + y^2 + z_M^2)^2}$$

Noting that,

$$\frac{1}{((x-x_R)^2+(y-y_R)^2+z_M{}^2)^2(x^2+y^2+z_M{}^2)^2} = \frac{A}{((x-x_R)^2+(y-y_R)^2+z_M{}^2)^2}+\frac{B}{(x^2+y^2+z_M{}^2)^2}$$

where

$$A = B = \frac{1}{z_M^4+(x_R^2+y_R^2+z_M^2)^2}$$

and using the identity

$$\iint_{R^2}\frac{dxdy}{(x^2+y^2+H^2)^2} = \frac{\pi}{H^2}$$

it follows that

$$P_{diffused}(T,R) \approx \frac{2\rho A_R}{\pi}\frac{z_M^2}{z_M^4+(x_R^2+y_R^2+z_M^2)^2} = \frac{2\rho A_R}{\pi}\frac{H^2}{H^4+(r^2+H^2)^2} \qquad (6\text{-}6)$$

where H is the vertical separation of the source (receiver) and the ceiling and r is the horizontal separation between the source and the receiver. This shows that the received optical power from the first bounce decreases as the distance between the transmitter and receiver increases. The rate of decrease is proportional to the 4th order of the source-receiver distance, r^4. Note that the first bounce light rays carry most and not all the received optical energy to the receiver. Therefore, this provides a pessimistic estimate of the received optical power.

Another important conclusion that is made from equation (6-6) is the importance of the distant to the ceiling for the diffuse configuration. The received optical power is almost proportional to $1/H^2$ and therefore, as the ceiling height increases, the received optical power decreases. This shows that the effective range of communication using a diffuse configuration rapidly decreases as the ceiling height increases. Therefore, this configuration may not be appropriate for places with high ceilings such as theaters and shopping malls.

The analysis of the received optical power for a LOS case is very similar to what was presented. Assuming the source is at a location M on the ceiling, the impulse response formula is given by equation (6-5) and the total received power is:

$$P_{LOS}(T,R) \approx \int_{-\infty}^{+\infty} h^{(0)}(t;T,R)dt = \frac{A_R}{\pi}\frac{H^2}{(H^2+r^2)^2}$$

where H is the vertical separation of the source and receiver and r is their horizontal separation. The received power is inversely proportional to the r^4 as in the diffuse case. It should be noted that the rapid decrease of the received power for LOS configuration is an artifact of using a sub-optimal Lambertian radiation pattern. An optimally designed source power distribution would yield a uniform distribution of the received power [12]. However, the optimal radiation pattern is room-dependent and almost impractical to implement.

6.3 MEASUREMENT PROCEDURE AND RESULTS

Measurements have been performed to study the variation of channel properties when the receiver is moved to different parts of a given room. The measurements are performed using the setup that was described in Chapter 3 using the following procedure. The infrared transmitter is located at the center of the room and the infrared receiver is located at the corner of the room at $\{x, y, z\}$. The channel transfer function is recorded and then the receiver is moved to $\{x+\Delta, y, z\}$ and the measurement is performed again. Moving the receiver in one direction in steps of Δ continues until it reaches the end of the room and then the receiver is moved back to $\{x, y+\Delta, z\}$ for the next measurement. The procedure continues until all locations of the room on a grid pattern specified by $\{x+m\Delta, y+n\Delta, z\}$ are covered. The variation of the received optical power as well as the channel delay spread can then be related to the location of the receiver and its distance to the source, ceiling and walls. These measurements were performed in rooms B, F and L. In each room, the LOS as well as the diffused configurations were studied.

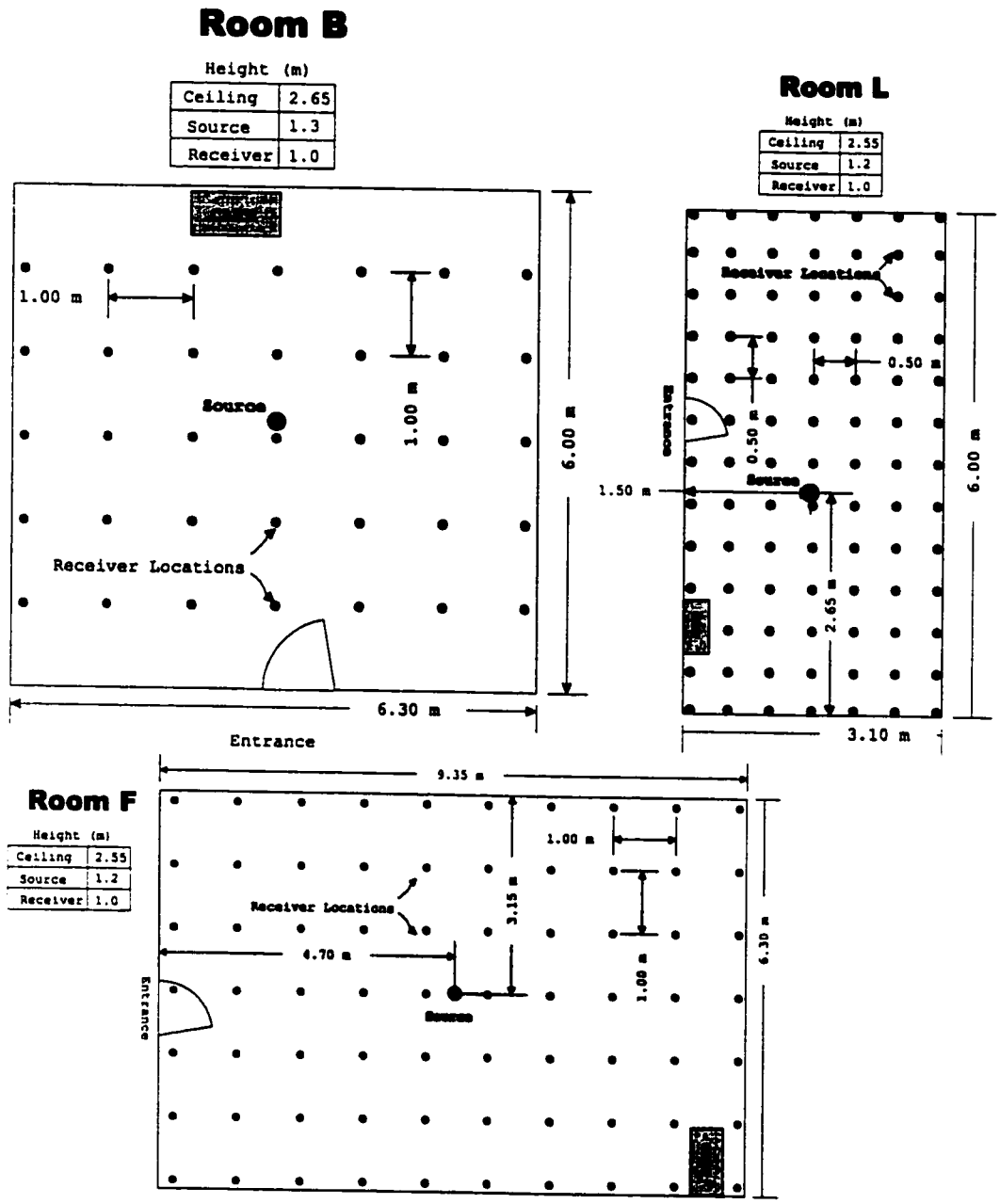

Figure 44. Top view of rooms B (CBY E016), F (CBY B202) and L (CBY LM305) used for measurement of the effects of receiver displacement on indoor infrared channel. The receiver is moved on the shown grid patterns and for each location, the channel transfer function for both LOS and diffuse configurations are recorded.

Figure 44 shows the location of transmitter as well as the grid pattern covered in each room by the receiver. All rooms are in the Colonel By building at the main campus of the University of Ottawa. Room B is a square shaped classroom of size 6m × 6.3m with 4 rows of chairs, 8 chairs per row. Walls are rough concrete type with yellowish color. Ceiling is flat with the same color. Green board extends over the entire width of the class. There are 12 flourescent lamps with transparent plastic covers on the ceiling each is 1.2m × 0.3m. In the diffuse measurements where the ceiling is illuminated by the infrared radiation, little energy is reflected from these covers and most of the received energy passes through the covers and is absorbed. Room F is a moderate size classroom of size 9m × 6m with 7 rows of chairs and desks, and has enough capacity for 50 students. The wall to the left of entrance has a rough surface with yellowish color. Other walls have smooth surface but different colors. The east wall (right wall in figure) is white. The upper half of the west wall is white and the lower half is green. The north wall is covered by green board in half. The bottom part of the wall is white. Room L is an empty small office of size 3m × 6m with the same type of ceiling as in room B. The walls have a rough surface and are colored in light green. There are no furniture or office supplies inside this room.

The results of these measurements are in Figure 45, Figure 46 and Figure 47. In room L, the smallest of the three rooms, the average received optical power is –57 dBo and 90% of the room area receives more than –61.5 dBo of optical energy. In room B that is larger than room L, the average received optical power decreases to around –58.5 dBo and the 90^{th} percentile of the power is reduced to –62.4 dBo. This is around 2 dBo lower than the values in room L. For room F, the average received optical power drops even lower to –60.4 dBo and the 90^{th} precentile coverage reduces to –62.4 dBo. These results clearly indicate that the average received optical power decreases as the room size increases. In all rooms, the peak of the received optical energy is around –52 dBo and that is when the receiver and the transmitter are very close to each other. As the receiver moves towards the corner of the room, received power drops.

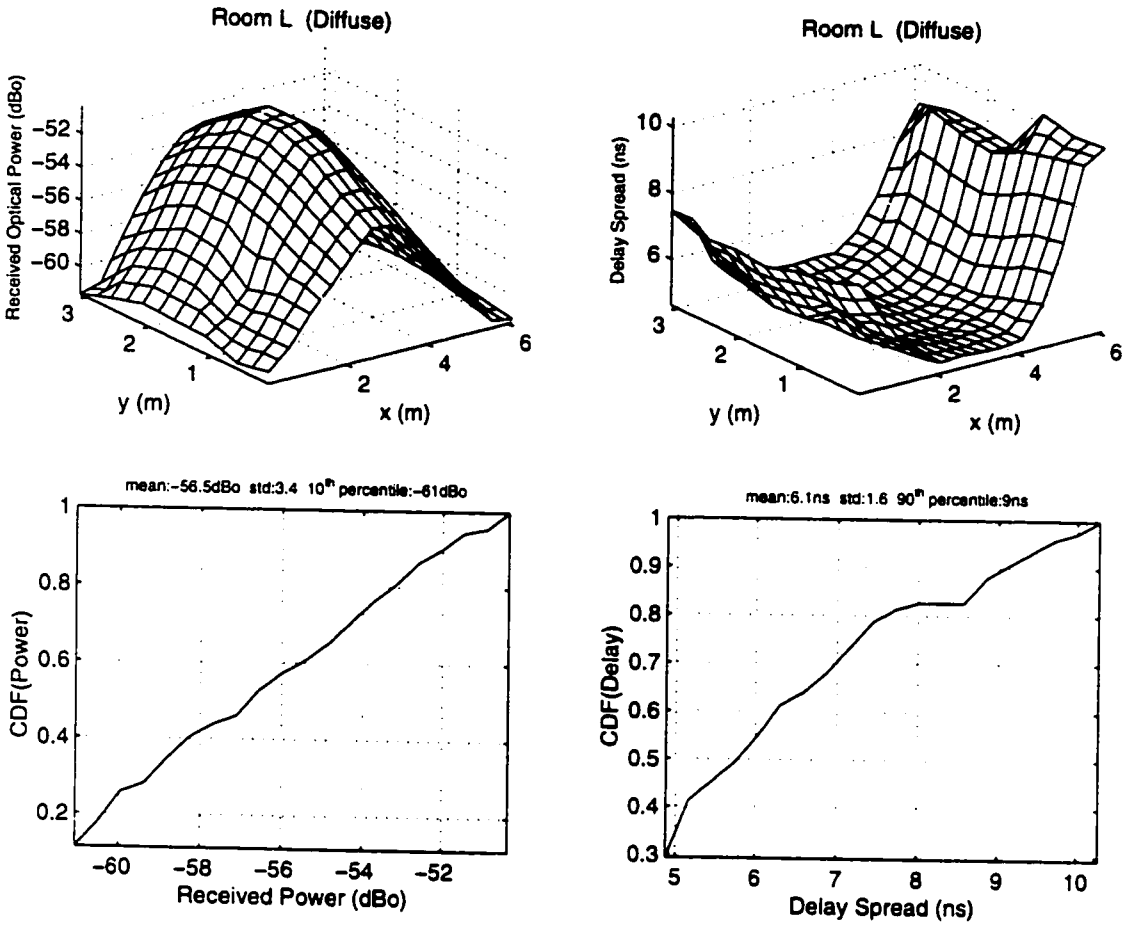

Figure 45. The received optical power and the channel delay spread for room L are shown in these graphs. The two top plots show the spatial distribution of these parameters. The bottom two graphs show the cumulative distribution function (CDF) of the received power and the delay spread parameters as well as their average, standard deviation and 10^{th}(90^{th}) percentile.

The average channel delay spread for room L, as depicted in Figure 45 is around 6.1 ns with 10% of the area having a delay spread larger than 9ns. For room B, (Figure 46) the average increases to around 7.4 ns and the 10^{th} percentile of the delay increases to 10 ns. In Room F, which is larger than the other two rooms, average of the delay spread is around 8.2 ns and the 10^{th} percentile coverage of the room is 12.5 ns.

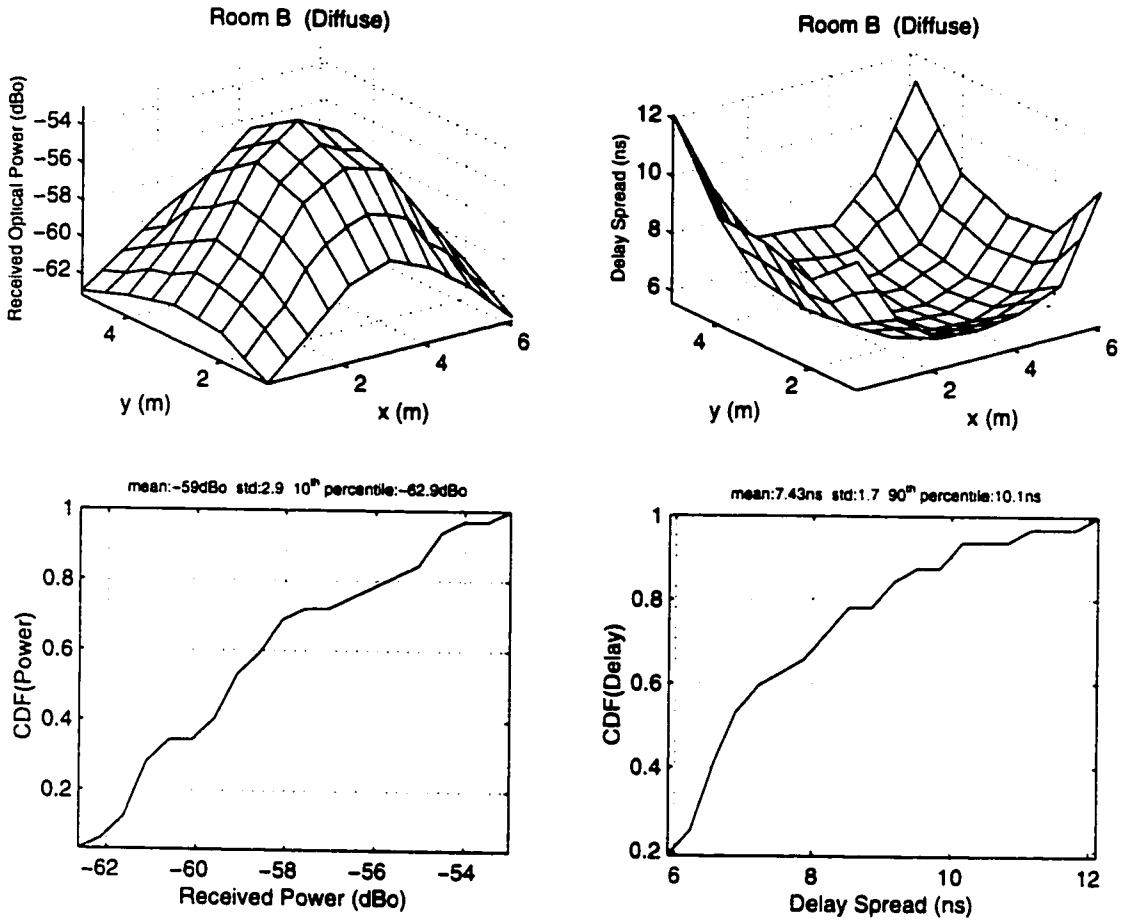

Figure 46. The received optical power and the channel delay spread for room B are shown in these graphs. The two top plots show the spatial distribution of these parameters. The bottom two graphs show the cumulative distribution function (CDF) of the received power and the delay spread parameters as well as their average, standard deviation and 10^{th}(90^{th}) percentile.

It is evident that as the room size increases, the average delay spread of the infrared channel increases and the percentage of the areas that have less than a given delay spread decreases. Also, as shown on the graphs, as these receiver moves away from the source, the delay spread increases.

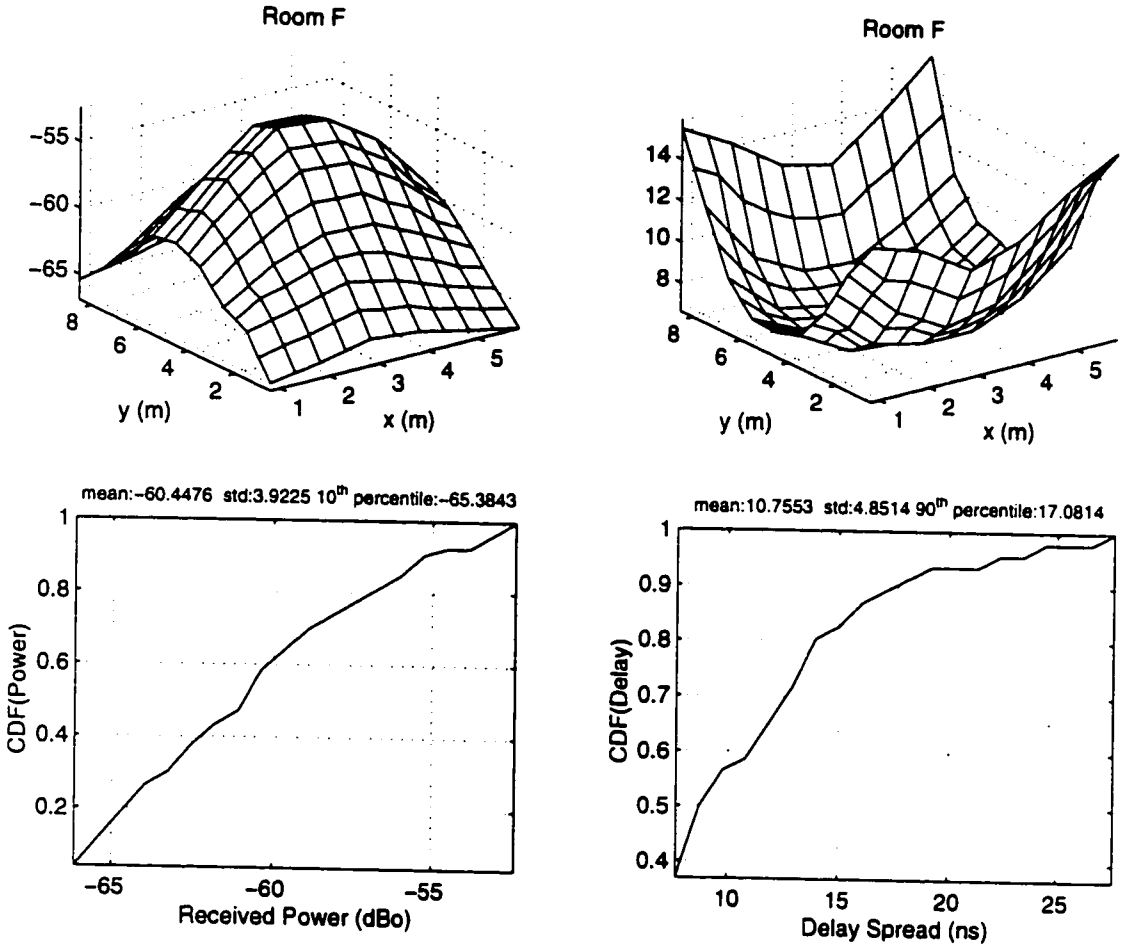

Figure 47. The received optical power and the channel delay spread for room F are shown in these graphs. The two top plots show the spatial distribution of these parameters. The bottom two graphs show the cumulative distribution function (CDF) of the received power and the delay spread parameters as well as their average, standard deviation and $10^{th}(90^{th})$ percentile.

6.4 ENHANCING THE SIMULATION RESULTS

In Section 2 of this chapter, equations that describe the channel impulse response using a simplified one-bounce model are presented. In this section, the objective is to show that the results of these simplified equations can be adjusted using the data that are derived from the measurements.

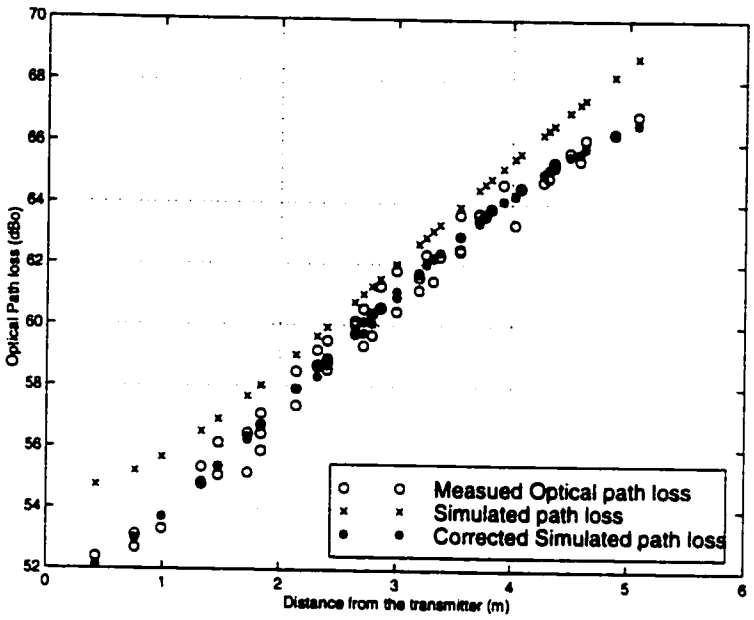

Figure 48. The graph shows the variation of the channel path loss versus the distance between the infrared source and the infrared receiver in room F as described by the simplified one bounce model. Measurement results as well as corrected simulation results are also shown.

Figure 48 shows the variation of the channel path loss versus the distance between the infrared source and the infrared receiver as described by the simplified one bounce model. The points in the graph marked by (×) show the results of the path loss as predicted by equation (6-5) assuming a ceiling reflection coefficient of 0.7. Measurement results for the channel path loss obtained in room F are also shown using circles (o) on the graph. It is clear that the simplified model overestimates channel path loss. The amount of error in calculation of the path loss is around 2.5dBo when receiver is far from the transmitter. This error decreases to less than 1dBo when the distance between the infrared source and the infrared receiver is between 2 and 3 meters. The model overestimates the path loss because a considerable part of the transmitted energy arrives at the receiver after undergoing two or more reflections and this is not included in the simplified model. As it was demonstrated in Chapter 3, accurate ray tracing for these rays is computationally intensive and almost impractical for 4 or more bounces. Note that, walls act as a source of reflected infrared energy that are not considered in the simplified

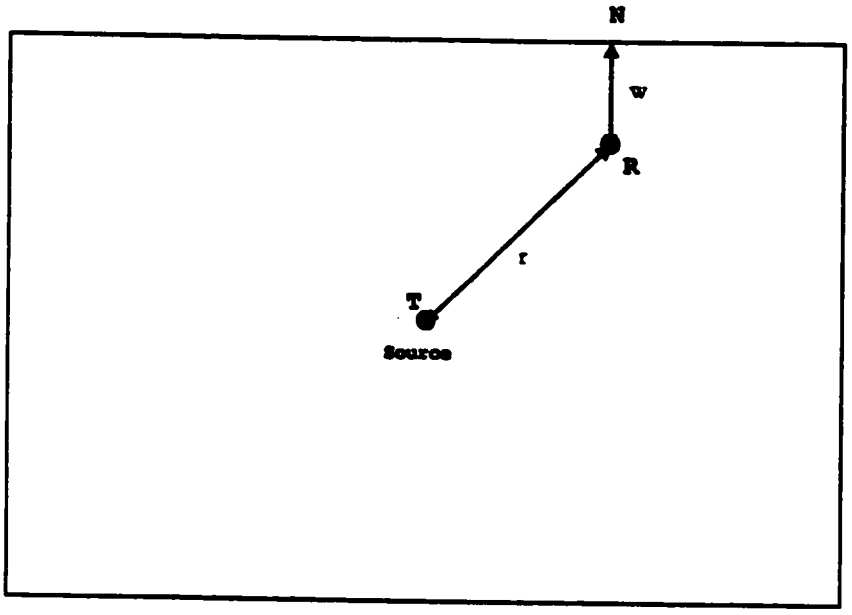

Figure 49. Top view of an infrared source and receiver in a given room.

model described by equation (6-5). Therefore, for correcting the results of the simulation, the distance of the receiver to the wall must be included.

6.5 ENHANCING THE ACCURACY OF THE SIMULATION RESULTS

Figure 49 shows the top view of an infrared source and an infrared receiver in a given room. TR is the distance between the source and the receiver. RN is the distance between the receiver and the closest wall. Let's define r = TR and w = RN. Investigating the relation between the error in path loss estimation and the coordinates of the receiver in the room reveals a close relationship between the error value and the two parameters r and w for each point. It has been found that the error can be well approximated by a second order function of r and w. Therefore,

$$PL_{err}(r,w) = PL_m(r,w) - PL_s(r,w)$$

$$PL_{err}(r,w) \approx f_{PL}(r,w) = a_1 r^2 + a_2 w^2 + a_3 r + a_4 w + a_5 rw + a_6$$

where PL_{err} is the difference between the measured path loss PL_m and the simulated path loss PL_s all represented in optical dB (dBo). An optimization algorithm is used to find the second order approximation function. For all the points in a given room, the values of PL_{err} are

Room Name	Path loss error without correction		Path loss error with correction	
	Avg. Path Loss (dBo)	Max. Path Loss (dBo)	Avg. Path Loss (dBo)	Max. Path Loss (dBo)
Room L	2.1	4.3	0.6	2.2
Room B	1.2	2.2	0.4	1.1
Room F	1.2	2.5	0.4	1.0

Table 4. The simulation results can be enhanced by applying a correction factor that is derived from the measurements. This table shows the average and the maximum path loss error with and without correction. A considerable increase in the accuracy of the results is noticeable when the left two columns are compared against the right two columns.

calculated and used as input for the optimization algorithm. As it was mentioned before, a Nelder-Mead type simplex search method can be used to find the desired set of coefficient values. In this case, the objective is to find the set of $\{a_1, a_2, a_3, a_4, a_5, a_6\}$ that minimizes the $PL_{err}(r,w) - f_{PL}(r,w)$ for the set of all $\{r,w,PL_{err}\}$. Knowing the coefficients of the polynomial, it can be used to correct the path loss simulation derived from the single-bounce method. For any given transmitter and receiver configuration, knowing the value of r and w, the correction factor can be evaluated. Adding the correction factor to the estimated path loss from the simplified method generates a very accurate path loss estimate. Combining the displacement measurement results for rooms B, F and L, the function that minimizes the estimated error is found to be:

$$f_{PL}(r,w) \approx 0.47r^2 + 1.43w^2 - 2.7r + 1.4w - 0.5rw + 4.1 \qquad (6\text{-}7)$$

Figure 48 shows the results of applying the above function to the simulation results for room F. The average difference between the simulation result and the measurement results is reduced from 1.3 dBo to 0.4 dBo and the maximum difference is reduced from 2.1 dBo to 0.9 dBo. In other words, the average error is reduced in half and the maximum error is reduced by almost 60%. Similar increase of accuracy in estimating the path loss is found when the correction described by equation (6-7) is applied to the simulation results in room B and room L. A summary of the improvements in the path loss estimation for all displacement measurement sites is presented in Table 4.

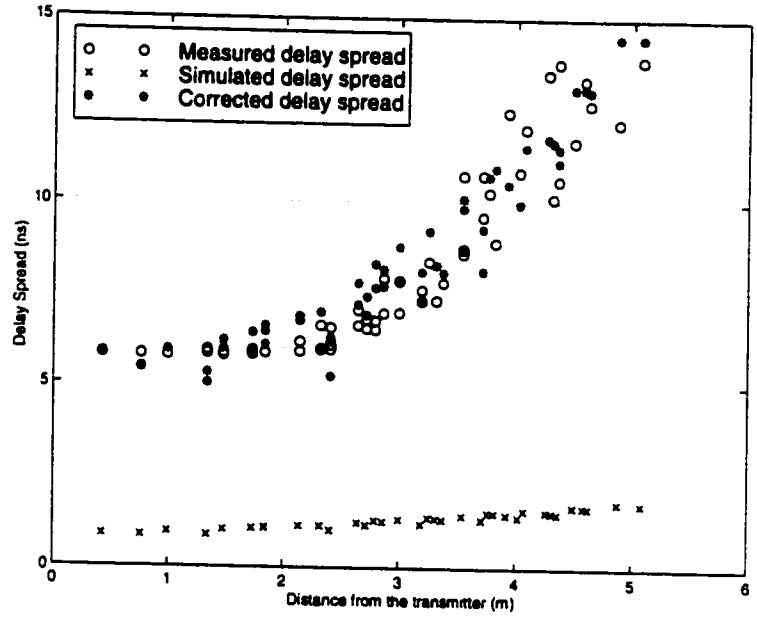

Figure 50. The initial estimate, corrected estimate and measured value of the channel delay spread for room F are shown in this graph. Note the enhancement in the accuracy of the estimates by applying the correction factor.

The same process can be applied to the calculations of the channel delay spread. The equation (6-3) can be used to approximate the delay spread for any given point inside the room. Since this equation considers only the rays that are reflected once, the resulting channel impulse response has a very small delay spread value. The channel delay spread increases considerably because of the rays that are received after two or more bounces to the receiver. Using the one-bounce simulation results as the basis and comparing the results against the measurement results, a correction factor can be found that corrects the value of the delay spread as calculated by equation (6-3). It has been found that the same parameters, i.e. distance between source and receiver (r) and distance between receiver and closest wall (w) can be used to form a second order correcting polynomial to correct the results of the simulation. Define $D_{err}(r, w)$ as the ratio between the measured channel delay spread and the simulated value at a given point:

$$D_{err}(r, w) = D_m(r, w) / D_s(r, w)$$

The objective is to find a polynomial that closely matches the value of $D_{err}(r, w)$ for all the measured points.

$$D_{err}(r, w) \approx f_D(r, w) = b_1 r^2 + b_2 w^2 + b_3 r + b_4 w + b_5 rw + b_6$$

The same procedure that was used to find the second order polynomial in the cases of path loss correction can be used here. The minimization algorithm receives the set of all $\{r, w, D_{err}(r, w)\}$ for the three measurement sites. Using these inputs, the algorithm finds the set of $\{b_1, b_2, b_3, b_4, b_5, b_6\}$ that minimizes the distance between the desired polynomial and the error ratio for each point, i.e. $D_{err}(r, w) - f_D(r, w)$.

Applying this algorithm and using the results of receiver displacement measurements performed in rooms B, F and L, the following correcting polynomial is found:

$$f_D(r, w) = -0.02r^2 - 0.46w^2 + 1.36r + 2.86w - 0.82rw + 2.61 \qquad (6\text{-}8)$$

Figure 50 shows the initial estimate of the channel delay spread as well as the corrected values of the channel delay spread when the correction factor given by the equation is applied. It is clear that without applying the correction factor, the value of the channel delay spread can not be realistically used for system simulation purposes. However, after applying the correction factor the estimated results are very close to the measured results. In the case of room F, the average channel delay spread from the one-bounce model is around 1.27 ns while the average of the measured delay spread is 8.1 ns. By applying the correction polynomial to the results of the one-bounce model, the average is raised to 8.4 ns. The average difference between the one-bounce model and the measured values is 6.9 ns while the average difference between the corrected values and the measurement results is less than 0.8 ns.

Table 5 shows a summary of the enhancement results for the three measurement sites, room L, B and F. It is seen that the results show considerable improvements in the accuracy of the estimated channel delay spread when the correction factor is applied.

Room Name	Delay spread error without correction		Delay spread error with correction	
	Average error (ns)	Maximum error (ns)	Average error (ns)	Maximum error (ns)
Room L	5.1	8.9	0.54	1.8.
Room B	6.3	10.7	0.48	2.1
Room F	6.9	12.3	0.7	2.7

Table 5. The simulation results can be enhanced by applying a correction factor that is derived from the measurements. This table shows the average and the maximum path loss error with and without correction. A considerable increase in the accuracy of the results is noticeable when the left two columns are compared against the right two columns.

6.6 RELATION OF PATH LOSS AND DELAY SPREAD FOR RECEIVER DISPLACEMENT

As the receiver changes its position or direction in a given room, the received optical power and the channel delay spread vary. However, the relation between these two channel parameters depends on the type of receiver displacement. In this section, the relationship between the channel path loss and the channel delay spread for receiver displacement is studied. The displacement of the receiver is as described in Section 3 of this chapter, i.e. moving the receiver to cover a grid pattern in a given room.

Figure 51 shows the measurement results for the path loss as well as the channel delay spread for the rooms L, B and F. It is clear that the two parameters are strongly correlated when the receiver moves in a grid pattern. Based on this graph, a second order fit seems to be a good approximation that relates the channel delay spread to the path loss. Applying a minimum mean square error algorithm to fit a second order curve to the measured values for these three rooms results in:

$$\sigma = 0.0535PL^2 - 5.79PL + 169.3 \qquad (6\text{-}9)$$

where σ is the channel delay spread and PL is the channel path loss in dBo.

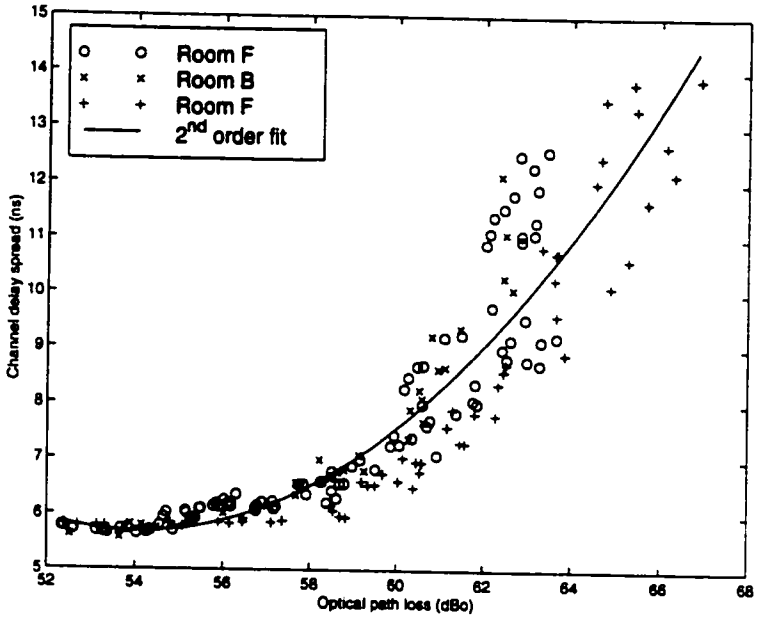

Figure 51. The relationship between the channel path loss and the channel delay spread when the receiver is moved in a grid pattern is shown in this graph. It is clear that a second order curve fit would provide a good approximation for the relationship between these two parameters.

As it can be seen in Figure 51, the curve fit provides a good approximation for the relationship between these two parameters when the path loss is smaller than 60dBo. For diffused configuration, this translates into a distance of about 2.5m between source and receiver in a typical office (see Figure 48). For path loss values above 60dBo, the approximation does not provide accurate estimate for the delay spread as it can be seen in the graph. As an example, for a path loss of 63dBo, the measured delay spread value ranges between 8.5ns to 13ns while the curve fit predicts a value of 10ns. This approximation could prove useful for some applications. However, in general, the correction method described in the previous section provides a more accurate approximation for the channel delay spread. The simple relationship described by equation (6-9) can provide an easy method for estimating the channel delay spread when the path loss is known and the receiver is close to the source.

6.7 SUMMARY AND CONCLUSIONS

In this chapter, a simplified one-bounce model was developed to predict the channel path loss and the channel delay spread. A closed form expression for the channel path loss was also derived to describe the variation of the channel path loss vs. the source to receiver distance (r). A set of measurements were performed to investigate the effects of receiver displacement on the characteristics of the indoor infrared channel.

The measurement procedure and its results were reported. The results were then used to find correction factors that can be used to enhance the accuracy of the simplistic simulation method. It was shown that using the correction factors, the channel path loss as well as the channel delay spread could be accurately predicted. This method generalizes the measurement results and provides an effective estimation tool that can generate accurate path loss and delay spread values for different physical configurations. For a new room or transceiver location, one would simply apply the one-bounce model that was developed in Section 2 to find an initial estimate for the channel path loss and the channel delay spread. The correction factors described by equations (6-7) and (6-8) can then be used to accurately predict the channel path loss and the channel delay spread.

Finally, it was shown that based on the measurement results, the displacement of the receiver in a grid pattern produces a set of channel delay spread values that is closely related to the channel path loss values. The relationship can be approximated by a second order curve fit that provides a good estimation of the channel delay spread when the distance between source and receiver is less than 3 m in a typical office environment.

CHAPTER SEVEN

7 EFFFECTS OF SHADOWING ON INFRARED CHANNELS

7.1 INTRODUCTION

These measurements were performed to assess the change of the characteristics of the infrared channels due to shadowing. Infrared light, being very close to visible light in its propagation properties, is subject to shadowing. An infrared source or receiver could be totally blocked by a non-transparent object. Therefore, a worst case for shadowing means no transmission at all. It is desired to observe the effects of moving people around an unobstructed infrared communication system and see how this would affect the channel properties.

In practice, the channel can be subject to short time shadowing of the source or receiver. A properly designed infrared communications system should tolerate the shadowing by transmitting at lower bit rates or stopping the transmission temporarily. It should be able to hold its state in case of severe shadowing and continue operation after the communication path is free of shadowing again.

Another factor that should be considered in the design of indoor infrared communications systems is that the time duration of shadowing is orders of magnitude larger than the bit or symbol duration. Therefore, it is considered a very long term effect and its effects are not expected to vary the channel on a symbol by symbol basis (assuming bit rates above 1 Mbps).

Many factors affect shadowing. Some of the important factors are:

- height of the receiver
- distance between the source and the receiver
- distance of the shadowing object from the receiver

A human body causes the most common type of path obstruction in a regular office environment. Therefore, the study is focused on the effect of shadowing by a person who is called "shadower" on the infrared receiver. Shadowing is more severe when the shadower moves on the line connecting the source and the receiver. This is well described by noting the similarity between the shadowing of the visible light and infrared light.

7.2 MEASUREMENT SETUP

In our measurements, each of the above parameters is changed and the channel transfer function was measured. The shadower is a person with a height of 170 cm and weight of 86 kg that moves on the line between the source and the receiver and stands at distances of 25cm, 50cm, 75cm and 100cm from the receiver. For each of these points, the height of the receiver was changed from 60cm to 120cm in steps of 20cm. Therefore, measurement results are recorded for 4 different heights of 60cm, 80cm, 100cm and 120cm. In addition, a reference set with no shadowing was recorded for each of the above conditions. This would be used to judge the relative shadowing effects. The above set of measurements were repeated for the source-receiver distances of 150cm, 250cm, 350cm and 450cm to result in 5×4×4=80 sets of transfer functions. This set of measurements is performed for both LOS and diffuse configurations. The measurements were performed in two different rooms in Colonel By Hall (CBY), University of Ottawa, resulting in 160×2=320 transfer functions.

The first set, named room G set, were performed in a conference room of size 6.0 m×7.8 m×2.3 m. This is a relatively small lounge adjacent to a large conference room. Removable grey colored full-height partitions at the right side of the room build a wall that separate this lounge from the adjacent conference room. There are 12 comfortable chairs around a coffee table in the lounge. The floor is covered with blue color carpet and the windows that are shown in top and right wall of the figure cover half the wall height. During measurements, windows were covered with shades of grey color. The ceiling of the room is a white flat plane with places for lamps and air conditioning inlets. The second set of data, named "room H" measurements, were collected in the auditorium of the same building. The

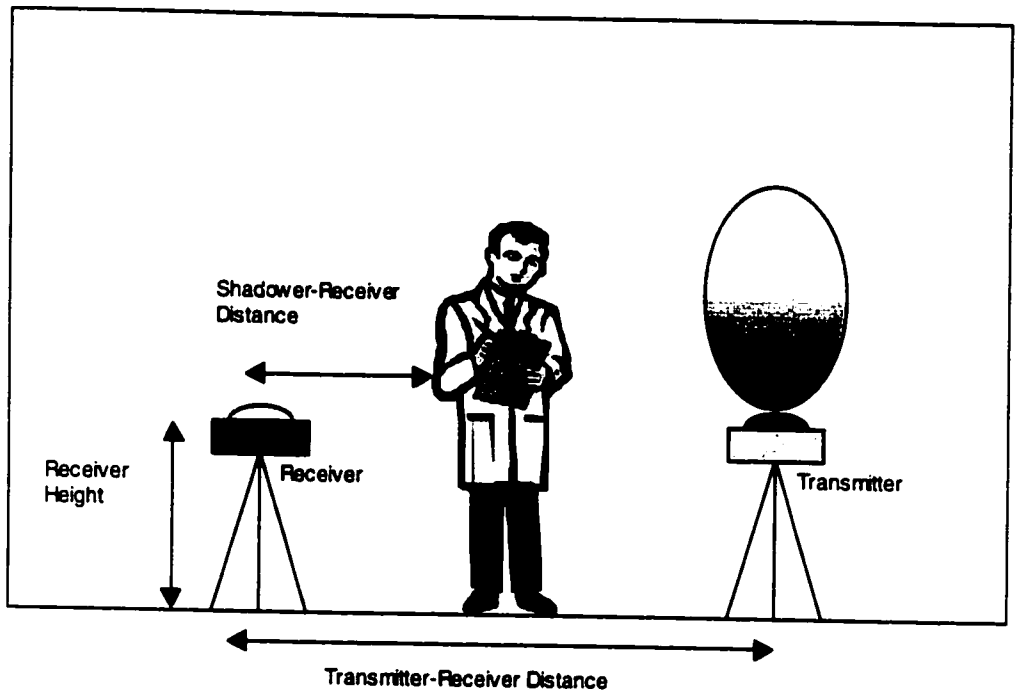

Figure 52. Three important parameters that determine the shadowing effect for the infrared channel are shown in this figure. These parameters have been changed and their effects on the channel characteristics have been have been studied.

auditorium has an almost rectangular shape, but the ceiling height increases from the entrance to the stage. The ceiling surface is edgy and it contains ventilation windows, speakers, local illumination lamps and similar objects typical to auditoriums. The walls are made of brown brick and the ceiling is a dark brown rough surface. Figure 53 shows the location of source, receiver and shadower in these measurements. Note that in room H, the first position of the receiver starts at a 2m distance from the receiver (instead of 1.5 m in room G). The rest of the set-up is the same for both rooms.

As before, each transfer function is recorded as 128 complex points in frequency ranging from dc to 400 MHz. The results were normalized to compensate for the transmitter and receiver filtering. The time domain characteristics of the channel, e.g., the channel delay spread were extracted by converting the transfer function to its corresponding impulse response.

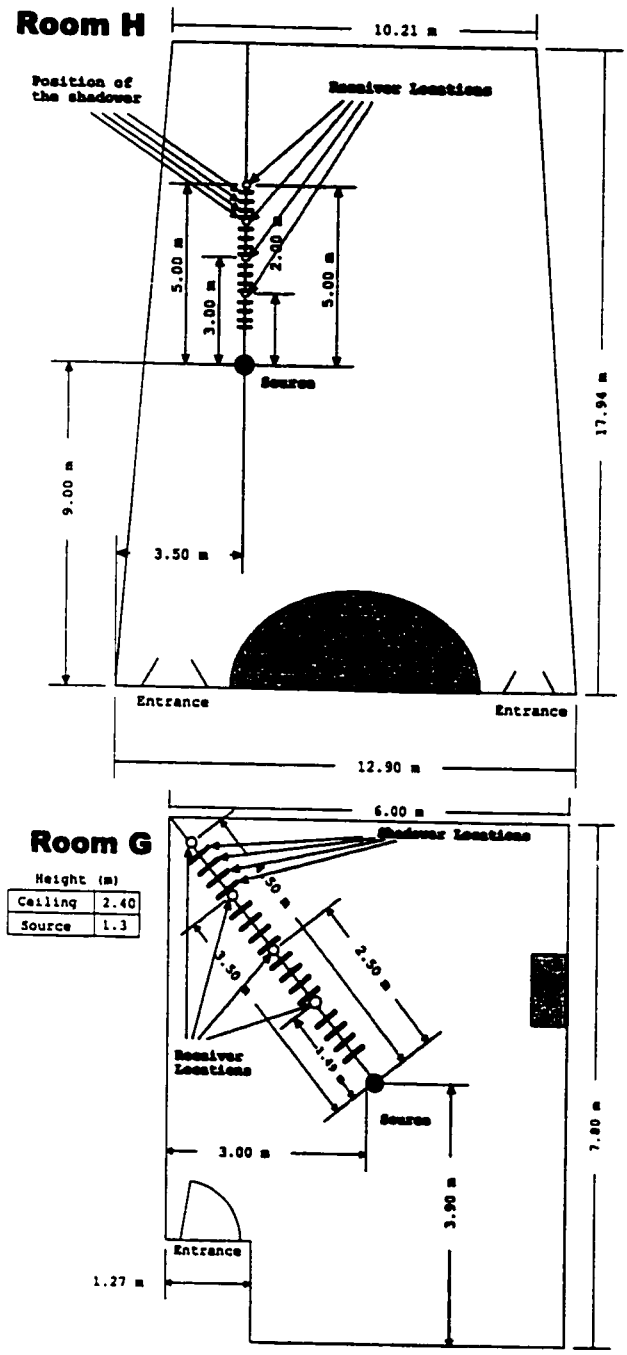

Figure 53. The above two pictures show the measurement room for shadowing experiments. Receiver was placed at positions indicated by small circles (4 positions in each room). For each receiver position, the shadower stood at positions indicated by bars (4 shadowing positions and one measurement without shadowing). For each of these pair of receiver-shadower positions, 4 different $H(f)$'s were recorded that corresponded to 4 different receiver heights of 60, 80, 100 and 120 centimeters.

7.3 MEASUREMENT RESULTS AND OBSERVATIONS

As before, the channel path loss and the channel delay spread are the two channel properties that are extracted from the results. Figure 54 to Figure 57 show the results for the path loss due to changes in the shadowing parameters. The path loss values are normalized by subtracting the value of the PL_{ongn} from the results. PL_{ongn} is the path loss for a case in which the receiver is closest to the source and there is no shadowing. For example in room G, PL_{ongn} is the path loss for the case where the receiver to source distance is 1.5 m, receiver is at a height of 60 cm and there is no shadowing. This is the lowest recorded path loss for a given room and transmission configuration.

The results after normalization clearly show the effects of shadowing, source to receiver distance and receiver height on the channel path loss. In these figures, each plot corresponds to a certain receiver to transmitter distance as specified in the plot label. For example, the top left plot corresponds to the case where this distance is 1.5 m. In each plot, there are four sets of lines specified by different markers. These lines correspond to different heights of the receiver for that particular measurement. The legend of graph that specifies the receiver height is (*) 60 cm, (o) 80 cm, (×) 100 cm, (+) 120 cm. The vertical axis is the normalized path loss, which is the added path loss due to shadowing, moving the receiver away from the source and changing the receiver height. Horizontal axis shows the shadower distance to the receiver. To show the 'un-shadowed' case on the same graphs, they are included on the right edge of the graphs. Therefore, marks on the right vertical axis represent the normalized un-shadowed path loss results. These results are also numerically tabulated and presented in Table 7.

7.4 OBSERVATIONS ON THE PATH LOSS RESULTS

- Path loss increases as the shadower moves towards the receiver.
- Shadowing has a stronger impact on the path loss when the receiver and transmitter are close to each other. As the distance between source and receiver increases, the effect of shadowing in increasing the path loss is less important. For example, considering room G, diffuse set results, it is seen that the path loss increase due to shadowing is between 3.8 to 7 dBo when the source and receiver are at a distance of 1.5 m (lines marked by *). In the same room and under the same conditions, when the distance between source and receiver

is 4.5 m, the shadowing effect increases the path loss between 2.5 to 3 dBo. Same observation is valid for the room H results.

- Shadowing has a stronger impact on the path loss when the receiver is closer to the ground. As the receiver height is changed from 60cm to 120cm, the shadowing effect becomes less important. The graphs show that when the receiver height is 120 cm, the path loss change due to shadowing is smaller than the case where the receiver height is 60 cm. This is seen in the graphs by comparing the lines marked by (+) (receiver height=120 cm) with the lines marked by (*) (receiver height=60 cm). As an example, in room H, diffuse set results, the maximum change of path loss due to shadowing for a receiver at height 120 cm is around 6 dBo. In the same room, the variations of up to 9 dBo due to shadowing is observed for a receiver at height 60 cm.

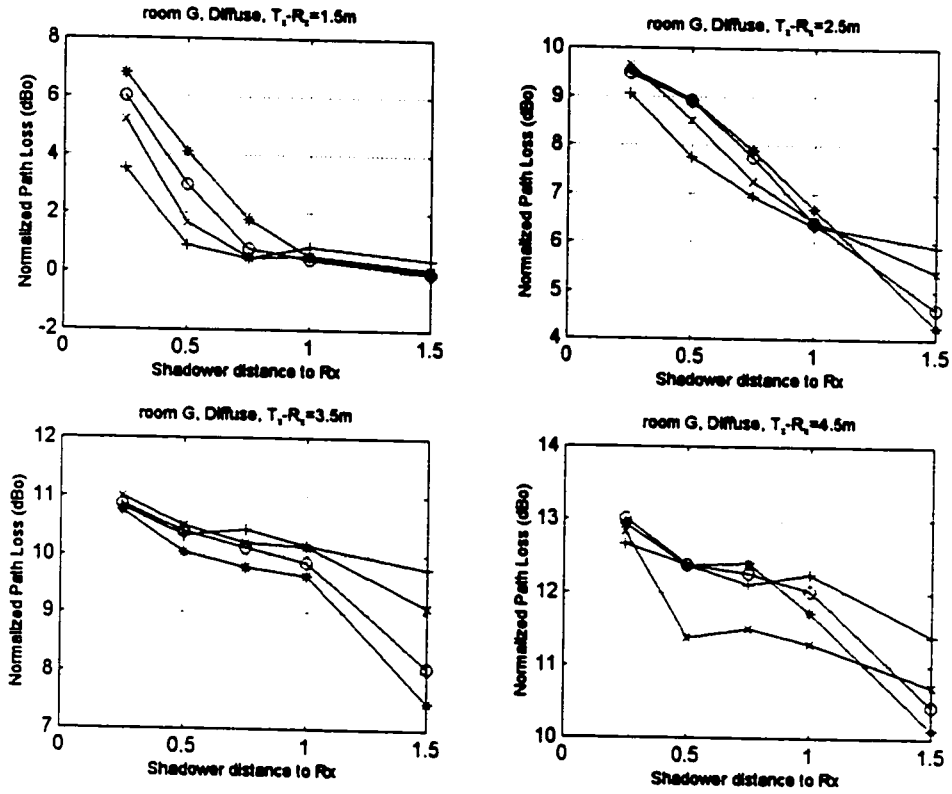

Figure 54. Normalized path loss in room G using the diffuse configuration. Each plot corresponds to a different distance between the receiver and the transmitter as specified in the plot titles. Inside each plot, there are four sets of lines that correspond to the receiver height for each measurement. ([(*) 60 cm, (o) 80 cm, (×) 100 cm, (+) 120cm])

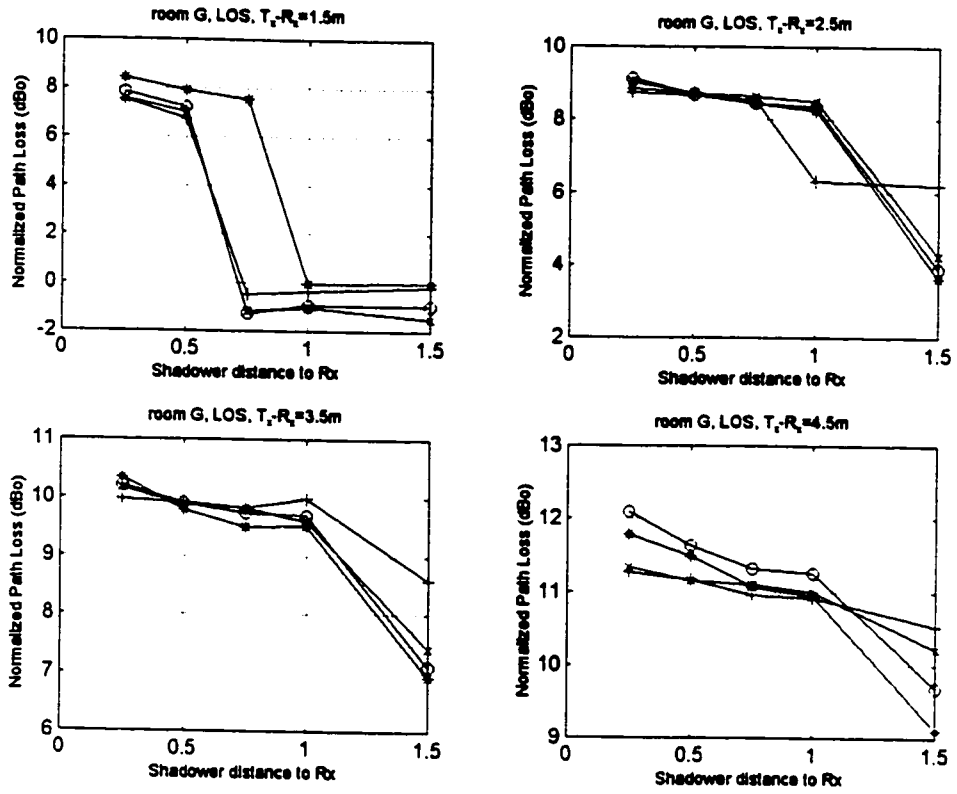

Figure 55. Normalized path loss in room G using the LOS configuration. Each plot corresponds to a different distance between the receiver and the transmitter as specified in the plot titles. Inside each plot, there are four sets of lines that correspond to the receiver height for each measurement. ([(*) 60 cm, (o) 80 cm, (×) 100 cm, (+) 120cm])

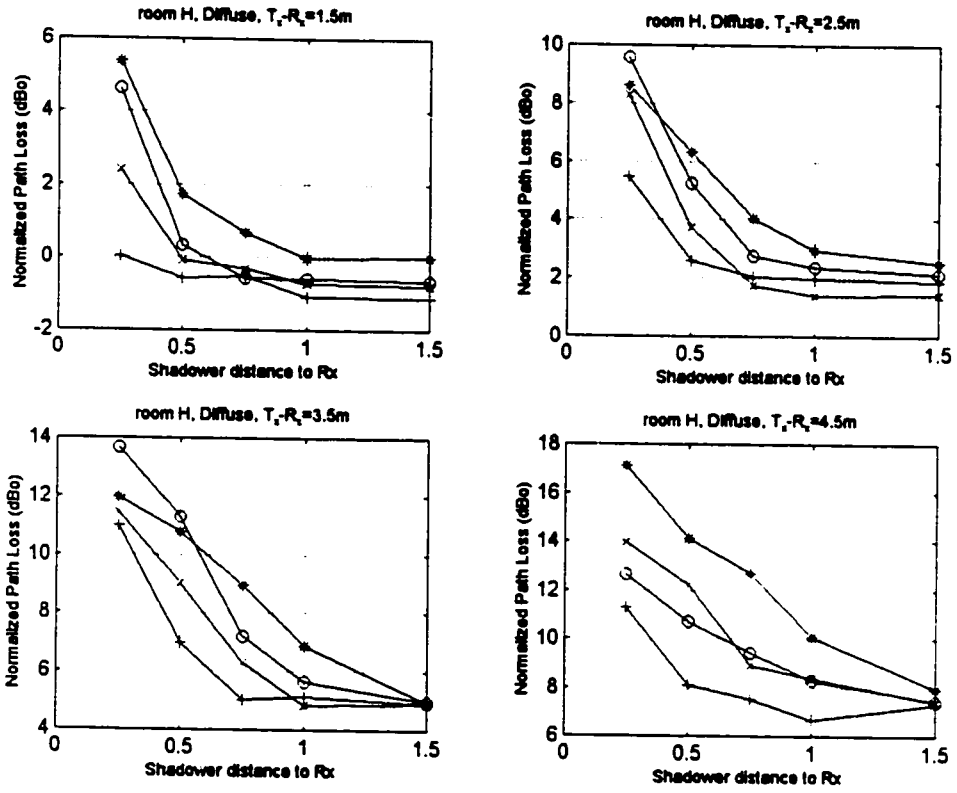

Figure 56. Normalized path loss in room H using the diffuse configuration. Each plot corresponds to a different distance between the receiver and the transmitter as specified in the plot titles. Inside each plot, there are four sets of lines that correspond to the receiver height for each measurement. ([(*) 60 cm, (o) 80 cm, (×) 100 cm, (+) 120cm]).

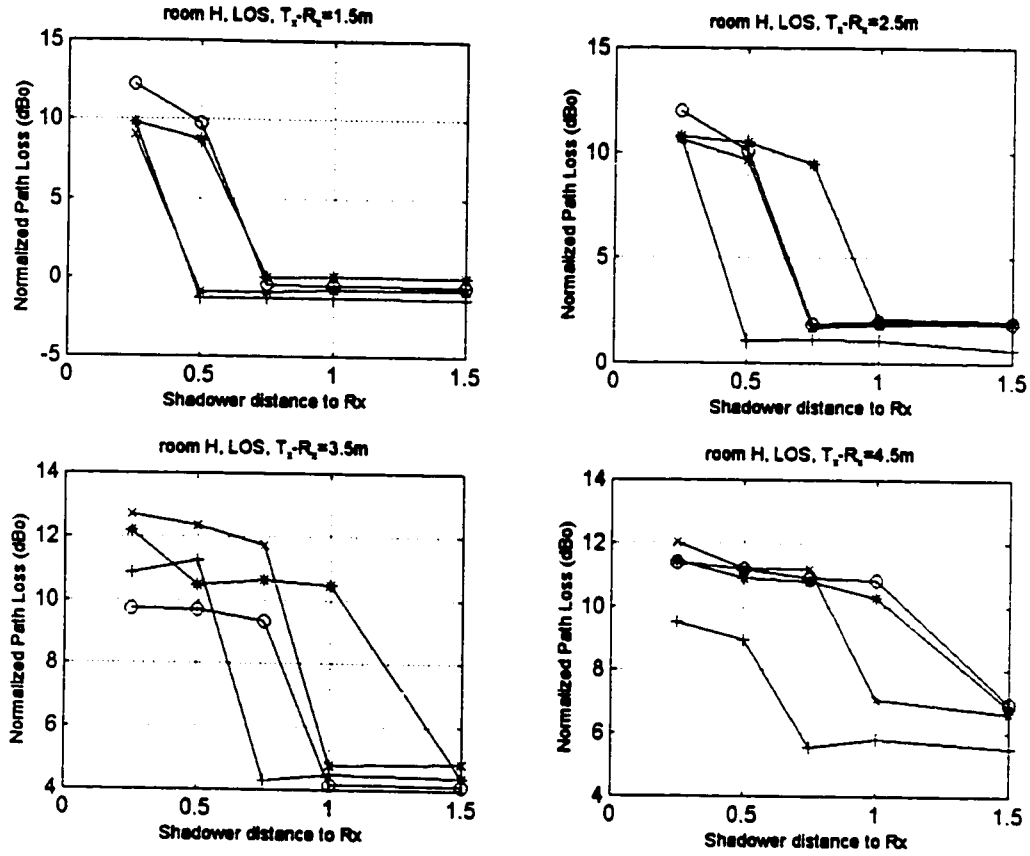

Figure 57. Normalized path loss in room H using the LOS configuration. Each plot corresponds to a different distance between the receiver and the transmitter as specified in the plot titles. Inside each plot, there are four sets of lines that correspond to the receiver height for each measurement. ([(*) 60 cm, (o) 80 cm, (×) 100 cm, (+) 120cm]).

For LOS configuration, shadowing is an abrupt process. Path loss changes drastically as the shadow drops on the receiver. However, for a diffuse system, the path loss due to shadowing increases monotonically as the shadower gets closer to the receiver. Abrupt changes in path loss are not observed in the diffuse results. For example, considering results obtained in room G, it is seen that the path loss changes about 8 dB when the shadower comes 25 cm closer to the receiver in the LOS case (line marked by *). Under the same conditions, the drop in the path loss is less than 1 dBo for the diffuse configuration. In fact, there is not a single case in the diffuse shadowing measurements where the drop of power due to shadowing is higher

than 3 dBo when the shadower changes its position by 25cm. This reduced susceptibility to shadowing is the most important advantage of the diffuse configuration over the LOS configuration.

- Transmission is less susceptible to shadowing when receiver is high above the ground and far away from the source. When the receiver height is 120cm, maximum change in the path loss due to shadowing is 1 dBo for diffuse and 0.6 dBo for LOS. This is when the shadower is at a distance of 25cm to the receiver and the result is compared against the same configuration with no shadowing.
- Worst susceptibility to shadowing happens when receiver is close to the ground and the source. When the source to receiver distance is 1.5m and the receiver height is 60cm, the maximum change in the path loss due to shadowing is 7 dBo for diffuse and 16 dBo for the LOS case. This is when the shadower is at a distance of 25cm from the receiver and the result is compared against the same configuration in the absence of shadowing.

7.5 RELATION BETWEEN THE CHANNEL PATH LOSS AND THE CHANNEL DELAY SPREAD

The delay spread of the measured channels has also been calculated. The results show that the channel delay spread values are strongly correlated with the path loss values. The graphs in Figure 58 show the path loss versus delay spread graphs. When the delay spread is represented on a log scale, it shows a linear correlation with the path loss. This is very similar to the results obtained previously which showed a strong correlation between these two parameters when the receiver rotates. Parameters for the numerical fit are shown on each graph and are summarized in Table 6. These parameters show the numerical value for a regression line that relates the power and the delay spread by:

$PL = \alpha \log_{10}(\sigma) + \beta$

where PL is the path loss and σ is the delay spread. The following observations are made from these graphs.

7.6 OBSERVATIONS ON THE DELAY SPREAD RESULTS

For the diffuse configuration, the variation of delay spread vs. path loss is smooth. As power drops, the delay spread increases and the strong correlation is seen between the delay spread and the path loss. The top two graphs in Figure 58 show the results for the diffuse configuration. It is clearly seen that the distribution of points is continuous across the regression line.

- For LOS configurations, there are two regions on the graphs. One region with very small values for the delay spread corresponding to no-shadowing and another region with results corresponding to shadowing which include large values for the delay spread. The linear relationship between the two variables on the log scale is clearly seen on the graph.
- In LOS, the values of the delay spread have a higher dynamic range. When the path between the transmitter (spot on the ceiling) and the receiver is not blocked, the delay spread is very low and when it is blocked, the delay spread is very high.

Room	Diffuse Configuration				Line Of Sight Configuration			
	α	β	MSE	Xcorr	α	β	MSE	Xcorr
Room G	13.29	52.87	2.06	.9345	18.62	49.55	2.12	.9233
Room H	11.9	60.5	3.36	.9126	9.3	61.9	2.66	.9379

Table 6. Linear regression between the channel delay spread and the channel path loss are shown here. The value of correlation coefficient (Xcorr) is close to 1 in all cases showing a strong correlation between the two parameters regardless of the room or configuration of the transceivers.

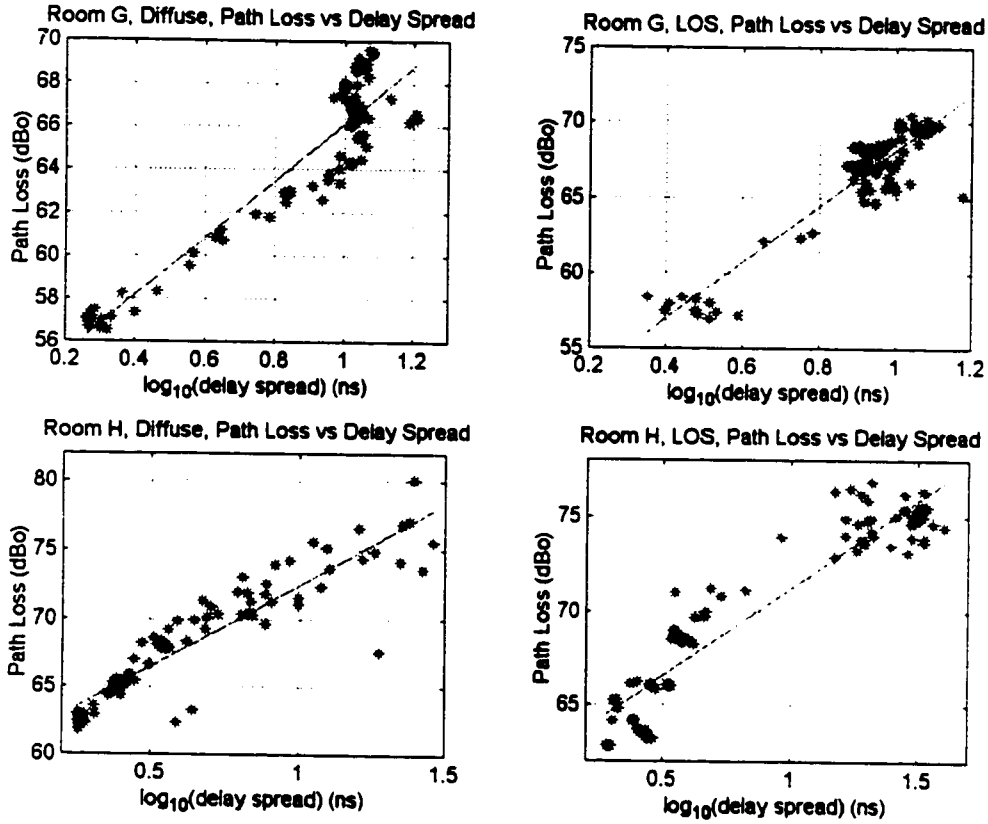

Figure 58. Graphs show the correlation between the channel path loss and its delay spread for various shadowing conditions. A linear fit with its parameters is also included on each graph. It can be seen from the correlation coefficients that the two variables are strongly correlated.

7.7 SUMMARY AND CONCLUSIONS

Measurements have been performed to investigate the effects of shadowing on the characteristics of the indoor infrared channel. Shadowing reduces the received optical power and increases the channel delay spread. Some of the important parameters that specify the impact of shadowing on the characteristics of the channel were included in the measurement plans. Therefore, the performed measurements include different scenarios to investigate the effects of receiver height, receiver to shadower distance, receiver to source distance and the configuration type (LOS vs. diffuse) on the shadowing. The variation of channel path loss due

to shadowing and due to these parameters was studied and detailed result presented. It was shown that the channel path loss can increase by up to 8 dBo in the worst case shadowing scenarios in diffuse configuration. That is when the source and receiver are very close, the receiver is very close to the ground and the shadower is 25 cm away from the receiver. For the LOS configuration, the shadowing has a much more important effect and can increase the channel path loss by more than 16 dBo as it was presented in the results.

It was shown that the shadowing increases the channel delay spread. For the measured shadowing results, the channel path loss and the channel delay spread are correlated and their relationship can be expressed by $PL = \alpha \log_{10}(\sigma) + \beta$.

D1→	1.5				2.5				3.5				4.5			
D2→	0.6	0.8	1.0	1.2	0.6	0.8	1.0	1.2	0.6	0.8	1.0	1.2	0.6	0.8	1.0	1.2
D3↓	Room G, Diffuse															
∞	56.6	56.6	56.7	57.0	60.8	61.2	62.0	62.5	64.1	64.6	65.7	66.3	66.7	67.0	67.3	68.0
1.00	0.54	0.44	0.44	0.41	2.42	1.77	1.04	0.44	2.17	1.79	1.03	0.40	1.61	1.57	0.57	0.85
0.75	1.79	0.79	0.39	0.05	3.64	3.13	1.86	1.03	2.31	2.06	1.11	0.67	2.30	1.82	0.79	0.71
0.50	4.12	2.99	1.58	0.48	4.69	4.30	3.13	1.84	2.56	2.33	1.40	0.58	2.26	1.93	0.66	0.98
0.25	6.80	6.04	5.14	3.11	5.30	4.86	4.27	3.14	3.27	2.79	1.91	1.05	2.83	2.58	2.12	1.27

D1→	1.5				2.5				3.5				4.5			
D2→	0.6	0.8	1.0	1.2	0.6	0.8	1.0	1.2	0.6	0.8	1.0	1.2	0.6	0.8	1.0	1.2
D3↓	Room G, LOS															
∞	58.5	57.5	57.0	58.3	62.1	62.3	62.7	64.7	65.4	65.6	65.9	67.0	67.6	68.1	68.7	69.0
1.00	1.83	0.93	0.75	1.08	5.90	5.60	5.00	2.28	3.91	3.50	2.38	2.10	2.71	2.69	2.16	1.39
0.75	9.43	0.62	0.59	0.98	6.07	5.72	5.13	4.51	3.90	3.56	2.61	1.93	2.84	2.75	2.26	1.43
0.50	9.79	9.10	8.81	8.19	6.35	5.96	5.21	4.67	4.19	3.71	2.67	2.03	3.25	3.06	2.31	1.64
0.25	10.3	9.73	9.32	8.98	6.47	6.39	5.54	4.72	4.74	4.02	2.95	2.08	3.55	3.54	2.50	1.74

D1→	1.5				2.5				3.5				4.5			
D2→	0.6	0.8	1.0	1.2	0.6	0.8	1.0	1.2	0.6	0.8	1.0	1.2	0.6	0.8	1.0	1.2
D3↓	Room H, Diffuse															
∞	62.9	62.3	62.1	61.8	65.4	65.1	64.3	64.8	67.9	67.9	67.8	67.8	70.9	70.4	70.3	70.2
1.00	6.31	5.77	5.53	4.84	5.05	4.11	2.38	2.43	5.77	3.94	2.09	1.73	6.33	4.22	4.02	1.62
0.75	7.01	5.78	5.94	5.40	6.16	4.50	2.73	2.51	7.82	5.48	3.54	1.62	8.93	5.33	4.53	2.48
0.50	8.08	6.69	6.18	5.35	8.43	6.97	4.70	3.05	9.63	9.58	6.27	3.57	10.3	6.60	7.86	3.06
0.25	11.74	11.01	8.67	5.97	10.72	11.31	9.27	5.93	10.83	11.95	8.70	7.58	13.36	8.55	9.59	6.22

D1→	1.5				2.5				3.5				4.5			
D2→	0.6	0.8	1.0	1.2	0.6	0.8	1.0	1.2	0.6	0.8	1.0	1.2	0.6	0.8	1.0	1.2
D3↓	Room H, LOS															
∞	64.2	63.6	63.3	62.8	66.1	66.1	66.1	64.8	68.5	68.3	69.0	68.5	71.0	71.1	70.8	69.7
1.00	7.63	7.08	6.67	5.85	5.44	4.92	4.06	2.77	10.58	3.67	3.27	2.29	7.75	7.96	3.93	1.98
0.75	7.56	7.15	6.58	5.85	12.80	4.83	3.90	2.80	10.74	8.85	10.21	2.12	8.26	8.04	8.06	1.74
0.50	16.29	17.37	6.54	5.82	13.80	13.05	11.85	2.77	10.57	9.21	10.83	9.07	8.37	8.32	8.06	5.15
0.25	17.42	19.79	16.54	17.01	14.09	14.98	12.85	12.40	12.31	9.24	11.18	8.69	8.90	8.51	8.89	5.69

Table 7. These tables show all the recorded path loss results for the shadowing measurements. D1 represents the distance between the source and the receiver, D2 represents the height of the receiver and D3 represents the distance between shadower and the receiver in meters. When there is no shadowing, the path loss is measured and reported in dBo in the row that corresponds to D3=∞. The entries in the rows with D3=1.0, 0.75, 0.5 and 0.25 show the increased path loss due to shadowing as compared to the no-shadower path loss reported in the corresponding column. Each table corresponds to a specific room/physical configuration as specified in the third row of the table. These same results can be graphically viewed in Figure 54 to Figure 57.

CHAPTER EIGHT

8 HOLOGRAPHIC DIFFUSERS FOR INDOOR INFRARED COMMUNICATION SYSTEMS

8.1 INTRODUCTION

The potential data rate for the infrared system is more limited by the available power budget rather than by dispersion. Therefore, a major challenge in an indoor environment is to distribute the received optical power as uniformly as possible in a given area and at the same time to provide as much tolerance to the shadowing as possible. There are safety standards limiting the maximum allowable transmitted optical power from a laser source. The use of diffusers is very important in meeting the standard limits since a diffuser distorts the directionality of the laser beam and allows for higher transmission power from the laser without causing side effects for the eye. Efficient use of the transmitted laser power and eye safety related issues would also require the use of diffusers. Diffusers can also shape the infrared radiation pattern. Optimization of radiation pattern for an indoor infrared transmitter has been reported in [12][87].

Commercially available glass diffusers have fixed scattering patterns and do not provide flexibility. Diffusers fabricated by holographic techniques can be tailored to have the desired scattering patterns. Holographic diffusers have been reported for homogenizing the radiation patterns for other applications [104]. Holographic light shaping diffusers are also commercially available for different purposes [65]. A major advantage of holographic diffuser is in its higher

achievable transmittance compared to the glass diffusers. Other potential advantages in using holographic diffusers are:

- Capability to tailor the light shaping patterns to our specifications.
- Light weight and compactness.
- Potential of inexpensive reproduction.

Considering the eye safety issue, a holographic diffuser can have the same radiation pattern as a glass diffuser if the proper diffusing pattern is superimposed on the hologram. In other words, a holographic diffuser can have the same advantages offered by a glass diffuser for eye safety with proper steps taken during its design and fabrication process. Off-the-shelf diffusers, however, do not provide proper scattering patterns for infrared wireless communications applications. One possible solution is to employ computer generated holograms where the incident laser light is split into a number of beams with overlapping diffraction patterns in the far field [74].

This chapter reports on the use of holographic diffusers with a three-dimensional multiple-lobe scattering pattern for shaping the infrared source radiation for wireless infrared communications. a multiple-exposure holographic technique has been employed by Dr. Eli Simova, a research associate of BCRL at the University Of Ottawa to fabricate the diffusers. The holographic recording geometry provides control over the angular and dispersion characteristics of the diffuser. A set of measurements has been conducted to investigate the relative performance of the proposed holographic diffuser with an opal glass diffuser. Optical path loss and its distribution for different choices of diffusers are of particular importance and have been studied in this exercise. The results show noticeable improvements in the distribution of optical power in a given area and more tolerance to shadowing by using the holographic diffuser. In the following sections, The holographic diffuser and its design and implementation procedure is briefly explained. Then, the measurement objectives and procedure is described. Finally, the results of the measurements and the conclusions made from this exercise will end the chapter.

8.2 HOLOGRAPHIC MULTIPLE-LOBE DIFFUSER

8.2.1 Concept

For fabrication of multiple-lobe holographic diffusers, a modified multiple-exposure technique based on Bragg degeneracy effect is employed [110]. For a square room, a scattering pattern with multiple-lobes provides a relatively uniform distribution, as shown by computer simulations in [87]. Therefore, four- and six-lobe diffusers were fabricated, although the concept can be applied to a larger number of lobes.

For a holographic diffuser with an N-lobe pattern, N/2 symmetrical transmission holographic gratings of equal period are multiplexed onto the photosensitive recording medium [111]. Each of the gratings to be multiplexed must be in the volume regime of diffraction for the operation wavelength, i.e., exhibit only one diffraction order and all the diffracted light is concentrated in the first diffraction order. For that, the relation $Q = 2\pi\lambda d / n\Lambda \geq 10$ must hold, where d is the thickness of the recording film, n is the refractive index of the material and Λ is the grating period. For the recording wavelength, the gratings may not be in the volume regime of diffraction. The gratings are recorded in a standard two-beam interferometric set-up. The laser beam is split into two. These two beams are expanded and overlap on the photosensitive material. They form an interference pattern with a period in accordance to Bragg condition, i.e., $n\,\Lambda \sin(\theta) = \lambda$, where θ is the angle of the incident beam. After exposure of the photosensitive film to the interference pattern, the film is rotated around its normal by $\varphi = 2\pi/N$ degrees and is exposed to the interference pattern again. That procedure is repeated until the necessary number of multiplexed gratings is reached.

At the reconstruction of the hologram, the angle of the incident light beam comes from a direction that satisfies Bragg condition for the operating wavelength. There are N/2 volume holographic gratings recorded in the photosensitive material that have N/2 different direction of their first-order diffraction. Because of the Bragg degeneracy effect that takes place, however, the incident light is split into N directions. Bragg degeneracy effect happens when the hologram is reconstructed from a specific direction, i.e., the direction in the orthogonal plane where the volume grating is not angularly selective. For a holographic grating, Bragg diffraction also occurs for beams tilted from the recording angle in the direction orthogonal to the plane containing the two recording wave-vectors. Beam pairs defining surfaces of two end-

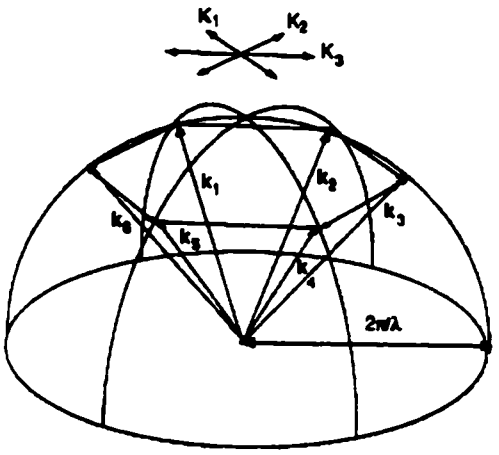

Figure 59. k-space diagram illustrating the recording of a six-lobe pattern and replay at a different wavelength. K1, K2 and K3 are grating vectors, k_i's are the directions of the output.

to-end cones form the same angle with respect to the grating. This specifies a strip on the *k*-sphere with the size of the grating-vector normal to all wave-vector pairs. The strips from all multiplexed grating-vectors K_i, intersect one another in N points of a regular N-polygon made out of N/2 grating vectors in the upper half of the *k*-sphere shown in Figure 59. The wave-vectors of the incident light k_i whose tips lie at these points simultaneously satisfy Bragg conditions for two adjacent grating-vectors. The first-order-diffracted beams satisfy Bragg condition for the adjacent two grating-vectors. They are re-diffracted again until the diffracted light is distributed to all the N points. When the incident light comes from one of these directions, it will be split into N beams, one transmitted and (N-1) diffracted, with the directions of the k_i vectors.

The concept is shown in Figure 59 for a six-lobe diffraction pattern consisting of three multiplexed gratings rotated by φ =60 degrees where K_i, i=1, 2, 3 represent the grating vectors, and k_i , i=1, ..., 6 - the replay directions. Only half of the *k*-sphere is shown for the sake of clarity. To achieve a diffused pattern in the lobes, an additional exposure is made by recording a holographic image of a glass diffuser without a reference beam. When a light beam is incident on the holographic element in accordance with Bragg condition, the resulting transmitted pattern consists of six lobes pointing at different directions with each lobe having the scattering pattern of the recorded glass diffuser. This diffuses the light in each direction

generated by the hologram to make it comply with the eye safety standards. A schematic representation of the pattern is shown in Figure 59. Bragg condition controls the angle between the lobes. The holographic recording geometry and the recorded image of the diffuser control the scattering pattern of each lobe. The holographic diffuser can be used for different wavelengths. Bragg condition is automatically satisfied for different wavelengths by re-adjusting the corresponding Bragg angles due to wavelength shift, as can be seen in Figure 59.

8.2.2 Recording procedure

DuPont's photopolymers were used as the photosensitive medium for the hologram recording. They feature high diffraction efficiency, low absorption and scatter, easy and repeatable processing. The processed holograms are stable, insensitive to humidity and temperature. The simple and reliable procedure for producing holograms in DuPont's photopolymers is an advantage over the wet chemical processing required for the widely used dichromated gelatin (DCG), and silver-halide emulsions. Hologram recording consists of exposure, UV cure, and heat process. According to the product information sheet, the exposure requirements are 50 mJ/cm^2, curing condition requires 50-100 mJ/cm^2 and baking after curing is at 120 C^o for two hours. The photopolymer film is protected on both sides with Mylar sheets to avoid shrinkage due to loss of volatile components.

The holographic recording film used in this application was DuPont HRF-600X001 of 20 μm thickness and sensitive to the Ar^+ wavelength λ = 514 nm. The films are suitable for transmission holographic elements. The films were exposed with the base and cover sheets intact by coupling them to a black absorbing plate with an index-matching liquid. This is done to suppress back-reflected light from being recorded into the photosensitive material that could deteriorate the diffraction efficiency and the signal-to-noise ratio. A holographic grating is formed in real-time during exposure with a significant refractive index modulation. During exposure, the sensitizing dye is visibly photo-bleached. The uniform UV exposure is required to complete polymerization. Complete photo bleaching occurs after the heat processing which enhances the index modulation and respectively the diffraction efficiency and leaves the material transparent and with a very low absorption. Because of the symmetric design, thickness changes in the photosensitive material after processing do not affect the performance.

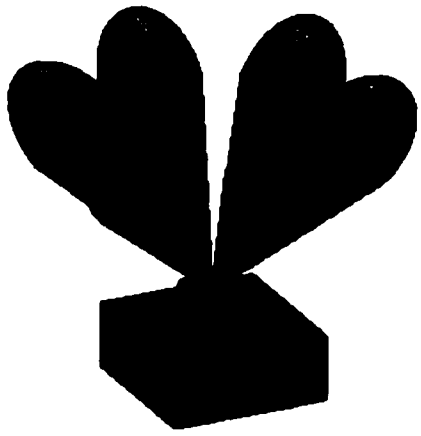

Figure 60. Diagram of the six-lobe scattering pattern of the holographic diffuser.

Diffusers with four- and six-lobe scattering patterns have been fabricated in DuPont's holographic recording films the two-beam interferometer. For the four-lobe diffuser, two gratings of equal periods Λ= 1.2 μm were perpendicularly superimposed, i.e. crossed gratings. Three gratings of equal periods Λ= 1.2 μm were multiplexed at 60 degrees for the six-lobe diffuser. In the final exposure, the hologram of a ground glass diffuser was recorded with most of the diffused light within a cone of a 10 degrees half-angle. When the incident beam comes from the direction satisfying Bragg condition, the resulting radiation pattern consists of four lobes with each lobe having the scattering pattern of the glass diffuser recorded in the photosensitive material. According to the eye-safety standards evaluated in [86], assuming a source diameter of 4 mm, the transmitted power of 200 mW, in the presence of the diffuser, is below the hazardous levels of exposure under normal operating conditions. That is if they are looked at from a distance of 5 cm for less than 15 min.

8.3 MEASUREMENT SETUP

To examine the properties of the infrared channel, the frequency response of the channel was measured by using the measurement set up that was described before. A swept-frequency signal from a network analyzer was amplified and converted to an optical signal in the optical transmitter using a 808-nm semiconductor laser diode. The optical head of the transmitter consists of either a glass diffuser or a holographic diffuser. A sealed box was used for the glass diffuser to minimize the loss of optical power due to back scattering and multiple-reflections.

In the case of holographic diffuser, the lightwave emitted by the laser diode illuminated the holographic diffuser through an optical system assembled to reduce the beam divergence. The light passing through the holographic diffuser was diffracted into a multiple-lobe diffused pattern. The transmitter was placed at a height of 60 cm and directed to the ceiling. The light was diffusely reflected from the ceiling toward the floor. Depending on the type of used holographic diffuser, four or six illuminated areas were generated on the ceiling where each one became a secondary distributed source of infrared radiation. A portable optical receiver facing the ceiling picked up the signal.

In this particular set of measurements, the emitted optical power was around 130 mW from the laser diode. The optical loss in the transmitter was around 4 dBo for the glass diffuser and around 3 dBo for the holographic diffuser and its corresponding optical subsystem. It should be noted, however, that using a proper optical packaging can reduce the optical path loss of a system employing holographic diffuser while the loss in the glass diffuser is inherent to the volume scattering mechanism in the glass. In fact, the loss in our system was mainly due to the optical subsystem that was used in conjunction with the holographic diffuser, and the loss of the holographic element itself was less than 0.5 dBo.

The optical receiver consisted of an interference filter of a 70 nm FWHM for filtering out the background fluorescent light and a 25 mm^2 -area avalanche photodiode (APD) with a large dynamic range. The receiver sensitivity was 10 nW providing power margins of more than 70 dB. The frequency response of the system was measured from dc to 300 MHz. The measurement results were calibrated by measuring the frequency response of the transmitter and receiver in a back-to-back configuration that is almost flat up to 300 MHz. The same calibration method, which was described in previous chapters, was used for these measurements again.

8.4 MEASUREMENT PROCEDURE

The objective of the experiment was to compare the performance of the holographic diffuser with the opal glass diffuser based on the spatial distribution of the received optical power and the channel delay spread. The frequency response of the channel was measured in two different rooms (room K and L), as shown in Figure 61 where the location of the transmitter is also shown. To find the spatial distribution of the desired channel parameters, the receiver was

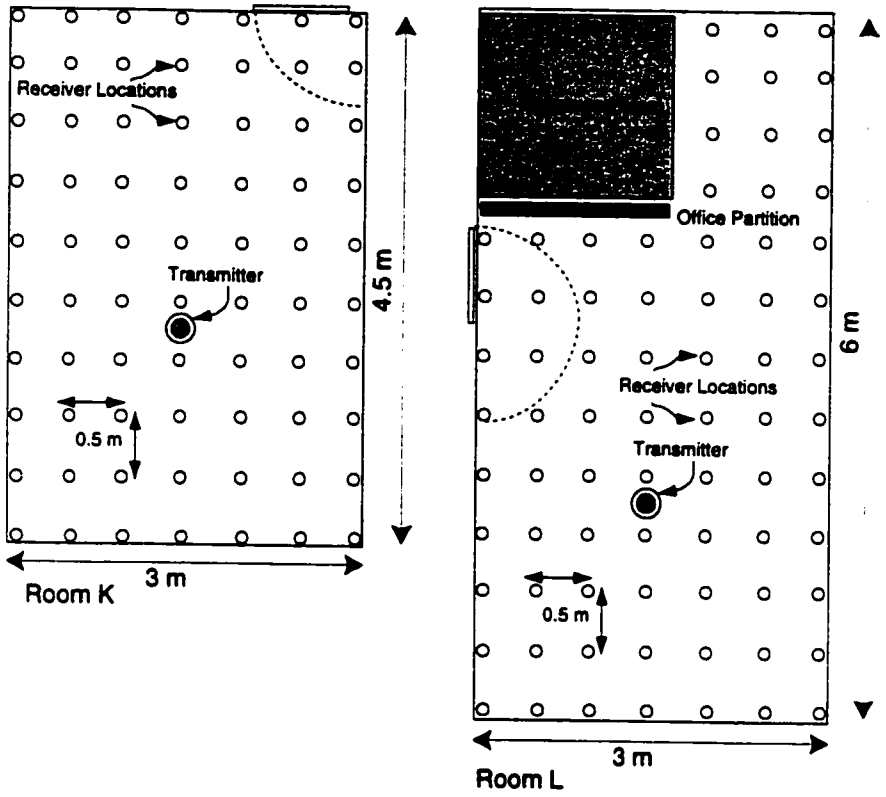

Figure 61. Two rooms were used for comparison between holographic diffuser and glass diffuser. In each room, the channel frequency response was measured in all the specified points. (70 points in room K and 91 points in room L). Tolerance of the system to shadowing was also investigated by using a partition as shown in the figure.

parameters, the receiver was moved in 0.5m steps in both directions on a grid pattern that covered the entire room. The height of the receiver was 1 m and it faced the ceiling.

In room K, one set of data was collected using a glass diffuser and the second set corresponds to the six-lobe holographic diffuser. In room L, results for two four lobe holographic diffusers with different angles between the lobes are reported. There are also reports on two sets of measurements collected by using the glass and holographic diffusers without using an optical filter at the receiver. Removing the optical filter from the receiver increases its FOV and changes the results accordingly. Therefore, in summary, room L results contain two sets of measurements with the glass diffuser, with and without filter; two sets using a six-lobe

holographic diffuser, with and without filter, and two sets of data using two different four-lobe holographic diffusers with an optical filter.

The Lambertian radiation pattern generated by the glass diffuser illuminates the entire ceiling, making it a distributed power source with more power coming from the ceiling area that is right above the transmitter. This enhances the shadowing problem in the corners. The holographic diffuser generated multiple secondary sources of radiation on the ceiling which are also different in their physical locations. Looking to the ceiling through an infrared camera, these secondary sources of infrared energy can be seen as bright circles with radiuses of around 30cm for our holographic diffusers. Therefore, it is more unlikely for a shadower to block all the power coming from these multiple sources. This is in effect, a form of transmission diversity. It generates a better spatial distribution of power and reduces the chance of blockage of all the received optical power. To examine the shadowing problem, an office partition was placed in the corner of room L, as shown in Figure 61. For all the points affected by shadowing (as marked in this figure), the channel transfer function is recorded. The recording was done using both the glass diffuser and the holographic diffuser. The effect of shadowing was compared for the two diffuser types.

8.5 MEASUREMENT RESULTS

The results of the measurements are plotted in Figure 62 to Figure 68. Each figure consists of six plots. The first row of plots represents the spatial distribution of the received optical power and the delay spread. These two plots show how changing the diffuser affects the pattern of the received power and the delay spread.

The second row contains the cumulative distribution of the same two parameters. The statistical parameters derived from these distributions are printed in the corner of each plot. The average, the standard deviation (std) and also the 10^{th} percentile (90^{th} percentile for the delay spread) are shown in each graph. The physical meaning of 10^{th} percentile for the power distribution is that 10 percent of the room area receive an amount of power that is smaller than the 10^{th} percentile mentioned in the graph. For the delay spread, it could be said that 90 percent of the room area has delay spread that is smaller than the indicated number on the delay spread graph.

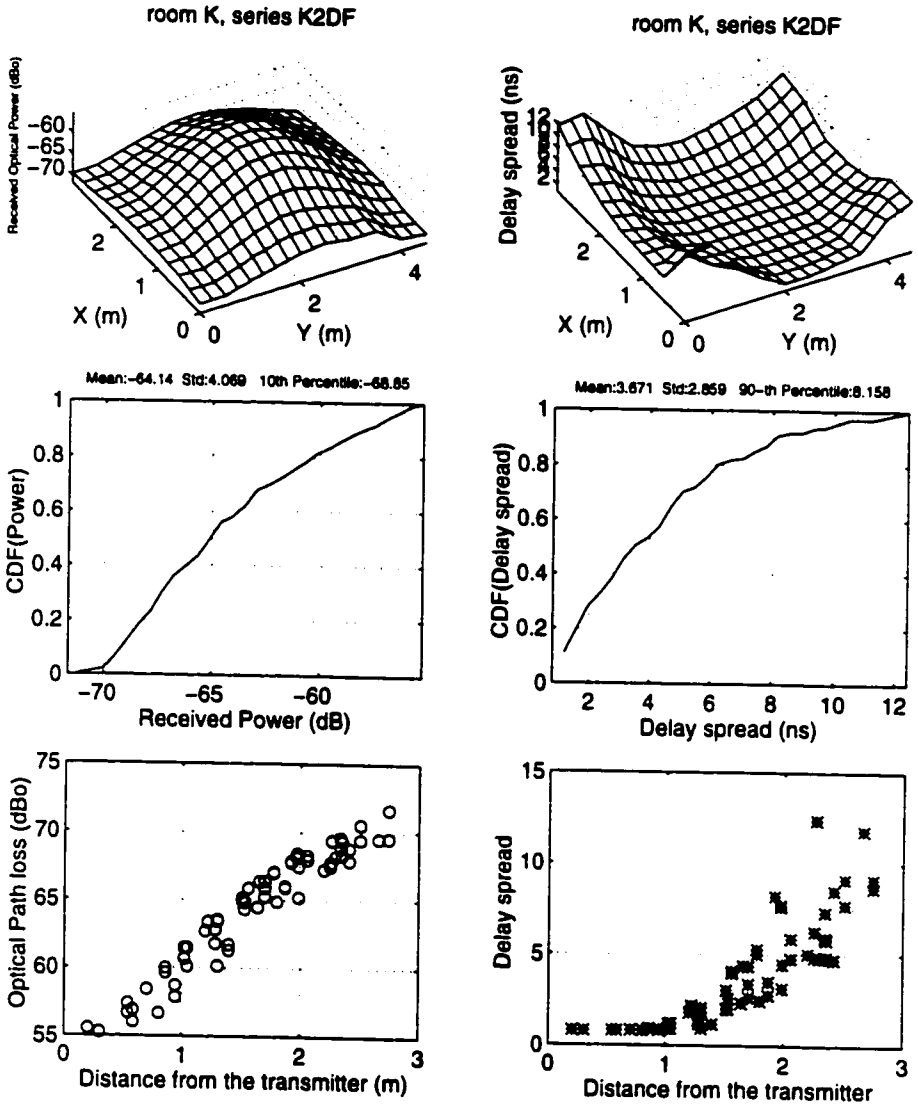

Figure 62. Received optical power and the channel delay spread for room K using a glass diffuser. The two plots on the first row are the spatial distributions of these parameters. The second row plots correspond to the cumulative distribution of these parameters. Some statistical parameters are also mentioned on the title of these graphs. The third row is a plot of these parameters versus the distance between the transmitter and the receiver.

The third row contains the values of the measured parameters versus the distance between the transmitter and the receiver. This distance is defined to be the smallest direct path between the location of the transmitter and the location of the receiver. In an ideal case, we would like the

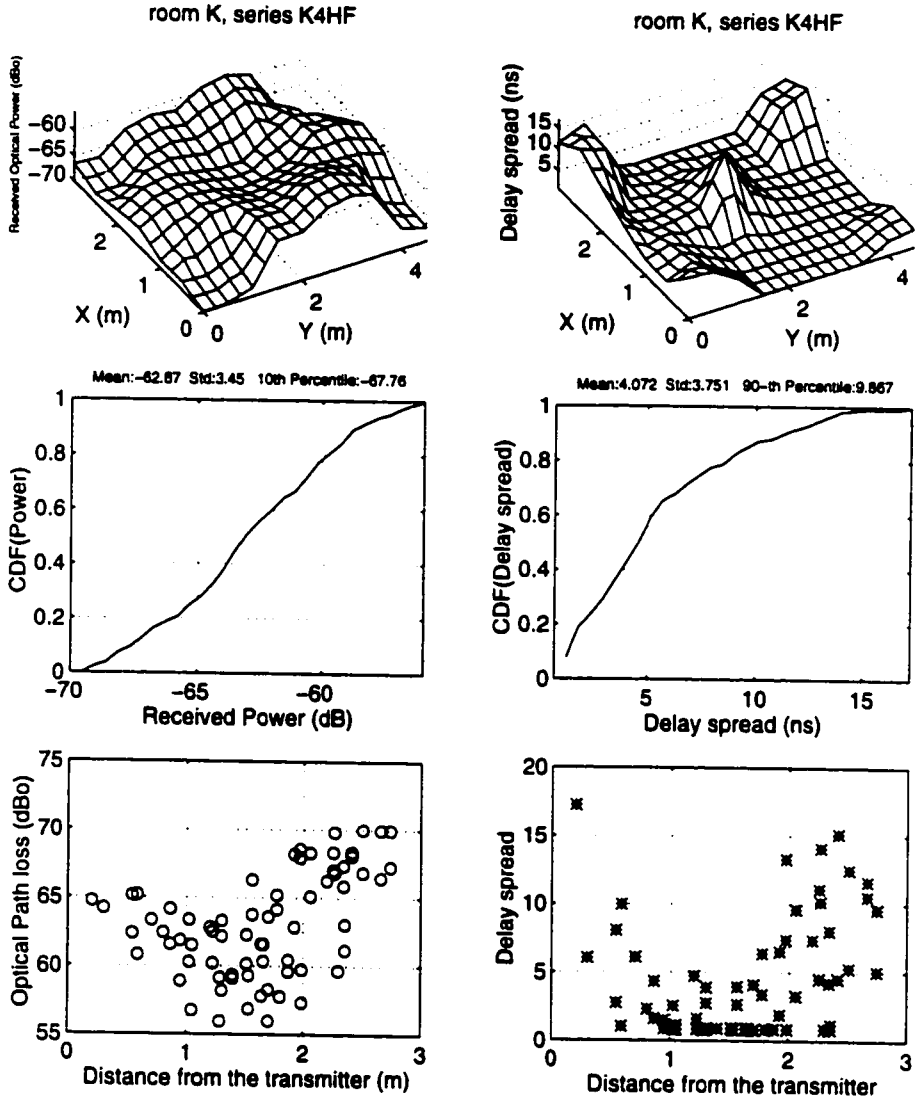

Figure 63. The received optical power and the channel delay spread for room K using a six-lobe holographic diffuser. The two plots on the first row are the spatial distributions of these parameters. The second row plots correspond to the cumulative distribution of these parameters. Some statistical parameters are also mentioned on the title of these graphs. The third row is a plot of these parameters versus the distance between the transmitter and the receiver.

channel parameters to be insensitive to the distance between the transmitter and the receiver. These graphs show how close are the measured results to the ideal case using different diffusers.

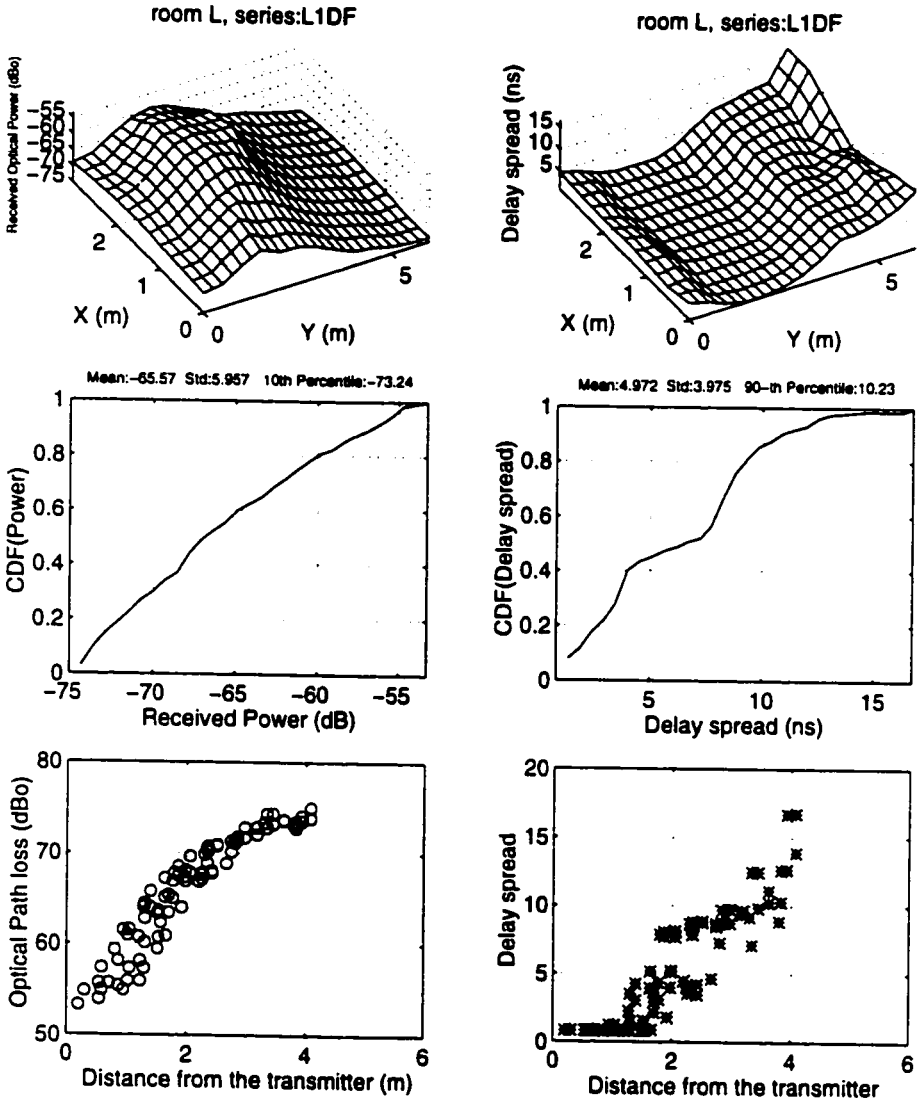

Figure 64. The received optical power and the channel delay spread for room L using a glass diffuser. The two plots on the first row are the spatial distributions of these parameters. The second row plots correspond to the cumulative distribution of these parameters. Some statistical parameters are also mentioned on the title of these graphs. The third row is a plot of these parameters versus the distance between the transmitter and the receiver.

The results for room K are shown in Figure 62 and Figure 63. The received optical power distribution has a smooth shape with a peak at the center when the glass diffuser is used. Using

the holographic diffuser results in multiple smaller peaks distributed in the room. Therefore, the variance of the power distribution is smaller when the holographic diffuser is used. It is also seen that in this particular case, there is an improvement of about 2 dBo in the average and 1 dBo in the 10^{th} percentile of the received optical power. The delay spread for the two cases has some noticeable change in terms of spatial distribution and the average is slightly higher when the holographic diffuser is used.

The results for room L when a filter is used are shown in Figure 64 to Figure 66. Again, the change in the pattern of the received optical power and the delay spread could be seen on the graphs. Since the optical filter has a limited field-of-view (FOV), the spatial distribution of the received optical power is approximately following the illuminated pattern on the ceiling. The peaks occur when the receiver is below a brighter spot on the ceiling. The performance degrades when it moves towards the corners. Comparing the results obtained by using the holographic diffusers in room L with the glass diffuser results, it is seen that the six-lobe holographic diffuser increases the average received optical power by about 1.3 dBo. The 10^{th} percentile of the received power increases by about 2.4 dBo. That means an improvement of at least 2.4 dBo in the received optical power for more than 90% of the room area.

The corresponding gains in the received optical power when a four lobe holographic diffuser is used are 1.4 dBo and 1.7 dBo, respectively. This is a very good advantage in terms of power efficiency. Note that, although the average delay spread of the channel in these configurations have increased compared to the glass diffuser case, the main reason of this increase is the receiver optical filter that was used in these measurement.

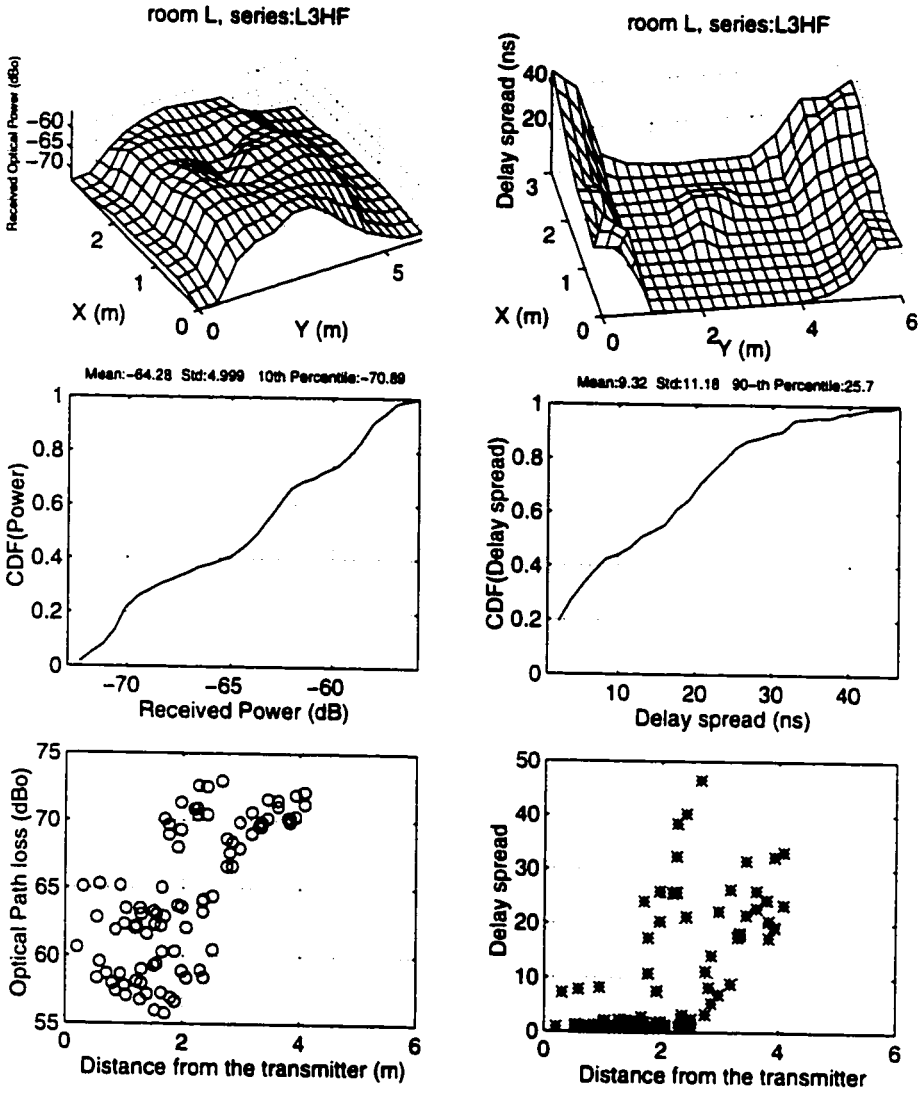

Figure 65. The received optical power and the channel delay spread for room L using a six-lobe holographic diffuser. The two plots on the first row are the spatial distributions of these parameters. The second row plots correspond to the cumulative distribution of these parameters. Some statistical parameters are also mentioned on the title of these graphs. The third row is a plot of these parameters versus the distance between the transmitter and the receiver.

The average delay spread of the system employing holographic diffuser would not be much more than that of a glass diffuser if the receiver has a wide FOV. The wide FOV could be achieved by employing a proper filter that is designed to provide a small optical line-width to reject the ambient noise and at the same time have a wide FOV.

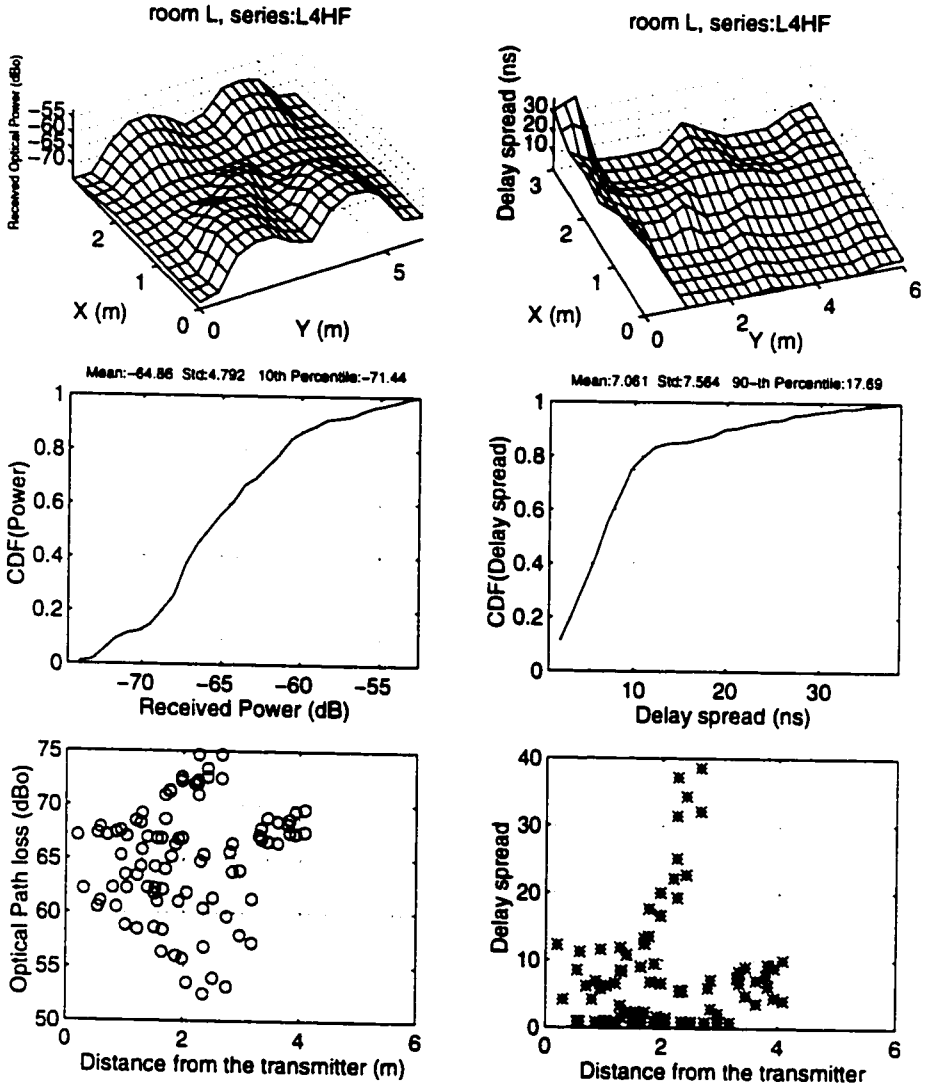

Figure 66. The received optical power and the channel delay spread for room L using a four-lobe holographic diffuser. The two plots on the first row are the spatial distributions of these parameters. The second row plots correspond to the cumulative distribution of these parameters. Some statistical parameters are also mentioned on the title of these graphs. The third row is a plot of these parameters versus the distance between the transmitter and the receiver.

Figure 67 and Figure 68 contain the measurement results for room L using the 6-lobe holographic diffuser and the glass diffuser without using optical filter at the receiver. The filter used in these experiments is a glass filter with a narrow FOV and a full width half magnitude wavelength of about 50 nm centered at 808 nm. The narrow FOV of the filter severely limits

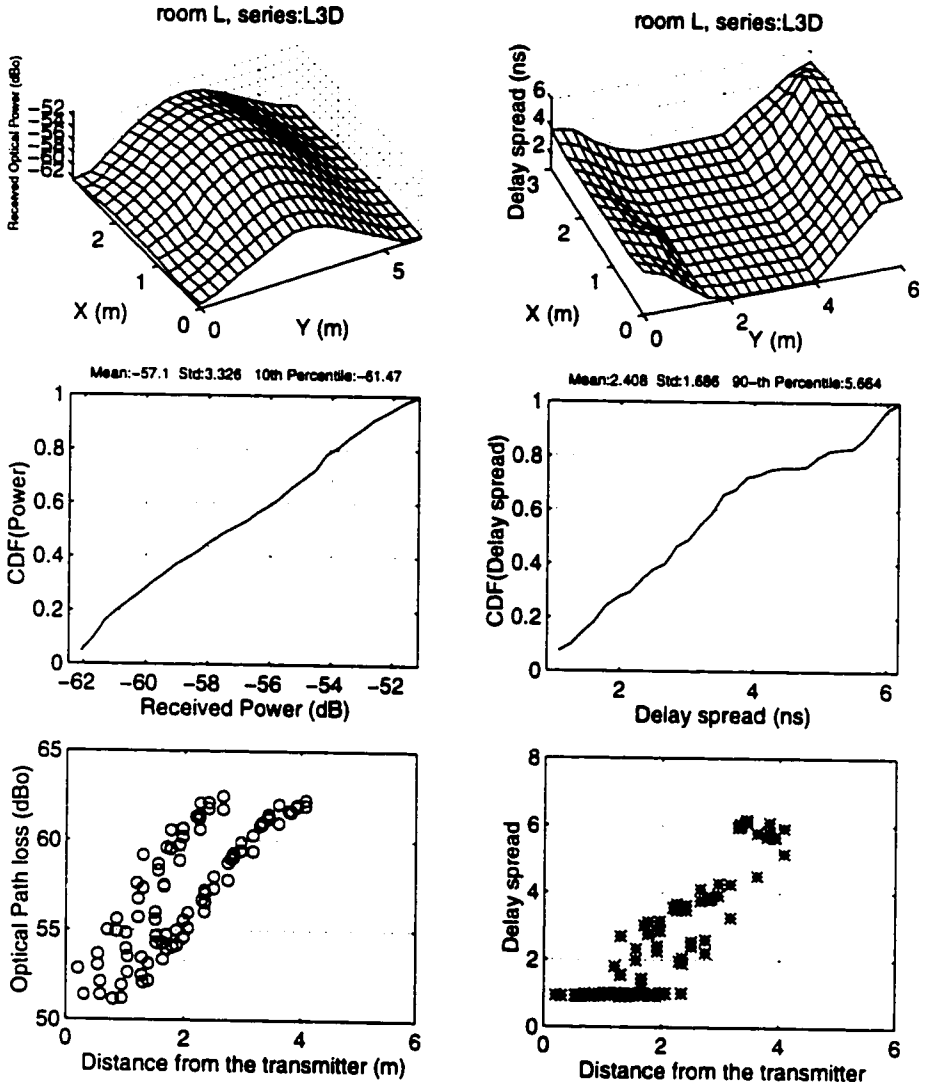

Figure 67. The received optical power and the channel delay spread for room L using a glass diffuser and without using the optical filter at the receiver. Top two plots show the spatial distributions of these parameters. The second row plots correspond to their cumulative distribution. Some statistical parameters are also mentioned on the title of these graphs. Plots in the third row show their variations versus the distance between the transmitter and the receiver.

the received optical signal and causes power loss as well as degradation in the impulse response shape that in turns increases the delay spread of the system. Much better filters can be designed for this application with wider FOV and lower attenuation [53].

The effect of the used filter is more severe for the holographic diffuser than it is for the glass diffuser. Therefore, a fair comparison between the two diffuser types should include a case where the receiver has a wide FOV. To do this comparison, the filter was removed. Since the removal of the filter increases the receiver FOV, it is observed that the spatial distribution of the received optical power has changed for the holographic diffuser case. In the corners, the receiver can see the brighter spots on the ceiling. Therefore, the received optical power distribution is smoother, and the delay spread is much smaller for the holographic case. In terms of power distribution, there is an increase of about 0.7 dBo on the average received optical power and 1.5 dBo in the 10^{th} percentile. The variance of the received optical power is also 1 dBo smaller for the holographic diffuser case, showing a smoother distribution of the received power across the room. The delay spread in this case is also much smaller when the holographic diffuser is used. For example, compared to the glass diffuser, there is a reduction of about 1.5 ns in the 90^{th} percentile of the delay spread when the holographic diffuser is used.

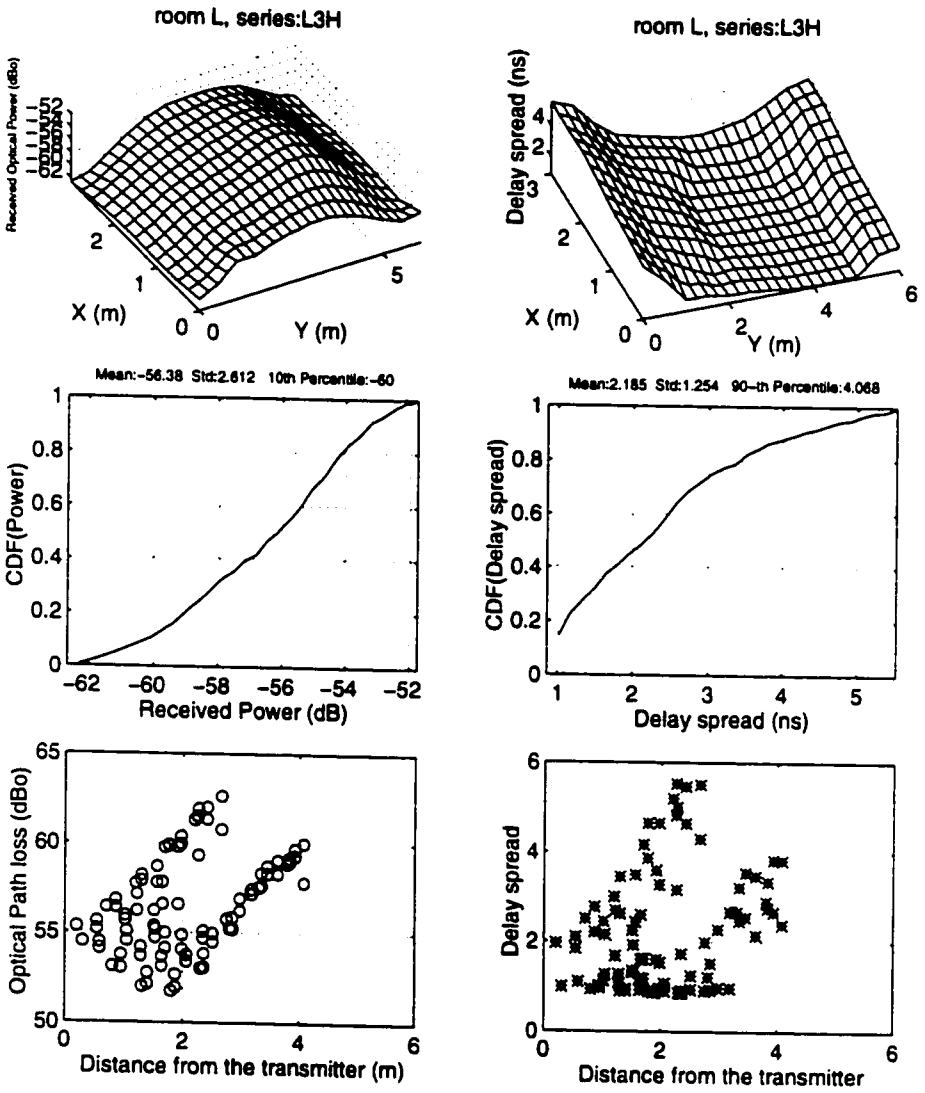

Figure 68. The received optical power and the channel delay spread for room L using a six-lobe holographic diffuser and without using the optical filter at the receiver. The two plots on the first row are the spatial distributions of these parameters. The second row plots correspond to the cumulative distribution of these parameters. Some statistical parameters are also mentioned on the title of these graphs. The third row is a plot of these parameters versus the distance between the transmitter and the receiver.

This clearly shows the benefits of having a combination of a properly diffused source with a wide FOV receiver. Such wide FOV receiver includes properly designed optical filters to make the system useful in the presence of the background radiation sources. This combination

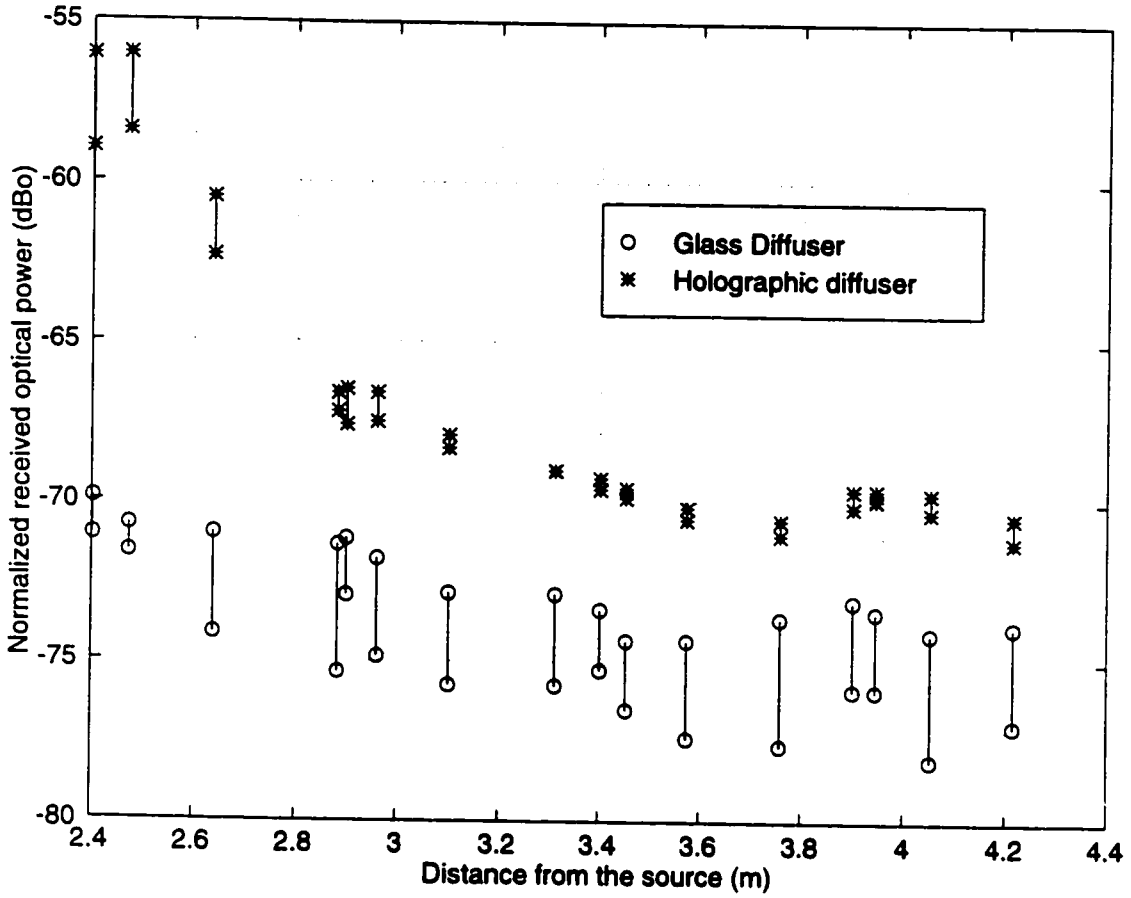

Figure 69. Effect of shadowing on the received optical power in the shadowed area of room L. The drop in the received optical power is more severe when a glass diffuser is used. The system that uses a holographic diffuser is more tolerant to shadowing.

increases the power efficiency of the system and reduces the delay spread. A summary of the results for the distribution of the received optical power in room K and room L is reported in Table 8.

The shadowing experiment shows another clear advantage for the holographic diffuser. For each of the points specified in shadowed area in Figure 61, the received optical power is measured in the presence and absence of the shadowing partition. The drop in the value of the received optical power due to partition shadowing is shown in Figure 69. The results show that the shadowed points had a drop in their received power from 2 dBo to 5 dBo when the glass diffuser was used. However, the same shadowing configuration resulted in a drop of 0.1 dBo

Room	Room K (without filter)		Room L (with filter)			Room L (without filter)	
Diffuser	Glass Diffuser	6-lobe Holographic Diffuser	Glass Diffuser	6-lobe Holographic Diffuser	4-lobe Holographic Diffuser	Glass Diffuser	6-lobe Holographic Diffuser
Average	-64.1	-62.9	-65.6	-64.3	-64.8	-57.1	-56.3
Maximum	-55	-55	-54	-50	-53	-51	-52
Minimum	-72	-68	-74	-72	-73	-62	-62
10^{th}	-68.9	-67.8	-73.3	-70.9	-71.5	-61.5	-60
Variance	4	3.4	6	5	4.8	3.3	2.6

Table 8. Normalized received optical power (in dBo) using holographic diffuser and glass diffuser.

to 2 dBo when the holographic diffuser was used. This could be intuitively understood by noting that the holographic diffuser generates multiple separate illuminated areas on the ceiling directed toward the corners. Having multiple sources and making them widely separated helps to reduce the probability of blocking the optical signal that is detected in the receiver.

8.6 SUMMARY AND CONCLUSIONS

Diffusers are needed to modify the radiation pattern of laser sources and provide an eye-safe radiation pattern. Glass diffusers are the most widely used type of diffusers and they provide a Lambertian radiation pattern which is not an optimal pattern for diffuse configuration. Holographic diffusers can be designed and used to provide more efficient radiation patterns. Two types of holographic diffusers are designed and built to verify the advantages of holographic diffusers. Measurements in two rooms were conducted to investigate the effects of the radiation patterns generated by these holograms and the results are reported. It is shown that the holographic diffusers provide more uniform distribution of optical power across the room and at the same time increase the resistance of the infrared link to shadowing. The latter is achieved by providing transmission diversity through multiple lobes of the radiation pattern.

CHAPTER NINE

9 CONCLUSION

9.1 SUMMARY OF RESULTS AND CONCLUSIONS

Design of an indoor broadband wireless system using infrared needs careful attention to the details of transmission and reception subsystems as well as detailed knowledge on the characteristics of the channel. To investigate the channel effects, a simulation algorithm that is well known in infrared literature is reviewed and its implementation details are discussed.

Using this simulation algorithm, it is shown that a proper design of such a system involves proper design of the transmission subsystem and proper arrangements of the transmitters and/or diffusers. Overall, it is shown that by using proper design and implementation of the transmission system, an improvement of 4 to 8 dBo in the received optical power can be achieved. Also, the channel delay spread and the dynamic range of the power can be made smaller by choosing proper configurations. The proposed configurations in Chapter 4 are just samples of possible choices and they just confirm the fact that a proper link design includes optimization of transmission arrangements. Depending on the applications and the environment type, configurations that use multiple diffused sources (ceiling mounted or table top) show better characteristics compared to simple one source diffused or LOS. Furthermore, when more than one transmitter is used, a proper power control algorithm can be used to turn-on only the desired optical sources. This can be thought as a transmission diversity that can save transmission power and reduce the risk of shadowing.

A wide-band measurement system that has been used to characterize the infrared channel has been described and its parameters have been summarized. Measurements have been performed to investigate the effects of receiver rotation, receiver displacement, shadowing and transmission configuration on the channel characteristics.

A database of channel transfer functions for 136 sets of rotation cases in 9 different rooms containing more than 5000 channel transfer functions has been collected. This database is used to show that the variation of channel path loss versus the receiver elevation angle has some general, room independent properties. It is shown that the receiver path loss is a smooth, predictable function of elevation angle and the location of its minimum can be predicted. A nonlinear curve-fitting algorithm can be used to interpolate between a few known values in any rotation set to find the path loss at every desired elevation angle. It was shown that this curve could be approximated by applying an enhancement algorithm on the results of the simple one-bounce simulation algorithm. It was demonstrated that the channel path loss and the channel delay spread are correlated values for a rotating receiver.

The effects of receiver displacement on the variation of the channel path loss and the channel delay spread were investigated in Chapter 6. Results of the simulation algorithm were presented and a general algorithm to enhance the accuracy of the one-bounce model was presented. The measurement results were used to show the accuracy improvements by using the proposed algorithm.

Shadowing measurement results are reported in Chapter 7. The relationship between the amount of expected drop in optical power and the receiver height, receiver to transmitter distance and the distance of the shadower to the receiver was described. The changes in the value of the channel delay spread in the presence of shadowing were also discussed and numerical results from the measurements were presented.

Chapter 8 contains the report on fabrication and use of holographic diffusers for shaping and diffusing the infrared light in an indoor infrared transmission system. The holographic elements have the advantage of lightweight and they could be designed and fabricated to match the required transmission parameters such as a given optical distribution pattern. They could also be inexpensively mass-produced and easily packaged. The reported measurements verified that employing a properly designed holographic diffuser could reduce the path loss of a non-directed optical link. Using these elements will also provide a uniform distribution of the received optical power in a given area. The results also demonstrated another advantage of

using the proposed holographic diffuser, which is the added tolerance of the link to shadowing.

9.2 SUGGESTIONS FOR FUTURE RESEARCH

The research on IR wireless access is far from being complete. There are many interesting problems, which need the attention of the scientific community for solution.

Starting from the solid state physics, more research is anticipated that could extend the efficiency of the semiconductor infrared lasers and provide more cost-effective manufacturing mechanisms to reduce the cost of these devices. Furthermore, proper use of holographic diffusers could allow a one-shot manufacturing process in which the diffusers are integrated as parts of the laser heads to provide optimum and eye-safe optical power distribution patterns. Improving the eye-safety of the transmission by using proper holographic diffusers with proper diffusing layers on them needs more investigation and practical experiments. Efficient, eye-safe and controlled transmission of infrared power is an essential issue for any cost-effective implementation of high-speed infrared communications systems.

Optical filters that are essential parts of the infrared receivers can also be enhanced to provide a smaller bandwidth while being less sensitive to the angle-of-arrival of the optical signal. The use of holograms as optical filters and concentrators could also provide revolutionary implementation mechanisms and cost-effectiveness to the infrared receivers.

On the system side, further research could provide better and more efficient coding and modulation schemes for the transmission and better detection on the receiver side. The use of trellis and turbo codes in conjunction with PPM or OOK modulation schemes needs further investigation. Also, efficient detection and equalization schemes may improve the power requirements of the transmission system and provide more margin to resist shadowing and background noise.

Infrared links are subject to shadowing and this is one of their weak aspects. If these are to be implemented for all-purpose indoor networking, the higher layers of the networking software should be able to handle interruptions in the data flow and deal with it properly. This demonstrates the need for further work on the software side of implementing networks based on infrared.

Investigation of the effects of channel rotation, displacement and shadowing can further be improved by collecting more information about the channel variation under broader set of environmental conditions. For example, the enhancement accuracy algorithms that were provided in chapters 5 and 6 could be verified for rooms with higher ceilings. This may not change the algorithm, but may change the derived parameters of the proposed polynomials.

APPENDIX A: VARIATION OF THE RECEIVED OPTICAL POWER FOR A ROTATED RECEIVER

The graphs in this appendix show the measured variation of the received optical power for a rotating infrared receiver in different rooms/conditions. They also include the results for the same conditions as reported by the simulation program and the peak-estimation technique developed in Chapter 4.

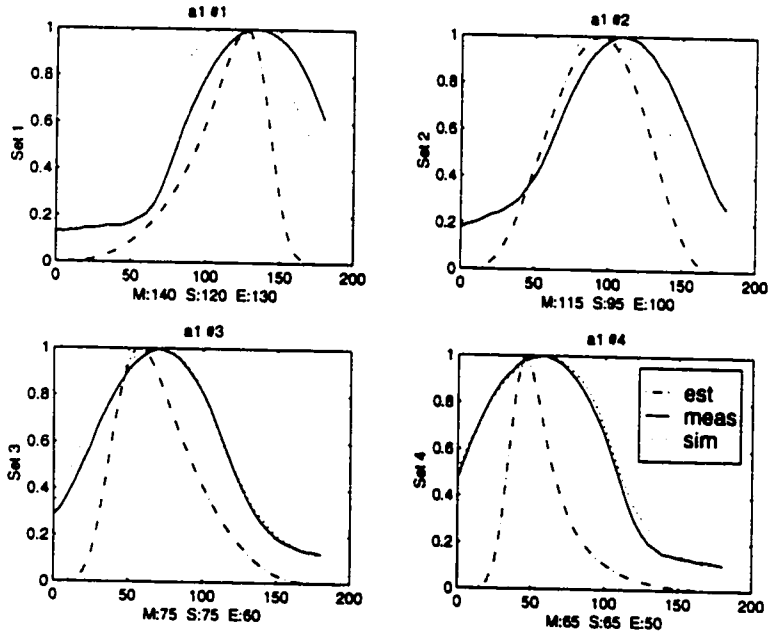

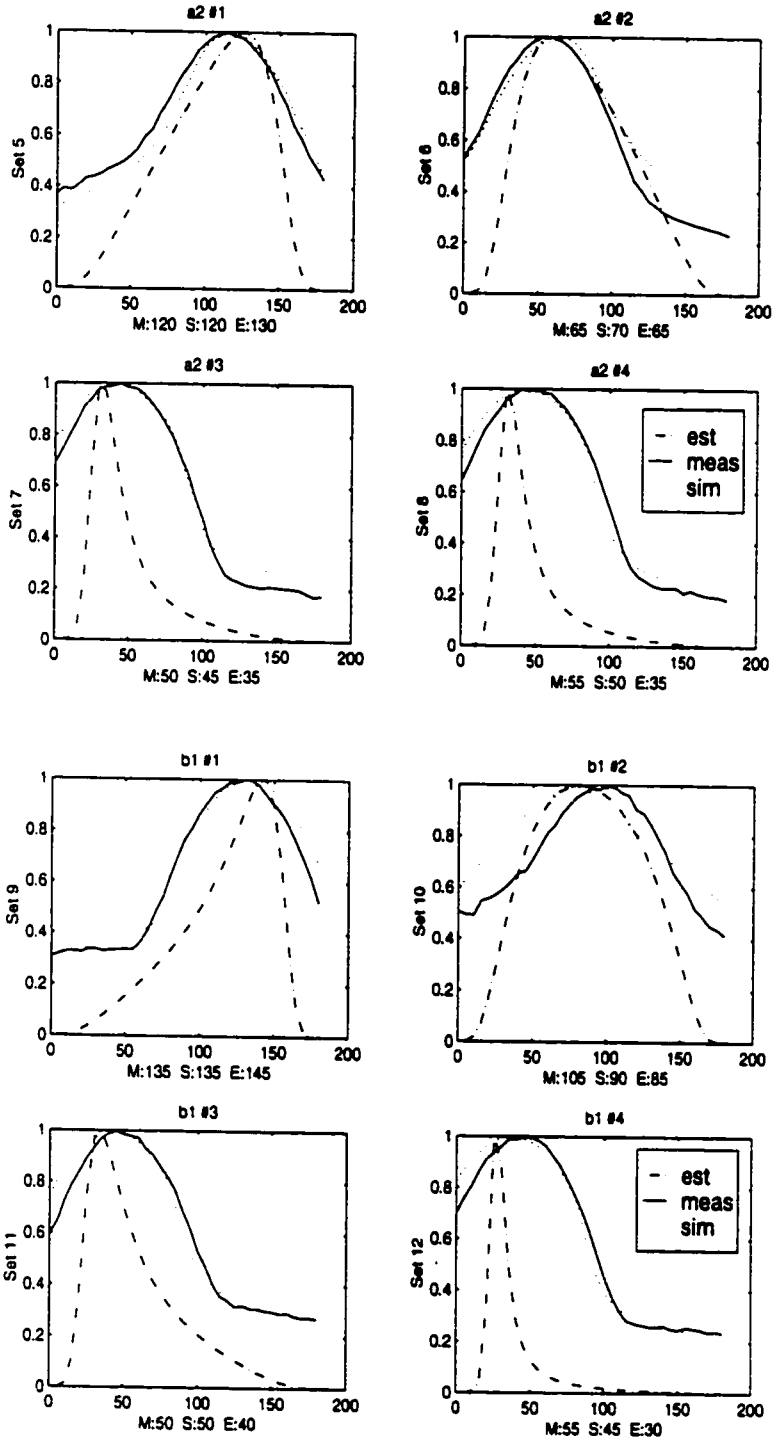
a2 #1
Set 5
M:120 S:120 E:130
a2 #2
Set 6
M:65 S:70 E:65
a2 #3
Set 7
M:50 S:45 E:35
a2 #4
Set 8
est
meas
sim
M:55 S:50 E:35
b1 #1
Set 9
M:135 S:135 E:145
b1 #2
Set 10
M:105 S:90 E:85
b1 #3
Set 11
M:50 S:50 E:40
b1 #4
Set 12
est
meas
sim
M:55 S:45 E:30

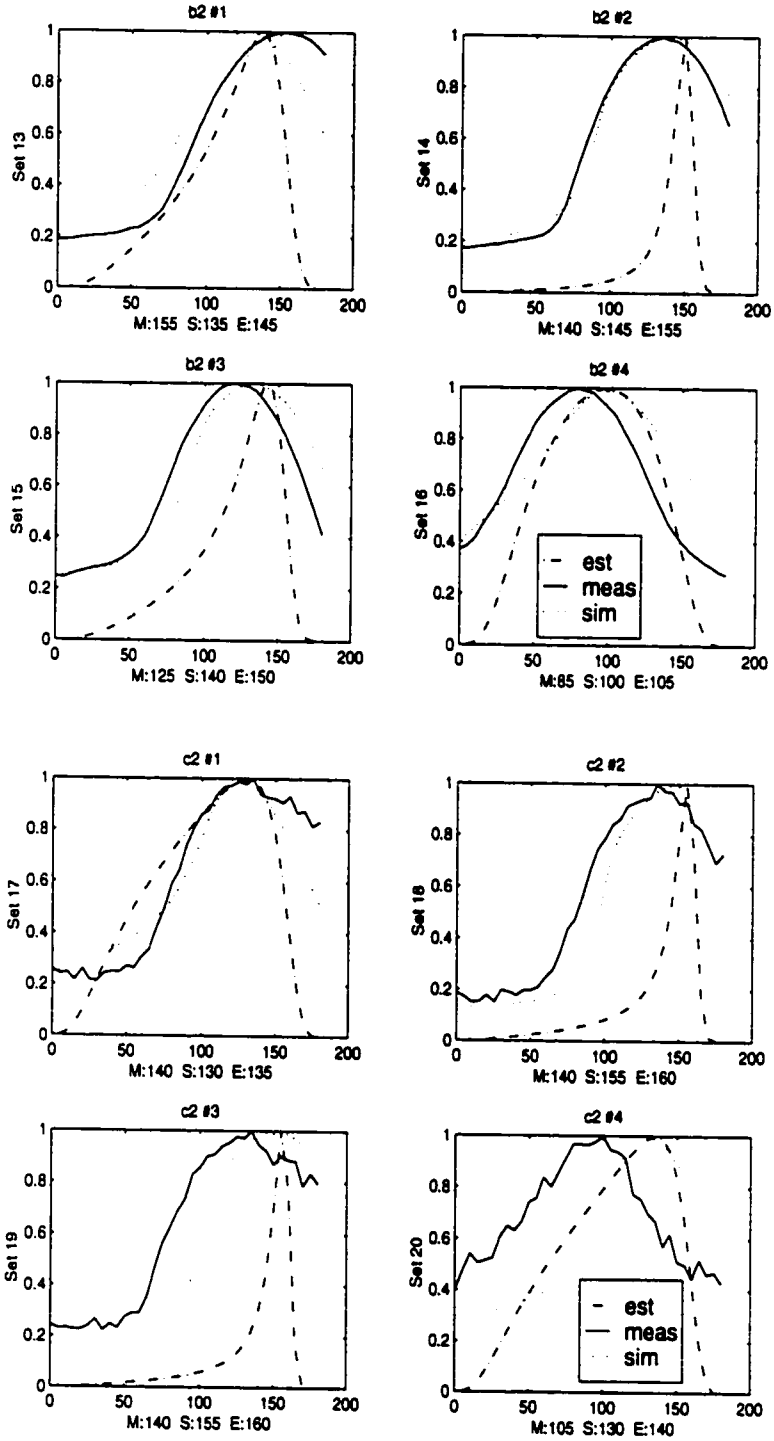
b2 #1
Set 13
M:155 S:135 E:145
b2 #2
Set 14
M:140 S:145 E:155
b2 #3
Set 15
M:125 S:140 E:150
b2 #4
Set 16
M:85 S:100 E:105
est
meas
sim
c2 #1
Set 17
M:140 S:130 E:135
c2 #2
Set 18
M:140 S:155 E:160
c2 #3
Set 19
M:140 S:155 E:160
c2 #4
Set 20
M:105 S:130 E:140

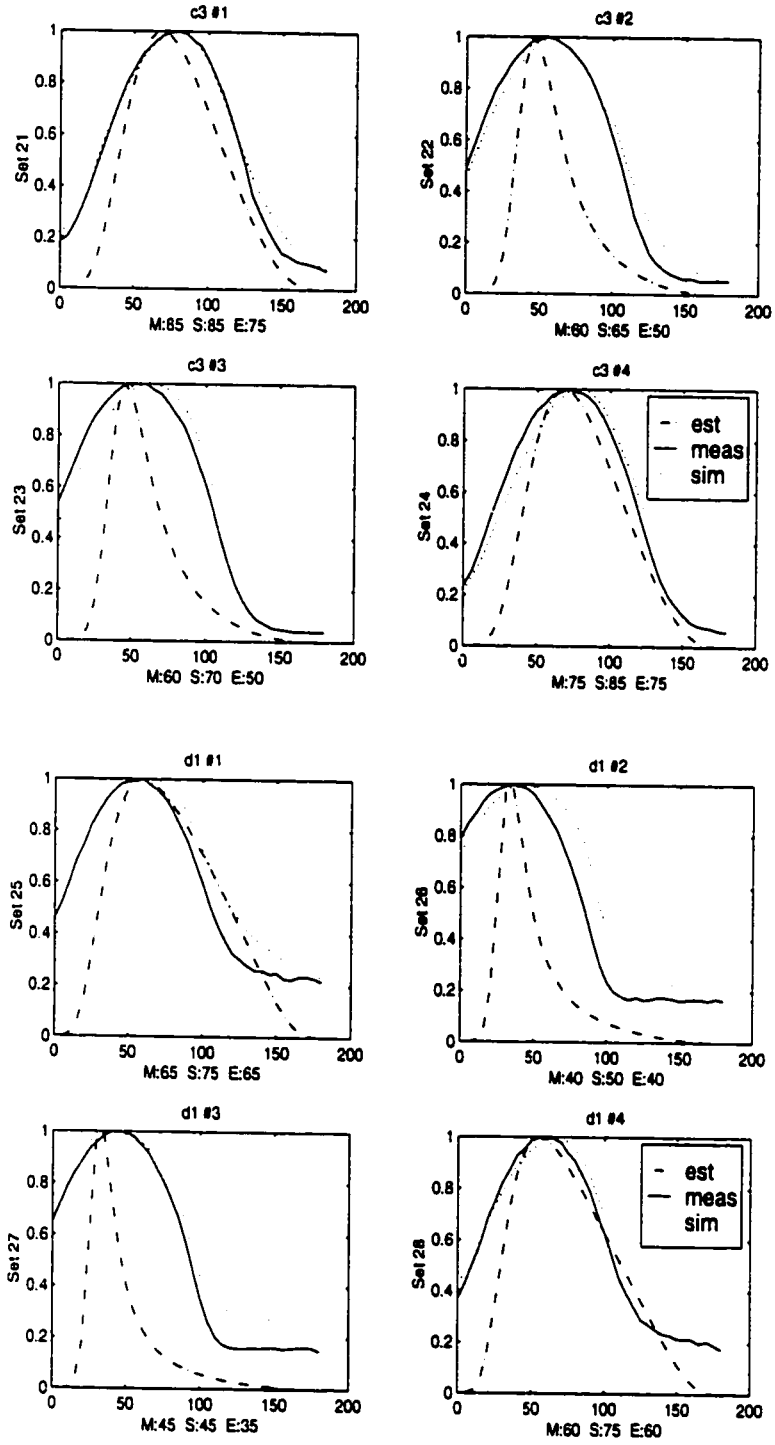
c3 #1
Set 21
M:85 S:85 E:75
c3 #2
Set 22
M:60 S:65 E:50
c3 #3
Set 23
M:60 S:70 E:50
c3 #4
Set 24
M:75 S:85 E:75
est
meas
sim
d1 #1
Set 25
M:65 S:75 E:65
d1 #2
Set 26
M:40 S:50 E:40
d1 #3
Set 27
M:45 S:45 E:35
d1 #4
Set 28
M:60 S:75 E:60
est
meas
sim

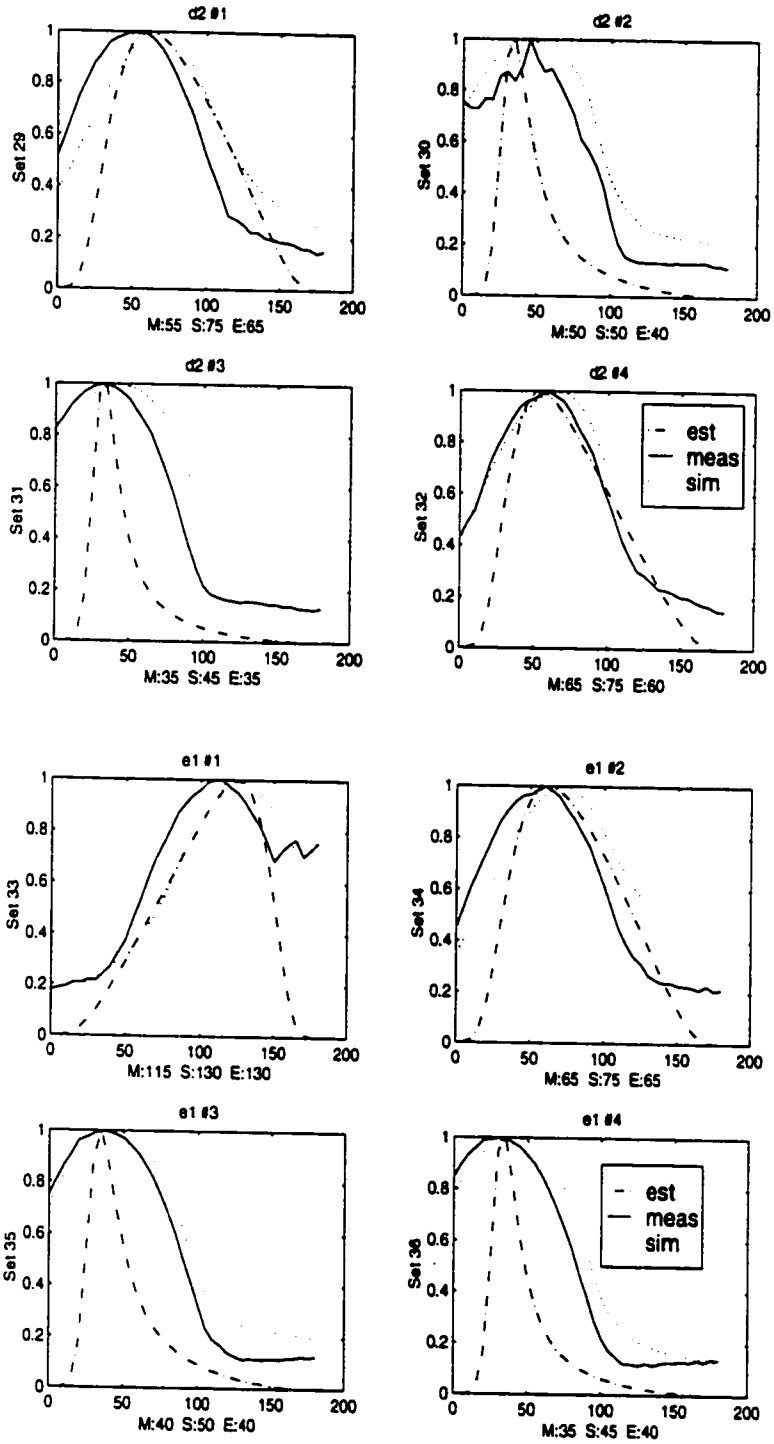
d2 #1
Set 29
M:55 S:75 E:65
d2 #2
Set 30
M:50 S:50 E:40
d2 #3
Set 31
M:35 S:45 E:35
d2 #4
Set 32
est
meas
sim
M:65 S:75 E:60
e1 #1
Set 33
M:115 S:130 E:130
e1 #2
Set 34
M:65 S:75 E:65
e1 #3
Set 35
M:40 S:50 E:40
e1 #4
Set 36
est
meas
sim
M:35 S:45 E:40

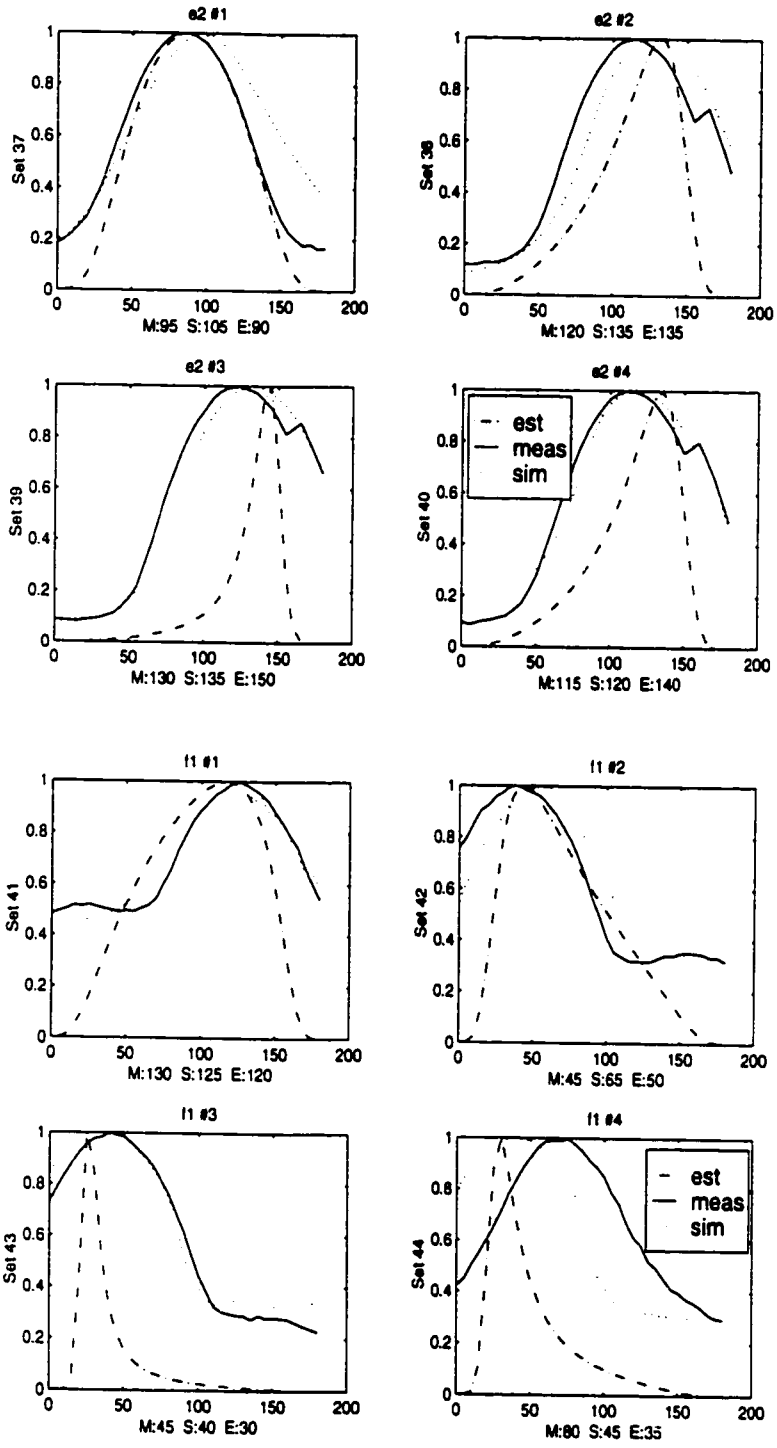
e2 #1
Set 37
M:95 S:105 E:90
e2 #2
Set 38
M:120 S:135 E:135
e2 #3
Set 39
M:130 S:135 E:150
e2 #4
Set 40
est
meas
sim
M:115 S:120 E:140
f1 #1
Set 41
M:130 S:125 E:120
f1 #2
Set 42
M:45 S:65 E:50
f1 #3
Set 43
M:45 S:40 E:30
f1 #4
Set 44
est
meas
sim
M:80 S:45 E:35

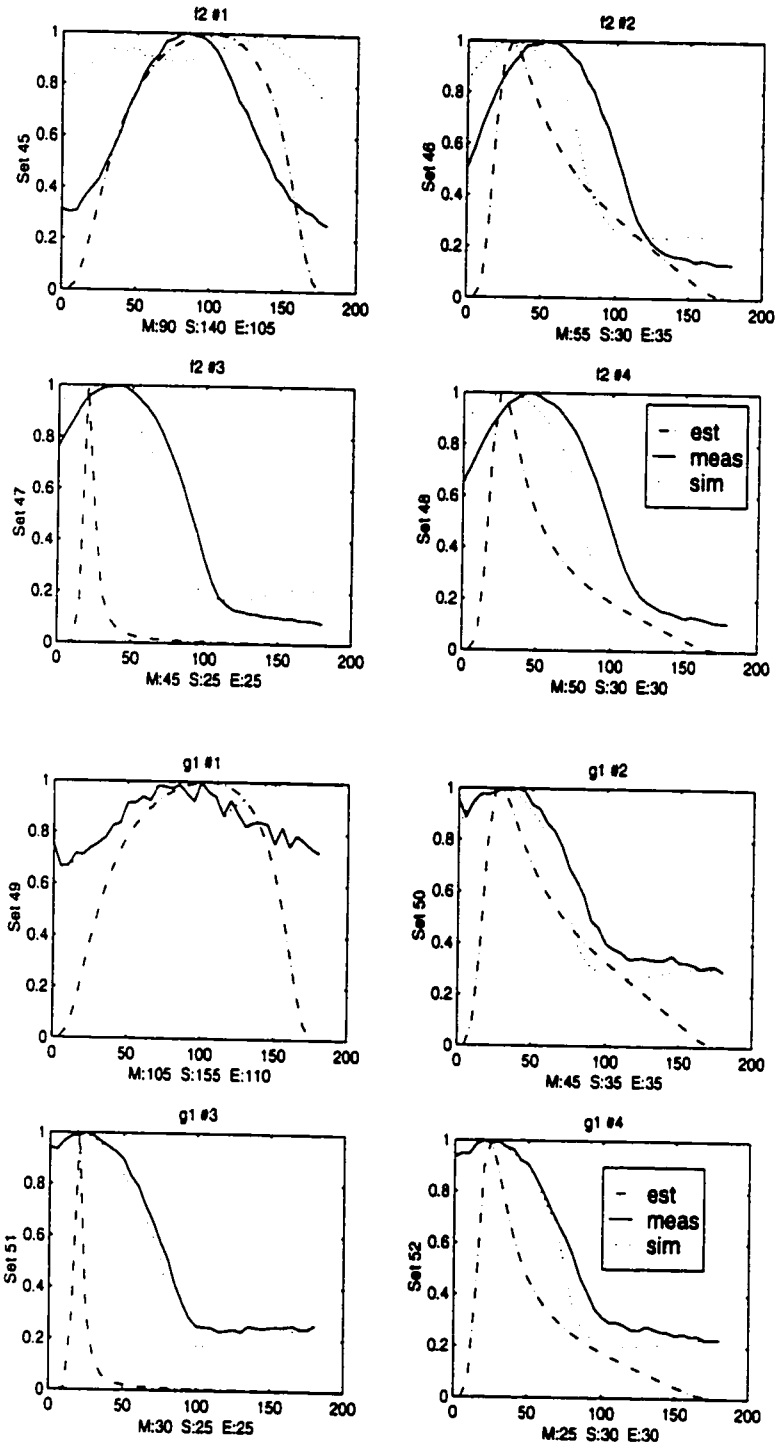
f2 #1
Set 45
M:90 S:140 E:105
f2 #2
Set 46
M:55 S:30 E:35
f2 #3
Set 47
M:45 S:25 E:25
f2 #4
Set 48
est
meas
sim
M:50 S:30 E:30
g1 #1
Set 49
M:105 S:155 E:110
g1 #2
Set 50
M:45 S:35 E:35
g1 #3
Set 51
M:30 S:25 E:25
g1 #4
Set 52
est
meas
sim
M:25 S:30 E:30

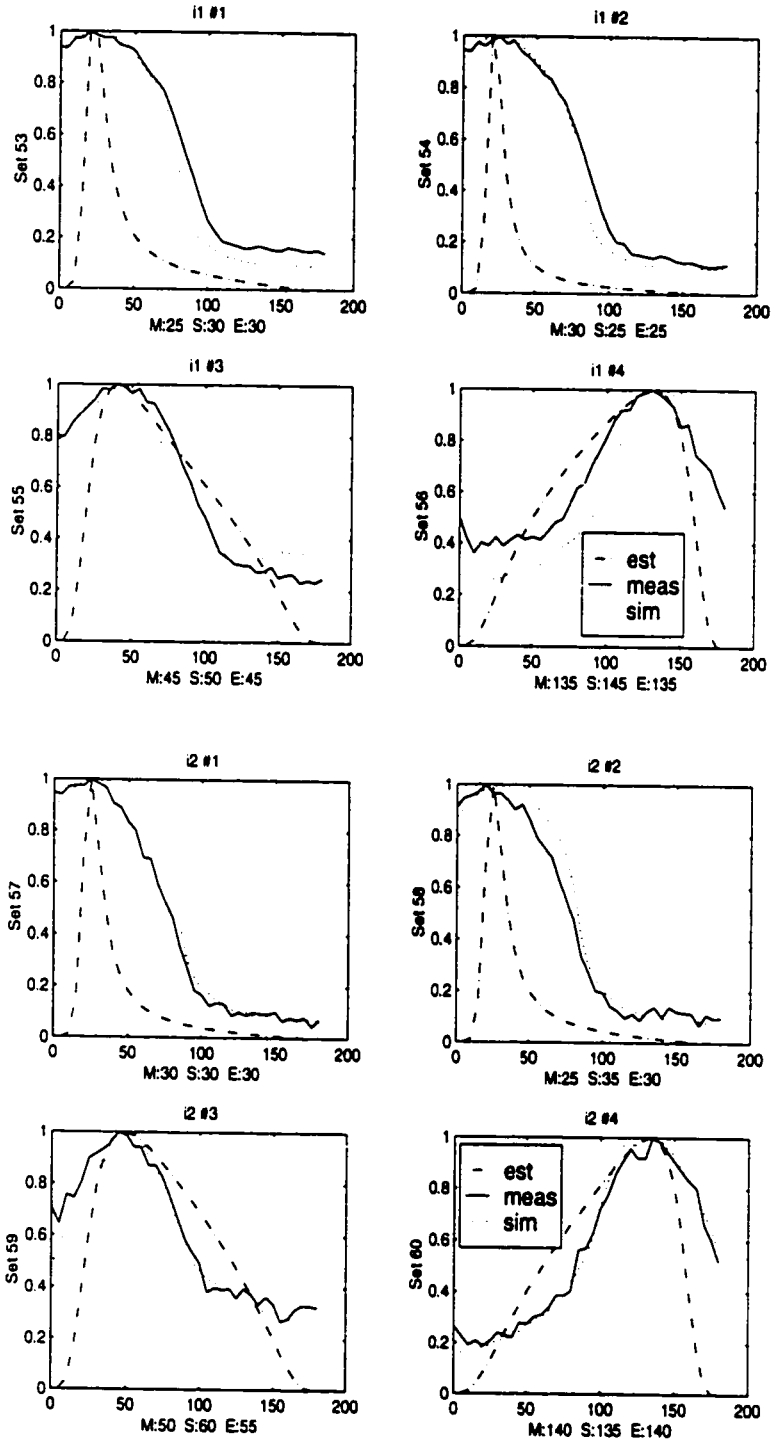
i1 #1
Set 53
M:25 S:30 E:30
i1 #2
Set 54
M:30 S:25 E:25
i1 #3
Set 55
M:45 S:50 E:45
i1 #4
Set 56
est
meas
sim
M:135 S:145 E:135
i2 #1
Set 57
M:30 S:30 E:30
i2 #2
Set 58
M:25 S:35 E:30
i2 #3
Set 59
M:50 S:60 E:55
i2 #4
Set 60
est
meas
sim
M:140 S:135 E:140

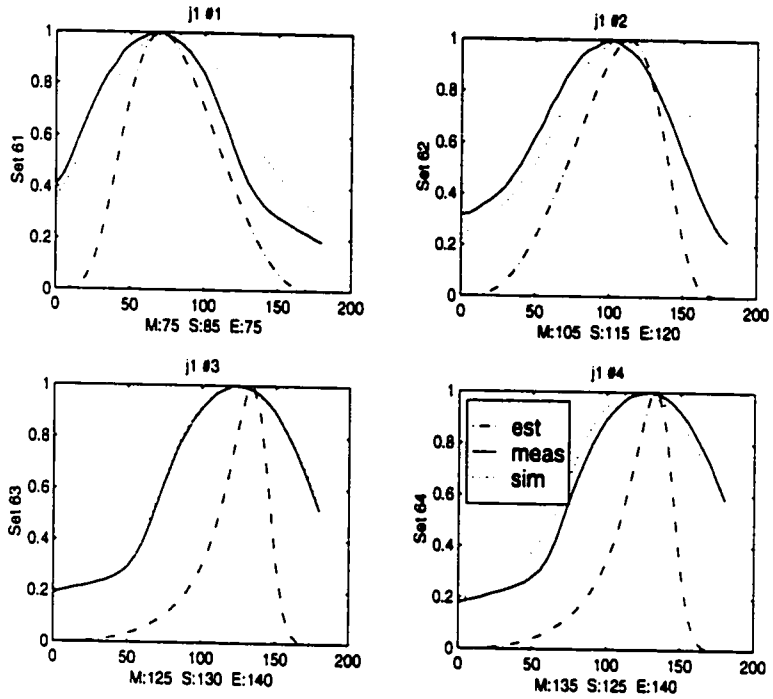
j1 #1
Set 61
M:75 S:85 E:75
j1 #2
Set 62
M:105 S:115 E:120
j1 #3
Set 63
M:125 S:130 E:140
j1 #4
Set 64
M:135 S:125 E:140
est
meas
sim

APPENDIX B: MESUREMENT SITES

This appendix contains the shapes and physical dimensions of the rooms that were used for the receiver rotation measurements. The location of the infrared source, receiver and the directions of receiver rotation are also shown in the graphs. Measurements are performed in the Colonel By (CBY) building at the main campus of the University of Ottawa. This building is the main building for engineering programs. The subsequent four letters specify the room number in the CBY building. For example, room A is specified by CBY: E015 that means the room E015 at the ground floor of the CBY building. Figures are intended to show the approximate size of the room and placement of the source and receiver. Not all objects inside the rooms are specified in the figures. A short description of the measurement environment provides important distinctive characteristics of each particular measurement site.

Room A

Height (m)	
Ceiling	2.55
Source	1.3
Receiver	1.0

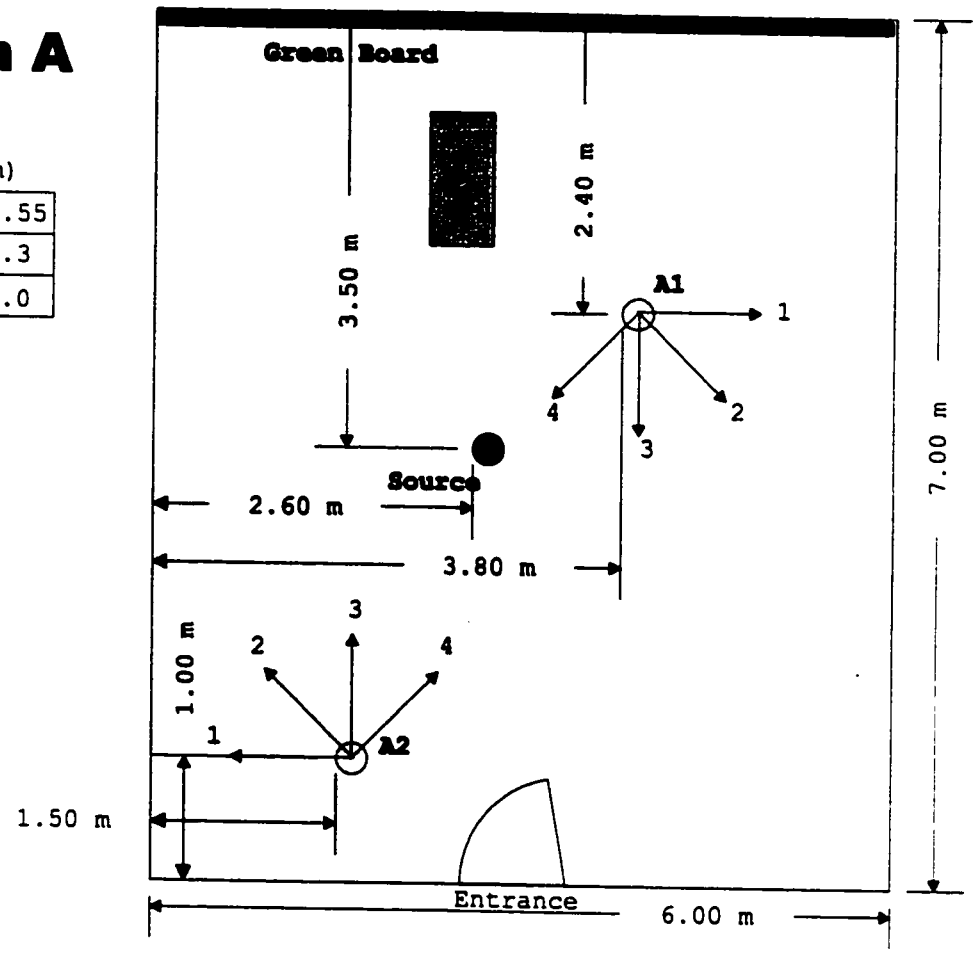

Room A (CBY E015)

A classroom with 5 rows of chairs, a total of 33 chairs for students. Walls are rough concrete type with yellowish color. Ceiling is flat with the same color. Green board extends over the entire width of the class. There are 16 flourescent lamps with transparent plastic covers on the ceiling each is 1.2m by 0.3m. In the diffuse measurements where the ceiling is illuminated by the infrared radiation, it seems that little energy is reflected from these covers and most of the received energy passes through the covers and is being absorbed. All office and class environments that are used for measurements have the same type of ceiling unless otherwise specified in the room description.

Room B

Height (m)	
Ceiling	2.65
Source	1.3
Receiver	1.0

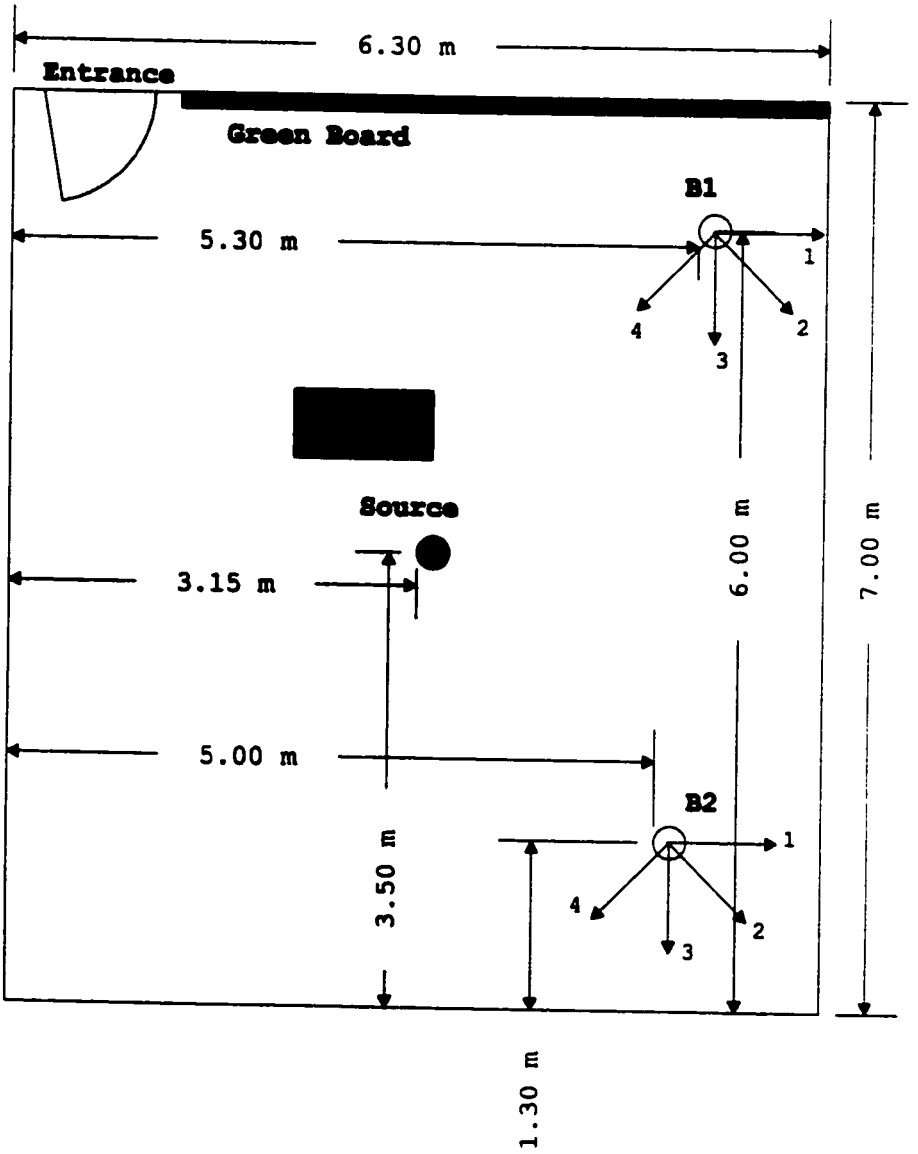

Room B (CBY E016)

A square shaped classroom with 4 rows of chairs, 8 chairs per row. A green board in one side of the room with the wall surface type being very similar to room A.

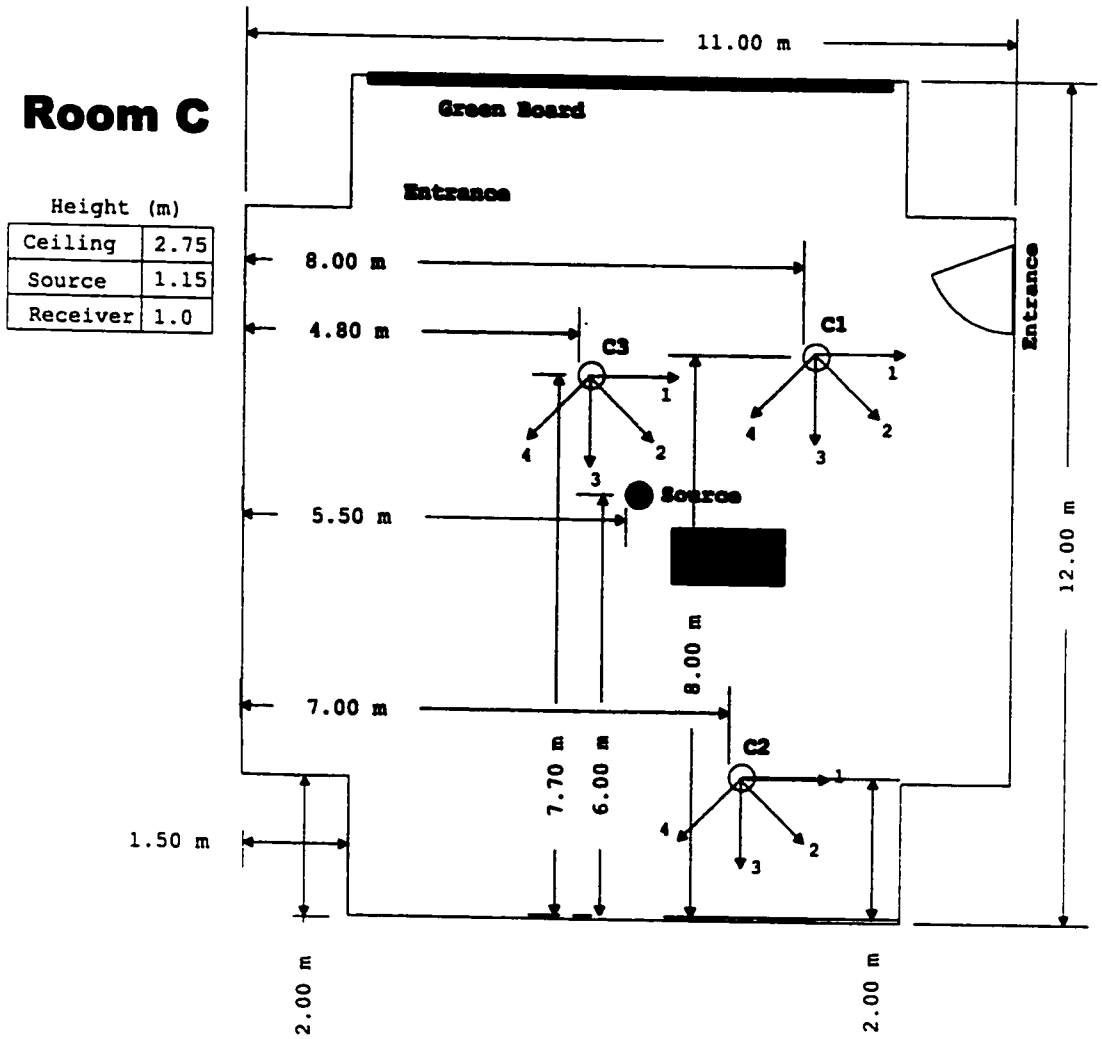

Room C (CBY D207)

A large square-shaped classroom with 9 rows of desks and chairs, a total of 110 chairs. Walls are rough surfaces painted in white.

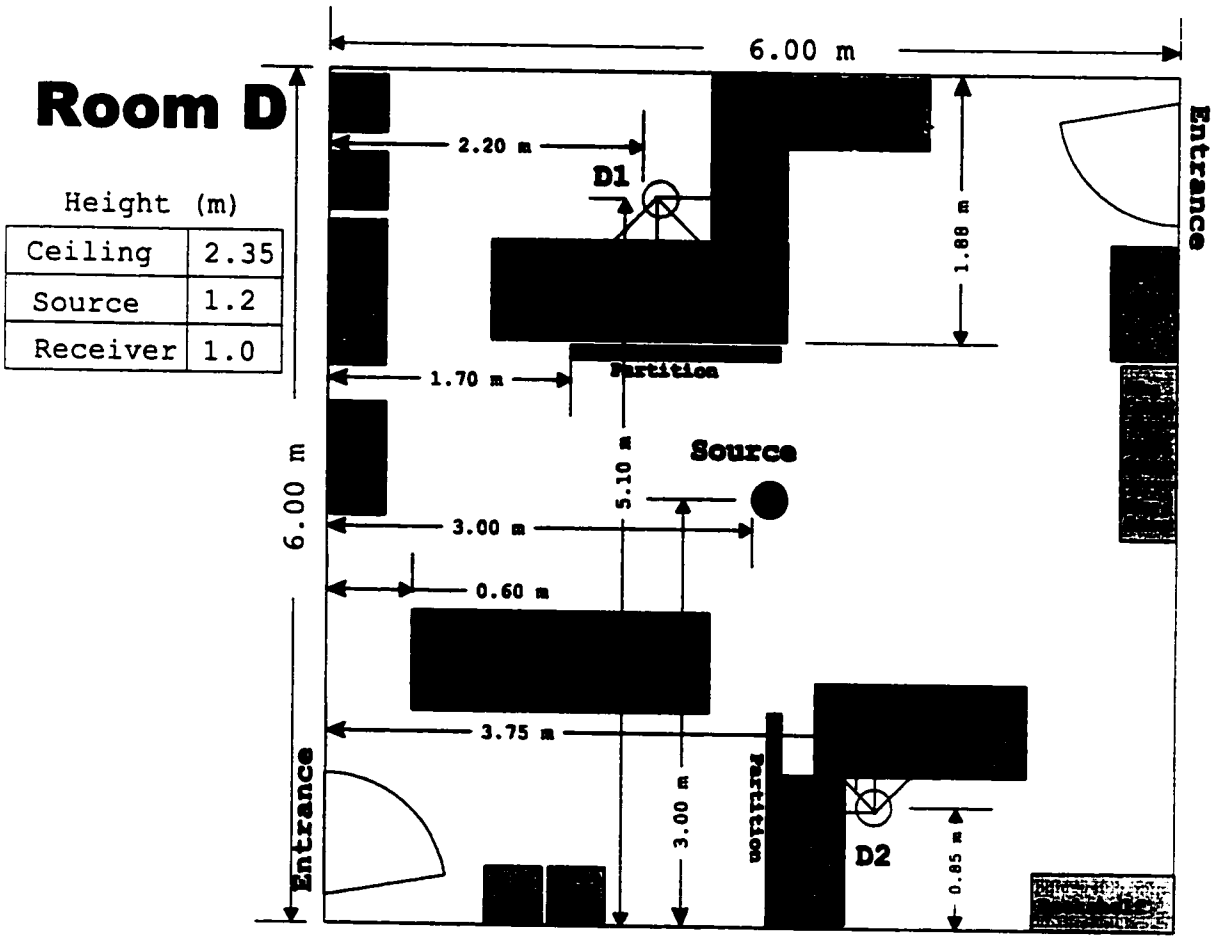

Room D (CBY A605)

An office environment for two secretaries. It is a crowded room with lots of office equipment such as filing cabinets, desks, chairs and computers. There are two partitions in the room as marked in the figure. Each partition is covered with orange colored clothing. There are narrow windows of width 25cm besides each door extending from the floor to the ceiling. In location D1, the partition is at the desk height and does not block the line of sight between the location of transmitter and the location of the receiver.

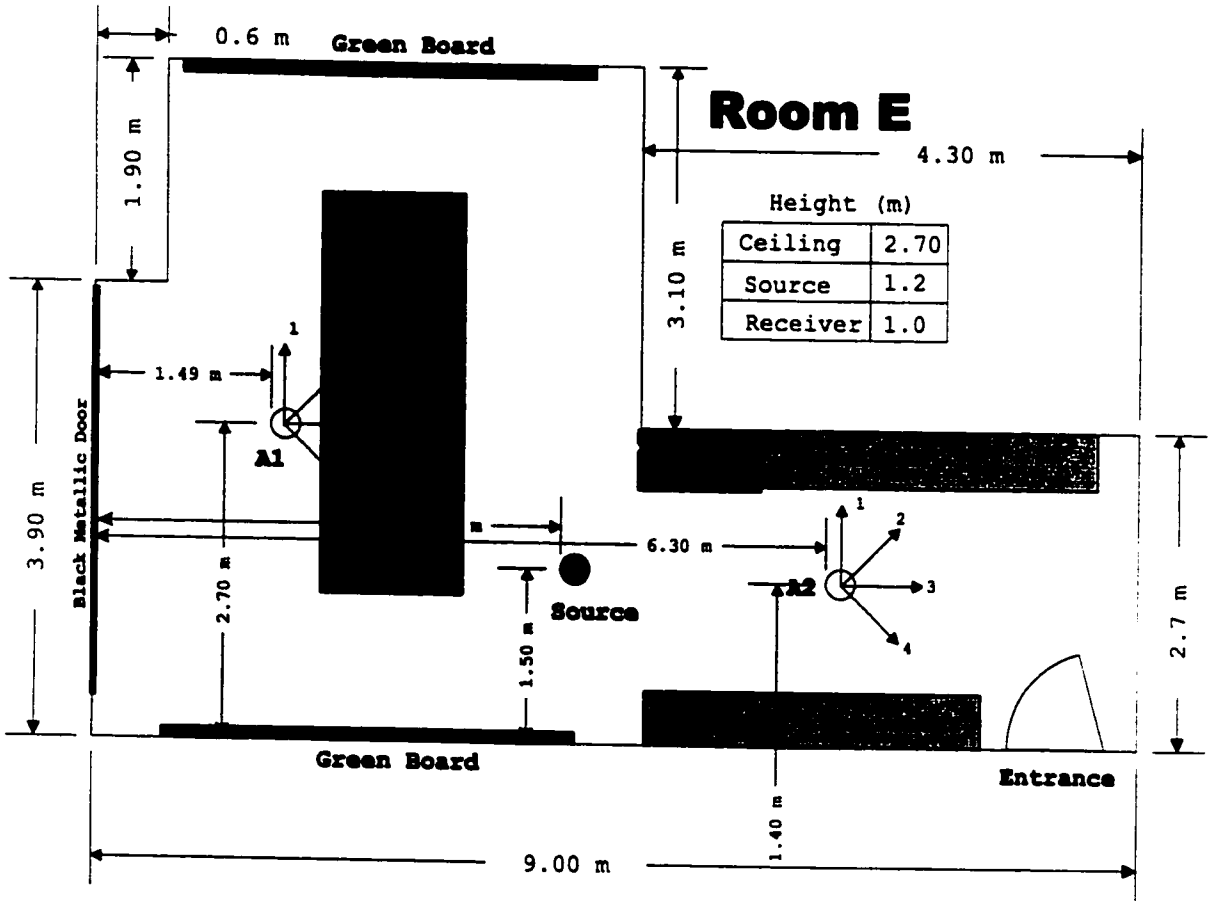

Room E (CBY C506)

A relatively small conference room with some bookshelves near the room entrance and a big conference table in the middle. There are green boards on two sides of the room as marked in the above figure. There is a metallic black door in one side of the room.

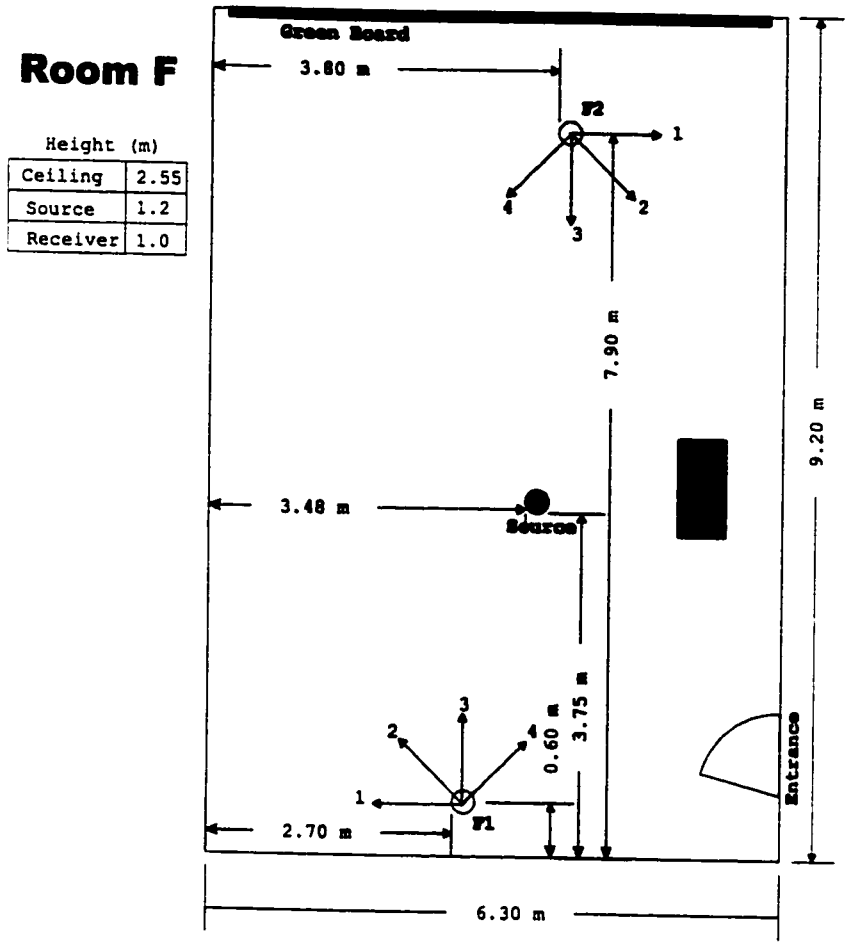

Room F (CBY B202)

A moderate size classroom with 7 rows of chairs and desks, and the capacity for 50 students. The wall to the left of entrance has a rough surface with yellowish color. Other walls have smooth surface but different colors. The east wall (right wall in figure) is white. The upper half of the west wall is white and the lower half is green. The north wall is covered by green board in half. The bottom part of the wall is white.

Room G

Height (m)

Ceiling	2.40
Source	1.3
Receiver	1.0

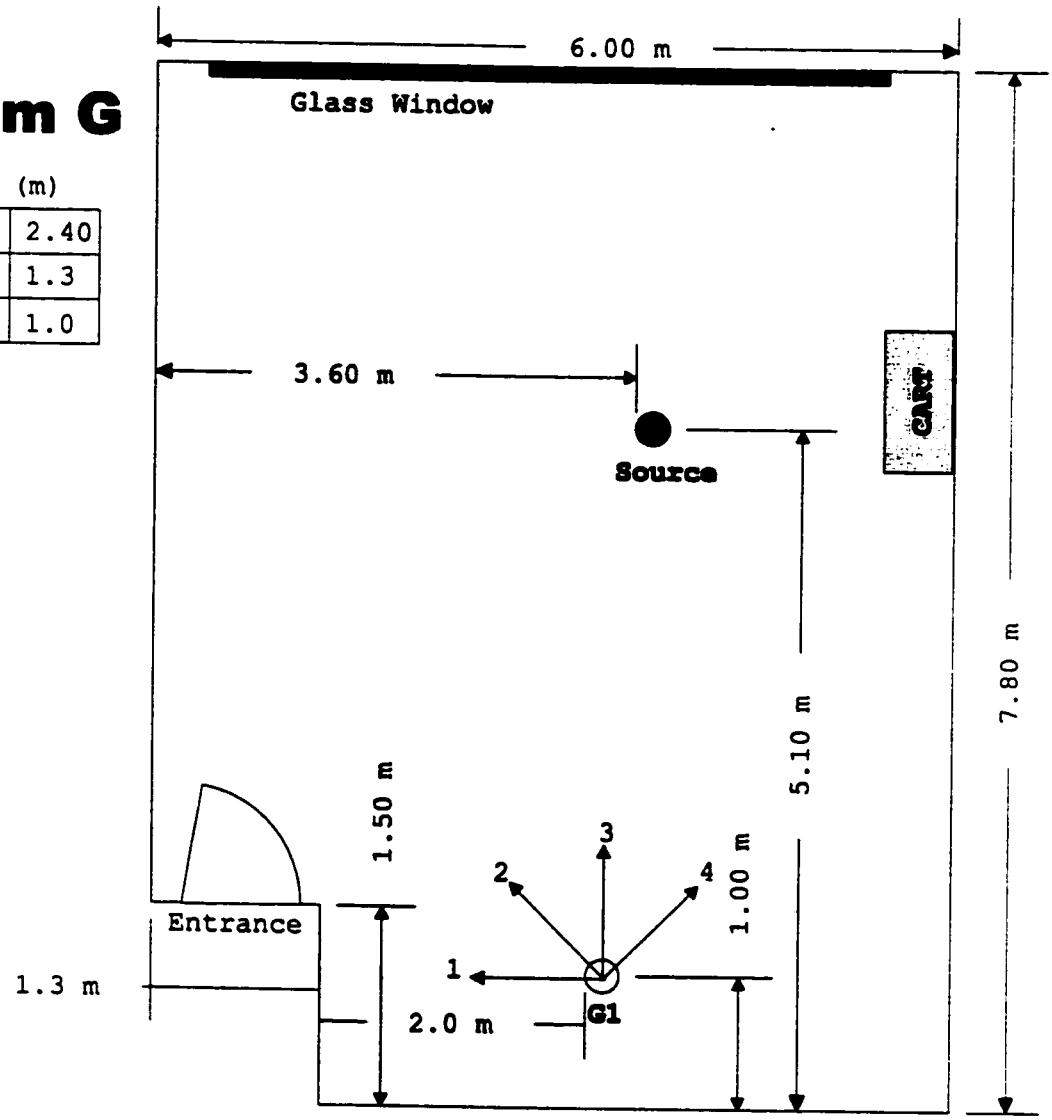

Room G (CBY 707A)

A relatively small lounge adjacent to a large conference room. Removable grey colored full-height partitions at the right side of the room build a wall that separate this lounge from the adjacent conference room. There are 12 comfortable chairs around a cofee table in the lounge. The floor is covered with blue color carpet and the windows that are shown in top and right wall of the figure cover half the wall height. During measurements, windows were covered with shades of grey color.

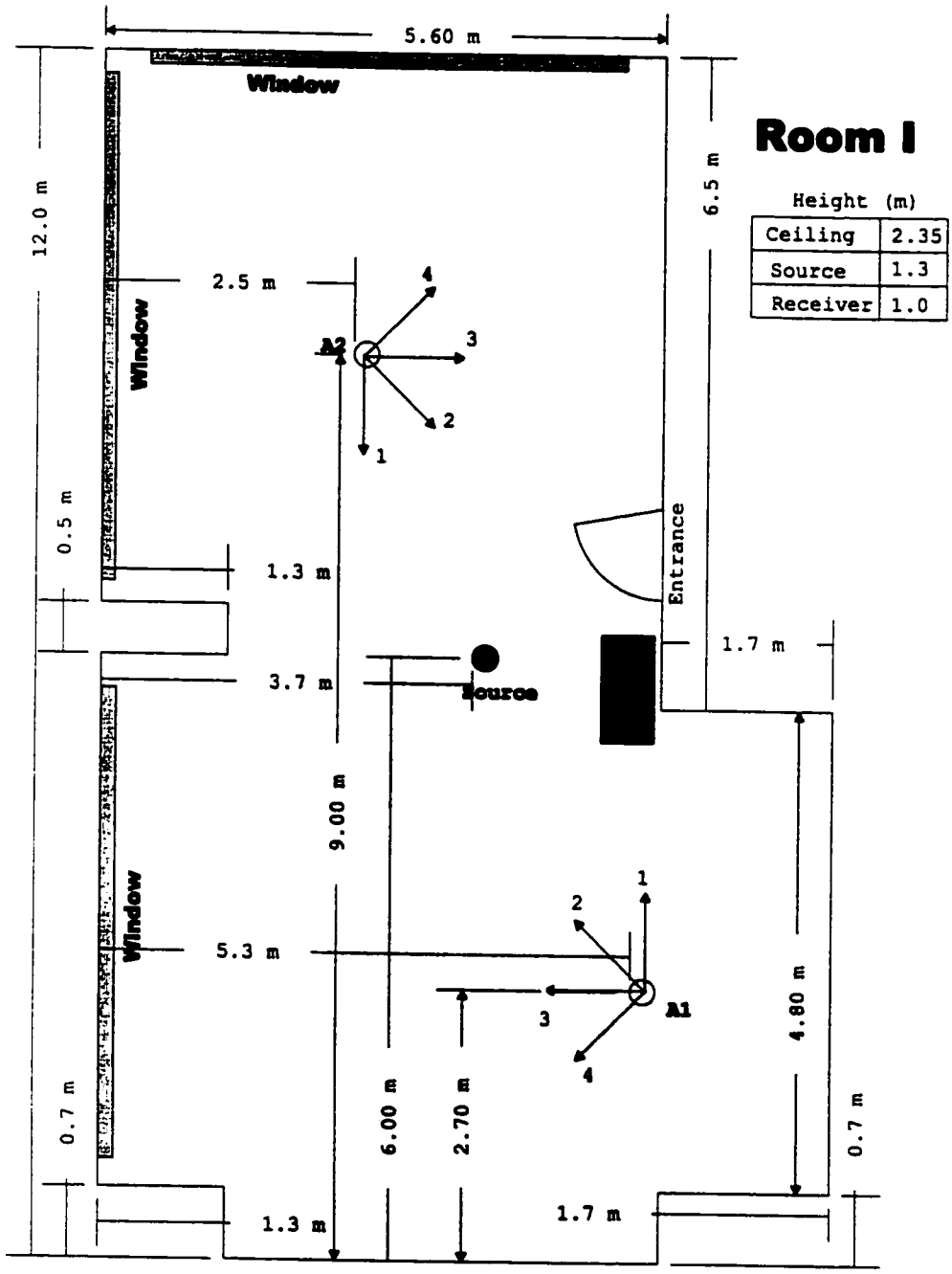

Room I (CBY 707B)

A large conference room with a long conference table in the middle and a number of chairs around it. As shown in the figure, there are windows on two sides of the room with a height of 1.2 m starting approximately 0.3m from the ceiling. There are light brown curtains covering the windows during measurements.

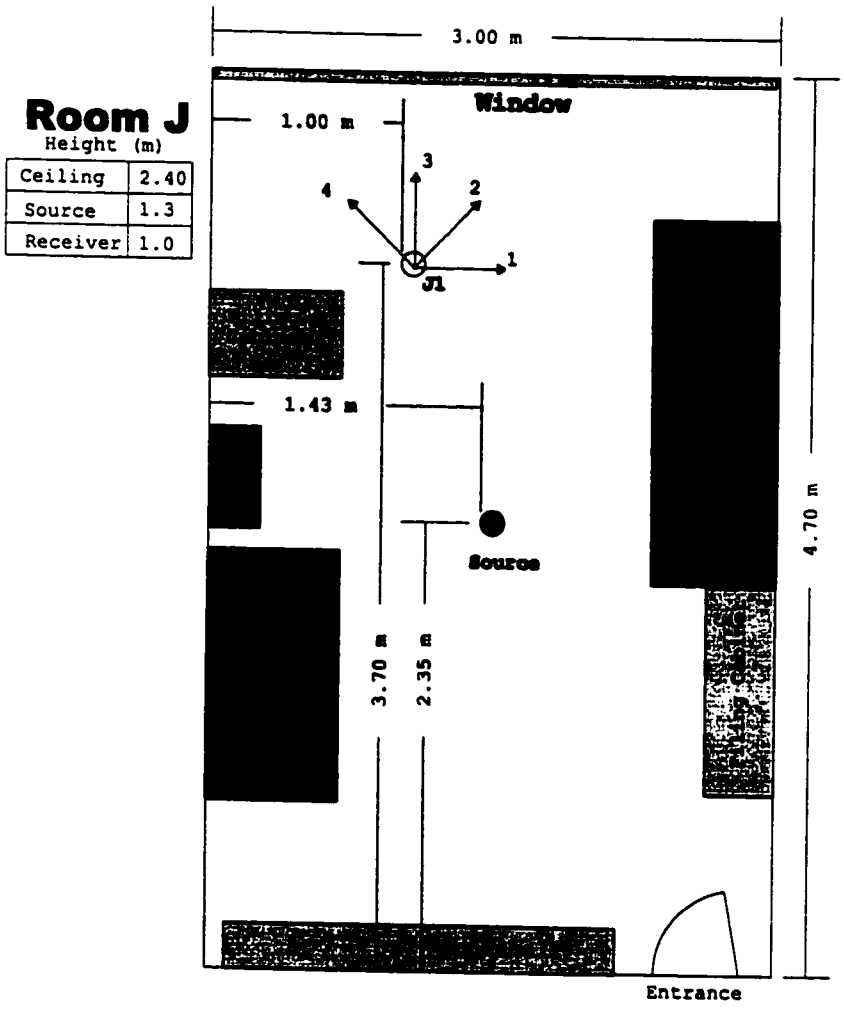

Room J (CBY A510)

A small office that has typical office equipments such as desk, filing cabinets and bookshelves. One side of the office is covered by windows that are starting 0.3 m from the ceiling and have a 1.2m height. Windows are covered with grey colored curtains during measurements.

REFERENCES

[1] "American National Standard for the Safe Use of Lasers," ANSI/Z136.1-1986, American National Standard Institute, New York, 1986.

[2] M. Abtahi, H. Hashemi, "Simulation of Indoor Propagation Channel at Infrared Frequencies in Furnished Office Environments," *IEEE International Symposium on Personal Mobile Indoor Radio Communications (PIMRC'95)*, Toronto, Ontario, Canada, September 1995.

[3] Adriano J.C.Moreira, Rui T.Valadas, A.M.de Oliveira Duarte, "Characterization and Modeling of Artificial Light Interference in Optical Wireless Communication Systems," *International Symposium on Personal, Indoor, and Mobile Radio Communications (PIMRC'95)*, Canada,Vol.1, pp. 326-331, September 1995.

[4] H. A. Ankerman, "Transmission of audio signals by infrared light carrier," *SMPTE Journal*, Vol. 89, pp. 834-837, November 1980.

[5] M.D. Audeh, J.M. Kahn, "Performance simulation of baseband OOK modulation for wireless infrared LAN at 100 Mb/s," *Proceedings of the IEEE International Conference on Selected Topics in Wireless Communications*, Vancouver, B. C., Canada, pp. 271-274, June 25-26, 1992.

[6] M.D. Audeh, J.M. Kahn, "Performance evaluation of L-Pulse Position modulation on Non-directed indoor infrared channels," *Proceedings of the international Conference on Communications (ICC '94)*, pp. 660-664, 1994.

[7] M. D. Audeh, J. R. Barry, "Performance of PPM with Maximum-Likelihood Sequence Detection on Measured Non-Directed Indoor Infrared Channels," *Proceedings of the International Conference on Communications (ICC'95)*, Seattle, USA, pp. 1177-1181, 1995.

[8] M.D. Audeh, J.M. Kahn , J.R. Barry, "Performance of Pulse-Position Modulation on Measured Non-Directed Indoor Infrared Channels," *IEEE Transaction on Communications*, vol. 44, pp. 654-659, June 1996.

[9] M.D. Audeh, J.M. Kahn , J.R. Barry, "Decision-Feedback Equalization of Pulse-Position Modulation on Measured Non-Directed Indoor Infrared Channels," *IEEE Transaction on Communications*, vol. 47, pp. 500-503, April 1999.

[10] G. Berline , E. Perratore, "Wireless LANs," *PC Magazine*, pp. 291-314, Feb 1992.

[11] J. Barry, J. M. Kahn, E.A. Lee, , D.G. Messerschmitt, "High speed nondirective optical communication for wireless networks," *IEEE Network Magazine*, pp. 44-54, November 1991.

[12] J. Barry, "Wireless communication using non-directed infrared light," Ph.D. dissertation, University of California at Berkeley, December 1992.

[13] J. Barry, J. M. Kahn, J. Krause, E. A. Lee, D. G. Messerschmitt, "Simulation of multipath impulse response for indoor wireless optical channels," *IEEE Journal on Selected Areas in Communications*, Vol. 11, No. 3, pp. 367-379, April 1993.

[14] J. Barry , J.M. Kahn, "Link Design for Non-Directed Wireless Infrared Communications," *Applied Optics*, vol. 34, no. 19, pp. 3764-3776, July 1995.

[15] M.J. Betancor, F.J. Gabiola, F. J. Lopez-Hernandez, "IR Wireless system on ARCNet Local Area Network," *Proceedings of 15th Conference on Local Computer Networks*, pp. 183-187, October 1990.

[16] M J. Betancor, J. Martin-Bernardo, A. Santamaria, V. M. Melian, F. J. Lopez-Hernandez, "Infrared wireless system for high speed RS-232/RS-423/RS-422 communications," *Proceedings of IEEE International Conference on Communications (ICC'92)*, pp. 505-510, 1992.

[17] M J. Betancor, J. Martin, J. Rivero, V. M. Melian, F. J. Gabiola, F. J. Lopez-Hernandez, "IEEE-488.2 communications by infrared wireless link," *Proceedings of IEEE International Conference on Communications (ICC'92)*, pp. 500-504, 1992.

[18] E. Braun, S. Schon, "A cordless infrared telephone," *Telecommunications report 3*, No. 2, pp. 83-86, 1980.

[19] W. L. Casey, et al., "Design considerations for air-to-air laser communications," *SPIE*, Vol. 1417, pp. 89-98, 1991.

[20] J.B. Carruthers , J.M. Kahn, "Multiple Sub-carrier Modulation for Non-Directed Wireless Infrared Communication," *IEEE Journal of Selected Areas in Communications*, vol. 14, pp. 538-546, April 1996.

[21] J.B. Carruthers, J.M. Kahn, "Modeling of Non-directed Wireless Infrared Channels," *IEEE Transaction on Communications*, vol. 45, no. 10, pp. 1260-1268, October 1997.

[22] J.B. Carruthers, J.M. Kahn, "Angle Diversity for Non-directed Wireless Infrared Communication," submitted to *IEEE Transaction on Communications*, July, 1997.

[23] K. Chen, "On-Off keying optical transmission and channel capacity for indoor high rate wireless data networks," *Proceedings of the IEEE GLOBECOM '91 Conference*, pp. 0418-0422, 1991.

[24] T.S. Chu, M.J. Gans, "High speed infrared local wireless communication," *IEEE Communication Magazine*, Vol. 25, No. 8, pp. 4-10, August 1987.

[25] Cipriano R.A.T. Lomba, Rui T. Valadas, A.M. de Oliveira Duarte, "Sectored Receivers to Combat the Multipath Dispersion of the Indoor Optical Channel," *International Symposium on Personal, Indoor, and Mobile Radio Communications (PIMRC'95)*, Toronto, Vol.1, pp. 321-325, September 1995

[26] Cipriano R.A.T. Lomba, Rui T. Valadas, A. M. de Oliveira Duarte, "Flexible Emitter Radiation Pattern for Indoor Wireless Local Area Networks," *COMCON V - International Conference on Advances in Communication & Control*, Crete, Greece, 26-30 June 1995.

[27] R. Citta, "An infrared wireless speaker system utilizing a super wide-band FM carrier," *IEEE Transaction on Consumer Electronics*, CE-21 , pp. 115-119, 1975.

[28] Cotton, Casey, "Narrow-band optical interference filters," *Proceedings of Electronic Laser '91*, Los Angeles, CA, January 1992.

[29] J. M. Cour, M. Misson, T. Val, "Using infrared impulse to transfer data asynchronously," *Proceedings of 16th Conference on Local Computer Networks*, Minneapolis USA, pp. 282-287, October 1992.

[30] M. P. Dames, R. J. Dowling, P. McKee, D. Wood, "Efficient optical elements to generate intensity weighted spot arrays: design and fabrication," *Applied Optics*, Vol. 30, No. 19, pp. 2685-2691, 1991.

[31] L. Diana, J.M. Kahn, "Rate-Adaptive Modulation Techniques for Infrared Wireless Communications," *Proceedings of IEEE International Conference on Communications (ICC '99)*, Vancouver, B.C., Canada, June 6-10, 1999.

[32] P. Djahani, J.M. Kahn, "Analysis of Infrared Wireless Links Employing Multi-Beam Transmitters and Imaging Diversity Receivers" submitted to *IEEE Transaction on Communications*, August 1998.

[33] D. D. Falconer, M. Abdulrahman, N. W. K. Lo, B. R. Peterson, A. U. Sheikh, "Advances in equalization and diversity for portable wireless systems," *Digital Signal Processing*, pp.148-162, 1993.

[34] F.J. Gabiola, N.J. Betancor, A. Santamaria, A. Polo, F. J. Lopez-Hernandez, "Optical-Electrical interface for IR wireless Ethernet local area network," *Proceedings 16th LCN '92*, pp. 273-275, 1992.

[35] F.J. Gabiola, K.L. Prentzas, "Signal power requirements for indoor directive and diffuse infrared communications channels," *Microwave and Optics Technology Journal*, Vol. 5, No. 3, pp. 148-152, 1992.

[36] F.J. Gabiola, N.J. Betancor, A. Santamaria, A. Polo, F.J. Lopez-Hernandez, "Irradiance analysis for indoor point-to-point and quasi-diffuse infrared channels," *Microwave and Optics Technology Journal*, Vol. 6, No. 9, pp. 557-560, July 1993.

[37] V.C. Georgopoulos, "Suppressing background-light interference in an in-house infrared communications system by optical filtering," *International Journal of Optics*, Vol. 3, No. 3, pp. 247-256, 1988.

[38] V.C. Georgopoulos, C.J. Gerorgopolous," A multiple IR/ RF wireless transmission system for indoor and outdoor communications," *Proceedings of IEEE International Conference on Communications (ICC'86)*, pp. 955-959, 1986.

[39] F. R. Gfeller, U. Bapst, "Wireless in-house data communication via diffuse infrared radiation," *IEEE Proceedings*, Vol. 67, No. 11, pp. 1474-1486, November 1979.

[40] F. R. Gfeller, P. Bernasconi, W. Hirt, C. Elisii, B. Weiss, "Dynamic cell planning for wireless infrared in-house data transmission," *Proceedings of International Zurich Seminar on Digital Communications*, Switzerland, pp. 261-272, 1994.

[41] A. Gunn, "Connecting over the airwaves," *PC Magazine*, pp. 359-384, August 1993.

[42] D. Hash, J. Hillery, J. White, "IR roomnet: Model and measurement," *IBM Communications ITL Conference*, June 1986.

[43] H. Hashemi, G. Yun, M. Kavehrad, F. Behbahani, P. Galko, "Frequency Response Measurement of the Wireless Indoor Channel at Infrared Optics," *Proceedings of International Zurich Seminar on Digital Communications*, Switzerland, pp. 273-284, 1994.

[44] H. Hashemi, G. Yun, M. Kavehrad, F. Behbahani, P. Galko, "Indoor Propagation Measurements at Infrared Frequencies for Wireless Local Area Networks Applications," *IEEE Transaction on Vehicular Technology*, Vol.43 No. 3, pp. 562-576, August 1994.

[45] K.P. Ho, J.M. Kahn, "Compound Parabolic Concentrators for Narrow-Band Wireless Infrared Receivers," *Optical Engineering*, vol. 34, no. 5, pp. 1385-1395, May 1995.

[46] P. Hortensius, "Research and development plan of the infrared portable data link," internal report, IBM T. J. Watson Res. Cent., Yorktown Heights, New York, 1990.

[47] IEC 60-825: "Safety of Laser Products," equipment classification, requirements and user's guide.

[48] M. Ishida, E. Toide, "A spatial optical transmission system for digital audio," *Mitsubishi Electronic Advances*, Vol. 58, pp. 36-38, 1992.

[49] Q. Jiang, M. Kavehrad, M. Pakravan, M. Tai," Wideband Optical Propagation Measurement System for Characterization of Indoor Wireless Infrared Channel," *Proceedings of the International Conference on Communications (ICC'95)*, Seattle, USA, pp. 1173-1176, 1995.

[50] D. P. Johnson, D. J. Cowan, "Free space local area network (FIRLAN), " *SPIE*, Vol. 32, No. 9, pp.2114-2117, 1993.

[51] J.M. Kahn, J.R. Barry, M.D. Audeh, E.A. Lee, D.G. Messerschmitt, "Design of high-speed wireless link using non-directional infrared radiation," *Proceedings of Third WINLAB Workshop on Third Generation Wireless Information Networks*, East Brunswick, N. J., April 28-29, 1992.

[52] J.M. Kahn, W.J. Krause, "Experimental characterization of multipath free-space infrared channels for wireless in-building networks," *Proceedings of 19th European Conference on Optical Communications*, Montreux, Switzerland, September 1993.

[53] J. M. Kahn, J. R. Barry, M. D. Audeh, J. B. Carruthers, W. J. Krause, G. W. Marsh, "Non-directed Infrared links for High-capacity wireless LANs," *IEEE Personal Communication Magazine*, Second quarter 1994, pp. 12-25, 1994.

[54] J.M. Kahn, W.J. Krause, J.B. Carruthers, "Experimental Characterization of Non-Directed Indoor Infrared Channels," *IEEE Transaction on Communications*, vol. 43, pp. 1 613-1623, April, 1995.

[55] J.M. Kahn, J.R. Barry, "Wireless Infrared Communications," *Proceedings of the IEEE*, pp. 265-298, February 1997.

[56] J.M. Kahn, P. Djahani, A.G. Weisbin, K.T. Beh, A.P. Tang, R. You, "Imaging Diversity Receivers for High-Speed Infrared Wireless Communication," *IEEE Communications Magazine*, vol.36 no.12, pp. 88-99, December 1998.

[57] M. Kavehrad, G. Yun, "Optical taper for increasing the effective area of a photodiode in atmospheric free space communications applications," Patent Number 5,192,863, United States patent, 09 March 1993.

[58] M.D. Kotzin, "Short-range communications using diffusely scattered infrared radiation," Ph.D. Dissertation, Northwestern University, June 1981.

[59] M.D. Kotzin, A.P. van den Heuvel, "A duplex infrared system for in-building communications," *Proceedings of IEEE Vehicular Technology Conference '86*, pp. 179-185, 1986.

[60] W. Krause, "Experimental characterization of Non-directive Indoor infrared channels," Master's report, University of California at Berkeley, December 1992.

[61] D.C. Lee, J.M. Kahn, M.D. Audeh, "Trellis-Coded Pulse-Position Modulation for Indoor Wireless Infrared Communications," *IEEE Transaction on Communications*, vol. 45, pp. 1080-1087, September 1997.

[62] D.C. Lee, J.M. Kahn, "Experimental 25-Mb/s Wireless Infrared Link Using 4-PPM with Scalar Decision-Feedback Equalization," *Proceedings of IEEE International Conference on Communications (ICC '98)*, Atlanta, GA, June 7-11, 1998.

[63] D.C. Lee, J.M. Kahn, "Coding and Equalization for PPM on Wireless Infrared Channels," *IEEE Transaction on Communications*, vol. 47, no. 2, pp. 255-260, February 1999.

[64] W. R. Leeb, "Degradation to signal to noise ratio in optical free space data links due to background illumination," *Applied Optics*, Vol. 28, No. 15, pp. 3443-3449, 15 August 1989.

[65] J. M. Lerner, R. Shie, J. Petersen, "Holographic Light Shaping Diffusers," *POC, Torrance, CA, presented at The Aerospace Lighting Institute, Advanced Seminar*, February 1994, Los Angeles 1994.

[66] A. Lessard, M. Gerla, "Wireless communications in the automated factory environment," *IEEE Network*, Vol. 2, No. 3, pp.64-69, May 1988.

[67] D. Liu, J.H. Herzog, "OptoNet, an omnidirectional optical data communication system," *IEEE Pacific Rim Conference on Communication, Computer, and Signal Processing*, pp. 95-97, May 1991.

[68] C. R. A. T. Lomba, R. T. Vladas, A. M. de Oliveria Durate, "Propagation losses and impulse response of the indoor optical channel: a simulation package," *Proceedings of International Zurich Seminar on Digital Communications*, Switzerland, pp. 285-297, 1994.

[69] M. Marhic, M. Kotzin, van den Heuvel, "Reflectors and immersion lenses for detectors of diffuse radiation," *Journal of Optical Society of America*, Vol. 72, No. 3, pp. 352-355, March 1982.

[70] G.W. Marsh, J.M. Kahn, "Performance Evaluation of Experimental 50-Mb/s Diffuse Infrared Wireless Link using On-Off Keying with Decision-Feedback Equalization," *IEEE Transaction on Communications*, vol. 44, no. 11, pp. 1496-1504, November 1996.

[71] G.W. Marsh, J.M. Kahn, "Channel Reuse Strategies for Indoor Infrared Wireless Communications," *IEEE Transaction on Communications*, vol. 45, no. 10, pp. 1280-1290, October 1997.

[72] MATLAB, Reference Guide, The MathWorks, Inc., 1997.

[73] M. J. McCullagh, I. Neild, D. R. Wisely, "A 1 Gb/s Optical Wireless LAN Supporting Mobile Transceivers, " pp. 468-480, *Wireless '94, Calgary*, Canada, July 94.

[74] M.J. McCullagh, D.R. Wisely, P.L. Eardley, P.P. Smyth, "A 50 Mb/s optical wireless LAN link using novel optical and electronic enabling technologies," *Proceedings of International Zurich Seminar on Digital Communications*, Switzerland, pp. 298-309, 1994.

[75] P. McKee, D. Wood, P. P. Smyth, "Applications of computer generated, free space diffracted optics from interconnections and packaging to optical wireless antennas," *Fourth International Conference on Holographic Systems, Components and Applications*, September 1993.

[76] T. Minami, K. Yano, T. Touge, H. Morikawa, O. Takahashi, "Optical wireless modem for office communications," *Proceedings AFIPS National Computer Conference*, Vol. 52, pp. 721-728, May 1983.

[77] A.J.C. Moreira, R.T. Valadas, A.M. de Oliveira Duarte," Performance of infrared transmission systems under ambient light interference," *IEE Proceedings Optoelectronics*, Vol. 143, No. 6, December 1996.

[78] A.J.C. Moreira, A. Tavares, R.T. Valadas, A.M. de Oliveira Duarte, "Modulation methods for wireless infrared transmission-Performance under ambient light noise and interference," *Proceedings of SPIE's Photonics East'95 Symposium*, pp. 226-237, Philadelphia, USA, October 1995.

[79] A.C. Moreira, R.T. Valadas, Duarte, "Reducing the Effects of Artificial Light Interference in Wireless Infrared Transmission Systems," *Proceedings of the IEE Colloquim on Optical Free Space Communication Links*, Savoy Place, London, UK, pp. 5/1-5/9, February 1996.

[80] Y. Nakata, J. Kashio, T. Kojima, T. Nouguchi, "In-house wireless communication system using infrared radiation," *Proceedings of International Conference on Computer Communications*, pp. 333-337, 1984.

[81] A. Paepcke, R. Crawford, C. Freeman, F. Lee, R. Paull, "An optical local area network," *Conference Karlsruhe*, W. Germany, March 1985.

[82] K. Pahlavan, "A review of wireless in-house data communication systems," *Proceedings of Computer Networking Symposium*, pp. 129-136, 1984.

[83] K. Pahlavan, "Wireless communications for office information networks," *IEEE Communications Magazine*, Vol. 23, No. 6, pp. 19-27, June 1985.

[84] K. Pahlavan, "Wireless data communication techniques for indoor applications," *Proceedings of IEEE International Conference on Communications (ICC'85)*, pp.372-378, 1985.

[85] M. R. Pakravan, M. Kavehrad, "A Solution to Multipath Problem in Indoor Infrared Wireless Broadband Communications," *17th Biennial Symposium on Communications*, Kingston, Canada, pp. 341-345, 1994.

[86] M. R. Pakravan, "Broadband Indoor Wireless Communications using Infrared," M.Sc. Thesis, University of Ottawa, Canada, August 1994.

[87] M. R. Pakravan, M. Kavehrad, "Design Considerations for Broadband Indoor Infrared Wireless Communication Systems," *International Journal on Wireless Information Networks*, Vol. 2, No. 4, 1995.

[88] M. Pakravan, M. Kavehrad, "Direction Diversity for Broadband Indoor Wireless Communications," *Proceedings of the international Conference on Communications (ICC'95)*, Seattle, USA, pp. 1340-1346, 1995.

[89] M.R. Pakravan, "Estimation of Indoor Infrared Channel parameters Using Neural Networks," *IEEE International Symposium on Personal Mobile Indoor Radio Communications (PIMRC'95)*, Toronto, pp. 311-316, September 1995.

[90] M. R. Pakravan, M. Kavehrad, "Distribution of Infrared Light Power for Indoor Broadband Wireless Communications," *Proceedings of Personal Indoor Mobile Radio Communications*, Toronto, pp. 316-320, September 1995.

[91] M. R. Pakravan, H. Hashemi, M. Kavehrad, "Indoor Infrared Channel Modeling, " *Annual CITR Conference*, August 96, Montebello, Canada

[92] M. R. Pakravan, E. Simova, M. Kavehrad, " Holographic Diffusers For Indoor Infrared Wireless Communications, " *International Conference on Global Communications (Globecomm'96)*, November 96.

[93] M. R. Pakravan, E. Simova, M. Kavehrad, "Holographic Diffusers For Indoor Infrared Wireless Communications, " *International Journal of Wireless Information Networks*, December 1997.

[94] M. Pakravan, M. Kavehrad, H. Hashemi, "Measurement of Rotation effects in an indoor Infrared Channel," *Proceedings of the IEEE Vehicular Technology Conference (VTC'98)*, Ottawa, Ontario, Canada, May 1998.

[95] 1. M. R. Pakravan, M. Kavehrad, H. Hashemi, " Effects of Rotation on the Path Loss and the Delay Spread in Indoor Infrared Communications," *Proceedings of the IEEE International Conference on Communication (ICC'98)*, Atlanta, GA, USA, July 1998.

[96] 1. M. R. Pakravan, M. Kavehrad, H. Hashemi, "Investigation of the Receiver Rotation and Shadowing Effects in Indoor Infrared Channel," Submitted for publication to *IEEE Transaction of Vehicular Technology*, Oct. 1998.

[97] H. Park, J. R. Barry, "Modulation Analysis for Wireless Infrared Communications," *1995 International Conference on Communications*, Seattle, vol. 2, pp. 1182-1186, June 1995.

[98] H. Park, J. R. Barry, "The Performance of Multiple Pulse-Position Modulation on Multipath Channels," *IEE Proceedings - Optoelectronics*, vol. 143, no. 6, pp. 360-364, December 1996.

[99] H. Park, J. R. Barry, "Performance Analysis and Channel Capacity for Multiple-Pulse Position Modulation on Multipath Channels," *International Symposium on Personal, Indoor and Mobile Radio Communications* (PIMRC 96), vol. 1, pp. 247-251, Taipei, October 15-18, 1996.

[100] H. Park, J. R. Barry, "Trellis-Coded Multiple Pulse-Position Modulation for Wireless Infrared Communication," *IEEE Global Communications Conference (Globecom'98)*, Sydney, November 1998.

[101] H. Park, J. R. Barry, "A Partial-Response Pre-coding Scheme for Wireless Infrared Communication," *International Symposium on Personal, Indoor, and Mobile Radio Communications (PIMRC'98)*, Boston, September 1998.

[102] I.A. Parkin, J. Zic, "An application of Infra-red Communication," *Journal of Electrical and Electronic Engineering*, Australia, Vol. 4, No. 4, pp.331-336, December 1984.

[103] D. R. Pauluzzi, P. R. H. McConnell, R. L. Poulin, "Free-space, undirected infrared (IR) voice and data communications with a comparison to RF systems," *Proceedings of the IEEE International Conference on Selected Topics in Wireless Communications*, pp. 279-285, 1992.

[104] R. Pawluczyk, "Holographic Diffusers," SPIE, Vol. 2042, pp. 156-168, *Photopolymers and Application in Holography, Optical Data Storage, Optical Sensors, and Interconnections*, Quebec, 16-18 August 1993.

[105] R.L. Poulin, D.R. Pauluzzi, M. R. Walker, "A multi-channel infrared telephony demonstration system for public access applications," *Proceedings IEEE International Conference on Selected Topics in wireless Communications*, pp. 286-291, 1992.

[106] A. Santamaria, J. L. Munoz, F. J. Gabiola, F. J. Lopez-Hernandez, "IR wireless system for Ethernet local area network," *Proceedings of the 9th annual European Fiber Optic Communications and LAN Conference*, Vol: LAN, pp. 126-130, June 1991.

[107] D. Shiu, J.M. Kahn, "Shaping and Non-Equiprobable Signaling for Intensity Modulated Signals," submitted to *IEEE Transaction on Information Theory*, July 1998.

[108] D. Shiu, J.M. Kahn, "Differential Pulse-Position Modulation for Power-Efficient Optical Communication," to be published in *IEEE Transaction on Communications*, vol. 47, no. 8, pp. 1201-1210, August, 1999.

[109] D. Shiu, J.M. Kahn, "Power Allocation Strategies for Wireless Systems with Multiple Transmit Antennas," submitted to *IEEE Transaction Communications*,

[110] E. Simova, M. Kavehrad, "Holographic Stars," *Applied Optics*, Vol. 34, 6350-6353, October 1995.

[111] E. Simova, M. Kavehrad, "Light Shaping Diffusers for Indoor Infrared Communications via a Holographic Approach," *SPIE*, San Jose, USA, February 1996.

[112] P. P. Smyth, M. McCullage, D. Wisely, S. Ritchie, P. Eardley and Cassidy, "Optical wireless Local Area Networks-enabling technologies," *British Telecom Technical Journal*, Vol. 11, No. 2, April 1993.

[113] P.P. Smyth, D. Wood, S. Ritchie, S. Cassidy, "Optical wireless: New enabling technologies," *Proceedings of the International Conference on Communications (ICC'93)*, Vol. 1, pp. 562-566, 1993.

[114] A.P. Tang, J.M. Kahn, K.-P. Ho, "Wireless Infrared Communication Links using Multi-Beam Transmitters and Imaging Receivers," *Proceedings of IEEE International Conference on Communications (ICC'96)*, pp. 180-186, Dallas, Texas, June 23-27, 1996.

[115] A. Tavares, R. Valadas, A.M.de Oliveira Duarte, "Performance of an optical sectored receiver for indoor wireless communication system in presence of artificial and natural noise sources," *SPIE's 1st International Symposium on Photonics Technology and Systems for Voice and Data Communications*, USA , pp. 264-273,October 1995.

[116] A. Tavares, A. Moreira, C. Lomba, L. Moreira, R. Valadas, O. Duarte, "Experimental Results of a 1 Mbps IR Transceiver for Indoor Wireless LANs," *COMCON International Conference on Advances in Communications & Control*, Crete, Greece, June 1995.

[117] R. Valadas, A. Moreira, A. Durate, "Hybrid (wireless infrared/coaxial) Ethernet local area networks," *Proceedings of the IEEE International Conference on Wireless LAN Implementation*, pp. 21-29, September 1992.

[118] R. Valadas, A. Moreira, C. Oliveira, L. Moreira, C. Lomba, A. Tavares, A. Duarte, "Experimental Results of a Pulse Position Modulation Infrared Transceiver," *International Symposium on Personal, Indoor, and Mobile Radio Communications (PIMRC'96)*, Taipei, Taiwan, pp.252-256, October 1996.

[119] R. Valadas, "Interference Modeling for the Simulation of IEEE 802.11 Infrared Local Area Networks," *International Symposium on Personal, Indoor, and Mobile Radio Communications (PIMRC'96)*, Taipei, Taiwan, pp.257-261, October 1996.

[120] J. H. Winters, "Optimum Combining in Digital Mobile Radio with Co-channel Interference," *IEEE Journal on Selected Area in Communications*, Vol. SAC-2, No. 4, July 1984.

[121] "Wireless networking," *BYTE Magazine*, pp. 291-294, April 1992.

[122] Y. Yamauchi, M. Sato, T. Namekawa, "In-house wireless optical digital SSMA," *Electronics and Communications in Japan*, Part 1, Vol. 70, No. 6, 1987.

[123] G. Yun, M. Kavehrad, "Spot diffusing and fly-eye receivers for indoor infrared wireless communications," in *Proceedings of the IEEE International Conference on Selected Topics in Wireless Communications*, Vancouver, B. C., Canada, pp. 262-265, 1992.

[124] C.S. Yen, R.D. Crawford, "The use of directed optical beams in wireless computer communications," *Proceedings of the IEEE GLOBECOM '85 Conference*, New Orleans, pp. 1181-1184, December 2-5, 1985.